Massive MIMO for 5G Scenarios with OFDM and FBMC/OQAM Waveforms

Alexis Bazin

UNIVERSITE BRETAGNE LOIRE / MATHSTIC

INSA RENNES

THESE DE DOCTORAT DE

L'INSA RENNES
COMUE UNIVERSITE BRETAGNE LOIRE

ECOLE DOCTORALE N° 601
Mathématiques et Sciences et Technologies de l'Information et de la Communication
Spécialité : *Télécommunications*

Par
Alexis BAZIN

Massive MIMO for 5G Scenarios with OFDM and FBMC/OQAM Waveforms

Thèse présentée et soutenue à Rennes, le 24/09/2018
Unité de recherche : IETR INSA Rennes
Thèse N° : 18ISAR 17 / D18 - 17

Rapporteurs avant soutenance :

Daniel Roviras	Professeur, CNAM, Paris
Eric Simon	Maître de conférences HDR, USTL, Villeneuve d'Ascq

Composition du Jury :

Daniel Roviras	Professeur, CNAM, Paris / Rapporteur et Président
Eric Simon	Maître de conférences HDR, USTL, Villeneuve d'Ascq / Rapporteur
Mérouane Debbah	Professeur, CentraleSupelec, Gif-sur-Yvette / Examinateur
Charbel Abdel Nour	Maître de conférences, IMT Atlantique, Brest / Examinateur
Bruno Jahan	Ingénieur, Orange, Cesson-Sévigné / Co-Encadrant
Maryline Hélard	Professeur, INSA, Rennes / Directrice de thèse

Invité

Hao Lin	Ingénieur, Orange, Cesson-Sévigné

Intitulé de la thèse :

Massive MIMO for 5G Scenarios with OFDM and FBMC/OQAM Waveforms

Alexis BAZIN

En partenariat avec :

Acknowledgements

After these three years, it is a great pleasure for me to express my feelings of gratitude to everyone who contributed to this thesis.

First and foremost, I would like to express my sincere thanks to my supervisors, Maryline Hélard and Bruno Jahan, for giving me the opportunity to make this PhD thesis. I am truly grateful for that. Thank you also for your insightful guidance and advices and for your support throughout these three years. Above all, thank you for your enthusiasm and for your sympathy. It was a pleasure to work with you.

I would like to thank the members of my thesis committee, Mérouane Debbah, Charbel Abdel Nour, Daniel Roviras and Eric Simon for accepting to review, evaluate and discuss this work.

I would like to express my sincere thanks to Philippe Blusseau, my Orange team leader, and to his predecessor Jean-Christophe Rault, for welcoming me at Orange and for their availability. More generally, I would like to warmly thank all my colleagues, the whole CREM team, my daily coffee companions, PhD students and interns, with whom I really enjoyed spending time. Thank you for your help, your support. Thank you for the interesting and inspiring discussions. And most of all, thank you for your kindness.

Last but not least, I am heartily thankful to my friends and family. I extend special thanks to my partner Elaine, who has always been there for me in every situation. Finally, I deeply thank my parents Evelyne and Antoine, who have always supported and encouraged me for everything I have done. Without you, this thesis would not have been possible.

Alexis BAZIN

Résumé Étendu en Français

Introduction

Depuis le début des années 90, les réseaux cellulaires ont constamment évolué afin de s'adapter aux nouveaux besoins. Avec l'augmentation du trafic de données, la multiplication des objets connectés et la diversification des types de communication, la génération actuelle de réseaux cellulaires (4G) sera inadaptée dans les années à venir. Ainsi, une nouvelle génération de réseaux cellulaires (5G) est en cours d'étude afin de répondre aux futurs besoins [1–4]. La Figure 1 compare les exigences de la 5G avec celles de la 4G actuelle.

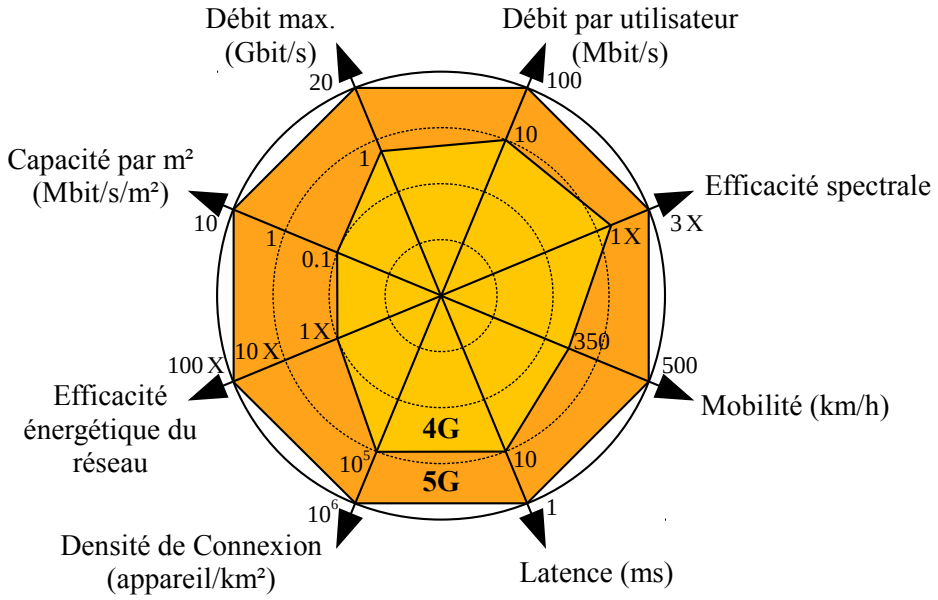

FIGURE 1 : Comparaison entre les exigences de la 4G et celles de la 5G (source : ITU-R [1]).

Les systèmes "massive Multiple-Input Multiple-Output (MIMO)" font partie des technologies clés susceptibles de répondre aux besoins décrits précédemment. En effet, en utilisant un grand nombre d'antennes et des techniques de traitement de signal adaptées, les systèmes "massive MIMO" permettent d'améliorer les performances du réseau en termes de débit,

de couverture ou encore d'efficacité énergétique. En parallèle, l'utilisation de la modulation FBMC/OQAM, au lieu de la modulation OFDM utilisée dans le réseau 4G, pourrait améliorer les performances des systèmes dans certaines situations. Les systèmes "massive MIMO" ainsi que les modulations OFDM et FBMC/OQAM sont introduits dans une première partie. Nous nous intéressons ensuite à deux scénarios 5G distincts. Le premier scénario, traité dans la deuxième partie de cette thèse, concerne les applications véhiculaires. Dans ce contexte, les systèmes "massive MIMO" sont proposés dans le but de combattre les interférences dues à l'effet Doppler pour la voie montante. Le second scénario, traité dans la troisième partie de cette thèse, s'intéresse aux communications dans les zones mal desservies. Dans ce contexte, les systèmes "massive MIMO" permettent de créer un lien sans fil longue portée de type "backhaul" entre deux stations de base et réduisent par ce biais le coût de déploiement des réseaux cellulaires.

Modulations Multiporteuses et Massive MIMO

La première partie de cette thèse est destinée à décrire les concepts sur lesquels elle se base : la modélisation des canaux de propagation, les modulations OFDM et FBMC/OQAM et les systèmes "massive MIMO".

Canaux de Propagation

Le canal de propagation caractérise les modifications subies par un signal entre l'émetteur et le récepteur. Sa compréhension est nécessaire pour bien évaluer les performances des systèmes de communication. Le Chapitre 1 introduit la modélisation des canaux de propagation sans fil.

Pour les communications cellulaires, le canal de propagation considéré est généralement un canal de propagation multi-trajet. Celui-ci caractérise les multiples réflexions du signal envoyé sur différents obstacles (sol, immeubles, arbres, etc.). Généralement, la modélisation de ce canal de propagation prend en compte l'étape de transposition du signal envoyé de la bande de base à la fréquence porteuse au niveau de l'émetteur et l'étape de transposition du signal reçu de la fréquence porteuse à la bande de base au niveau du récepteur [5,6]. On parle de canal de propagation en bande de base. Ce canal de propagation peut être caractérisé par la perte de puissance en propagation et par les composantes multi-trajets dues aux réflexions du signal envoyé.

A cause des composantes multi-trajets, le canal de propagation agit comme un filtre à réponse impulsionnelle finie. Cela induit une variation dans le domaine fréquentiel du canal de propagation. On parle de sélectivité fréquentielle du canal de propagation. En parallèle, la mobilité de l'émetteur, du récepteur ou d'éléments du canal de propagation (voiture, train, etc.) fait varier temporellement les composantes multi-trajets à cause de l'effet Doppler, ce

qui induit une variation dans le domaine temporel du canal de propagation. On parle de sélectivité temporelle du canal de propagation.

Afin de représenter les canaux de propagation multi-trajets, il est nécessaire de définir des modèles. Trois types de canaux de propagation sont introduits dans cette thèse. Leur description est donnée ci-dessous.

- Les *canaux de Rayleigh* permettent de modéliser des environnements "Non-Line-Of-Sight" (NLOS), lorsque l'émetteur n'a pas une vue directe sur le récepteur. Avec ce modèle, les variations temporelles du canal de propagation sont dues à un type particulier d'effet Doppler appelé le "Doppler spread".

- Les *canaux de Rice* modélisent des environnement "Line-Of-Sight" (LOS), lorsque l'émetteur a une vue directe sur le récepteur. Avec ce modèle, les variations temporelles du canal de propagation sont dues à l'addition de deux types d'effet Doppler, le "Doppler spread" et le "Doppler shift".

- Les *canaux géométriques* prennent en compte les caractéristiques spatiales de l'environnement de propagation (hauteur des antennes, distance émetteur-récepteur, etc.). Ainsi, ils permettent une évaluation plus précise des systèmes de communication et notamment des systèmes "massive MIMO" en comparaison des canaux de Rayleigh et de Rice. En revanche, leur complexité est plus élevée.

Modulations Multiporteuses

En distribuant les données à envoyer dans le domaine fréquentiel, les modulations multiporteuses permettent une bonne résistance face à la sélectivité fréquentielle du canal de propagation. C'est pourquoi elles sont largement utilisées dans les systèmes actuels. Dans le Chapitre 2, les deux modulations multiporteuses étudiées dans cette thèse, la modulation OFDM et la modulation FBMC/OQAM, sont introduites.

La modulation "Orthogonal Frequency-Division Multiplexing" (OFDM) est une des modulations multiporteuses les plus utilisées actuellement (DVB, WiFi, 4G LTE). Les symboles OFDM sont mis en forme par un signal rectangulaire dans le domaine temporel. Classiquement, un préfixe cyclique (CP) est ajouté entre chaque symbole. Il s'agit d'une recopie de la fin de chaque symbole positionnée au début de celui-ci [7]. Ce CP permet d'éviter les interférences entre symboles (ISI) en contrepartie d'une perte d'efficacité spectrale. Une des particularités de la modulation OFDM est que les données se chevauchent dans le domaine fréquentiel mais n'interfèrent pas entre elles. Ainsi, la modulation OFDM est orthogonale dans le champ complexe et il n'y a pas d'interférence entre sous-porteuses (ICI). Pour finir, l'implémentation de la modulation OFDM se révèle relativement peu complexe grâce aux algorithmes "Fast Fourier Transform" (FFT) et "Inverse Fast Fourier Transform" (IFFT) [8].

La modulation "Filter-Bank Multi-Carrier with Offset Quadrature Amplitude Modulation" (FBMC/OQAM) est une modulation multiporteuse alternative [9]. Contrairement à la modulation OFDM, celle-ci peut être mise en forme par un grande variété de "filtres prototypes". Cela permet d'obtenir une meilleure localisation en temps et en fréquence du signal modulé. Ainsi, la modulation FBMC/OQAM n'a pas besoin de CP et présente donc une meilleure efficacité spectrale que la modulation OFDM. En revanche, l'orthogonalité de la modulation FBMC/OQAM n'est cette fois-ci vraie que dans le champ réel. Contrairement à la modulation OFDM, la sélectivité fréquentielle du canal de propagation induit de l'ISI et de l'ICI, appelées "interférences intrinsèques". Ces interférences sont cependant négligeables la plupart du temps grâce à la bonne localisation temporelle et fréquentielle des filtres prototypes. Pour finir, l'implémentation de la modulation FBMC/OQAM se fait grâce à un banc de filtres et à des blocs FFT/IFFT [9]. Cependant, en comparaison de l'OFDM, les algorithmes FFT et IFFT doivent fonctionner deux fois plus rapidement avec la modulation FBMC/OQAM ce qui induit une complexité plus grande.

Massive MIMO

Les systèmes "massive MIMO" utilisent un grand nombre d'antennes (plusieurs dizaines) en association avec des techniques de traitement de signal adaptées afin d'améliorer les performances en termes de débit, de couverture ou encore d'efficacité énergétique. En se basant sur les résultats de [10,11], de nombreux travaux ont étudié les systèmes "massive MIMO" [12–22]. Ainsi, les systèmes "massive MIMO" ont été identifiés comme une des technologies clés pour le développement de la 5G [2, 4, 23]. Ces systèmes font l'objet du Chapitre 3.

Pour la voie montante, une station de base "massive MIMO" utilisée en réception offre un grand nombre d'avantages. En particulier, cela permet de recevoir et de traiter simultanément les signaux provenant des plusieurs utilisateurs. Par ailleurs, le rapport signal sur interférence plus bruit (SINR) peut être significativement augmenté [12, 15]. Les principales techniques pouvant être utilisées à cet effet sont décrites ci-dessous.

- La technique *"Maximum Ratio Combining" (MRC)* permet de maximiser le rapport signal sur bruit (SNR).
- La technique *"Zero Forcing" (ZF)* annule les interférences multi-utilisateurs (MUI).
- La technique *"Minimum Mean Square Error" (MMSE)* offre un compromis entre la maximisation du SNR et la minimisation des MUI.

On peut noter que la complexité est plus importante pour les techniques ZF et MMSE que pour la technique MRC.

Pour la voie descendante, une station de base "massive MIMO" utilisée à l'émission permet de focaliser spatialement l'énergie transmise et offre la possibilité de servir plusieurs

utilisateurs en même temps [19–21]. On parle de "Space-Division Multiple-Access" (SDMA). Les techniques de précodage, ou précodeurs, pouvant être utilisées à cet effet sont décrites ci-dessous.

- La technique *"Maximum Ratio Transmission" (MRT)* permet de maximiser les puissances reçues par les utilisateurs.
- La technique *ZF* annule les interférences multi-utilisateurs (MUI).
- La technique *MMSE* ou *"Regularized Zero Forcing" (RZF)* offre un compromis entre la maximisation de la puissance reçue et la minimisation des MUI.

La technique MRT offre une complexité plus faible que les techniques ZF et MMSE.

Massive MIMO pour des Applications Véhiculaires

Dans cette deuxième partie, nous nous intéressons aux scénarios véhiculaires ou "Vehicle-to-Everything" (V2X) où la vitesse de l'émetteur et/ou du récepteur est élevée. En particulier, les systèmes "massive MIMO" sont étudiés dans le but de réduire l'impact des interférences liées à l'effet Doppler.

Contexte de l'Étude

Avec le développement des trains à grande vitesse et des voitures connectées, les communications véhiculaires sont au centre de nombreuses études [24–28]. D'après le "Radiocommunication Sector of International Telecommunication Union" (ITU-R) [1], la 5G devra permettre des communications pour des vitesses allant jusqu'à 500 km/h. Dans ce contexte, les interférences dues à l'effet Doppler peuvent avoir un effet néfaste sur les performances des systèmes.

Dans le Chapitre 4, l'impact de l'effet Doppler sur les performances d'un système "massive MIMO" est évalué pour la voie montante. Dans ce but, une communication entre un utilisateur en mouvement équipé d'une seule antenne et une station de base "massive MIMO" équipée d'un grand nombre d'antennes est considérée. Ce scénario est décrit par la Figure 2. Cette

FIGURE 2 : Voie montante d'une communication entre un utilisateur en mouvement équipé d'une seule antenne et une station de base "massive MIMO" équipée d'un grand nombre d'antennes.

étude prend en compte les modulations OFDM et FBMC/OQAM pour des environnements NLOS et LOS. De plus, la technique MRC est utilisée en réception, pour sa faible complexité.

La modélisation du système effectuée dans le Chapitre 4 prend en compte la sélectivité temporelle du canal de propagation et permet de tirer les conclusions suivantes.

- Avec la *modulation OFDM*, la mobilité de l'utilisateur induit la création d'ICI liées à l'effet Doppler. En particulier, ces interférences sont dues au "Doppler spread" pour les environnements NLOS et à l'addition du "Doppler spread" et du "Doppler shift" pour les environnements LOS.

- Avec la *modulation FBMC/OQAM*, la mobilité de l'utilisateur induit la création d'ICI et d'ISI dues à l'effet Doppler. Ces interférences viennent s'ajouter aux interférences intrinsèques liées à la sélectivité fréquentielle du canal de propagation. En particulier, elles sont dues au "Doppler spread" pour les environnements NLOS et à l'addition du "Doppler spread" et du "Doppler shift" pour les environnements LOS.

Cette modélisation sert de base pour la suite de l'étude.

Massive MIMO pour Réduction de l'Effet Doppler

Dans le Chapitre 5, l'étude se centre sur des communications OFDM en environnement NLOS. Ainsi, l'effet Doppler se résume au "Doppler spread" dans ce contexte. L'objectif du Chapitre 5 est d'étudier l'impact d'une augmentation du nombre d'antennes de réception sur les ICI dues au "Doppler spread".

En se basant sur la modélisation du système du Chapitre 4, une étude analytique est réalisée pour faire le lien entre le nombre d'antennes sur la station de base et le rapport signal sur interférence (SIR). Cette étude permet d'exprimer le SIR asymptotique, lorsque le nombre d'antennes sur la station de base tend vers l'infini. Par ailleurs, cette analyse donne une condition nécessaire et suffisante pour que le SIR augmente avec l'augmentation du nombre d'antennes. Cependant, ces deux résultats reposent sur la connaissance de propriétés statistiques du canal de propagation. En utilisant une décomposition en somme-de-sinusoïdes du canal de propagation [29], ces propriétés statistiques, sur lesquelles se basent l'expression du SIR asymptotique et la condition nécessaire et suffisante, sont exprimées de manière analytique.

Les résultats numériques permettent d'une part, de vérifier l'expression du SIR asymptotique et, d'autre part, de prouver que l'augmentation du nombre d'antennes sur la station de base induit une diminution de l'impact des interférences dues au "Doppler spread". Pour conclure, le Chapitre 5 met en avant la possibilité de réduire l'impact du "Doppler spread" en utilisant un système "massive MIMO" combiné avec un récepteur MRC à faible complexité.

OFDM Versus FBMC/OQAM

Dans le Chapitre 5, la diminution de l'impact du "Doppler spread" avec l'augmentation du nombre d'antennes de réception a été démontrée. Cependant, il n'est pas dit que le système étudié permette de réduire l'impact du "Doppler shift" lorsqu'un environnement LOS est considéré. Par ailleurs, la modulation FBMC/OQAM est connue pour être plus robuste que la modulation OFDM face à l'effet Doppler pour des communications "Single-Input Single-Output" (SISO) [30–33]. On peut alors se demander si cette supériorité est toujours vraie dans un contexte "massive MIMO". Ainsi, dans le Chapitre 6, les modulations OFDM et FBMC/OQAM sont comparées pour la voie montante d'un système "massive MIMO" avec mobilité. Contrairement au Chapitre 5, des environnements NLOS et LOS sont considérés.

En se basant sur la modélisation du système du Chapitre 4, une étude analytique permet de donner l'expression de la capacité asymptotique du système, lorsque le nombre d'antennes sur la station de base tend vers l'infini, pour les modulations OFDM et FBMC/OQAM. Ces travaux amènent aux contributions décrites ci-dessous.

- Les résultats analytiques permettent d'examiner le choix du filtre prototype pour la modulation FBMC/OQAM dans un système "massive MIMO". Il en ressort qu'un filtre court est plus robuste face à la sélectivité temporelle du canal de propagation due à l'effet Doppler, tandis qu'un filtre long est plus robuste face à la sélectivité fréquentielle du canal de propagation et limite les interférences intrinsèques.
- Les résultats analytiques permettent une première comparaison des deux modulations considérées en termes de capacité asymptotique du système. En particulier, la modulation OFDM surpasse la modulation FBMC/OQAM en environnement NLOS, tandis qu'en environnement LOS, la modulation FBMC/OQAM offre de meilleures performances.

Des simulations sont ensuite conduites pour compléter cette étude. Elles permettent d'une part de vérifier les expressions analytiques de la capacité asymptotique des systèmes OFDM et FBMC/OQAM et, d'autre part, de comparer ces deux modulations en termes de taux d'erreur binaire (BER) en environnements NLOS et LOS. Pour illustrer ces résultats, les BER avec codage de canal en fonction du SNR sont donnés pour les modulations OFDM et FBMC/OQAM en environnement NLOS par la Figure 3 et en environnement LOS par la Figure 4. Les détails concernant les paramètres de simulation sont donnés dans la partie 6.4. Les résultats des simulations permettent de donner les conclusions suivantes.

- Dans un *environnement NLOS*, l'impact de l'effet Doppler diminue rapidement lorsque le nombre d'antennes augmente, grâce à la réduction du "Doppler spread" prouvée dans le Chapitre 5. Ainsi, cet impact devient négligeable même avec un faible nombre d'antennes en réception (16 antennes). Les deux modulations considérées mènent alors aux mêmes performances en termes de BER.

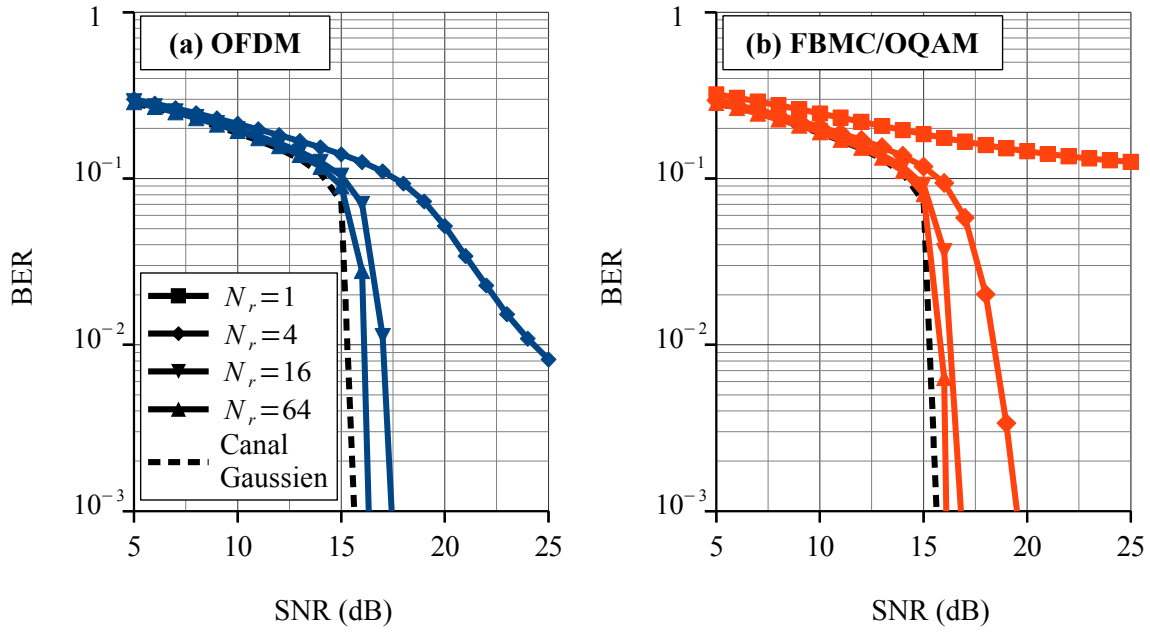

FIGURE 3 : BER avec codage de canal en fonction du SNR et du nombre d'antennes de réception N_r sur un canal de propagation EVA (environnement NLOS). (a) La modulation OFDM est utilisée. (b) La modulation FBMC/OQAM est utilisée.

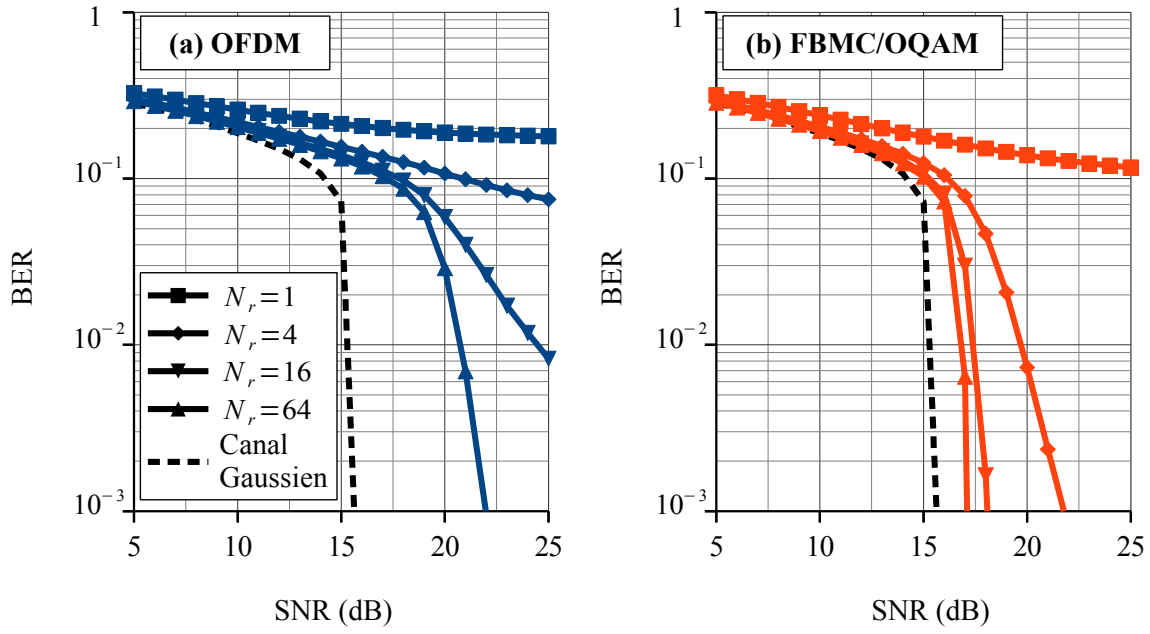

FIGURE 4 : BER avec codage de canal en fonction du SNR et du nombre d'antennes de réception N_r sur un canal de propagation RA4 (environnement LOS). (a) La modulation OFDM est utilisée. (b) La modulation FBMC/OQAM est utilisée.

- Dans un *environnement LOS*, le "Doppler shift" impacte les performances de la modulation OFDM même avec un grand nombre d'antennes de réception. En revanche, la modulation FBMC/OQAM offre une meilleure robustesse que la modulation OFDM

face au "Doppler shift". Ainsi, l'utilisation de la modulation FBMC/OQAM permet un gain significatif en termes de BER.

Massive MIMO pour une Liaison de Type "Backhaul" Sans Fil

Cette troisième partie concerne les communications dans les zones à faible revenu moyen par utilisateur (ARPU), généralement mal desservies. Dans ce contexte, les systèmes "massive MIMO" permettent la création d'un lien sans fil de type "backhaul" entre deux stations de base. Par ce biais, le coût de déploiement du réseau est réduit et la qualité de service peut être améliorée.

Contexte de l'Étude

Parmi les exigences requises pour la 5G, la couverture est un point important. En effet, un des objectifs est de fournir un débit satisfaisant (minimum 100 Mbps [1]) pour tous les utilisateurs du réseau. Dans les zones à faible ARPU, le déploiement du réseau est contraint par son coût. Il est alors difficile de fournir une bonne qualité de service dans ce contexte. En particulier, le déploiement des liaisons de type "backhaul" entre le cœur du réseau et les stations de base est particulièrement coûteux lorsqu'un lien filaire est utilisé [34]. Pour réduire ce coût, il est possible de créer un lien sans fil entre deux stations de base, la première servant de relai à la seconde. Dans le Chapitre 7, un système "massive MIMO" est proposé afin de réaliser ce lien sans fil.

L'utilisation d'une bande de fréquence dédiée pour la réalisation du lien "backhaul" peut s'avérer coûteuse, en particulier pour les fréquences inférieures à 6 GHz. C'est pourquoi, une communication "in-band" est proposée dans cette étude, signifiant que la même bande de fréquence est utilisée pour le lien "backhaul" et pour les liens d'accès (liens entre les stations de base et les utilisateurs). En revanche, lorsque ces deux types de lien sont multiplexés spatialement, des interférences peuvent apparaitre au niveau des utilisateurs [35–39].

Dans cette thèse, l'étude se centre sur la voie descendante d'un duplex par séparation temporelle (TDD), comme décrit par la Figure 5. En particulier, on s'intéresse au précodeur utilisé au niveau du réseau d'antennes "massive MIMO" de la station de base d'émission. Celui-ci permet d'effectuer le lien "backhaul", indiqué par la flèche pleine rouge sur la Figure 5, tout en contrôlant éventuellement les interférences qui apparaissent au niveau des utilisateurs, indiquées par les flèches pointillées rouges sur la Figure 5. La modélisation du système effectuée dans le Chapitre 7 prend en compte les spécificités du canal de propagation entre les deux stations de base, à savoir sa forte composante LOS et la longue distance entre l'émetteur et le récepteur. Elle permet d'évaluer l'impact du précodeur "massive MIMO" utilisé sur le

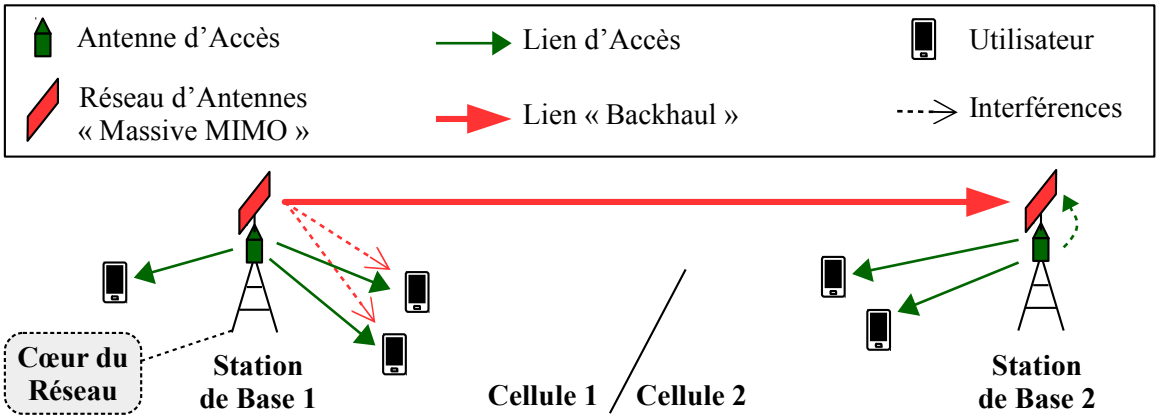

FIGURE 5 : Illustration de la voie descendante du système TDD considéré. Un lien "backhaul" sans fil "in-band" est créé grâce aux réseaux d'antennes "massive MIMO" situés sue les stations de base 1 et 2.

signal reçu au niveau de la station de base de réception et sur les signaux reçus au niveau des utilisateurs.

Nouveau Précodeur Massive MIMO pour Liaison "Backhaul" "In-Band" Sans Fil et Longue Portée

En se basant sur la modélisation du système définie dans le Chapitre 7, un nouveau précodeur "massive MIMO" est proposé dans le Chapitre 8. Ce précodeur utilise une structure RZF et est nommé "Regularized Zero Forcing with Controlled Interference" (RZF-CI). Il permet de maximiser la puissance utile reçue au niveau de la station de base de réception tout en limitant la dégradation des performances au niveau des utilisateurs induite par le lien "backhaul". Plus précisément, la métrique Δ est définie comme suit :

$$\Delta = \rho/\gamma,$$

ρ et γ étant respectivement le SNR et le SINR au niveau de l'utilisateur considéré. Plus l'impact des interférences dues au lien "backhaul" est important, plus le SINR γ diminue et plus la métrique Δ augmente. Le précodeur RZF-CI est conçu de manière à contrôler cette métrique Δ en la gardant en dessous d'une valeur maximale Δ_{max} prédéfinie.

Une étude analytique est effectuée dans cette thèse pour comparer le précodeur RZF-CI aux précodeurs MRT et ZF utilisés dans la littérature [35, 37–39]. Il est démontré que la technique proposée permet de limiter l'impact des interférences dues au lien "backhaul" contrairement à la technique MRT. De plus, avec le précodeur RZF-CI, la puissance utile reçue au niveau de la station de base de réception est toujours supérieure ou égale à celle reçue avec le précodeur ZF.

Des simulations sont également effectuées avec un modèle de canal géométrique afin d'éva-

luer les performances de la solution proposée en pratique. Le BER au niveau de l'utilisateur considéré est illustré par la Figure 6 pour les précodeurs MRT, ZF et RZF-CI. Les détails concernant les paramètres de simulation sont donnés dans le tableau 8.1 de la partie 8.4. Les résultats sur cette Figure confirment que l'impact du lien "backhaul" est contrôlé avec

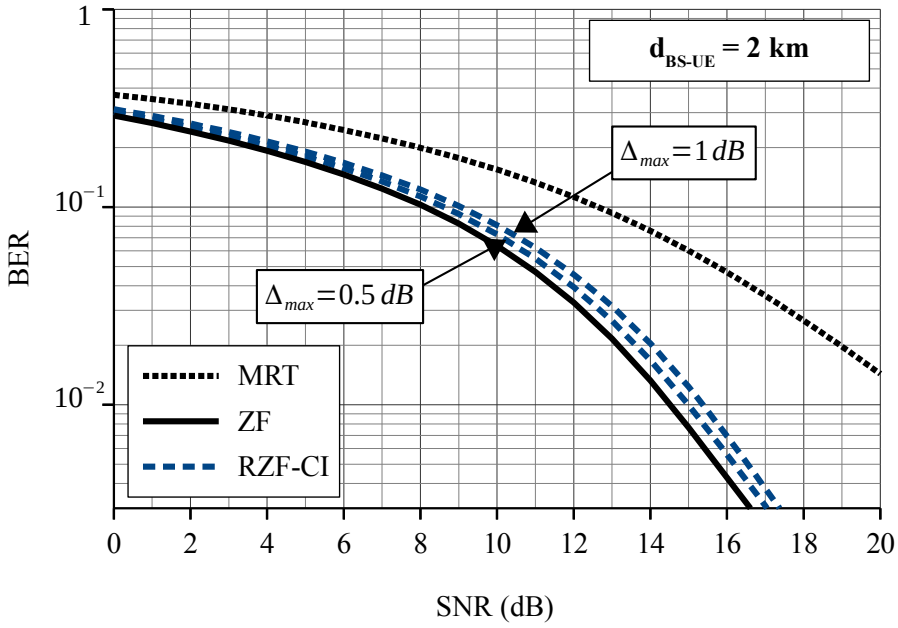

FIGURE 6 : BER en fonction du SNR au niveau de l'utilisateur considéré pour les précodeurs MRT, ZF et RZF-CI. La distance entre la station de base d'émission et l'utilisateur d_{BS-UE} est fixée à 2 km.

le précodeur RZF-CI via la valeur donnée à Δ_{max}. En revanche, les performances en termes de BER sont grandement impactées avec le précodeur MRT puisque celui-ci ne contrôle pas les interférences liées au lien "backhaul". La puissance utile normalisée reçue au niveau de la station de base de réception est ensuite donnée en fonction de la distance entre la station de base d'émission et l'utilisateur considéré (d_{BS-UE}) sur la Figure 7. Les détails concernant les paramètres de simulation sont également donnés dans le tableau 8.1 de la partie 8.4. Ces résultats montrent que le précodeur RZF-CI permet d'obtenir un gain important en comparaison du précodeur ZF (jusqu'à 8 dB en bordure de cellule). De plus, la perte de puissance utile reçue en comparaison du précodeur MRT est relativement limitée (maximum 1.5 dB). Ces simulations confirment donc les bénéfices apportés par la solution proposée dans cette thèse.

Liaison "Backhaul" Sans Fil Asynchrone

Les résultats du Chapitre 8 sont valides sous l'hypothèse d'une synchronisation temporelle et fréquentielle parfaite entre le lien "backhaul" et les liens d'accès. Une telle hypothèse est difficilement réalisable dans la pratique à cause de limitations matérielles. Dans le Chapitre 9, l'impact d'une désynchronisation temporelle entre les liens "backhaul" et accès est étudié.

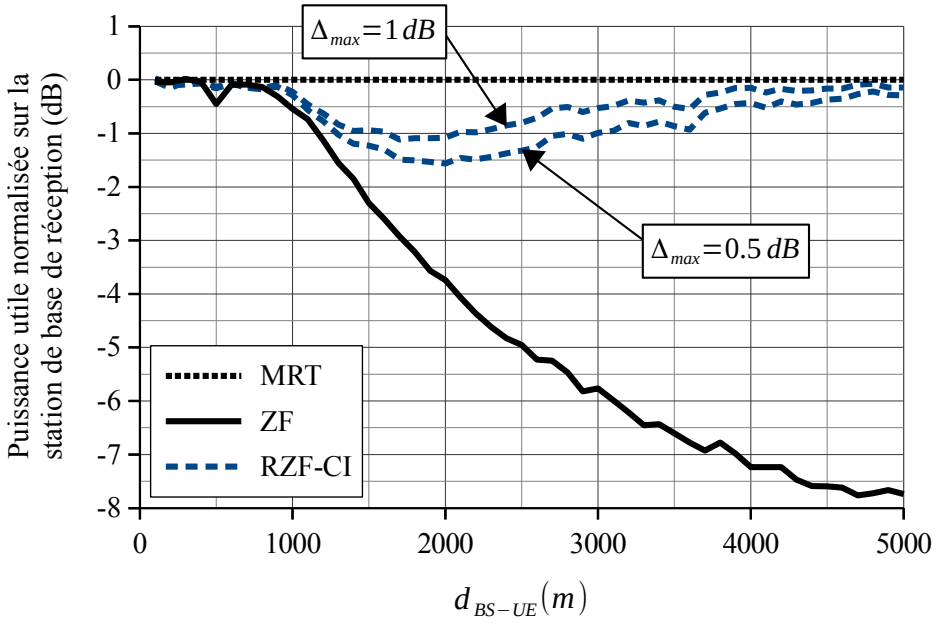

FIGURE 7 : Puissance utile normalisée reçue au niveau de la station de base de réception en fonction de la distance entre la station de base d'émission et l'utilisateur considéré (d_{BS-UE}) pour les précodeurs MRT, ZF et RZF-CI.

Dans un premier temps, une étude analytique est effectuée et permet de montrer les aspects décrits ci-dessous.

- Au niveau de l'utilisateur considéré, la désynchronisation temporelle induit un étalement en fréquence des interférences dues au lien "backhaul".
- Au niveau de l'utilisateur considéré, la désynchronisation temporelle peut induire une augmentation de la puissance des interférences dues au lien "backhaul". Cependant, cette augmentation est localisée au niveau des sous-porteuses situées aux bords de la bande de fréquence dédiée à l'utilisateur.

Dans un second temps, les résultats des simulations montrent que la désynchronisation temporelle des liens "backhaul" et accès a, en réalité, un impact très limité sur le BER au niveau de l'utilisateur considéré. Ces résultats sont donnés par la Figure 8. Les paramètres de simulation sont détaillés dans le tableau 9.1 de la partie 9.3.

Puisqu'un lien "backhaul" asynchrone est possible, on peut imaginer utiliser des paramètres de modulation différents pour le lien "backaul" et pour les liens d'accès (longueurs de CP différentes par exemple). On peut également imaginer utiliser une modulation autre que la modulation OFDM pour le lien "backhaul". Dans le Chapitre 9, la modulation FBMC/OQAM est proposée pour le lien "backhaul" afin d'augmenter son efficacité spectrale. Cette proposition est évaluée par simulation en comparant les BER au niveau de l'utilisateur considéré avec un lien "backhaul" synchrone utilisant la modulation OFDM et avec un lien "backhaul" asynchrone utilisant la modulation FBMC/OQAM. Les résultats sont donnés par la Figure

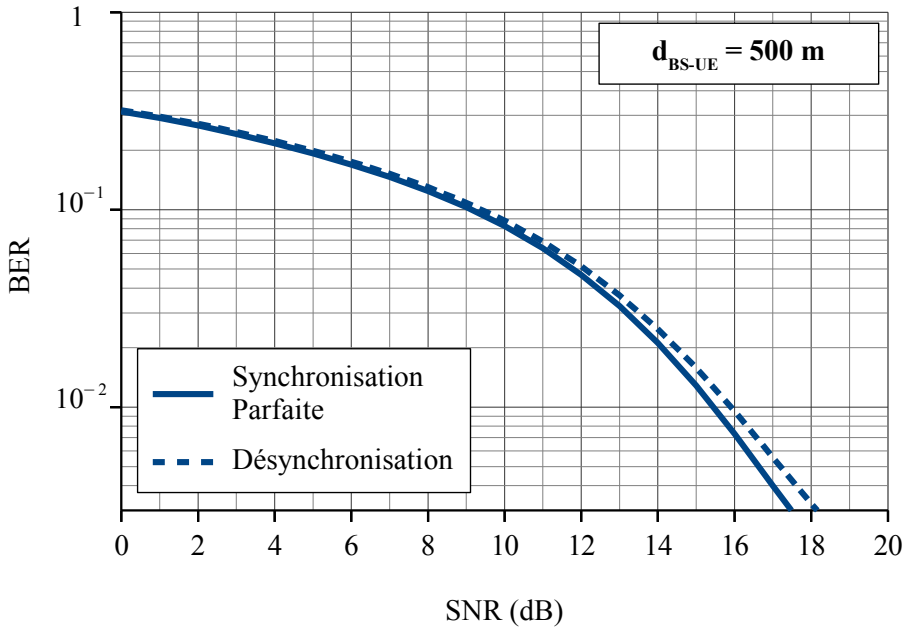

FIGURE 8 : BER en fonction du SNR au niveau de l'utilisateur considéré pour le précodeur RZF-CI, avec et sans désynchronisation du lien "backhaul". La distance entre la station de base d'émission et l'utilisateur d_{BS-UE} est fixée à 500 m.

9 et les paramètres de simulation sont détaillés dans le tableau 9.1 de la partie 9.3. Sur cette

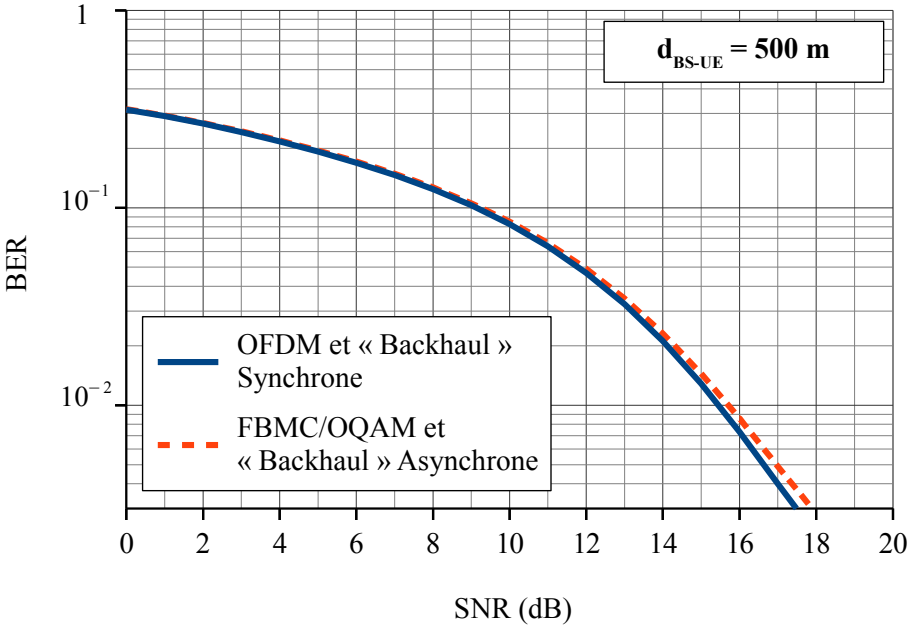

FIGURE 9 : BER en fonction du SNR au niveau de l'utilisateur considéré pour le précodeur RZF-CI, avec un lien "backhaul" synchrone utilisant la modulation OFDM et avec un lien "backhaul" asynchrone utilisant la modulation FBMC/OQAM. La distance entre la station de base d'émission et l'utilisateur d_{BS-UE} est fixée à 500 m.

Figure, on peut voir que l'utilisation d'un lien "backhaul" asynchrone utilisant la modulation

FBMC/OQAM n'a qu'un impact négligeable sur le BER au niveau de l'utilisateur considéré. Ainsi, la modulation FBMC/OQAM peut être utilisée dans ce contexte pour augmenter l'efficacité spectrale et ainsi le débit du lien "backhaul".

Conclusion

Pour conclure, plusieurs études ont été effectuées sur les systèmes "massive MIMO" combinés avec les modulations multiporteuses OFDM et FBMC/OQAM. En particulier, ces travaux de thèse ont permis de contribuer au développement de la 5G pour deux types de scénarios.

Le premier scénario considère des applications véhiculaires où la vitesse des utilisateurs impacte les performances des systèmes de communication à cause de l'effet Doppler. En environnement NLOS, les études menées ont permis de démontrer qu'un système "massive MIMO" permet de réduire de manière drastique l'impact de l'effet Doppler pour la voie montante avec un simple récepteur MRC. Par ailleurs, en environnement LOS, il est montré que la modulation FBMC/OQAM permet d'augmenter significativement les performances des systèmes "massive MIMO" en comparaison de la modulation OFDM. Ces études peuvent être complétées en traitant le problème de l'estimation du canal de propagation dans ce contexte, en étendant le scénario considéré aux communications multi-utilisateurs ou encore en prenant en compte les caractéristiques géométriques du canal de propagation.

Le second scénario considère l'extension de la couverture dans les zones à faible ARPU. Plus particulièrement, l'étude de systèmes "massive MIMO" pour créer un lien "backhaul" sans fil et "in-band" entre deux stations de base a permis les contributions suivantes. Un nouveau précodeur "massive MIMO", le précodeur RZF-CI, a été créé pour la voie descendante. Il permet de maximiser la puissance utile reçue au niveau de la station de base de réception tout en limitant la dégradation des performances au niveau des utilisateurs induite par le lien "backhaul". De plus, il a été montré que ce lien "backhaul" peut être complètement désynchronisé des liens d'accès avec un impact négligeable sur la qualité de service au niveau des utilisateurs. Enfin, il est possible d'utiliser la modulation FBMC/OQAM pour le lien "backhaul" dans le but d'augmenter l'efficacité spectrale et ainsi le débit de ce lien. Afin de poursuivre ces travaux, il est possible d'étudier la voie montante du scénario considéré ou encore d'étendre ce scénario aux communications multi-utilisateurs. Par ailleurs, il serait intéressant d'étudier l'intégration du précodeur RZF-CI dans un système hybride numérique et analogique afin d'en réduire la complexité.

Contents

List of Figures

List of Tables

Acronyms

3GPP 3rd Generation Partnership Project.

4G forth generation of cellular networks.

5G fifth generation of cellular networks.

ADSL Asymmetric Digital Subscriber Line.

ARPU Average Revenue Per User.

AWGN Additive White Gaussian Noise.

BER Bit Error Rate.

BH Backhaul.

BS Base Station.

C-RAN Cloud Radio Access Networks.

CP Cyclic Prefix.

CSI Channel State Information.

DFT Discrete Fourier Transform.

DPC Dirty Paper Coding.

DVB Digital Video Broadcasting.

EGT Equal Gain Transmission.

ETU Extended Typical Urban.

EVA Extended Vehicular A.

FANTASTIC-5G Flexible Air iNTerface for Scalable service delivery wiThin wIreless Communication networks of the 5th Generation.

FBMC Filter-Bank Multi-Carrier.

FBMC/OQAM Filter-Bank Multi-Carrier with Offset Quadrature Amplitude Modulation.

FDD Frequency-Division Duplex.

FDM Frequency-Division Multiplexing.

FDMA Frequency-Division Multiple-Access.

FFT Fast Fourier Transform.

FIR Finite Impulse Response.

GSCM Geometry-based Stochastic Channel Model.

HetNet Heterogeneous Networks.

ICI Inter-Carrier Interference.

IDFT Inverse Discrete Fourier Transform.

IFFT Inverse Fast Fourier Transform.

IoT Internet of Things.

ISI Inter-Symbol Interference.

ITU-R Radiocommunication Sector of International Telecommunication Union.

LOS Line-Of-Sight.

LTE Long Term Evolution.

M2M Machine-to-Machine.

MBB Mobile Broadband.

MCC Mission Critical Communications.

METIS Mobile and wireless communications Enablers for the Twenty-twenty Information Society.

MF Matched Filter.

MIMO Multiple-Input Multiple-Output.

MISO Multiple-Input Single-Output.

MMSE Minimum Mean Square Error.

MRC Maximum Ratio Combining.

MRT Maximum Ratio Transmission.

MU-MIMO Multi-User Multiple-Input Multiple-Output.

MUI Multi-User Interference.

NLOS Non-Line-Of-Sight.

OFDM Orthogonal Frequency-Division Multiplexing.

ONE5G E2E-aware Optimizations and advancements for the Network Edge of 5G New Radio.

QuaDRiGa Quasi Deterministic Radio Channel Generator.

RA4 Rural Area with 4 taps.

RMa Rural Macro-cell.

RZF Regularized Zero Forcing.

RZF-CI Regularized Zero Forcing with Controlled Interference.

SCM Spatial Channel Model.

SDMA Space-Division Multiple-Access.

SINR Signal-to-Interference-plus-Noise Ratio.

SIR Signal-to-Interference Ratio.

SISO Single-Input Single-Output.

SNR Signal-to-Noise Ratio.

TDD Time-Division Duplex.

TFL1 Time Frequency Localization (K=1).

TR Time Reversal.

UE User Equipment.

V2V Vehicle-to-Vehicle.

V2X Vehicle-to-Everything.

VNI Visual Networking Index.

WINNER Wireless World Initiative for New Radio.

ZF Zero Forcing.

ZP Zero Padded.

Symbols

B_c Coherence bandwidth.

$E[\,\cdot\,]$ Expected value.

F_0 Inter-carrier spacing.

F_c Central frequency.

K Overlapping factor of a prototype filter.

K_h Rician K-factor.

L_g Length of a prototype filter.

L_h Number of paths for the propagation channel.

L_{CP} Length of a Cyclic Prefix.

M Number of sub-carriers for multi-carrier modulations.

N_r Number of receive antennas.

N_t Number of transmit antennas.

N_u Number of users.

P_h Path loss of the propagation channel.

T_0 Symbol duration ($T_0 = 1/F_0$).

T_c Coherence time.

T_s Sampling Time ($T_s = T_0/M$).

T_{CP} Cyclic Prefix duration.

$\Im[\,\cdot\,]$ Imaginary part.

$\Re[\,\cdot\,]$ Real part.

$\delta_{x,y}$ Kronecker symbol, equal to 1 if $x = y$ and 0 if $x \neq y$.

$\mathbf{I}_N$ Identity matrix of size $N \times N$.

$\mathbf{x}$ Vector or Matrix.

$\mathbf{x}^H$ Conjugate transpose of the matrix $\mathbf{x}$.

$\mathbf{x}^T$ Transpose of the matrix $\mathbf{x}$.

$\mathcal{F}[\,\cdot\,]$ Fourier transform operator.

f_D^{max} Maximum Doppler frequency.

f_D^{shift} Doppler shift frequency.

x^* **or** $\mathbf{x}^*$ Conjugate value of the scalar x or the matrix $\mathbf{x}$.

Introduction

Context and Motivations

Since the beginning of the 1990s, cellular communication systems have changed to follow the evolving needs. After a first analogical generation of cellular network, the second, the third and the fourth generation of cellular networks were created in order to enable consecutively mobile voice communications, video applications and mobile Internet. Therefore, the forth generation of cellular networks (4G) offers Mobile Broadband (MBB) capabilities with a theoretical data rate greater than 100 Mbps. Consumer habits are constantly changing and new use cases are emerging with them. For this reason, in the coming years the fifth generation of cellular networks (5G) will be necessary to fulfill the future requirements. These requirements are summarized by Figure 10 and are discussed thereafter.

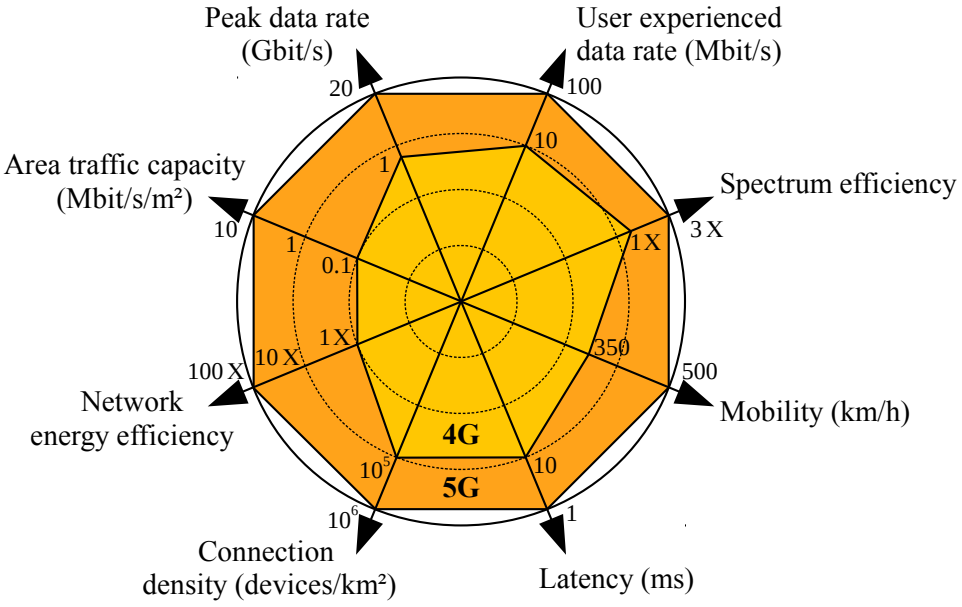

Figure 10: Comparison between the 4G and the 5G requirements according to the ITU-R [1]

Firstly, according to Cisco in its Visual Networking Index (VNI) [42] published in 2016, the global data traffic should increase nearly eightfold between 2015 and 2020. Thus, in [1] the Radiocommunication Sector of International Telecommunication Union (ITU-R) recommends to enhance the MBB capabilities in order to improve services in high user density context (stadium, shopping malls or festivals for example), in wide area context and/or in mobility context (cars or trains for example). In this regard, 5G should be an evolution of 4G and should carry the large amount of data that will be generated by MBB communications in the next years. To carry the increase of mobile data traffic for MBB, the first requirement of 5G is to increase the user data rate. According to [2] and [3], user data rates must be increased by a factor of 10 to 100 compared to 4G. Thus, a data rate of **100 Mbps in wide area** and 1 Gbps in hotspot should be expected [1]. However, this has to be done keeping a good coverage. Moreover, as the number of smartphones and tablets will widely increase, the data volume per area has to be multiplied by a factor of 1000 [2–4]. Finally, 5G will have to **increase the performances in terms of mobility**, for Vehicle-to-Everything (V2X) applications such as high speed trains connections or self-driving cars. In this context, a good quality of service is required with a **speed up to 500 km/h** as recommended by the ITU-R [1].

Additionally, a new type of communication is emerging. Instead of human-centric communications, Machine-to-Machine (M2M) communications include all data exchange between machines. This type of communication is also widely known as Internet of Things (IoT). Therefore, in 2020 the number of connected devices should exceed the number of human (1.5 per capita) [42] and the proportion of M2M devices will widely increase, from 5% in 2015 to 20% of IPv6-capable devices in 2020 [42]. M2M communications will be used in the coming years in a large set of applications such as home security and automation, maintenance or healthcare. These communicating objects could be small sensors as well as cars or medical devices for example. Another target of 5G is therefore to enable M2M communications taking into account the various requirements of the communicating devices. Unlike MBB, data rate is less important for the M2M communications, but the number of connected devices that can be handle is more critical. Indeed, FANTASTIC-5G and METIS projects suggested an increase by a factor of 10 to 100 of the number of connected devices [2, 3]. According to [1], 5G will therefore have to support a connection density of up to 10^6 devices by km^2. The M2M communications have also large constraints on energy consumption. Communicating machines are often cheap and low energy devices and 5G systems have to increase their battery life by a factor of 10 [2].

Finally, 5G is also the opportunity to add some specific applications. In [1], a use case named "Ultra-reliable and low latency communications" is added. The same use case is present for the European projects METIS and FANTASTIC-5G under the names "Super real-time and reliable connections" and "Mission Critical Communications (MCC)" respectively [2, 3], but a more common expression is "tactile internet" [43]. It regroups special applications such as industry automation, remote medical surgery or self-driving cars, where an ultra-reliable

and low latency communication is needed. For ultra-reliable/low-latency communications such as tactile internet, the goal is to reach 1 ms whereas for 4G the latency is on the order of 15 ms [1, 4]. Furthermore, the reliability have to reach a value of 99.999% [2, 3].

In order to build the future generation of cellular networks, the European commission launched a dozen of European projects, which gather together public and private organizations. Three of them are described thereafter.

- The Mobile and wireless communications Enablers for the Twenty-twenty Information Society (METIS) project was launched in 2012 with a budget of 27 million euros. It included 29 partners among telecommunications manufacturers, network operators, the automotive industry and academic members. The objective of the METIS project was to enable European lead on the development of 5G. It ended in 2017 after the development of more than 140 technology components and the publication of 23 journal papers and more than 170 conference papers.

- The Flexible Air iNTerface for Scalable service delivery wiThin wIreless Communication networks of the 5th Generation (FANTASTIC-5G) project started in 2015 and ended in 2017. 18 partners were involved in this project. Its objective was to investigate the air interface of 5G for frequencies below 6 GHz. This project leads to more than 30 significant contributions to the 5G standardization process, more than 16 patents and more than 50 published papers.

- The E2E-aware Optimizations and advancements for the Network Edge of 5G New Radio (ONE5G) project started in 2017 and should end in 2019. This ongoing project is the continuity of the FANTASTIC-5G project. Its objectives are to enhance the capacity of mobile networks, to improve their energy efficiency and to enable new use cases in dense urban areas as well as in rural environments. 14 partners are involved in this project.

This thesis takes place in the context of the development of 5G and focuses on two distinct use cases. The first one is **V2X communications**, where the speed of the cars or the trains (up to 500 km/h [1]) complicates the increase of the data rate. The second one concerns communications in **underserved wide areas**, where the extension of the coverage is highly constrained in terms of cost. This last study leads to a contribution to the ONE5G European project.

Thesis Organization

In a first part, the **background materials** are provided to serve as a basis for this thesis. In particular, Chapter 1 characterizes the wireless propagation channels for cellular communications, highlights their impact on the received signals and describes some techniques to model them. Chapter 2 focuses on the description of the two multi-carrier modulations

considered in this thesis, namely the Orthogonal Frequency-Division Multiplexing (OFDM) modulation and the Filter-Bank Multi-Carrier with Offset Quadrature Amplitude Modulation (FBMC/OQAM). Chapter 3 is dedicated to the description of massive Multiple-Input Multiple-Output (MIMO) systems, which hold a wide range of benefits by using a large number of antennas. To this end, system models are presented for the uplink and for the downlink along with the description of some state-of-the-art massive MIMO techniques.

The second part of this thesis focuses on **V2X communications** and, in particular, on the use of a massive MIMO system to counteract the impact of the Doppler effect, which is induced by the mobility of the transmitter. This situation is described more thoroughly in Chapter 4 where the uplink system model of Chapter 3 is modified in order to take into account the Doppler effect. Based on this, Chapter 5 aims at proving that a massive MIMO system can decrease the impact of the Doppler effect. Finally, in Chapter 6 the OFDM and the FBMC/OQAM modulations are compared in a massive MIMO uplink system with mobility. The objective is to find the modulation leading to the best performance depending on the context of the communication.

The third part is dedicated to the study of massive MIMO systems as a way to **extend the coverage of the network in underserved wide areas** for a low cost of deployment. In particular, massive MIMO systems are used in this study to replace part of the "Backhaul (BH)" wired link, between the core network and the Base Stations (BSs), by a wireless link. This study is presented in Chapter 7 along with the associated system model. In Chapter 8, a new massive MIMO precoding technique is presented in order to outperform the existing solutions. Finally, in Chapter 9, the impact of a desynchronized wireless BH link on the performance of the system is studied. Moreover, the use of the FBMC/OQAM modulation for the BH link is also discussed in this Chapter.

Publications

Peer Reviewed International Journal Paper

- A. Bazin, B. Jahan and M. Hélard, "Doppler Effect Reduction in an OFDM System Thanks to Massive MIMO," in *IEEE Access*, vol. 6, pp. 38498-38511, 2018.

Peer Reviewed National Conference

- A. Bazin, B. Jahan and M. Hélard, "Réduction de l'impact de l'effet Doppler dans un système OFDM grâce au « massive MIMO »," in *26th GRETSI Seminar*, September 2017.

Peer Reviewed International Conference

- A. Bazin, B. Jahan and M. Hélard, "Impact of the Doppler effect on the capacity of massive MIMO uplink systems: OFDM versus FBMC/OQAM," in *24th International Conference on Telecommunications (ICT)*, May 2017.

Patent

- A. Bazin and B. Jahan, "Système de télécommunication avec système d'antennes massive-MIMO pour un lien backhaul sans fil et procédé correspondant", french patent under submission.

Part I

Background Materials

1

Wireless Propagation Channels

The propagation channel is the characterization of the modifications suffered by the transmitted signal between the transmitter and the receiver. A good understanding of the wireless propagation channel is necessary to evaluate the performance of communication systems. Therefore, this part aims at characterizing the wireless propagation channels for cellular communications in order to highlight their impact on the received signal and to give a clue on how to model them.

1.1 Baseband Multipath Propagation Channel

The characterization of the propagation channel depends on the type of communication. Regarding cellular communications, the transmit electromagnetic signal is reflected against a multiplicity of obstacles (ground, buildings, etc.). Because of this phenomena, the received signal is the combination of several signals coming from different paths. Each of these signals is an attenuated and delayed version of the original signal. The attenuations and delays depend on the nature of the obstacles encountered and on the distance traveled by the signal. Such a propagation channel is a linear propagation channel and is called multipath propagation channel. This phenomena is illustrated by Figure 1.1.

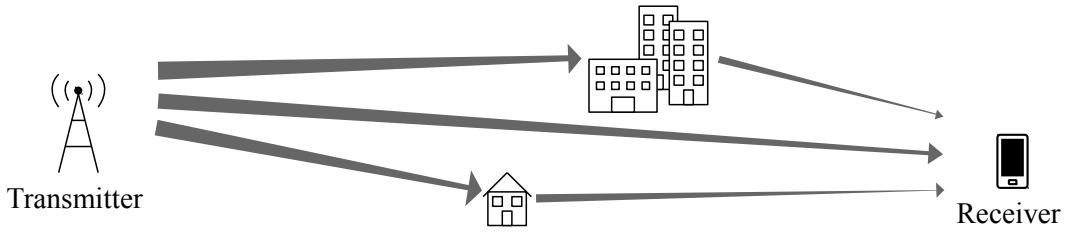

Figure 1.1: Illustration of a multipath propagation channel for cellular communications.

The multipath propagation channel could be modeled by the attenuation and the delay of each path. However, the channel models usually take into account the conversion of the

transmitted baseband signal $s(t)$ to the carrier frequency F_c on the transmitter side and the conversion of the received signal to the baseband received signal $r(t)$ [5, 6]. The equivalent propagation channel between $s(t)$ and $r(t)$ is called the baseband propagation channel and is represented in Figure 1.2.

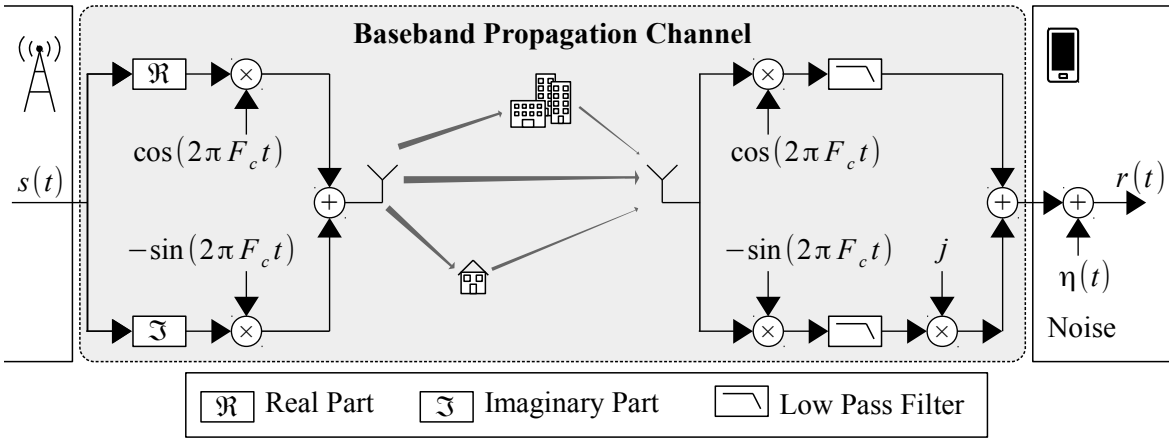

Figure 1.2: Representation of the baseband propagation channel.

The baseband propagation channel can be divided in two parts which are described thereafter.

1. The path loss or large-scale fading is the mean attenuation of the signal. This parameter is mainly due to the atmospheric absorption and to the shadowing effect caused by buildings or trees for example. The path loss thus relies on the distance between the transmitter and the receiver and is represented by P_h in this thesis. In other words, P_h is the mean power attenuation of the received signal $r(t)$ compared to the power of the transmitted signal $s(t)$.

2. The multipath components or small-scale fading are caused by the multiple reflections of the transmitted signal against obstacles such as the ground or buildings. The received signal is thus the sum of L_h paths. The l^{th} path, $l \in [0\ ,\ L_h-1]$, is described by a delay τ_l and by a complex multiplying factor denoted by $h_l(t)$, which varies more or less quickly in the time domain. The sum of the mean powers of $h_l(t)$ is equal to:

$$\sum_{l=0}^{L_h-1} E\left[|h_l(t)|^2\right] = 1. \tag{1.1}$$

Additionally, the thermal noise is an additive component. As it is usually a Gaussian-distributed complex random variable, this component is called Additive White Gaussian Noise (AWGN). In the time domain, the noise component is denoted by the complex variable

$\eta(t)$. According to these effects, the received baseband signal in the time domain is:

$$r(t) = \underbrace{\sqrt{P_h}}_{\text{Path Loss}} \times \underbrace{\left(\sum_{l=0}^{L_h-1} h_l(t).s(t-\tau_l) \right)}_{\text{Multipath Components}} + \underbrace{\eta(t)}_{\text{Noise}} . \tag{1.2}$$

Figure 1.3 summarizes the equivalent model of the baseband propagation channel.

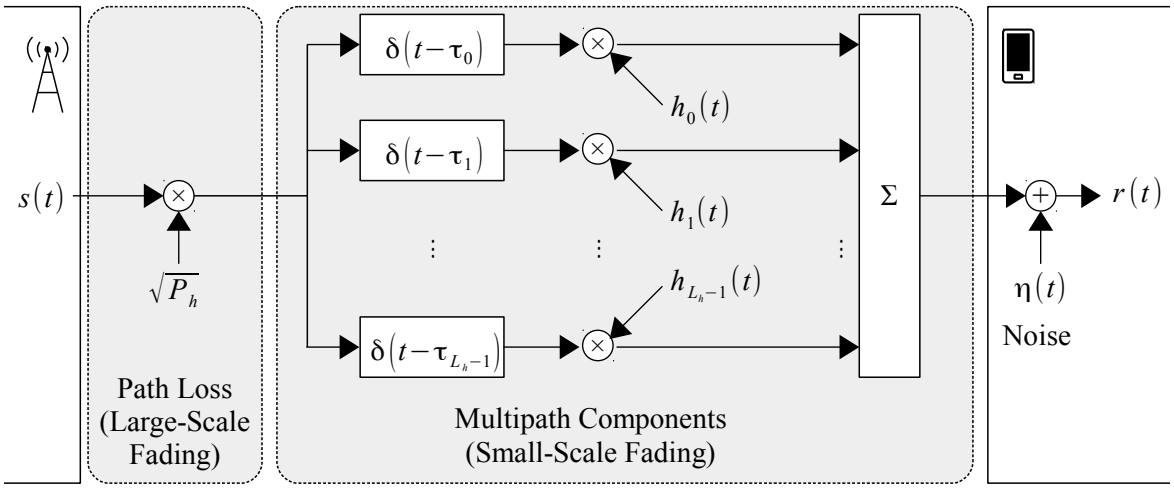

Figure 1.3: Equivalent model of the baseband propagation channel.

1.2 Time and Frequency Selectivity of the channel

In order to highlight the impact of the propagation channel on the received signal $r(t)$, the study of the so called time and frequency selectivity of the propagation channel is important. These fundamental notions are described thereafter.

At a given time t and if $L_h > 1$, the multipath components act as a Finite Impulse Response (FIR) filter of order (L_h-1), delays τ_l and coefficients $h_l(t)$. In the frequency domain, this filter induces variations of the propagation channel, which are quantified by the coherence bandwidth B_c [5]. Thus, the propagation channel is considered to be invariant in the frequency domain on a frequency band B only if $B \ll B_c$. Therefore, two signals separated by a frequency band greater than B_c experience two different propagation channels. This effect is called the frequency selectivity of the channel.

In the time domain, the multiplying factors $h_l(t)$ vary when the transmitter, the receiver or the elements of the propagation channel are moving, because of the Doppler effect. Thus, the FIR filter previously defined is actually changing over time. The rapidity of these variations is higher if the transmitter, the receiver or the elements of the propagation channel are quickly moving. These variations are quantified by the coherence time T_c [5], so that the

propagation channel is considered to be invariant in the time domain on a duration T only if $T \ll T_c$. Therefore, two signals separated by a duration greater than T_c experience two different propagation channels. This effect is called the time selectivity of the channel.

The selectivity of the propagation channel is thus the combination of the time selectivity and the frequency selectivity. In order to visualize this effect, the power attenuation of an Extended Vehicular A (EVA) (described in appendix A) baseband channel realization for a User Equipment (UE) moving at 50 km/h and a central frequency of $F_c = 6$ GHz is given by Figure 1.4.

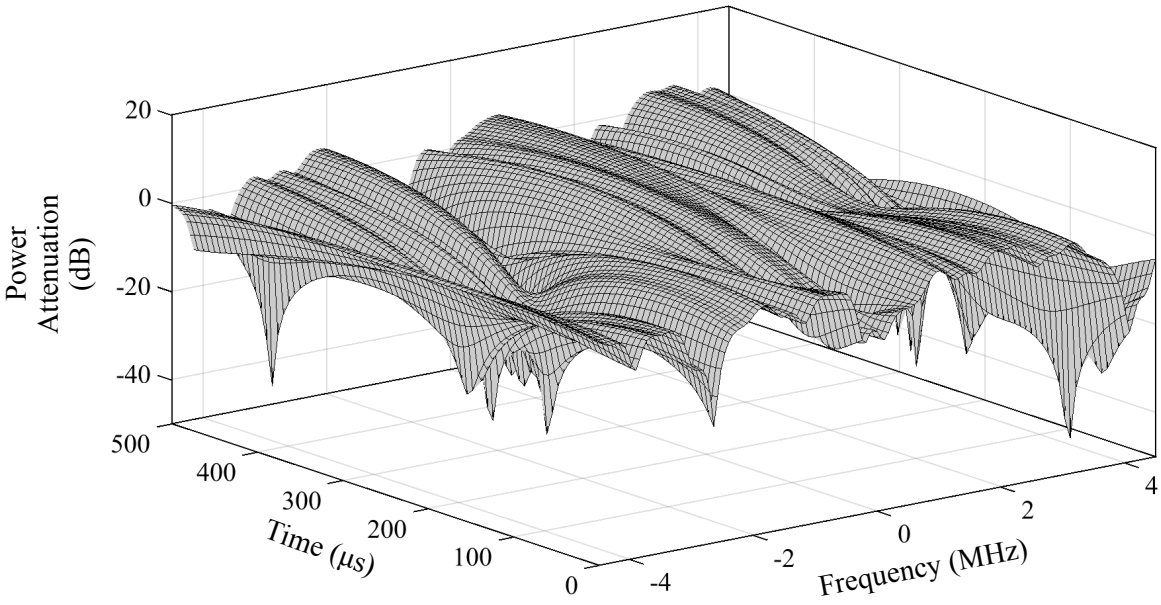

Figure 1.4: Power attenuation of an EVA baseband channel realization for a UE moving at 50 km/h and a central frequency of $F_c = 6$ GHz.

1.3 Modelization of the Propagation Channel

In order to simulate a propagation channel, a statistical model is necessary. Three models are presented here, the Rayleigh fading channel model, the Rician fading channel model and the Geometry-based Stochastic Channel Model (GSCM).

1.3.1 Rayleigh Fading Channel Model

The Rayleigh fading channel model is a statistical channel model used to simulate a multi-path component when this component is not a direct path between the transmitter and the receiver. If there is no direct path between the transmitter and the receiver, the propagation channel is Non-Line-Of-Sight (NLOS) and all multi-path components can be simulated using the Rayleigh fading channel model. Using a Rayleigh fading channel model for the l^{th} component

in (1.2), the delay τ_l is fixed and the multiplying factor $h_l(t)$ is a statistical variable.

Following the Rayleigh fading channel model, the l^{th} multipath component $h_l(t)$ can be defined as in [5,6] by:

$$h_l(t) = \sqrt{P_{h,l}} \times \frac{h_l^{(1)}(t) + j h_l^{(2)}(t)}{\sqrt{2}}, \tag{1.3}$$

where $P_{h,l}$ is the mean value of $|h_l(t)|^2$ and $(h_l^{(1)}(t), h_l^{(2)}(t))$ is a couple of two independent real statistical variables. The variations in the time domain of $(h_l^{(1)}(t), h_l^{(2)}(t))$ are caused by a specific type of Doppler effect, which is called the Doppler spread.

At a given time t, the variables $h_l^{(1)}(t)$ and $h_l^{(2)}(t)$ follow a standard normal distribution. Therefore, the amplitude of the l^{th} component $|h_l|$ is Rayleigh distributed with the following probability density function:

$$p_{|h_l|}(x) = \frac{2x}{P_{h,l}} \exp\left(-\frac{x^2}{P_{h,l}}\right). \tag{1.4}$$

This probability density function is illustrated by Figure 1.5.

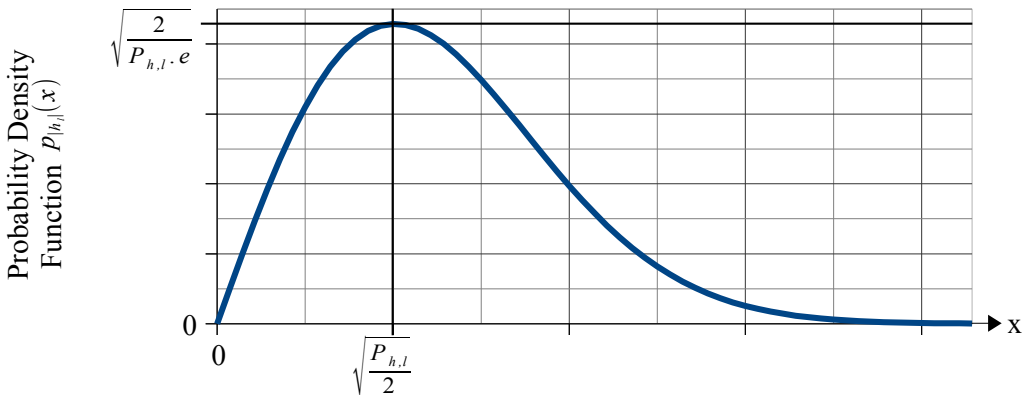

Figure 1.5: Illustration of the Rayleigh probability density function $p_{|h_l|}(x)$.

The moving elements of the propagation channel create the Doppler spread, which is responsible of the variations of $h_l(t)$ in the time domain. Defining the time-autocorrelation function $R_l(\tau)$ as follows:

$$R_l(\tau) = E\left[h_l(t).h_l^*(t-\tau)\right], \tag{1.5}$$

the statistical variations of $h_l(t)$ in the time domain follow the Doppler power spectral density $S_l(f)$, which is the Fourier transform of $R_l(\tau)$:

$$S_l(f) = \mathcal{F}\left[R_l(\tau)\right] = \int_{-\infty}^{+\infty} R_l(\tau) e^{-j2\pi f\tau} d\tau. \tag{1.6}$$

Usually, the Jakes' Doppler spectrum is assumed. According to [5,6], its expression is given

by:

$$S(f) = \begin{cases} \dfrac{1}{\pi f_D^{max} \sqrt{1 - (f/f_D^{max})^2}} & \text{if} \quad |f| < f_D^{max}, \\ 0 & \text{if} \quad |f| \geq f_D^{max}, \end{cases} \tag{1.7}$$

where f_D^{max} is the maximum Doppler frequency. This Jakes Doppler spectrum is illustrated by Figure 1.6. Therefore, the Doppler spread can be evaluated by the value of the maximum

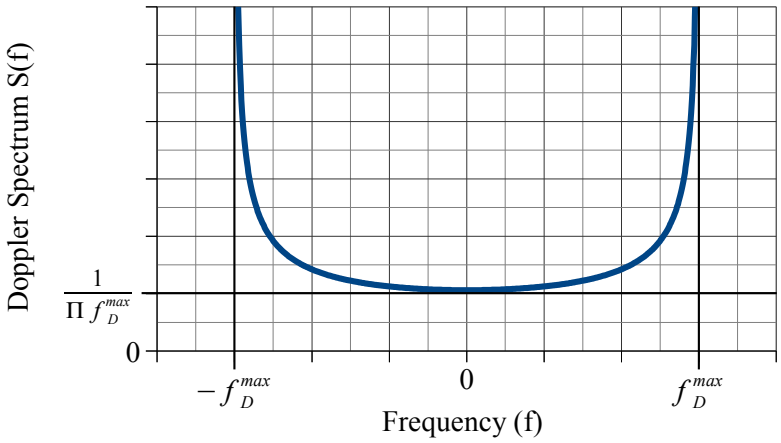

Figure 1.6: Illustration of the Jakes' Doppler spectrum $S(f)$.

Doppler frequency f_D^{max}, which is usually proportional to the speed difference between the transmitter and the receiver and to the central frequency F_c. The relation between the speed difference v, the central frequency F_c and the maximum Doppler frequency f_D^{max} is:

$$f_D^{max} = \frac{|v|}{c} F_c, \tag{1.8}$$

where $c = 3.10^8$ m/s is the speed of light. The higher the value of the speed difference v, the higher the value of f_D^{max}, the higher the impact of the Doppler spread.

In order to simulate a Rayleigh fading channel model, the sum-of-sinusoid representation can be used, as in [29]. Using this method, the variables $h_l^{(1)}(t)$ and $h_l^{(2)}(t)$ are defined by:

$$h_l^{(i)}(t) = \sqrt{\frac{2}{N_l}} \sum_{n=1}^{N_l} \cos\left(2\pi f_{l,n}^{(i)} t + \theta_{l,n}^{(i)}\right), \tag{1.9}$$

with N_l the considered number of sinusoids for the l^{th} path, $\theta_{l,n}^{(i)}$ a random variable having a uniform distribution over the interval $]0, 2\pi]$ and $f_{l,n}^{(i)}$ defined as follows:

$$f_{l,n}^{(i)} = f_D^{max} \cos\left(\frac{\pi}{2N_l}\left(n - \frac{1}{2}\right) + (-1)^{i-1} \frac{\pi}{4N_l} \frac{l}{L_h + 2}\right). \tag{1.10}$$

1.3.2 Rician Fading Channel Model

When the l^{th} multipath component is a direct path between the transmitter and the receiver, the Rician fading channel model is more appropriate. In this case, the channel has a Line-Of-Sight (LOS) component. As for the Rayleigh fading channel model, using a Rician fading channel model for the l^{th} component in (1.2), the delay τ_l is fixed and the multiplying factor $h_l(t)$ is a statistical variable.

The variations in the time domain of $h_l(t)$ are caused by two types of Doppler effect, the Doppler spread and the Doppler shift. Following the Rician fading channel model, the l^{th} multipath component $h_l(t)$ can be divided in two parts as in [5, 44, 45]:

$$h_l(t) = \tilde{h}_l(t) + \check{h}_l(t), \tag{1.11}$$

with $\tilde{h}_l(t)$ being the component due to the Doppler spread and $\check{h}_l(t)$ being the component due to the Doppler shift. More specifically, the component due to the Doppler spread is defined as follows:

$$\tilde{h}_l(t) = \sqrt{\tilde{P}_{h,l}} \times \frac{\tilde{h}_l^{(1)}(t) + j\tilde{h}_l^{(2)}(t)}{\sqrt{2}}, \tag{1.12}$$

with $\tilde{P}_{h,l}$ being the mean value of $|\tilde{h}_l(t)|^2$ and $(\tilde{h}_l^{(1)}(t), \tilde{h}_l^{(2)}(t))$ being a couple of two independent real statistical variables defined as in the previous part. The component due to the Doppler shift is defined as follows:

$$\check{h}_l(t) = \sqrt{\check{P}_{h,l}} \times \exp\left[j(2\pi f_D^{shift} t + \theta)\right], \tag{1.13}$$

with $\check{P}_{h,l}$ being the mean value of $|\check{h}_l(t)|^2$, f_D^{shift} being the Doppler shift frequency and θ being the initial phase. The Doppler shift frequency f_D^{shift} depends on the speed of the transmitter, the speed of the receiver and the relative position between the transmitter and the receiver. It can take values from 0 to f_D^{max}. Moreover, The value of θ relies on the distance between the transmitter and the receiver. The total mean power of $h_l(t)$ is:

$$P_{h,l} = E\left[|h_l(t)|^2\right] = \tilde{P}_{h,l} + \check{P}_{h,l}. \tag{1.14}$$

The Rician K-factor K_h is defined by the ratio between the mean power of the component due to the Doppler shift $\check{P}_{h,l}$ and the mean power of the component due to the Doppler spread $\tilde{P}_{h,l}$. Therefore, it comes:

$$\tilde{P}_{h,l} = \frac{1}{K_h + 1} P_{h,l}, \tag{1.15}$$

and:

$$\check{P}_{h,l} = \frac{K_h}{K_h + 1} P_{h,l}. \tag{1.16}$$

At a given time t, the variables $(\tilde{h}_l^{(1)}(t)$ and $\tilde{h}_l^{(2)}(t))$ follow a standard normal distribution as for the Rayleigh fading channel model. Therefore, the amplitude of the l^{th} component is

Rice distributed with the following probability density function:

$$p_{|h_l|}(x) = \frac{2\,(K_h+1)\,x}{P_{h,l}} \exp\left(-K_h - \frac{(K_h+1)\,x^2}{P_{h,l}}\right) I_0\left(2\sqrt{\frac{K_h\,(K_h+1)}{P_{h,l}}}x\right), \tag{1.17}$$

$I_0(\,.\,)$ being the modified Bessel function of the first kind with order zero. This probability density function is illustrated by Figure 1.7. Therefore, when the value of K_h increases, the

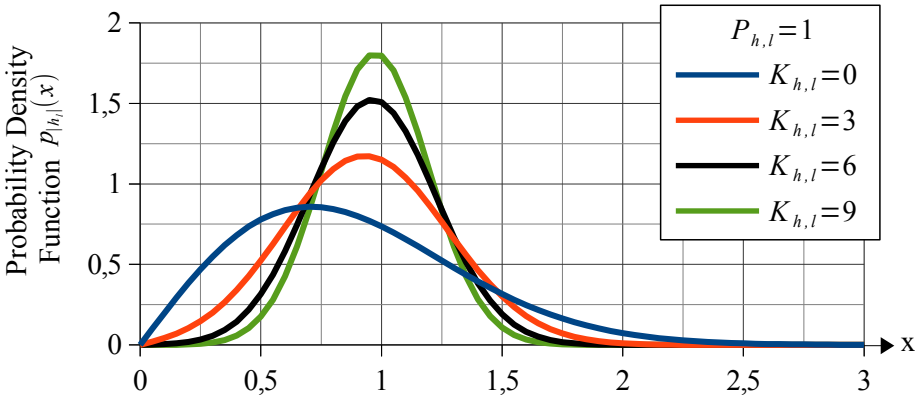

Figure 1.7: Illustration of the Rice probability density function $p_{|h_l|}(x)$.

amplitude of the multipath component becomes less fluctuating and tends to $\sqrt{P_{h,l}}$. On the opposite, when K_h= 0, the multipath component follows a Rayleigh fading channel model.

As for the Rayleigh fading channel model, the statistical variables $\tilde{h}_l^{(1)}(t)$ and $\tilde{h}_l^{(2)}(t)$ can be computed using the sum-of-sinusoid representation defined in (1.9).

1.3.3 Geometry-based Stochastic Channel Model (GSCM)

Unlike the Rayleigh and Rician fading channel models, a GSCM takes into account the spatial characteristics of the propagation environment. Using a GSCM the location in space of scatterers is randomly defined based on a certain probability distribution [46] and each scatterer is the source of a multipath component. A GSCM is of particular interest for MIMO communications where the geometry of the antenna arrays and the correlation between the antennas have a deep impact on the performance of the systems. However, simulating a GSCM is more complex than the classical Rayleigh and Rician fading channel models.

The evolution of GSCM is summarized in Figure 1.8. Most of them are based on the 3rd Generation Partnership Project (3GPP) Spatial Channel Model (SCM) [47]. In particular, the three phases of the Wireless World Initiative for New Radio (WINNER) project resulted in the creation of the WINNER I [48], WINNER II [49] and WINNER+ [50] channel models. Compared to the WINNER I channel models, the WINNER II channel models add new scenarios, while the WINNER+ channel models take into account 3D propagation environments. After these major contributions, the METIS project improved the accuracy of the

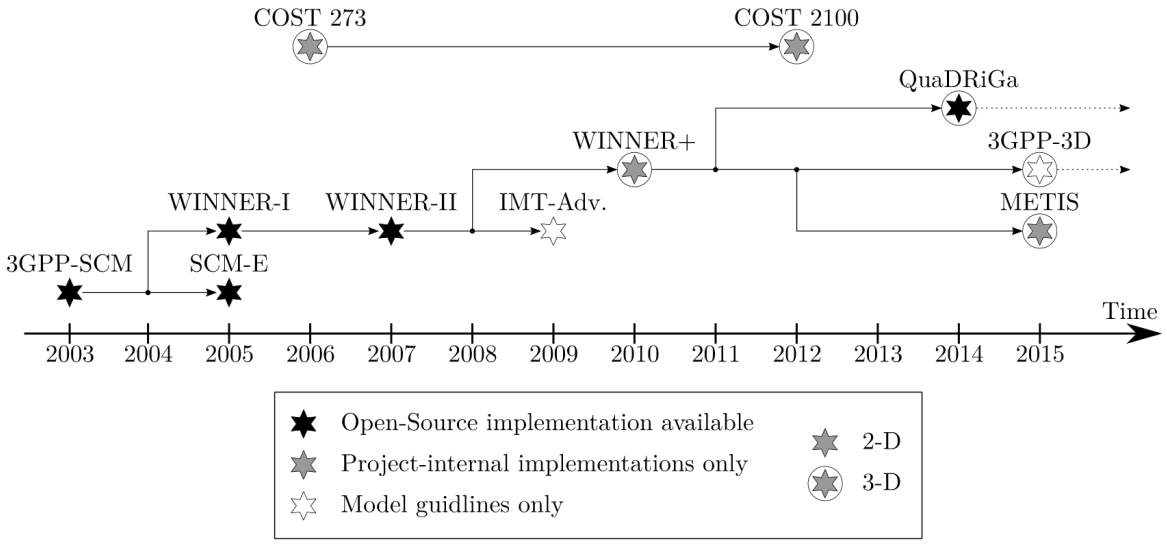

Figure 1.8: Evolution of GSCM (source: [40]).

WINNER+ channel models and extended them with millimeter wave communications [51]. In parallel, the 3GPP created new GSCM [52, 53], which also take into account 3D propagation environments. Finally, the Quasi Deterministic Radio Channel Generator (QuaDRiGa) channel models have been created by the Fraunhofer Heinrich Hertz Institute [40, 54]. In addition, they developed a software to implement the QuaDRiGa channel models and other GSCM such as the WINNER and the 3GPP 38.901 channel models.

Summary of this Chapter:

- For cellular communications, the propagation channel is most often a **multipath propagation channel**.
- Usually, the **baseband propagation channel** is defined and can be divided in two parts. Firstly, the **path loss** is the mean attenuation of the signal. Secondly, the **multipath components** are caused by the reflections of the transmitted signal against obstacles.
- The **reflections of the transmitted signal against obstacles** induce **variations of the propagation channel in the frequency domain**. This effect is called the **frequency selectivity** of the propagation channel.
- The **variations in the time domain of the multipath components due to the Doppler effect** induce **variations of the propagation channel in the time domain**. This effect is called the **time selectivity** of the propagation channel.
- The **Rayleigh fading channel model** is suitable for **NLOS propagation channels**. With this model, the **variations of the propagation channel in the time domain** are caused by a specific type of Doppler effect, the **Doppler spread**.

- The **Rician fading channel model** is suitable for **propagation channels with a LOS component**. With this model, the **variations of the propagation channel in the time domain** are caused by the **addition of two types of Doppler effect, the Doppler spread and the Doppler shift**.
- Unlike the classical Rayleigh and Rician fading channel model, a **GSCM takes into account the spatial characteristics of the propagation environment** but induces a **higher complexity**.

2

Multi-Carrier Modulations

A multi-carrier modulation distributes the information on several narrow-band sub-carriers to form a broadband signal. Doing so, it divides the broadband propagation channel into a multiplicity of narrow-band propagation channels. In a well dimensioned system, each one of these narrow-band propagation channels is considered to be non-selective in the time and frequency domains. Thus, a multi-carrier modulation presents a great robustness against the time and frequency selectivity of the propagation channel. That is why multi-carrier modulations are widely used in the current systems. Among all multi-carrier modulations, the OFDM modulation is one of its most popular member as it is used in a large number of existing services such as Digital Video Broadcasting (DVB), WiFi and 4G Long Term Evolution (LTE). However, the OFDM modulation has some limitations and thus other multi-carrier modulations are under investigation for the development of 5G. This section is dedicated to the description of the OFDM modulation and of an alternative multi-carrier modulation called the FBMC/OQAM modulation.

2.1 OFDM

The OFDM modulation is an evolution of the Frequency-Division Multiplexing (FDM) techniques and is based on the pioneering work of Chang [55], which used orthogonal pulse shapes to multiplex data in the frequency domain. The OFDM modulation was not used in a consumer-oriented application until the late 1980s and the deployment of the Asymmetric Digital Subscriber Line (ADSL). More recently, the OFDM modulation has been introduced in wireless applications with WiFi and LTE.

2.1.1 Modulation

The OFDM modulation multiplexes data over M consecutive sub-carriers, each one being spaced by a frequency distance F_0. Each OFDM symbol has a duration of $T_0 = 1/F_0$ and is

separated from the others by a guard interval in order to deal with Inter-Symbol Interference (ISI). This guard interval can be Zero Padded (ZP) or filled with a Cyclic Prefix (CP). The CP, which was first proposed by [7], is a copy of the end of each symbol positioned in the beginning of it as illustrated in Figure 2.1. The CP duration is denoted by T_{CP} and must

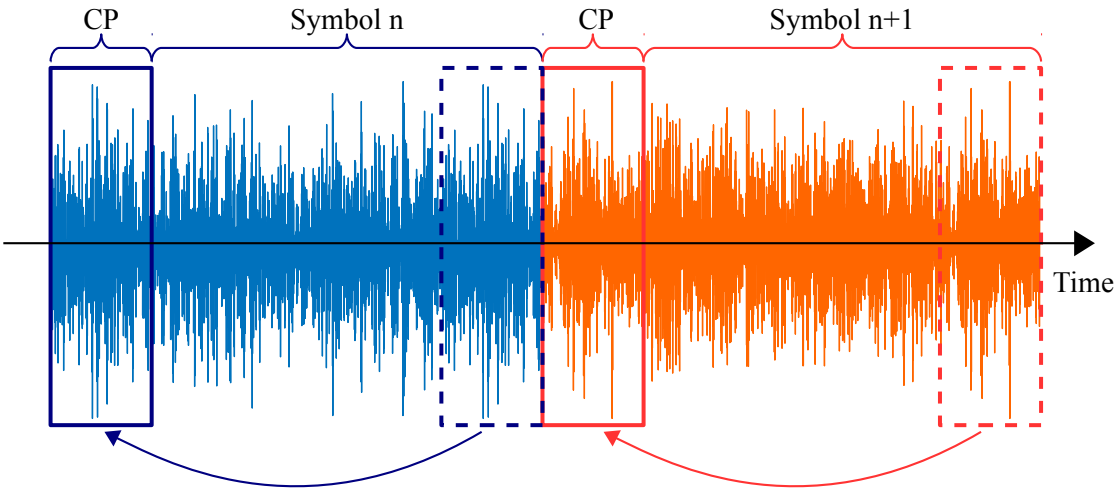

Figure 2.1: Construction of the CP.

verify $T_{CP} \geq \tau_l \ \forall l \in [0, L_h - 1]$ in order to avoid the ISI. In turn, this CP induces a reduced spectral efficiency.

Let us define $c[m,n]$ the complex data carried by the sub-carrier m for the symbol n, the OFDM baseband transmitted signal in the time-domain can be defined by:

$$s(t) = \sum_{n \in \mathbb{Z}} \sum_{m=0}^{M-1} c[m,n] \Pi_{m,n}(t), \tag{2.1}$$

where:

$$\begin{aligned} \Pi_{m,n}(t) &= \tfrac{1}{\sqrt{T_0}} \, \Pi_{(T_0+T_{CP})} \left(t - n\left(T_0 + T_{CP}\right) - \tfrac{T_0 - T_{CP}}{2} \right) \exp\left[j2\pi m F_0 \left(t - n\left(T_0 + T_{CP}\right) \right) \right], \\ &= \Pi^0_{m,n}(t) + \Pi^{CP}_{m,n}(t), \end{aligned} \tag{2.2}$$

with:

$$\begin{cases} \Pi^0_{m,n}(t) &= \tfrac{1}{\sqrt{T_0}} \, \Pi_{T_0} \left(t - \tfrac{T_0}{2} - n\left(T_0 + T_{CP}\right) \right) \exp\left[j2\pi m F_0 \left(t - n\left(T_0 + T_{CP}\right) \right) \right], \\ \Pi^{CP}_{m,n}(t) &= \tfrac{1}{\sqrt{T_0}} \, \Pi_{T_{CP}} \left(t + \tfrac{T_{CP}}{2} - n\left(T_0 + T_{CP}\right) \right) \exp\left[j2\pi m F_0 \left(t - n\left(T_0 + T_{CP}\right) \right) \right], \end{cases} \tag{2.3}$$

and:

$$\Pi_T(t) = \begin{cases} 1, & if \ |t| < \frac{T}{2}, \\ 0, & if \ |t| > \frac{T}{2}, \end{cases} \tag{2.4}$$

being the rectangular pulse shape. The pulse shapes $\Pi^0_{m,n}(t)$ aims at creating the useful parts of the OFDM symbol, while the pulse shapes $\Pi^{CP}_{m,n}(t)$ aims at creating the CP parts of the

OFDM symbol. Indeed, one can notice that:

$$\Pi_{m,n}^{CP}(t) = \Pi_{m,n}^{0}(t + T_0) \quad \text{for} \quad (n\,(T_0 + T_{CP}) - T_{CP}) \leq t \leq n\,(T_0 + T_{CP})\,. \tag{2.5}$$

Additionally, one particularity of the OFDM modulation is that the frequency spectra of one sub-carrier overlaps but does not interfere with the other sub-carriers because:

$$\begin{aligned} \int_{\mathbb{R}} \Pi_{m_1,n}^{*}(t)\Pi_{m_2,n}(t)dt &= \frac{1}{T_0} \int_{t=n(T_0+T_{CP})}^{n(T_0+T_{CP})+T_0} \exp\left[j2\pi(m_2 - m_1)F_0\left(t - n\left(T_0 + T_{CP}\right)\right)\right] dt, \\ &= \delta_{m_1,m_2}. \end{aligned} \tag{2.6}$$

This particularity is illustrated by Figure 2.2.

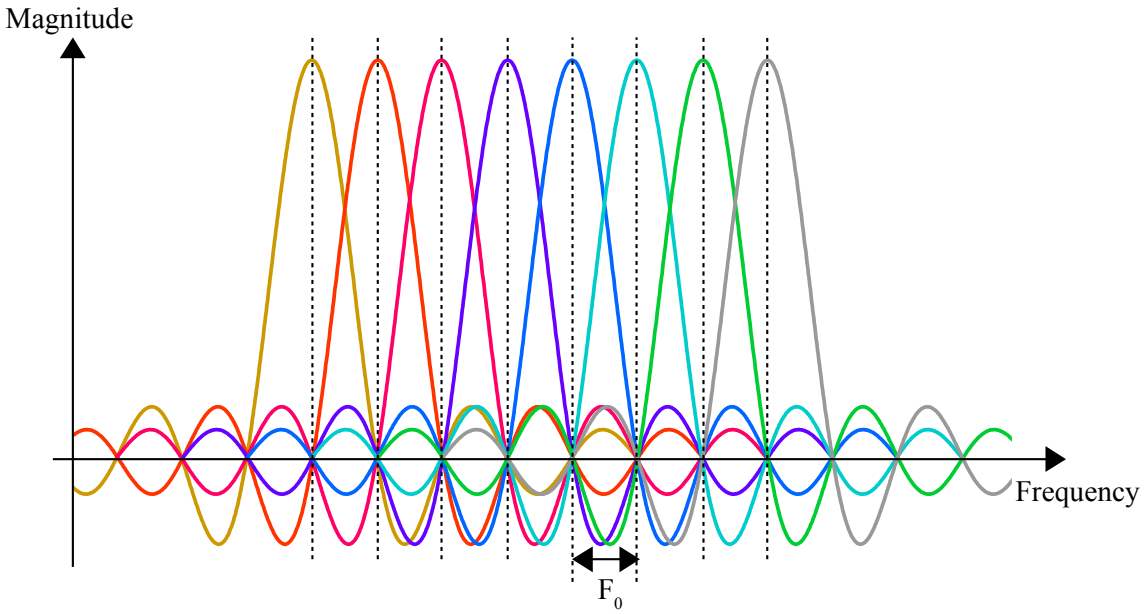

Figure 2.2: Illustration of the OFDM orthogonality with $M = 8$ sub-carriers. Each colored curve stands for one OFDM sub-carrier spectral magnitude.

2.1.2 Demodulation

The equation (1.2) gives the received baseband signal as follows:

$$r(t) = \sqrt{P_h}\left(\sum_{l=0}^{L_h-1} s\,(t - \tau_l)\,h_l(t)\right) + \eta(t), \tag{2.7}$$

with P_h the path loss, $h_l(t)$ the multiplying factors of the propagation channel, τ_l the delays and $\eta(t)$ the time domain noise component. Using (2.1) in (2.7), it comes:

$$r(t) = \sum_{n\in\mathbb{Z}} \sum_{m=0}^{M-1} c[m,n]\sqrt{P_h} \left(\sum_{l=0}^{L_h-1} \Pi_{m,n}\left(t-\tau_l\right) h_l(t) \right) + \eta(t). \tag{2.8}$$

For the frequency and time indexes (m_0, n_0), the received data obtained after the demodulation is:

$$y\left[m_0,n_0\right] = \int_{\mathbb{R}} r(t) \left(\Pi^0_{m_0,n_0}(t)\right)^* dt. \tag{2.9}$$

For the sake of simplicity, the time index n_0 used for the rest of this part is $n_0 = 0$. Moreover, the notations $m = m_0 - p$, $c_p = c[m_0 - p, 0]$ and $y = y[m_0, 0]$ are given and the mathematical set of useful sub-carriers Ω_p is defined as follows:

$$\Omega_p = \left\{ p \in \mathbb{Z} \mid c_p \neq 0 \right\}. \tag{2.10}$$

As $\tau_l < T_{CP}\ \forall l \in [0, L_h - 1]$ and using (2.8) in (2.9), it comes:

$$\begin{aligned} y &= \sum_{p\in\Omega_p} c_p\sqrt{P_h} \left(\sum_{l=0}^{L_h-1} \left(\tfrac{1}{T_0} \int_0^{T_0} h_l(t) \exp\left[-j2\pi p F_0 t\right] dt \right) \exp\left[-j2\pi(m_0-p)F_0\tau_l\right] \right) \\ &\quad + \int_{\mathbb{R}} \eta(t) \left(\Pi^0_{m_0,n_0}(t)\right)^* dt, \\ &= \sum_{p\in\Omega_p} \left(\sqrt{P_h}H_p\right) \times c_p + b, \end{aligned} \tag{2.11}$$

with:

$$H_p = \sum_{l=0}^{L_h-1} \left(\frac{1}{T_0} \int_0^{T_0} h_l(t) \exp\left[-j2\pi p F_0 t\right] dt \right) \exp\left[-j2\pi(m_0-p)F_0\tau_l\right], \tag{2.12}$$

and:

$$b = \int_{\mathbb{R}} \eta(t) \left(\Pi^0_{m_0,n_0}(t)\right)^* dt = \frac{1}{\sqrt{T_0}} \int_0^{T_0} \eta(t) \exp\left[-j2\pi m_0 F_0 t\right], \tag{2.13}$$

being the noise component at the frequency index m_0.

In a well-dimensioned system, $h_l(t)$ can be considered constant along time for one symbol and it comes $h_l(t) = h_l$. Therefore, as:

$$\frac{1}{T_0} \int_0^{T_0} \exp\left[-j2\pi p F_0 t\right] dt = \delta_{p,0}, \tag{2.14}$$

it comes:

$$y = \left(\sqrt{P_h}H\right) \times c + b, \tag{2.15}$$

with $c = c_0$ and:

$$H = H_0 = \sum_{l=0}^{L_h-1} h_l \exp\left[-j2\pi m_0 F_0 \tau_l\right], \tag{2.16}$$

being the propagation channel frequency response at the frequency index m_0. Moreover, as h_l and $h_{l'}$ are independent variables if $l \neq l'$ and according to (1.1):

$$E\left[|H|^2\right] = \sum_{l=0}^{L_h-1} E\left[|h_l|^2\right] = 1. \tag{2.17}$$

According to the equation (2.15), the OFDM modulation suffers neither from ISI nor Inter-Carrier Interference (ICI).

The per sub-carrier equalization process becomes simple as long as the receiver knows the component $\sqrt{P_h}.H_0$. For example, with a Zero Forcing (ZF) equalizer, the equalized received data at the frequency index m_0 is:

$$\hat{c} = c + \frac{b}{\sqrt{P_h}.H}. \tag{2.18}$$

2.1.3 Implementation

One advantage of the OFDM modulation is the low complexity of its implementation. In [56], the authors introduced the use of the Inverse Discrete Fourier Transform (IDFT) and Discrete Fourier Transform (DFT) blocks to design the OFDM transmitter and receiver respectively. The system complexity is then drastically reduced using the Inverse Fast Fourier Transform (IFFT) and Fast Fourier Transform (FFT) algorithms [8]. The baseband transmultiplexer scheme of a CP-OFDM system is presented in Figure 2.3.

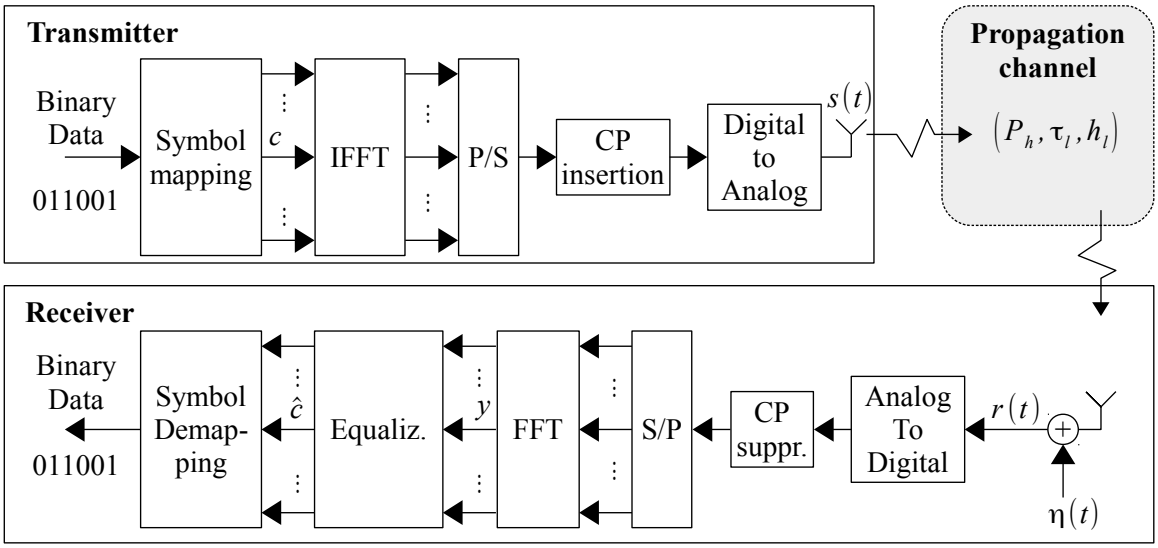

Figure 2.3: CP-OFDM baseband transmultiplexer.

2.2 FBMC/OQAM

The FBMC/OQAM modulation is part of the Filter-Bank Multi-Carrier (FBMC) modulations. It is actually another FDM technique based on the work of Chang [55]. It was further improved by Saltzberg [57] under the name OFDM/OQAM.

2.2.1 Modulation

While the OFDM modulation uses a rectangular pulse shape, the FBMC/OQAM modulation extends it to a large set of purely real prototype filters $g(t)$ to have a better time and frequency localization as illustrated in Figure 2.4 with the Malvar pulse shape [58]. This prototype filter

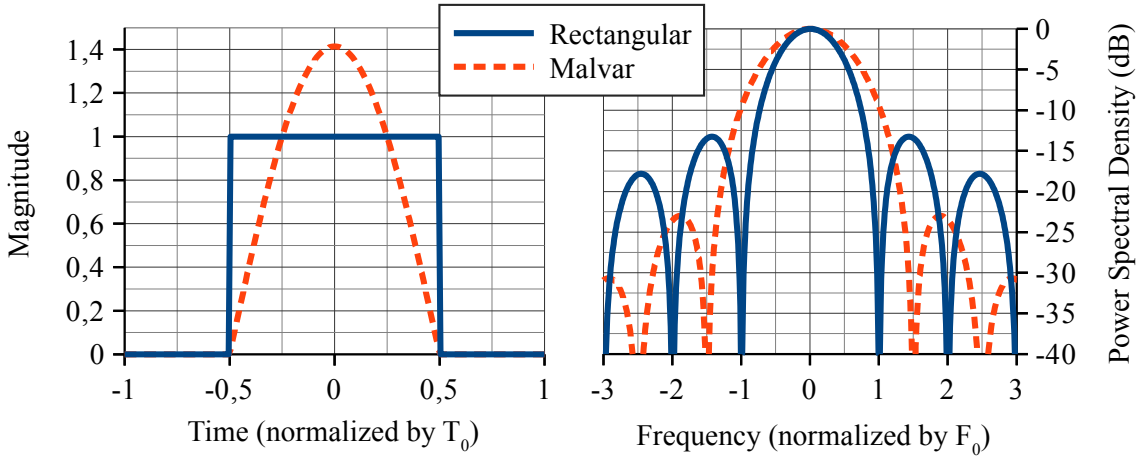

Figure 2.4: Time and frequency localization of the rectangular pulse used for the OFDM modulation and an example of a FBMC/OQAM pulse shape named the Malvar pulse shape.

is of length $K.T_0$ where K is called the overlapping factor. With such a pulse shape, the orthogonality has to be relaxed to the real field. This means that each complex data is splitted into a real part and an imaginary part and that each part is sent with an offset of $T_0/2$. Contrary to the OFDM modulation, the FBMC/OQAM symbols overlap in time as shown by the Figure 2.5.

Using the FBMC/OQAM modulation, the baseband transmitted signal in the time-domain can be defined by:

$$s(t) = \sum_{n\in\mathbb{Z}} \sum_{m=0}^{M-1} a[m,n] g_{m,n}(t), \tag{2.19}$$

with $a[m,n]$ the real data sent at frequency and time indexes (m,n), with:

$$g_{m,n}(t) = g\left(t - n\frac{T_0}{2}\right) e^{j2\pi m F_0 t} e^{j\phi[m,n]}, \tag{2.20}$$

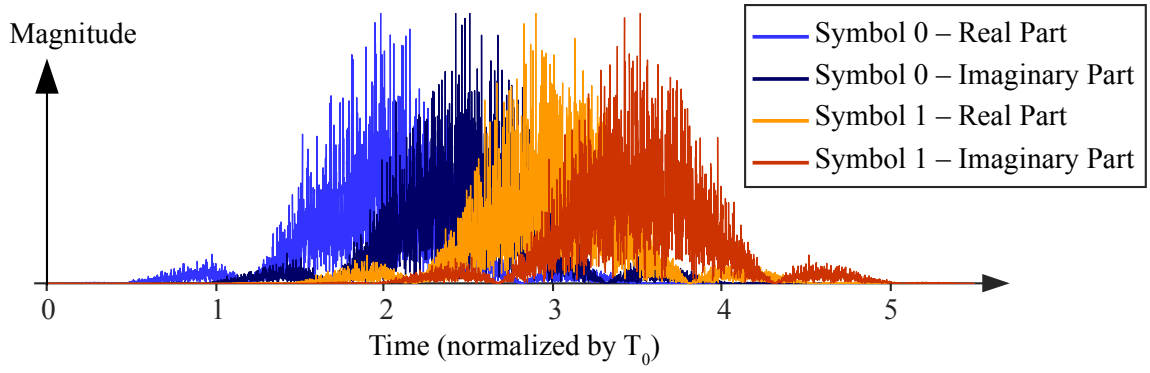

Figure 2.5: Illustration of the overlapping structure of the FBMC/OQAM signal for two symbols, with a Phydyas prototype filter [41] (K= 4).

and with:

$$\phi[m,n] = \frac{\pi}{2}(m+n) + \pi k_\phi[m,n],\ k_\phi[m,n] \in \mathbb{Z}. \tag{2.21}$$

According to [9], the following condition should be valid in order to ensure the orthogonality in the real field:

$$\Re\left[\int_{\mathbb{R}} g^*_{m_1,n_1}(t) g_{m_2,n_2}(t) dt\right] = \delta_{m_1,m_2}\delta_{n_1,n_2}. \tag{2.22}$$

2.2.2 Demodulation

The equation (1.2) gives the received baseband signal as follows:

$$r(t) = \sqrt{P_h}\left(\sum_{l=0}^{L_h-1} s\left(t-\tau_l\right) h_l(t)\right) + \eta(t), \tag{2.23}$$

with P_h the path loss, $h_l(t)$ the multiplying factors of the propagation channel, τ_l the delays and $\eta(t)$ the time domain noise component. Using (2.19) in (2.23), it comes:

$$r(t) = \sum_{n\in\mathbb{Z}}\sum_{m=0}^{M-1} a[m,n]\sqrt{P_h}\left(\sum_{l=0}^{L_h-1} g_{m,n}\left(t-\tau_l\right) h_l(t)\right) + \eta(t). \tag{2.24}$$

For the frequency and time indexes (m_0, n_0), the received data obtained after the demodulation is:

$$y\left[m_0,n_0\right] = \int_{\mathbb{R}} r(t) g^*_{m_0,n_0}(t) dt. \tag{2.25}$$

For the sake of simplicity, the time index n_0 used for the rest of this part is $n_0 = 0$. Moreover, the notations $m = m_0 - p$, $n = n_0 - q$, $a_{p,q} = a[m_0 - p, -q]$, $\phi_{p,q} = \phi[m_0 - p, -q]$ and

$y = y[m_0, 0]$ are given and the mathematical set $\Omega_{p,q}$ is defined as follows:

$$\Omega_{p,q} = \left\{(p,q) \in \mathbb{Z}^2 \mid a_{p,q} \neq 0 \ and \ (-2K+1) \leq q \leq 2K\right\}. \tag{2.26}$$

Using (2.24) in (2.25), it comes:

$$\begin{aligned} y &= \sum_{(p,q)\in\Omega_{p,q}} a_{p,q}\sqrt{P_h} \sum_{l=0}^{L_h-1} \left(\int_{\mathbb{R}} h_l(t) g^*_{m_0,n_0}(t) g_{m,n}\left(t-\tau_l\right) dt \right) \\ &\quad + \int_{\mathbb{R}} \eta(t) g^*_{m_0,n_0}(t) dt, \\ &= \sum_{p\in\Omega_{p,q}} \left(\sqrt{P_h} H_{p,q}\right) \times a_{p,q} + b, \end{aligned} \tag{2.27}$$

with:

$$H_{p,q} = \sum_{l=0}^{L_h-1} \left(\int_{\mathbb{R}} h_l(t) e^{j(\phi_{p,q}-\phi_{0,0})} g\left(t\right) g\left(t-\tau_l+q\frac{T_0}{2}\right) e^{-j2\pi pF_0 t} dt \right) e^{-j2\pi(m_0-p)F_0\tau_l}, \tag{2.28}$$

and:

$$b = \int_{\mathbb{R}} \eta(t) g^*_{m_0,n_0}(t) dt. \tag{2.29}$$

In a well-dimensioned system, $h_l(t)$ can be considered constant along time for one symbol and it comes $h_l(t) = h_l$. Therefore, the equation (2.28) can be rewritten as follows:

$$H_{p,q} = \sum_{l=0}^{L_h-1} h_l \left(\int_{\mathbb{R}} e^{j(\phi_{p,q}-\phi_{0,0})} g\left(t\right) g\left(t-\tau_l+q\frac{T_0}{2}\right) e^{-j2\pi pF_0 t} dt \right) e^{-j2\pi(m_0-p)F_0\tau_l}, \tag{2.30}$$

and $H_{p,q} \neq 0$. According to (2.27) and (2.30), the FBMC/OQAM modulation is affected by ISI and ICI called the intrinsic interference.

With a ZF equalization, the received equalized data is:

$$\hat{a} = a + \sum_{p\in\Omega_{p,q}\setminus\{(0,0)\}} \Re\left[\frac{H_{p,q}}{H}\right] \times a_{p,q} + \Re\left[\frac{b}{\sqrt{P_h}H}\right], \tag{2.31}$$

with $a = a_{0,0}$ and $H = H_{0,0}$.

If τ_l is small enough compared to T_0, it comes:

$$g\left(t-\tau_l+q\frac{T_0}{2}\right) \approx g\left(t+q\frac{T_0}{2}\right). \tag{2.32}$$

Therefore, the equation (2.30) can be rewritten as follows:

$$\begin{aligned} H_{p,q} &\approx \left(\sum_{l=0}^{L_h-1} h_l e^{-j2\pi(m_0-p)F_0\tau_l}\right)\left(\int_{\mathbb{R}} e^{j(\phi_{p,q}-\phi_{0,0})} g(t)\, g\left(t+q\tfrac{T_0}{2}\right) e^{-j2\pi pF_0 t} dt\right) \\ &\approx \left(\sum_{l=0}^{L_h-1} h_l e^{-j2\pi(m_0-p)F_0\tau_l}\right)\left(\int_{\mathbb{R}} g^*_{m_0,n_0}(t) g_{m_0-p,n_0-q}(t) dt\right), \end{aligned} \tag{2.33}$$

and:

$$H \approx \sum_{l=0}^{L_h-1} h_l \exp\left[-j2\pi m_0 F_0 \tau_l\right]. \tag{2.34}$$

As h_l and $h_{l'}$ are independent variables if $l \neq l'$ and according to (1.1):

$$E\left[|H|^2\right] = \sum_{l=0}^{L_h-1} E\left[|h_l|^2\right] = 1. \tag{2.35}$$

Additionally, by considering the propagation channel to be non-selective around the sub-carrier m_0, the equation (2.33) can be rewritten as follows:

$$\begin{aligned} H_{p,q} &\approx \left(\sum_{l=0}^{L_h-1} h_l e^{-j2\pi m_0 F_0\tau_l}\right)\left(\int_{\mathbb{R}} g^*_{m_0,n_0}(t) g_{m_0-p,n_0-q}(t) dt\right) \\ &\approx H \times \left(\int_{\mathbb{R}} g^*_{m_0,n_0}(t) g_{m_0-p,n_0-q}(t) dt\right). \end{aligned} \tag{2.36}$$

Finally, the equation (2.22) leads to the following approximation:

$$\hat{a} \approx a + \Re\left[\frac{b}{\sqrt{P_h}H}\right]. \tag{2.37}$$

Therefore, if $\tau_l \ll T_0 \ \forall l \in [0, L_h - 1]$, the intrinsic interference for the FBMC/OQAM modulation can be considered as negligible thanks to the good time an frequency localization of the FBMC/OQAM pulse-shape.

2.2.3 Implementation

As described in [9], a filter-bank structure can be used to design the transmitter and the receiver. Compared to the OFDM modulation, the complexity of the implementation is increased, partly because the FFT works twice as fast. Figure 2.6 depicts the transmitter structure and Figure 2.7 depicts the receiver structure. For both designs, the following notation is used:

$$G_m(z) = \sum_n g\left[k + nM\right] z^{-n}. \tag{2.38}$$

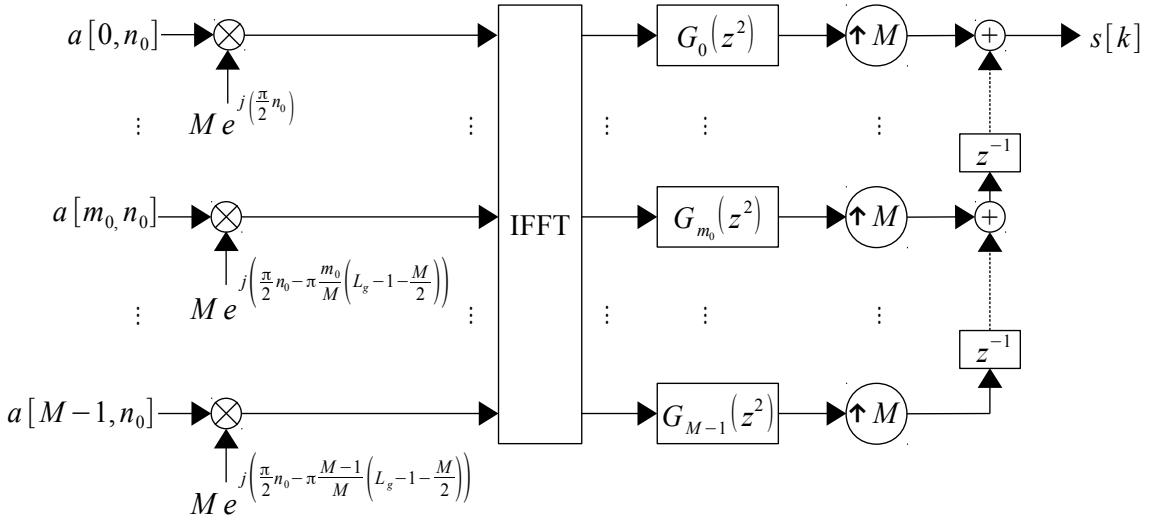

Figure 2.6: FBMC/OQAM baseband transmitter.

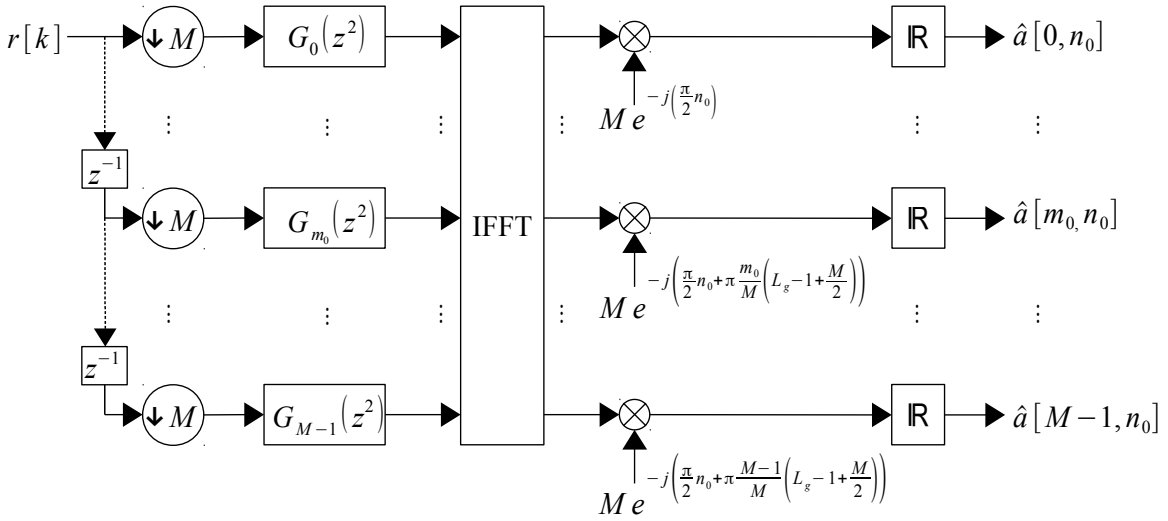

Figure 2.7: FBMC/OQAM baseband receiver.

Summary of this Chapter:

- The **OFDM** modulation is **widely used in the existing systems** (DVB, WiFi and 4G LTE).
- With the **OFDM** modulation, **a CP is added at the beginning of each symbol** in order to **avoid the ISI** due to the frequency selectivity of the propagation channel. However, this CP **reduces the spectral efficiency**.
- As the frequency spectra of one sub-carrier overlaps but does not interfere with the other sub-carriers, **the OFDM modulation is orthogonal in the complex field and avoids the ICI**.
- With the **OFDM** modulation, **the complexity of the implementation is rather**

limited thanks to the FFT and IFFT algorithms.

- The **FBMC/OQAM** modulation is an **alternative multi-carrier modulation**.
- By using a **prototype filter**, the FBMC/OQAM modulation has **a better localization in the time and frequency domains**, compared to the OFDM modulation. Thereby, it **does not need a CP** and **presents a better spectral efficiency**.
- Because of its prototype filter, **the orthogonality of the FBMC/OQAM modulation has to be relaxed to the real field**.
- Due to the frequency selectivity of the propagation channel, the **FBMC/OQAM** modulation is **affected by ICI and ISI called intrinsic interference**. However, **this interference is usually negligible** thanks to the good time and frequency localization of the FBMC/OQAM pulse shape.
- With the **FBMC/OQAM** modulation, **the complexity of the implementation is increased** compared to the one with the OFDM modulation.

3

Massive MIMO

The increase of the number of antennas, which is commonly called massive MIMO, is a popular trend for the development of 5G [2,4,23]. In [10], the author highlighted the benefits of multiple antennas on the BS side for multiuser communications and demonstrated that an increase of the number antennas on the BS side is always advantageous. The same author extended this work with an unlimited numbers of BS antennas in [11]. In this context, he shows that the noise, the Multi-User Interference (MUI), as well as the interference due to the channel estimation errors vanish for both the uplink and the downlink. Moreover, for a noncooperative multicellular system, the performance is only limited by the so called "pilot contamination" interference.

Based on this pioneering work, many studies have investigated massive MIMO uplink and downlink systems with a finite number of antennas on the BS side [13, 14], with a realistic propagation channel [22] or taking into account the signal distortion created by non-ideal hardware [17, 18]. They show that massive MIMO systems offer a substantial number of advantages. On the transmitter side, they are able to focus the energy in space [19–21] and, on the receiver side, they can increase the Signal-to-Interference-plus-Noise Ratio (SINR) [12, 15]. More generally, massive MIMO systems are interesting solutions to provide Space-Division Multiple-Access (SDMA) and to improve the spectral and energy efficiency of the systems [13, 14, 16, 59].

In this Chapter, a frequency domain analysis of massive MIMO systems is carried out considering the OFDM modulation and focusing on one sub-carrier. As in [10, 11, 13, 14], single-antenna UEs are considered for the sake of simplicity.

3.1 Massive MIMO Uplink Systems

In this part, simultaneous uplink communications are considered between N_u UEs and a BS equipped with N_r receive antennas. The maximum-likelihood multiuser detection technique [60] is optimal in this context at the price of a great complexity. However, massive MIMO

uplink systems with simple linear techniques are actually interesting solutions to reduce MUI as shown in [10]. In [15], the authors show how they can increase the energy and spectral efficiency of the systems highlighting their interest in this context. The linear combining techniques that are studied in this Chapter are the same as in [15].

3.1.1 System Model

The UE n_u sends the data c^{n_u} of variance σ_c^2 and the transmitted data vector $\mathbf{c}$ is defined as follows:

$$\mathbf{c} = \begin{bmatrix} c^0 & c^1 & \cdots & c^{N_u-1} \end{bmatrix}^T. \tag{3.1}$$

As the distance between the UE n_u and the receive antenna n_r is approximately equal $\forall n_r \in [0, N_r - 1]$, the path loss for the considered sub-carrier is independent of the receive antenna index n_r and equal to $P_H^{n_u}$ for the UE n_u. According to (2.15) and (2.17), the frequency domain channel between the UE n_u and the antenna n_r can be defined by a complex scalar denoted here by $\sqrt{P_H^{n_u}} H^{n_u,n_r}$, where H^{n_u,n_r} is the $(n_r, n_u)^{th}$ entry of the $(N_r \times N_u)$ channel matrix:

$$\mathbf{H} = \begin{bmatrix} \mathbf{H}^0 & \mathbf{H}^1 & \cdots & \mathbf{H}^{N_u-1} \end{bmatrix} \tag{3.2}$$

and $E\left[|H^{n_u,n_r}|^2\right] = 1$. Moreover, $P_H^{n_u}$ is the $(n_u, n_u)^{th}$ entry of the $(N_u \times N_u)$ diagonal matrix $\mathbf{P}_H$. On the BS side, the received data are defined by the vector:

$$\mathbf{y} = \begin{bmatrix} y^0 & y^1 & \cdots & y^{N_r-1} \end{bmatrix}^T = \mathbf{H}\mathbf{P}_H^{1/2}\mathbf{c} + \mathbf{b}, \tag{3.3}$$

y^{n_r} being the received data on the antenna n_r and $\mathbf{b}$ being the noise vector defined as follows:

$$\mathbf{b} = \begin{bmatrix} b^0 & b^1 & \cdots & b^{N_r-1} \end{bmatrix}^T. \tag{3.4}$$

Therefore, b^{n_r} is the noise component on the antenna n_r of variance σ_b^2. The following decoding matrix:

$$\mathbf{W} = \begin{bmatrix} \mathbf{W}^0 & \mathbf{W}^1 & \cdots & \mathbf{W}^{N_u-1} \end{bmatrix}, \tag{3.5}$$

where the $(n_r, n_u)^{th}$ entry is given by W^{n_u,n_r}, is then applied to the received data, so that the estimated data vector $\hat{\mathbf{c}}$ of size N_u is computed as follows:

$$\hat{\mathbf{c}} = \left(\mathbf{W}\boldsymbol{\xi}_W^{-1/2}\right)^H \mathbf{y} = \boldsymbol{\xi}_W^{-1/2}\mathbf{W}^H\mathbf{H}\mathbf{P}_H^{1/2}\mathbf{c} + \boldsymbol{\xi}_W^{-1/2}\mathbf{W}^H\mathbf{b}, \tag{3.6}$$

with $\boldsymbol{\xi}_W$ being a normalization $(N_u \times N_u)$ diagonal matrix, where $\xi_W^{n_u}$ is the $(n_u, n_u)^{th}$ entry. To summarize, the frequency domain system model is depicted in Figure 3.1. In the next part, the choice of the decoding matrix $\mathbf{W}$ is discussed.

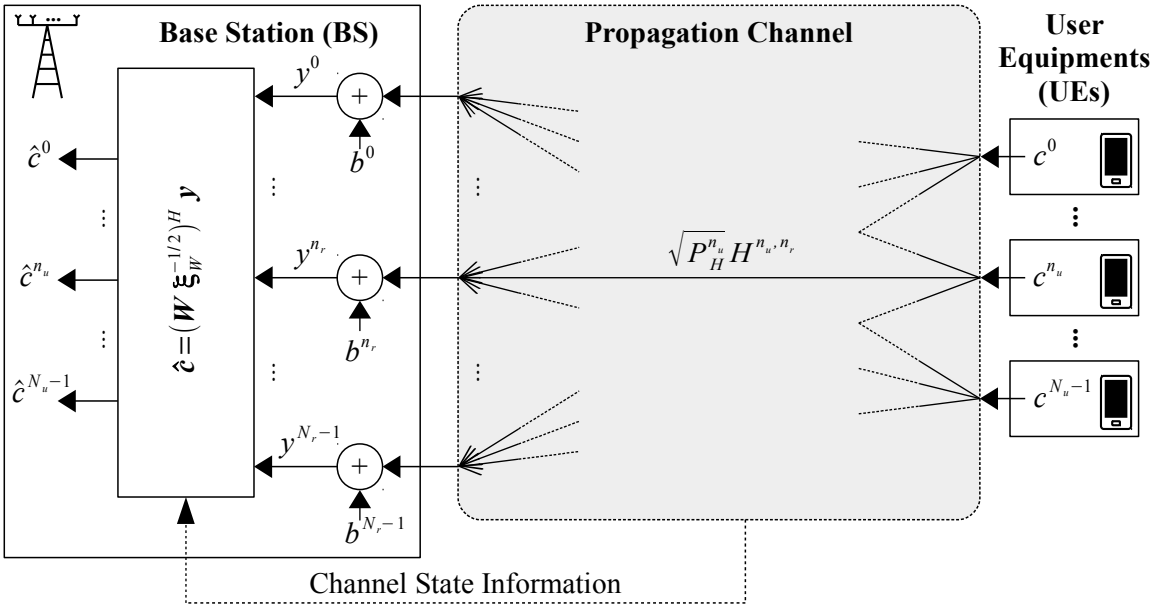

Figure 3.1: Description of the frequency domain massive MIMO uplink system model with N_u single-antenna UE and N_r receive antennas on the BS side.

3.1.2 Massive MIMO Combining Techniques

Many combining techniques can be used on the BS side in order to mitigate the received noise power and the MUI. In this part, we limit our study to the simple combining techniques described in [15] as they are well known and low complexity combining techniques.

Maximization of the SNR (MRC)

The Maximum Ratio Combining (MRC) technique, also called Matched Filter (MF), is intended to maximize the Signal-to-Noise Ratio (SNR). The decoding matrix $\mathbf{W}$ for the MRC is defined by:

$$\mathbf{W} = \mathbf{H}. \tag{3.7}$$

$\boldsymbol{\xi}_W$ can be build according to the instantaneous received power and thus $\xi_W^{n_u}$ is defined as follows:

$$\xi_W^{n_u} = P_H^{n_u} \left| (\mathbf{W}^{n_u})^H \mathbf{H}^{n_u} \right|^2 = P_H^{n_u} \left(\sum_{n_r=0}^{N_r-1} |H^{n_u,n_r}|^2 \right)^2. \tag{3.8}$$

In order to reduce the complexity of the receiver, the average received power can also be used. In this case, the normalization matrix is defined as follows:

$$\boldsymbol{\xi}_W = N_r^2 \mathbf{P}_H. \tag{3.9}$$

The complexity of the MRC technique is relatively low, which makes it a popular technique used in many papers as in [11]. However, for multiuser communications with a finite number of

receive antennas, the MUI penalizes the MRC technique and some other combining techniques can be used to improve the performance of the systems.

Minimization of the MUI (ZF)

The ZF combining technique can be used in order to completely suppress the MUI. The combining matrix is defined as follows:

$$\mathbf{W} = \mathbf{H}\left(\mathbf{H}^H\mathbf{H}\right)^{-1}, \tag{3.10}$$

and:

$$\boldsymbol{\xi}_W = \mathbf{P}_H. \tag{3.11}$$

The received data matrix $\hat{\mathbf{c}}$ is thus equal to:

$$\hat{\mathbf{c}} = \mathbf{c} + \mathbf{P}_H^{-1/2}\left(\mathbf{H}\mathbf{H}^H\right)^{-1}\mathbf{H}^H\mathbf{b}. \tag{3.12}$$

The MUI is completely removed, but the received data matrix is still corrupted by the noise component. According to [15], the ZF combining technique generally outperforms the MRC technique at the price of an increased complexity. However, in low SNR conditions, the noise power is preponderant compared to the MUI power and the MRC technique can outperform the ZF combining technique. For single-user transmissions, it can be noticed that the MRC technique with instantaneous power normalization and the ZF technique are equivalent.

Trade-off Between SNR and MUI (MMSE)

A trade-off between the SNR and the MUI power can be found with the so called Minimum Mean Square Error (MMSE) detector. With this technique, the decoding matrix is defined as follows:

$$\mathbf{W} = \mathbf{H}\left(\mathbf{H}^H\mathbf{H} + \alpha\mathbf{I}_{N_u}\right)^{-1}, \alpha \in \mathbb{R}^+, \tag{3.13}$$

and:

$$\xi_W^{n_u} = P_H^{n_u}\left|\left(\mathbf{W}^{n_u}\right)^H\mathbf{H}^{n_u}\right|^2. \tag{3.14}$$

If the UEs are at the same distance from the BS, then $P_H^{n_u} = P_H$, $\forall n_u \in [0,N_u-1]$. In this case, one can choose $\alpha = \sigma_b^2/(P_H\sigma_c^2) = \rho^{-1}$ as in [14, 15]. Indeed, the authors show that this technique outperforms both the MRC technique and the ZF technique. As with the ZF combining technique, the complexity of the MMSE combining technique is higher that this of the MRC technique.

3.2 Massive MIMO Downlink Systems

In wireless communication systems, beamforming methods allow providing SDMA and to simultaneously transmit data from a BS with N_t antennas to N_u UEs. From the point of view of a particular UE, the idea is to use the propagation channel properties to have a coherent addition of the useful parts of the signals coming from the N_t transmitting antennas, while having a destructive addition of the interfering parts of the receive signals. For a propagation channel with a LOS component, this leads to create a pencil beam between the BS and each receiver. For a NLOS channel, beamforming methods aim at focusing the signal power around each UE. Those techniques can increase the received signal power but can also create MUI. In [61], the author introduce Dirty Paper Coding (DPC) and shows that if the transmitter knows the interference, the channel capacity is the same as if there were no interference. In our context, it means that the capacity grows linearly with the minimum of the number of transmitting antennas and receiving antennas. However, no practical solution is provided in this paper. Until now DPC-based solutions are complex ones and require a lot of computational resources, as for example [62] and [63]. This part only focuses on less complex linear solutions, applicable in practice such as those described in [21].

3.2.1 System Model

The transmitted data are defined by the following vector:

$$\mathbf{c} = \begin{bmatrix} c^0 & c^1 & \cdots & c^{N_u-1} \end{bmatrix}^T, \tag{3.15}$$

c^{n_u} being the complex data transmitted to the UE n_u with a variance of σ_c^2. This vector is precoded by the following $(N_t \times N_u)$ matrix:

$$\mathbf{W} = \begin{bmatrix} \mathbf{W}^0 & \mathbf{W}^1 & \cdots & \mathbf{W}^{N_u-1} \end{bmatrix}. \tag{3.16}$$

The transmitted precoded data are defined by the following vector:

$$\mathbf{x} = \begin{bmatrix} x^0 & x^1 & \cdots & x^{N_t-1} \end{bmatrix}^T = \frac{1}{\sqrt{\xi_W}} \mathbf{W}\mathbf{c}, \tag{3.17}$$

ξ_W being a normalization factor designed to obtain an average or instantaneous transmit power equal to σ_c^2. Moreover, W^{n_t,n_u} is the $(n_t, n_u)^{th}$ entry of the matrix $\mathbf{W}$.

As in a massive MIMO uplink system, the distance between the transmit antenna n_t and the UE n_u is approximately equal $\forall n_t \in [0, N_t-1]$, the path loss for the considered sub-carrier is independent of the transmit antenna index n_t and is equal to $P_H^{n_u}$ for the UE n_u. According to (2.15), the channel between the transmit antenna n_t and the UE n_u can be defined by a complex scalar denoted here by $\sqrt{P_H^{n_u}} H^{n_t,n_u}$, where H^{n_t,n_u} is the $(n_u, n_t)^{th}$ entry of the channel matrix $\mathbf{H}$ of size $(N_u \times N_t)$. Moreover, $P_H^{n_u}$ is the $(n_u, n_u)^{th}$ entry of the $N_u \times N_u$

diagonal matrix $\mathbf{P}_H$. As for the uplink and according to (2.17), the expected power of H^{n_t,n_u} is equal to 1, meaning $E\left[|H^{n_t,n_u}|^2\right] = 1$, $\forall n_t \in [0,N_t-1]$ and $\forall n_u \in [0,N_u-1]$. The received data for the UE n_u is given by y^{n_u}. Therefore, the received data vector $\mathbf{y}$ is defined as follows:

$$\mathbf{y} = \begin{bmatrix} y^0 & y^1 & \cdots & y^{N_u-1} \end{bmatrix}^T = \frac{1}{\sqrt{\xi_W}} \mathbf{P}_H^{1/2} \mathbf{H}\mathbf{W}\mathbf{c} + \mathbf{b}, \tag{3.18}$$

with $\mathbf{b}$ the noise vector:

$$\mathbf{b} = \begin{bmatrix} b^0 & b^1 & \cdots & b^{N_u-1} \end{bmatrix}^T, \tag{3.19}$$

and b^{n_u} the frequency domain noise component for the ${n_u}^{th}$ UE. The same noise power is assumed for all UEs and the variance of b^{n_u} is σ_b^2 $\forall n_u \in [0,N_u-1]$. The frequency domain system model is described by Figure 3.2.

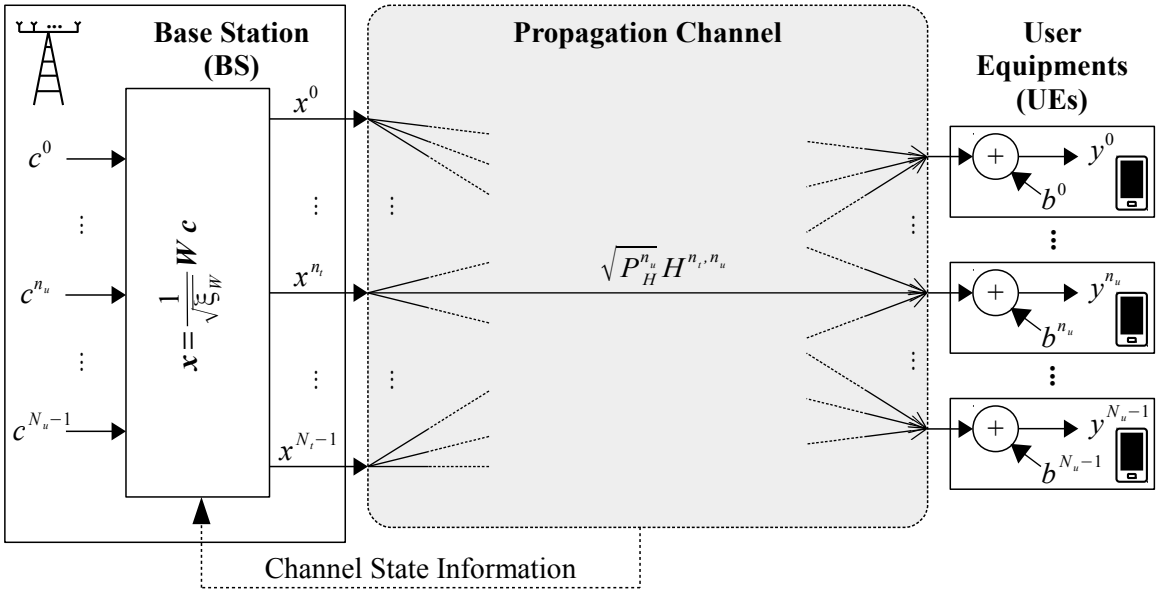

Figure 3.2: Description of the frequency domain massive MIMO downlink system model with N_t transmit antennas on the BS side and N_u single-antenna UE.

3.2.2 Massive MIMO Beamforming Techniques

As for the uplink, the study is limited to some simple linear beamforming techniques. their precoding matrix $\mathbf{W}$ are described thereafter.

Maximization of the Received Power (MRT)

The first strategy is to maximize the received power for each UE without taking into account the MUI. This is done using the matched filter of the channel, meaning:

$$\mathbf{W} = \mathbf{H}^H. \tag{3.20}$$

If ξ_W is defined to have the instantaneous power equal to σ_c^2, then:

$$\xi_W = \sum_{n_t=0}^{N_t-1} \sum_{n_u=0}^{N_u-1} |H^{n_t,n_u}|^2 . \tag{3.21}$$

In the literature, this beamforming method is known as Maximum Ratio Transmission (MRT), first introduced in [64] for a single-user MIMO transmission. This precoding matrix is actually comparable to the MRC decoding technique defined in the previous part for the uplink. Therefore, if N_u= 1, this solution is optimal as there is no MUI. Additionally, when the number of transmit antennas tends to infinity, the MUI vanishes (as shown in [11]) and this solution is still optimal. ξ_W can also be settled to have an average transmit power equal to σ_c^2:

$$\xi_W = N_t N_u. \tag{3.22}$$

In the literature, this method is often called Time Reversal (TR). This name actually refers to the more general concept of using the time inverse filter of the propagation channel. This technique allows performing spatial and temporal focusing in the field of ultrasounds [65]. More recently, time reversal was investigated for wireless communications in ultra-wideband systems [66] and in mobile networks systems [67]. Using an average normalization factor actually simplifies the transmitter design as each antenna can work separately. Nevertheless, in the single user case, the MRT technique exploits the full spatial diversity, whereas the TR technique only exploits half spatial diversity [68]. This means that the TR technique is less robust against the multipath propagation channels. With the previous precoding techniques, the transmitted power on one antenna can be relatively high, which can be a problem depending on the used power amplifier. To avoid this kind of problem, researches have been carried out to obtain an efficient precoding matrix with the constraint of an equal transmit power on each antenna. In [69, 70], the authors describe "constant envelope" precoding schemes to resolve this problem respectively in the single-user and multi-user cases. Their solutions are therefore relatively complex compared to the MRT and the TR precoding techniques. In [71], the authors describe a simple precoder with equal power on each antenna called Equal Gain Transmission (EGT). They work on the single-user MIMO scheme and show that the EGT exploits the full channel diversity. In [72], the authors analyse the BER for multi-user EGT scheme. For multiuser Multiple-Input Single-Output (MISO), the EGT precoding matrix can be defined by:

$$W^{n_t,n_u} = \left(\frac{H^{n_t,n_u}}{|H^{n_t,n_u}|} \right)^* \forall n_t \in [0, N_t - 1] \;\; and \; \forall n_u \in [0, N_u - 1] \, . \tag{3.23}$$

In this case, the normalization factor ξ_W is the same as in (3.22). The EGT method is therefore less complex than the MRT technique.

Minimization of the MUI (ZF)

The second strategy is to minimize the MUI. This can be done with the well-known ZF precoder, also known as channel inversion [73]:

$$\mathbf{W} = \mathbf{H}^H \left(\mathbf{H}\mathbf{H}^H\right)^{-1}. \tag{3.24}$$

In [73], the authors show that the average normalization factor is difficult to use as it could be infinite, for example when N_u=N_t. This is why an instantaneous normalization factor is a better option. In this case, it comes:

$$\xi_W = \sum_{n_t=0}^{N_t-1} \sum_{n_u=0}^{N_u-1} |W^{n_t,n_u}|^2 . \tag{3.25}$$

As for the ZF combining technique, this precoder completely removes MUI. In low noise power condition, the ZF precoder is known to outperform the MRT precoder [19] as the MRT performance is limited by the MUI. However, in high noise power condition, the MRT precoder outperforms the ZF precoder. Indeed, for the ZF precoder, the normalization factor ξ_W can be very high leading to a low received power. Furthermore, the ZF technique is more complex than the MRT technique as it needs to perform a matrix inversion.

Trade-off Between Received Power and MUI (MMSE)

One way to improve the performances of the ZF precoder at high noise power is to "regularize" the inverse matrix $\left(\mathbf{H}\mathbf{H}^H\right)^{-1}$ [73]. The precoding matrix then becomes:

$$\mathbf{W} = \mathbf{H}^H \left(\mathbf{H}\mathbf{H}^H + \alpha \mathbf{I}_{N_u}\right)^{-1}, \alpha \in \mathbb{R}^+. \tag{3.26}$$

The normalization factor is also defined by (3.25). This precoding method is known as transmit MMSE, transmit Wiener filter or Regularized Zero Forcing (RZF). As for the MMSE decoding technique, this solution is actually a trade-off between the MRT precoder and the ZF precoder. Indeed, for a high value of α, $\mathbf{W}$ tends to a MRT precoder, whereas for a low value of α, it tends to a ZF precoder.

Summary of this Chapter:

- **Massive MIMO systems** hold a **wide range of benefits** by using a **large number of antennas**. In particular, they allow providing **SDMA** and to improve the **spectral and energy efficiency** of the systems.
- For the **uplink**, **the users simultaneously communicate with a BS equipped with a large number of antennas** thanks to **massive MIMO combining techniques**.

- The **MRC**, **ZF** and **MMSE** combining techniques are used respectively to **maximize the SNR**, to **minimize the MUI power** and to have a **trade-off between the SNR and the MUI power**.
- For the **downlink**, **a BS equipped with a large number of antennas simultaneously serves the users** thanks to **massive MIMO beamforming techniques**.
- The **MRT**, **ZF** and **MMSE** combining techniques are used respectively to **maximize the received power**, to **minimize the MUI power** and to have a **trade-off between the received power and the MUI power**.

Part II

Massive MIMO for Vehicular Applications

4

Context and System Model

4.1 Context of the Study

In the past years, with the deployment of high speed railways and the development of connected cars, vehicular communications have gained a growing interest. Therefore, these emerging use cases are widely studied in the context of the development of 5G. Their associated scenarios are called Vehicle-to-Vehicle (V2V) or, more generally, V2X communications [2,3]. In those scenarios and according to [1], the speed of the users can be as high as 500 km/h. The main challenges associated to V2X communications are described thereafter [24].

- The network architecture must be adapted to high mobility communications. To this end, Heterogeneous Networks (HetNet) and Cloud Radio Access Networks (C-RAN) could be used [25].
- The fast and frequent handovers have to be managed. To this end, new schemes are investigated in [26, 27].
- The interference due to the Doppler effect might have a detrimental impact on the performance of the systems [28] especially when using multi-carrier modulations. Therefore, solutions are investigated to counteract this effect, stabilizing the high mobility communications.

Chapters 4, 5 and 6 focus on the third problem linked to the Doppler effect.

With the existing Doppler effect reduction schemes, a good performance comes with an increased complexity [74, 75]. Additionally, the use of multiple antennas in a MIMO system can be exploited to mitigate the interference due to the mobility. The creation of a beam using a directional antenna [76, 77] or several antennas allows limiting the Doppler effect. For example, in [78, 79] the authors use several antennas to create beams in predetermined directions in the context of flat fading channels. With the combination of signals coming from these fix directions and with Doppler compensation techniques, they show that this beam

partitioning technique can reduce the impact of the Doppler effect. Moreover, interference compensation techniques for MIMO-OFDM systems can take advantage of the spatial diversity on the transmitter side [80], on the receiver side [81, 82] or both on the transmitter side and on the receiver side [83, 84].

Massive MIMO systems described in Chapter 3 are studied in this part. Using the large diversity offered by massive MIMO systems, the performance can be greatly improved even with low-complexity transmitters and receivers. As developed in part 3.2, when these numerous antennas are used on the transmitter side, the transmitted signal can be focused towards the receivers, the received power is enhanced, the multiuser interference is reduced and thereby multiuser communications are allowed based on the so-called SDMA techniques [21]. This contribution focuses on a massive MIMO uplink system where the numerous number of antennas are located on the receiver side, as in part 3.1, and the transmitter is equipped with a single antenna. Therefore, the SINR is increased on the receiver side by reducing the noise power and the multiuser interference power as highlighted in [11, 13–15]. Accordingly, one may wonder if a massive MIMO system with a simple receiver could efficiently reduce the interference due to the Doppler effect.

Another proposition to reduce the Doppler effect is to use new waveforms [85]. In particular, the FBMC/OQAM modulation described in part 2.2 is an interesting solution when combined with a well localized prototype filter [9, 86]. Indeed, in a Single-Input Single-Output (SISO) system, the FBMC modulations can better prevent from the Doppler effect compared to the OFDM modulation as discussed in [30–33]. Massive MIMO techniques are often used with the OFDM modulation but they can also be efficiently combined with the FBMC modulations as demonstrated in [87, 88] in a multiuser context. However, even if the FBMC/OQAM modulation can outperform the OFDM modulation in a mobility context for a SISO link, its superiority in a massive MIMO context is not guaranteed.

Contribution of this Chapter:

In this Chapter, the massive MIMO uplink system model defined in part 3.1 is modified in order to take into account a moving user with a single antenna and to highlight the interference due to the Doppler effect in this context. Moreover, this system model is described for the OFDM modulation, but also for the FBMC/OQAM modulation defined in part 2.2. Thereby, this system model allows comparing these two modulations in a massive MIMO uplink system with mobility. This Chapter is used as a basis for Chapters 5 and 6.

Contribution of Chapter 5:

Chapter 5 only considers the OFDM modulation and focuses on NLOS communications. In this context, the effect of massive MIMO uplink systems on the interference due to the Doppler effect is studied based on the system model defined in Chapter 4. More specifically,

the effect of a very large number of uncorrelated receive antennas on the interference due to the Doppler effect is analytically studied in Chapter 5 considering the low-complexity MRC receiver described in part 3.1.2. In this context, Chapter 5 analytically highlights the impact of an increase of the number of receive antennas and the asymptotic behavior, when the number of receive antennas tends to infinity.

Contribution of Chapter 6:

Chapter 6 is based on the system model defined in Chapter 4 and aims at comparing the performance of the OFDM and the FBMC/OQAM modulations in a massive MIMO uplink system with mobility. Unlike in Chapter 5, propagation channels with an eventual LOS component are considered in this contribution. The asymptotic system capacity, when the number of receive antennas tends to infinity, is analytically evaluated and simulations are carried out in order to compare the performance of the OFDM and the FBMC/OQAM modulations in terms of system capacity and of Bit Error Rate (BER). Thereby, Chapter 6 gives an insight on the modulation leading to the best performance in terms of system capacity and of BER in a massive MIMO uplink system with mobility.

4.2 System Model

In order to evaluate the impact of the Doppler effect on massive MIMO uplink systems, a transmission between a moving UE equipped with a single antenna and a BS equipped with N_r antennas is considered in this Chapter. It may be noted that this scenario can be extended to a V2V scenario considering a moving receiver instead of a BS. According to part 1.2, the mobility of the user reduces the coherence time. In order to have accurate channel state informations, channel estimation and equalization processes are both conducted on the BS side during the same time slot. Therefore, the proposed scheme for uplink can be applied with Frequency-Division Duplex (FDD) or Time-Division Duplex (TDD) modes. Figure 4.1 depicts the considered scenario.

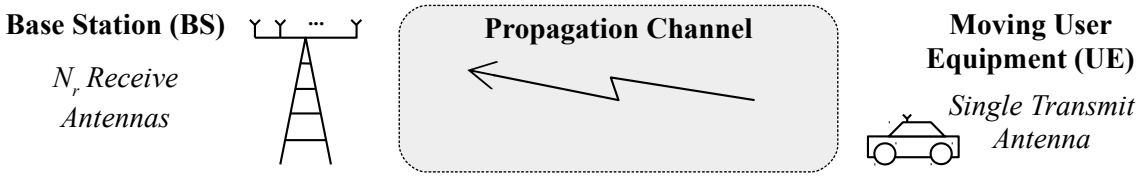

Figure 4.1: Uplink transmission between a moving UE equipped with a single antenna and a BS equipped with N_r antennas.

4.2.1 Propagation Channel

A multi-path propagation channel with a LOS component and with L_h independent paths is considered. The variations over time of the l^{th} multi-path component between the transmitter and the receive antenna n_r is given by $h_l^{n_r}(t)$ while the time delay of the l^{th} multi-path component is denoted by τ_l. Moreover, the receive antennas are sufficiently spaced so that $h_l^{n_r}(t)$ and $h_l^{n'_r}(t)$ can be assumed as independent variables if $n_r \neq n'_r$.

For the sake of simplicity, a normalized propagation channel is considered in this part meaning that the path loss P_H, defined in part 1.1, is equal to 1. Considering the receive antenna n_r, the first path of the propagation channel $h_0^{n_r}(t)$ follows a Rician fading model and can be described as in part 1.3.2 and in [5, 44, 45]. Therefore, it comes:

$$h_0^{n_r}(t) = \tilde{h}_0^{n_r}(t) + \check{h}_0^{n_r}(t), \tag{4.1}$$

$\tilde{h}_0^{n_r}(t)$ and $\check{h}_0^{n_r}(t)$ being two independent variables. In (4.1), $\tilde{h}_0^{n_r}(t)$ is the component due to the Doppler spread and is defined by:

$$\tilde{h}_0^{n_r}(t) = \sqrt{\tilde{P}_{h,0}} \times \frac{\tilde{h}_0^{(1)}(t) + j\tilde{h}_0^{(2)}(t)}{\sqrt{2}}. \tag{4.2}$$

It varies over time according to the Jakes' Doppler spectrum with the maximum Doppler frequency denoted by f_D^{max}. Moreover, $\check{h}_0^{n_r}(t)$ is the component due to the Doppler shift and is defined by:

$$\check{h}_0^{n_r}(t) = \check{h}^{n_r}(t) = \sqrt{\check{P}_{h,0}} \times \exp\left[j(2\pi f_D^{shift} t + \theta^{n_r})\right], \tag{4.3}$$

with the Doppler shift frequency f_D^{shift} and the initial phase θ^{n_r}. This phase term depends on the distance between the UE and the antenna n_r and thus on the geometrical characteristics of the receiver (type of antenna array, inter-antenna spacing, etc.). Accordingly, the Rician K-factor K_h is defined by the ratio between the mean power of the component due to the Doppler shift $\check{P}_{h,0}$ and the mean power of the component due to the Doppler spread $\tilde{P}_{h,0}$.

For the other paths ($l \neq 0$), there is no direct link between the transmitter and the receiver. Therefore, as in part 1.3.1:

$$h_{l\neq 0}^{n_r}(t) = \tilde{h}_{l\neq 0}^{n_r}(t) = \sqrt{\tilde{P}_{h,l}} \times \frac{\tilde{h}_l^{(1)}(t) + j\tilde{h}_l^{(2)}(t)}{\sqrt{2}}, \tag{4.4}$$

when considering the propagation channel between the transmit antenna and the receive antenna n_r. The variables $h_{l\neq 0}^{n_r}(t)$ follow a Rayleigh fading model and vary over time according to the Jakes' Doppler spectrum with the maximum Doppler frequency denoted by f_D^{max}.

Therefore, the received signal on the antenna n_r can be described by:

$$r^{n_r}(t) = \tilde{r}^{n_r}(t) + \check{r}^{n_r}(t) + \eta^{n_r}(t). \tag{4.5}$$

The component $\tilde{r}^{n_r}(t)$ is due to the Doppler spread and, according to the equation (1.2), is defined by:

$$\tilde{r}^{n_r}(t) = \sum_{l=0}^{L_h-1} s\left(t-\tau_l\right)\tilde{h}_l^{n_r}(t), \tag{4.6}$$

with $s(t)$ being the transmitted signal. The component $\check{r}^{n_r}(t)$ is due to the Doppler shift and, according to the equation (1.2), is defined by:

$$\check{r}^{n_r}(t) = s\left(t-\tau_0\right)\check{h}^{n_r}(t). \tag{4.7}$$

Finally, $\eta^{n_r}(t)$ is the AWGN component on the antenna n_r.

The time domain system model is summarized in Figure 4.2.

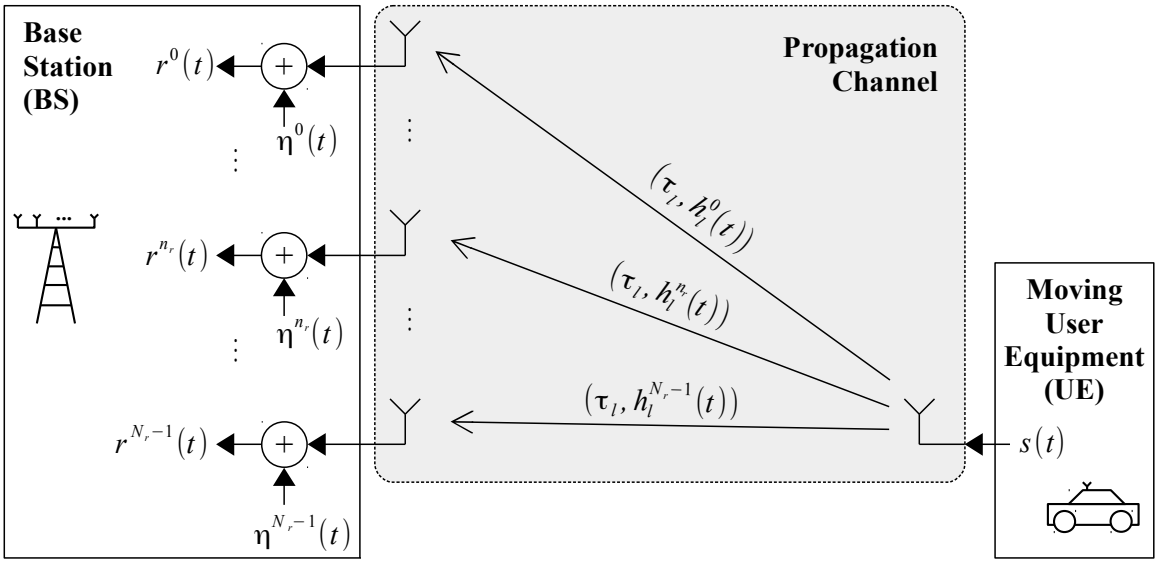

Figure 4.2: Description of the time domain system model for a massive MIMO uplink system with a moving UE equipped with a single antenna and N_r receive antennas on the BS side.

4.2.2 OFDM

This part provides the frequency domain OFDM system model for a massive MIMO uplink system with mobility. According to (2.1) in part 2.1, using an OFDM modulation, the baseband transmitted signal in the time domain is defined by:

$$s(t) = \sum_{n\in\mathbb{Z}}\sum_{m=0}^{M-1} c[m,n]\Pi_{m,n}(t), \tag{4.8}$$

with $\Pi_{m,n}(t)$ defined by (2.2), M being the FFT size and $c[m,n]$ the complex data for the time and frequency indexes (m,n).

Therefore, using (4.8) in (4.6) and (4.7), it comes:

$$\tilde{r}^{n_r}(t) = \sum_{n\in\mathbb{Z}} \sum_{m=0}^{M-1} c[m,n] \left(\sum_{l=0}^{L_h-1} \Pi_{m,n}\left(t-\tau_l\right) \tilde{h}_l^{n_r}(t) \right), \tag{4.9}$$

and:

$$\check{r}^{n_r}(t) = \sum_{n\in\mathbb{Z}} \sum_{m=0}^{M-1} c[m,n] \left(\Pi_{m,n}\left(t-\tau_0\right) \check{h}^{n_r}(t) \right). \tag{4.10}$$

According to (2.9), for the frequency and time indexes (m_0, n_0), the received data obtained after the demodulation stage on the antenna n_r is:

$$y^{n_r}\left[m_0,n_0\right] = \int_{\mathbb{R}} r^{n_r}(t) \left(\Pi^0_{m_0,n_0}(t)\right)^* dt, \tag{4.11}$$

with $\Pi^0_{m_0,n_0}(t)$ defined in (2.3). For the sake of simplicity, the time index n_0 is set to $n_0 = 0$. Moreover, the notations $m = m_0 - p$, $c_p = c[m_0 - p, 0]$ and $y^{n_r} = y^{n_r}[m_0, 0]$ are given and the mathematical sets of integer Ω_p and Ω_p^* are defined as follows:

$$\Omega_p = \left\{ p \in \mathbb{Z} \mid c_p \neq 0 \right\}, \tag{4.12}$$

being the set of useful sub-carriers and:

$$\Omega_p^* = \Omega_p \setminus \{0\}, \tag{4.13}$$

being the set of useful sub-carriers without the sub-carrier index m_0. As $\tau_l < T_{CP}\ \forall l \in [0, L_h - 1]$ and using (4.5), (4.9) and (4.10) in (4.11), it comes:

$$\begin{aligned} y^{n_r} &= \sum_{p\in\Omega_p} \underbrace{\left(\tilde{H}_p^{n_r} + \check{H}_p^{n_r}\right)}_{H_p^{n_r}} \times c_p + b^{n_r} \\ &= \left(\tilde{H}_0^{n_r} + \check{H}_0^{n_r}\right) \times c_0 + \underbrace{\sum_{p\in\Omega_p^*} \left(\tilde{H}_p^{n_r} + \check{H}_p^{n_r}\right) \times c_p}_{ICI} + b^{n_r}, \end{aligned} \tag{4.14}$$

with:

$$\begin{aligned} \tilde{H}_p^{n_r} &= \int_{\mathbb{R}} \left(\sum_{l=0}^{L_h-1} \Pi_{m_0-p,0}\left(t-\tau_l\right) \tilde{h}_l^{n_r}(t) \right) \left(\Pi^0_{m_0,0}(t)\right)^* dt \\ &= \sum_{l=0}^{L_h-1} \frac{1}{T_0} \left(\int_0^{T_0} \tilde{h}_l^{n_r}(t) e^{-j2\pi p F_0 t} dt \right) \exp\left[-j2\pi(m_0-p)F_0\tau_l\right], \end{aligned} \tag{4.15}$$

being the component due to the Doppler spread and:

$$\begin{aligned} \check{H}_p^{n_r} &= \int_{\mathbb{R}} \left(\Pi_{m_0-p,0}\left(t-\tau_0\right)\check{h}^{n_r}(t)\right)\left(\Pi_{m_0,0}^0(t)\right)^* dt \\ &= \frac{1}{T_0}\left(\int_0^{T_0}\check{h}^{n_r}(t)e^{-j2\pi pF_0t}dt\right)\exp\left[-j2\pi(m_0-p)F_0\tau_0\right], \end{aligned} \tag{4.16}$$

being the component due to the Doppler shift and finally:

$$b^{n_r} = \int_{\mathbb{R}} \eta^{n_r}(t)\left(\Pi_{m_0,n_0}^0(t)\right)^* dt = \frac{1}{\sqrt{T_0}}\int_0^{T_0}\eta^{n_r}(t)\exp\left[-j2\pi m_0F_0t\right]dt, \tag{4.17}$$

being the noise component. As $\tilde{h}_l^{n_r}(t)$ and $\check{h}^{n_r}(t)$ are two independent variables, $\tilde{H}_p^{n_r}$ and $\check{H}_p^{n_r}$ are also two independent variables.

If the propagation channel is static ($h_l(t) = h_l$), $\tilde{H}_{p\in\Omega_p^*}^{n_r} = \check{H}_{p\in\Omega_p^*}^{n_r} = 0$ and the OFDM modulation suffers neither from ISI nor ICI as shown in part 2.1. However, according to (4.14), as a moving UE is considered in this part, the components due to the Doppler spread and to the Doppler shift create ICI on the OFDM system. More specifically, for the link between the UE and the antenna of index n_r at the BS, $\tilde{H}_0^{n_r}$ and $\check{H}_0^{n_r}$ represent the components of the channel that allow for receiving the useful data c_0. On the contrary, $\tilde{H}_{p\in\Omega_p^*}^{n_r}$ (respectively $\check{H}_{p\in\Omega_p^*}^{n_r}$) are the channel components due to the Doppler spread (respectively Doppler shift) that lead to ICI on the data c_0 carried out by the adjacent sub-carriers $c_{p\in\Omega_p^*}$.

In order to take into account the ICI created by the Doppler effect, the following channel vectors are defined:

$$\tilde{\mathbf{H}}_p = \left[\tilde{H}_p^0 \quad \tilde{H}_p^1 \quad \cdots \quad \tilde{H}_p^{N_r-1}\right]^T, \tag{4.18}$$

for the components due to the Doppler spread,

$$\check{\mathbf{H}}_p = \left[\check{H}_p^0 \quad \check{H}_p^1 \quad \cdots \quad \check{H}_p^{N_r-1}\right]^T, \tag{4.19}$$

for the components due to the Doppler shift and:

$$\mathbf{H}_p = \tilde{\mathbf{H}}_p + \check{\mathbf{H}}_p, \tag{4.20}$$

with $p \in \Omega_p$. Moreover, the noise vector is defined by:

$$\mathbf{b} = \left[b^0 \quad b^1 \quad \cdots \quad b^{N_r-1}\right]^T, \tag{4.21}$$

and the received data vector before the equalization stage is given by:

$$\mathbf{y} = \left[y^0 \quad y^1 \quad \cdots \quad y^{N_r-1}\right]^T. \tag{4.22}$$

The propagation channel is estimated via pilot symbols on the BS side. A perfect channel estimation is assumed for the sake of simplicity and the receiver performs an equalization using the low-complexity MRC technique defined in part 3.1.2. Thus, after the MRC processing, the received data $\hat{c}$ is:

$$\hat{c} = \frac{1}{\sqrt{\xi_W}} \mathbf{W}^H \mathbf{y}, \tag{4.23}$$

with:

$$\mathbf{W} = \mathbf{H}_0, \tag{4.24}$$

according to (3.7), and:

$$\xi_W = \left(\|\mathbf{H}_0\|^2 \right)^2, \tag{4.25}$$

according to (3.8). Therefore, it comes:

$$\hat{c} = \frac{\mathbf{H}_0^H}{\|\mathbf{H}_0\|^2} \mathbf{y} = c_0 + \underbrace{\sum_{p \in \Omega_p^*} \frac{\mathbf{H}_0^H \mathbf{H}_p}{\|\mathbf{H}_0\|^2} c_p}_{\text{ICI}} + \frac{\mathbf{H}_0^H \mathbf{b}}{\|\mathbf{H}_0\|^2}. \tag{4.26}$$

Unlike in part 3.1, The received data $\hat{c}$ is here affected by the ICI due to the Doppler effect.

The frequency domain system model for the OFDM modulation is summarized in Figure 4.3.

4.2.3 FBMC/OQAM

This part provides the frequency domain FBMC/OQAM system model for a massive MIMO uplink system with mobility. According to (2.19) in part 2.2, using the FBMC/OQAM modulation, the baseband transmitted signal in the time domain is defined by:

$$s(t) = \sum_{n \in \mathbb{Z}} \sum_{m=0}^{M-1} a[m,n] g_{m,n}(t), \tag{4.27}$$

with M being the FFT size and $a[m,n]$ the real data sent at the frequency and time indexes (m,n). Moreover, $g_{m,n}(t)$ is defined by (2.20) as follows:

$$g_{m,n}(t) = g\left(t - n\frac{T_0}{2}\right) e^{j2\pi m F_0 t} e^{j\phi[m,n]}, \tag{4.28}$$

with $g(t)$ being the prototype filter and $\phi[m,n]$ the phase term defined in (2.21).

Therefore, using (4.27) in (4.6) and (4.7), it comes:

$$\tilde{r}^{n_r}(t) = \sum_{n \in \mathbb{Z}} \sum_{m=0}^{M-1} a[m,n] \left(\sum_{l=0}^{L_h-1} g_{m,n}\left(t - \tau_l\right) \tilde{h}_l^{n_r}(t) \right), \tag{4.29}$$

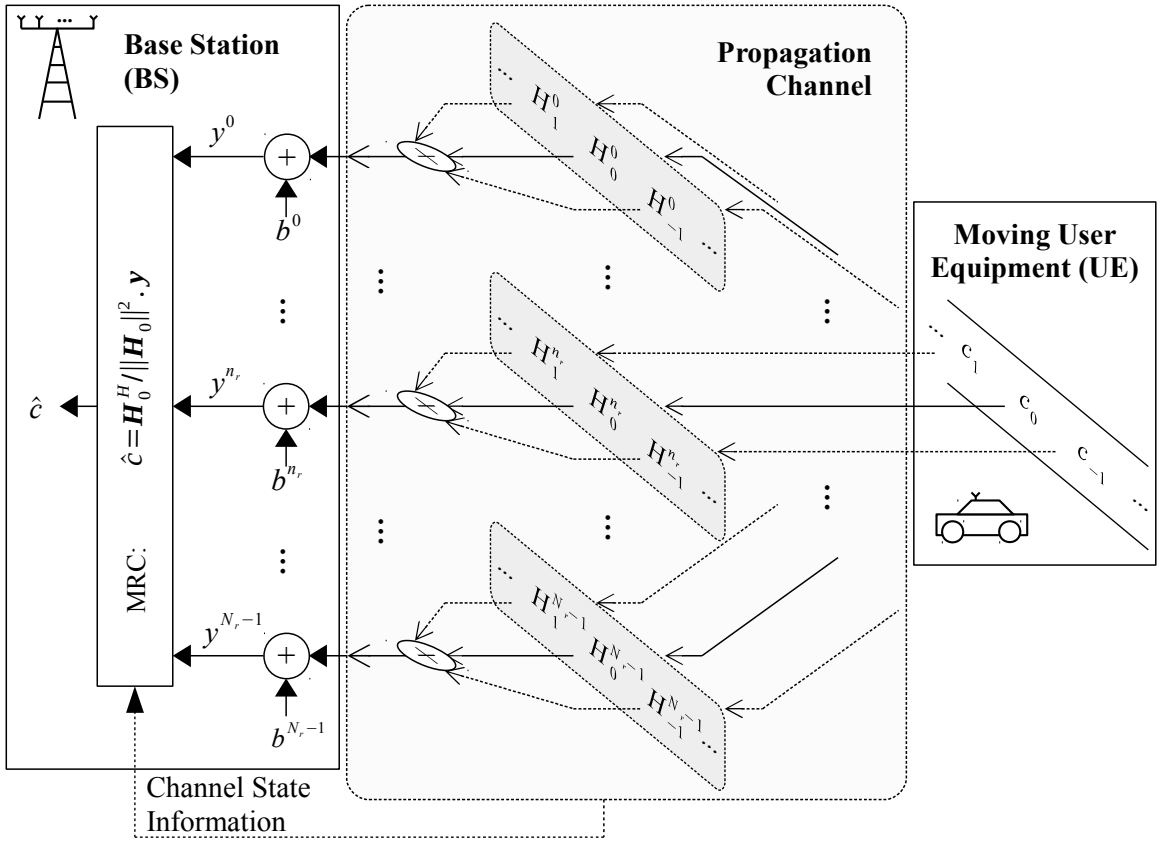

Figure 4.3: Description of the frequency domain OFDM system model for a massive MIMO uplink system. A moving UE equipped with a single antenna communicates with a BS equipped with N_r antennas.

and:

$$\check{r}^{n_r}(t) = \sum_{n\in\mathbb{Z}} \sum_{m=0}^{M-1} a[m,n] \left(g_{m,n}\left(t-\tau_0\right) \check{h}^{n_r}(t) \right). \tag{4.30}$$

According to (2.25), for the frequency and time indexes (m_0, n_0), the received data obtained after the demodulation stage on the antenna n_r is:

$$y^{n_r}\left[m_0,n_0\right] = \int_{\mathbb{R}} r^{n_r}(t) g^*_{m_0,n_0}(t) dt. \tag{4.31}$$

For the sake of simplicity, the time index n_0 is set to $n_0 = 0$. The notations $m = m_0 - p$, $n = n_0 - q$, $a_{p,q} = a[m_0 - p, -q]$, $\phi_{p,q} = \phi[m_0 - p, -q]$ and $y^{n_r} = y^{n_r}[m_0, 0]$ are given. Furthermore, the mathematical sets of integers $\Omega_{p,q}$ and $\Omega^*_{p,q}$ are defined as follows:

$$\Omega_{p,q} = \left\{ (p,q) \in \mathbb{Z}^2 \mid a_{p,q} \neq 0 \ and \ (-2K+1) \leq q \leq 2K \right\}, \tag{4.32}$$

and:

$$\Omega^*_{p,q} = \Omega_{p,q} \setminus \{(0,0)\}. \tag{4.33}$$

Using (4.29) and (4.30) in (4.31), it comes:

$$\begin{aligned} y^{n_r} &= \sum_{(p,q)\in\Omega_{p,q}} \underbrace{\left(\tilde{H}_{p,q}^{n_r} + \check{H}_{p,q}^{n_r}\right)}_{H_{p,q}^{n_r}} \times a_{p,q} + b^{n_r} \\ &= \left(\tilde{H}_{0,0}^{n_r} + \check{H}_{0,0}^{n_r}\right) \times a_{0,0} + \underbrace{\sum_{(p,q)\in\Omega_{p,q}^{*}} \left(\tilde{H}_{p,q}^{n_r} + \check{H}_{p,q}^{n_r}\right) \times a_{p,q}}_{ICI+ISI} + b^{n_r}, \end{aligned} \tag{4.34}$$

with:

$$\begin{aligned} \tilde{H}_{p,q}^{n_r} &= \int_{\mathbb{R}} \left(\sum_{l=0}^{L_h-1} g_{m_0-p,-q}\left(t-\tau_l\right) \tilde{h}_l^{n_r}(t) \right) g_{m_0,n_0}^{*}(t)dt \\ &= e^{j(\phi_{p,q}-\phi_{0,0})} \sum_{l=0}^{L_h-1} \left(\int_{\mathbb{R}} \tilde{h}_l^{n_r}(t) g\left(t\right) g\left(t-\tau_l+q\tfrac{T_0}{2}\right) e^{-j2\pi pF_0 t}dt \right) e^{-j2\pi(m_0-p)F_0\tau_l}, \end{aligned} \tag{4.35}$$

being the component due to the Doppler spread and:

$$\begin{aligned} \check{H}_{p,q}^{n_r} &= \int_{\mathbb{R}} \left(g_{m_0-p,-q}\left(t-\tau_0\right) \check{h}^{n_r}(t) \right) g_{m_0,n_0}^{*}(t)dt \\ &= e^{j(\phi_{p,q}-\phi_{0,0})} \left(\int_{\mathbb{R}} \check{h}^{n_r}(t) g\left(t\right) g\left(t-\tau_0+q\tfrac{T_0}{2}\right) e^{-j2\pi pF_0 t}dt \right) e^{-j2\pi(m_0-p)F_0\tau_0}, \end{aligned} \tag{4.36}$$

being the component due to the Doppler shift and finally:

$$b^{n_r} = \int_{\mathbb{R}} \eta^{n_r}(t) g_{m_0,n_0}^{*}(t)dt = \int_{\mathbb{R}} \eta^{n_r}(t) e^{-j\phi_{0,0}} g\left(t\right) e^{-j2\pi m_0 F_0 t}dt, \tag{4.37}$$

being the noise component. As $\tilde{h}_l^{n_r}(t)$ and $\check{h}^{n_r}(t)$ are two independent variables, $\tilde{H}_{p,q}^{n_r}$ and $\check{H}_{p,q}^{n_r}$ are also two independent variables.

According to (4.34), as a moving UE is considered in this part, the Doppler effect creates additional ISI and ICI, which add up to the intrinsic interference. More specifically, for the link between the UE and the antenna n_r, $\tilde{H}_{(p,q)\in\Omega_{p,q}^{*}}^{n_r}$ (respectively $\check{H}_{(p,q)\in\Omega_{p,q}^{*}}^{n_r}$) stand for the channel components due to the Doppler spread (respectively Doppler shift) that lead to the intrinsic interference and to the interference due to the Doppler effect.

In order to take into account the intrinsic interference and the ISI and ICI due to the Doppler effect, the following channel vectors are defined:

$$\tilde{\mathbf{H}}_{p,q} = \begin{bmatrix} \tilde{H}_{p,q}^{0} & \tilde{H}_{p,q}^{1} & \cdots & \tilde{H}_{p,q}^{N_r-1} \end{bmatrix}^T, \tag{4.38}$$

for the components due to the Doppler spread,

$$\check{\mathbf{H}}_{p,q} = \begin{bmatrix} \check{H}^0_{p,q} & \check{H}^1_{p,q} & \cdots & \check{H}^{N_r-1}_{p,q} \end{bmatrix}^T, \tag{4.39}$$

for the components due to the Doppler shift and:

$$\mathbf{H}_{p,q} = \tilde{\mathbf{H}}_{p,q} + \check{\mathbf{H}}_{p,q}, \tag{4.40}$$

with $(p,q) \in \Omega_{p,q}$.

The propagation channel is estimated via pilot symbols on the BS side. A perfect channel estimation is assumed for the sake of simplicity and the receiver performs an equalization using the low-complexity MRC technique defined in part 3.1.2. Thus, after the MRC processing, the received data $\hat{a}$ is:

$$\hat{a} = \Re\left[\frac{1}{\sqrt{\xi_W}}\mathbf{W}^H\mathbf{y}\right], \tag{4.41}$$

with:

$$\mathbf{W} = \mathbf{H}_0, \tag{4.42}$$

according to (3.7), and:

$$\xi_W = \left(\|\mathbf{H}_0\|^2\right)^2, \tag{4.43}$$

according to (3.8). Therefore, it comes:

$$\hat{a} = \Re\left[\frac{\mathbf{H}^H_{0,0}}{\|\mathbf{H}_{0,0}\|^2}\mathbf{y}\right] = a_{0,0} + \underbrace{\sum_{(p,q)\in\Omega^*_{p,q}} \Re\left[\frac{\mathbf{H}^H_{0,0}\mathbf{H}_{p,q}}{\|\mathbf{H}_{0,0}\|^2}\right] a_{p,q}}_{\text{ICI+ISI}} + \Re\left[\frac{\mathbf{H}^H_{0,0}\mathbf{b}}{\|\mathbf{H}_{0,0}\|^2}\right]. \tag{4.44}$$

Unlike in part 3.1, the received data $\hat{a}$ is here affected by the intrinsic interference and by the ICI and ISI due to the Doppler effect.

The frequency domain system model for the FBMC/OQAM modulation is summarized in Figure 4.4.

Summary of this Chapter:

- The **context of the proposed study** is described.
- The **frequency domain system model** for a **massive MIMO uplink system with mobility** is provided in this Chapter for the **OFDM** and the **FBMC/OQAM** modulations.
- With the **OFDM** modulation, unlike in part 2.1 and 3.1, **the mobility of the UE induces the creation of ICI because of the Doppler effect.**
- With the **FBMC/OQAM** modulation, unlike in part 2.2 and 3.1, **the mobility of**

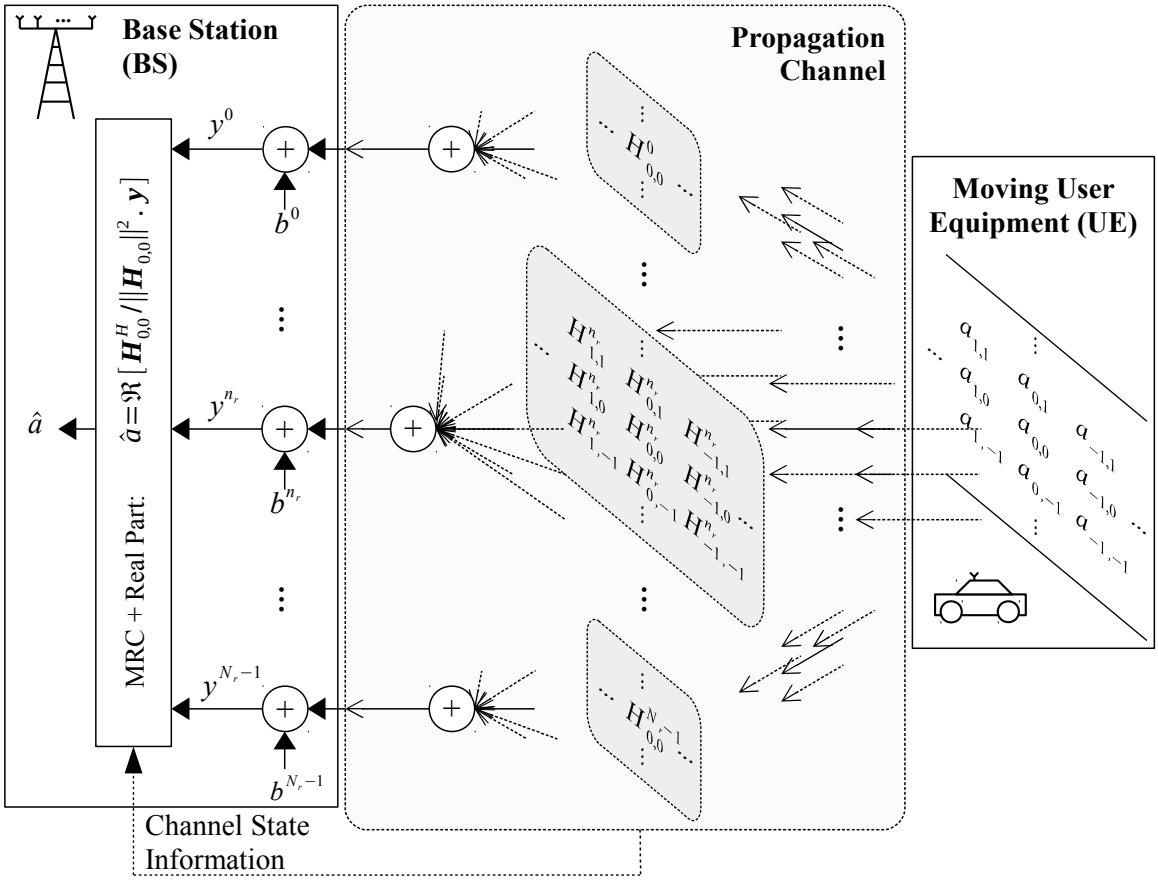

Figure 4.4: Description of the frequency domain FBMC/OQAM system model for a massive MIMO uplink system. A moving UE equipped with a single antenna communicates with a BS equipped with N_r antennas.

the UE induces the creation of additional ISI and ICI, which add up to the intrinsic interference, because of the Doppler effect.

- **The Doppler effect can be divided in two components**: the component due to the **Doppler spread** and the component due to the **Doppler shift**.

5

Massive MIMO for Doppler Effect Reduction in an OFDM System

This Chapter only considers the OFDM modulation and studies the effect of massive MIMO systems on the interference due to the Doppler effect based on the system model defined in Chapter 4. Unlike [78, 79], this contribution focuses on NLOS communications, where the received signals arrive from all directions with equal probability [24, 89, 90]. This situation happens frequently in an urban environment. While the previous studies take into account a small number of antennas on the receiver side (2 in [81, 82] and up to 5 in [83, 84]), the effect of a very large number of uncorrelated receive antennas on the interference due to the Doppler effect is analytically studied in this Chapter considering the low-complexity MRC receiver described in part 3.1.2. In this context, we analytically highlight the impact of an increase of the number of receive antennas and the asymptotic behavior, when the number of receive antennas tends to infinity.

The Signal-to-Interference Ratio (SIR) of the system is analyzed in part 5.1.1, as this metric allows for linking the impact of the Doppler effect and the number of receive antennas. This analysis leads to an expression of the asymptotic SIR, when the number of receive antennas tends to infinity. Moreover, a necessary and sufficient condition is proposed to show how an increase of the SIR is related to an increase of the number of receive antennas. However, both results rely on the statistical properties of the propagation channel. With the statistical analysis of the channel components in part 5.1.2, this problem is solved and the asymptotic SIR as well as the necessary and sufficient condition can be analytically expressed. Finally, the numerical results in part 5.2 aim at confirming the analytical results and allow drawing a conclusion in the last section.

5.1 Analytical Study

The system model used in this Chapter is the one described in part 4.2.2. However, as a NLOS propagation channel is considered, there is no component due to the Doppler shift. Therefore, the l^{th} multi-path component between the transmitter and the receive antenna n_r is defined by:

$$h_l^{n_r}(t) = \tilde{h}_l^{n_r}(t), \tag{5.1}$$

and the channel component $H_p^{n_r}$ is defined by:

$$H_p^{n_r} = \tilde{H}_p^{n_r}. \tag{5.2}$$

Moreover, when N_r receive antennas are considered, the following notation is given for this Chapter:

$$\mathbf{H}_p^{(N_r)} = \mathbf{H}_p, \tag{5.3}$$

in order to link the impact of the Doppler effect with the number of receive antennas.

The aim of this part is to analytically evaluate the impact of the ICI created by the Doppler effect as highlighted in equation (4.26). To this end, the SIR of the system is analyzed in part 5.1.1 and the statistical analysis of the channel components in part 5.1.2 allows completing this study.

5.1.1 SIR Analysis

One can see that the noise component in (4.26) is not impacted by the Doppler effect. Therefore, this noise component is not taken into account in this analytical study for the sake of clarity. In order to evaluate only the impact of the Doppler effect, the SIR is a relevant metric as the ICI component is the only interference affecting the received data. Firstly, the SIR with N_r receive antennas $\gamma^{(N_r)}$ is expressed using the system model of the previous Chapter. Then, the asymptotic value of this SIR when $N_r \to +\infty$ is given. Finally, a comparison between $\gamma^{(N_r)}$ and $\gamma^{(N_r+1)}$ provides a necessary and sufficient condition to have an increase of the SIR when increasing N_r.

From the equation (4.26), the SIR $\gamma^{(N_r)}$ with N_r receive antennas can be deduced:

$$\gamma^{(N_r)} = \frac{\left\| \tilde{\mathbf{H}}_0^{(N_r)} \right\|^4}{\sum_{p \in \Omega_p^*} \left| \left(\tilde{\mathbf{H}}_0^{(N_r)} \right)^H \tilde{\mathbf{H}}_p^{(N_r)} \right|^2} = \frac{\left(\sum_{n_r=0}^{N_r-1} \left| \tilde{H}_0^{n_r} \right|^2 \right)^2}{\sum_{p \in \Omega_p^*} \left| \sum_{n_r=0}^{N_r-1} \left(\tilde{H}_0^{n_r} \right)^* \tilde{H}_p^{n_r} \right|^2}. \tag{5.4}$$

Since the only interference taken into account is due to the Doppler effect, an increase of the SIR $\gamma^{(N_r)}$ is equivalent to a decrease of the impact of the Doppler effect. Obviously, the number of receive antennas N_r has an impact on $\gamma^{(N_r)}$ as it gives the size of the channel

vectors $\tilde{\mathbf{H}}_p^{(N_r)}$.

The variables $\tilde{H}_p^{n_r}$ and $\tilde{H}_p^{n_r'}$ are uncorrelated variables if $n_r \neq n_r'$, with the same expected value and the same variance. Owing to the law of large numbers, when the number of receive antennas N_r tends to infinity ($N_r \to +\infty$), the denominator of (5.4) becomes:

$$\begin{aligned} \sum_{p\in\Omega_p^*} \left| \left(\tilde{\mathbf{H}}_0^{(N_r\to+\infty)}\right)^H \tilde{\mathbf{H}}_p^{(N_r\to+\infty)} \right|^2 &= \sum_{p\in\Omega_p^*} \left| N_r E\left[\left(\tilde{H}_0^{n_r}\right)^* \tilde{H}_p^{n_r} \right] \right|^2 \\ &= N_r^2 \sum_{p\in\Omega_p^*} \left| E\left[\left(\tilde{H}_0^{n_r}\right)^* \tilde{H}_p^{n_r} \right] \right|^2, \end{aligned} \tag{5.5}$$

and the numerator of (5.4) becomes:

$$\left\| \tilde{\mathbf{H}}_0^{(N_r\to+\infty)} \right\|^4 = N_r^2 E\left[\left| \tilde{H}_0^{n_r} \right|^2 \right]^2. \tag{5.6}$$

Thereby, using (5.5) and (5.6) in (5.4), the asymptotic SIR is defined by:

$$\gamma_\infty = \frac{\left(\tilde{E}_0^{(1)}\right)^2}{\sum\limits_{p\in\Omega_p^*} \left|\tilde{E}_p^{(1)}\right|^2}, \tag{5.7}$$

with:

$$\tilde{E}_p^{(1)} = E\left[\left(\tilde{H}_0^{n_r}\right)^* \tilde{H}_p^{n_r} \right]. \tag{5.8}$$

Two different and independent cases are considered. The first one concerns a communication between the transmitter and a BS equipped with N_r receive antennas. The second one concerns a communication between the transmitter and a BS equipped with $(N_r{+}1)$ receive antennas. According to (5.4), the SIR with $(N_r{+}1)$ receive antennas is greater than the SIR with N_r receive antennas ($\gamma^{(N_r+1)} > \gamma^{(N_r)}$) if, and only if:

$$\left\| \tilde{\mathbf{H}}_0^{(N_r+1)} \right\|^4 \left(\sum_{p\in\Omega_p^*} \left| \left(\tilde{\mathbf{H}}_0^{(N_r)}\right)^H \tilde{\mathbf{H}}_p^{(N_r)} \right|^2 \right) > \left\| \tilde{\mathbf{H}}_0^{(N_r)} \right\|^4 \left(\sum_{p\in\Omega_p^*} \left| \left(\tilde{\mathbf{H}}_0^{(N_r+1)}\right)^H \tilde{\mathbf{H}}_p^{(N_r+1)} \right|^2 \right). \tag{5.9}$$

As the two cases are independent and by considering now a large number of channel realizations, the SIR with $(N_r{+}1)$ receive antennas is statistically greater than the SIR with N_r receive antennas, if and only if:

$$\begin{aligned} E\left[\left\| \tilde{\mathbf{H}}_0^{(N_r+1)} \right\|^4 \right] \left(\sum_{p\in\Omega_p^*} E\left[\left| \left(\tilde{\mathbf{H}}_0^{(N_r)}\right)^H \tilde{\mathbf{H}}_p^{(N_r)} \right|^2 \right] \right) \\ > E\left[\left\| \tilde{\mathbf{H}}_0^{(N_r)} \right\|^4 \right] \left(\sum_{p\in\Omega_p^*} E\left[\left| \left(\tilde{\mathbf{H}}_0^{(N_r+1)}\right)^H \tilde{\mathbf{H}}_p^{(N_r+1)} \right|^2 \right] \right). \end{aligned} \tag{5.10}$$

Equivalently, the SIR statistically grows as N_r increases if, and only if the propagation channel fulfills the inequation (5.10). This leads to the following Proposition.

Proposition 1. *The SIR statistically grows with the increase of N_r if, and only if:*

$$\gamma_\infty > \Gamma_{ref}, \tag{5.11}$$

with:

$$\Gamma_{ref} = \frac{\tilde{E}_0^{(2)}}{\sum\limits_{p \in \Omega_p^*} \tilde{E}_p^{(2)}}, \tag{5.12}$$

and:

$$\tilde{E}_p^{(2)} = E\left[\left|\left(\tilde{H}_0^{n_r}\right)^* \tilde{H}_p^{n_r}\right|^2\right]. \tag{5.13}$$

Proof. See appendix B.1. □

One can notice that the values of γ_∞ and Γ_{ref} do not depend on N_r but only on the statistical channel properties $\tilde{E}_p^{(1)}$ and $\tilde{E}_p^{(2)}$ defined respectively in (5.8) and (5.13). These statistical channel properties are investigated in the next part.

5.1.2 Statistical Analysis of the Channel Components

Both the expression of γ_∞ in (5.7) and Proposition 1 rely on the statistical channel properties $\tilde{E}_p^{(1)}$ and $\tilde{E}_p^{(2)}$, defined respectively in (5.8) and (5.13). This part aims at finding their analytical value. To this end, a statistical analysis of the variables $\tilde{H}_p^{n_r}$ is first carried out by modeling the Doppler effect with a sum-of-sinusoid representation, as proposed in [29] and described in part 1.3.1. Then, the analytical expressions of $\tilde{E}_p^{(1)}$ and $\tilde{E}_p^{(2)}$ are given. As $\tilde{E}_p^{(1)}$ and $\tilde{E}_p^{(2)}$ do not depend on the considered receive antenna and for the sake of clarity, the index n_r is removed in this part. Thus, $\tilde{h}_l^{n_r}(t)$ becomes $\tilde{h}_l(t)$ and $\tilde{H}_p^{n_r}$ becomes $\tilde{H}_p$.

Statistical Analysis of $\tilde{H}_p$

The channel components $\tilde{H}_p$ with $p \in \Omega_p$ are studied here. The propagation channel is modeled by the sum-of-sinusoid method defined in [29] and described in part 1.3.1. Indeed, the authors in [29] show that this method is useful to design and simulate Rayleigh fading channels and MIMO channels. In practice, this sum-of-sinusoid method is used in the communication system toolbox™ of the simulation environment MATLAB® [91]. Thereby:

$$\tilde{h}_l(t) = \sqrt{P_{h,l}} \times \frac{\tilde{h}_l^{(1)}(t) + j\tilde{h}_l^{(2)}(t)}{\sqrt{2}}, \tag{5.14}$$

with $P_{h,l}$ being the average power of the l^{th} path and $\tilde{h}_l^{(i)}(t)$ defined by:

$$\tilde{h}_l^{(i)}(t) = \sqrt{\frac{2}{N_l}} \sum_{n=1}^{N_l} \cos\left(2\pi f_{l,n}^{(i)} t + \theta_{l,n}^{(i)}\right). \tag{5.15}$$

In (5.15), N_l is the considered number of sinusoids for the l^{th} path, $\theta_{l,n}^{(i)}$ is a random variable having a uniform distribution over the interval $]0, 2\pi]$ and $f_{l,n}^{(i)}$ is defined as follows:

$$f_{l,n}^{(i)} = f_D^{max} \cos\left(\frac{\pi}{2N_l}\left(n - \frac{1}{2}\right) + (-1)^{i-1}\frac{\pi}{4N_l}\frac{l}{L_h + 2}\right), \tag{5.16}$$

f_D^{max} being the maximum Doppler frequency. This value is related to the speed of the user according to the equation (1.8) and the higher the speed of the user, the higher the maximum Doppler frequency f_D^{max}. Moreover, $\theta_{l,n}^{(i)}$ and $\theta_{l',n'}^{(i')}$ are two independent variables if $(i, l, n) \neq (i', l', n')$.

For the sake of clarity, the mathematical set of integer $\Omega_{l,n}$ is defined as follow:

$$\Omega_{l,n} = \left\{(l, n) \in \mathbb{N}^2 \mid 0 \leq l \leq (L_h - 1) \text{ and } 1 \leq n \leq N_l\right\}. \tag{5.17}$$

Moreover, the following variables are defined:

$$\begin{cases} S_{p,l,n}^{(i)-} = \text{sinc}\left(p - \frac{f_{l,n}^{(i)}}{F_0}\right), \\ S_{p,l,n}^{(i)+} = \text{sinc}\left(p + \frac{f_{l,n}^{(i)}}{F_0}\right), \end{cases} \tag{5.18}$$

and:

$$\theta_{l,n}^{\prime(i)} = \pi\frac{f_{l,n}^{(i)}}{F_0} + \theta_{l,n}^{(i)} \text{ modulo } 2\pi. \tag{5.19}$$

As $\theta_{l,n}^{(i)}$ is a random variable having a uniform distribution over the interval $]0, 2\pi]$, $\theta_{l,n}^{\prime(i)}$ is also an random variable having a uniform distribution over the interval $]0, 2\pi]$ and $\theta_{l,n}^{\prime(i)}$ and $\theta_{l',n'}^{\prime(i')}$ are two independent variables if $(i, l, n) \neq (i', l', n')$.

Thus, the development in Appendix B.2 shows that the components $\tilde{H}_p$ can be defined by:

$$\tilde{H}_p = \sum_{(l,n)\in\Omega_{l,n}} \underbrace{\tilde{H}_{p,l,n}^{(1)} + j\tilde{H}_{p,l,n}^{(2)}}_{\tilde{H}_{p,l,n}}, \tag{5.20}$$

with:

$$\tilde{H}_{p,l,n}^{(i)} = \sqrt{\frac{P_{h,l}}{4N_l}}(-1)^p \left(S_{p,l,n}^{(i)-} e^{j\theta_{l,n}^{\prime(i)}} + S_{p,l,n}^{(i)+} e^{-j\theta_{l,n}^{\prime(i)}}\right) \exp\left[-j2\pi(m_0 - p)F_0\tau_l\right]. \tag{5.21}$$

As $\mathrm{sinc}(x)$ is an even function, one can notice that:

$$S_{0,l,n}^{(i)-} = S_{0,l,n}^{(i)+} = \mathrm{sinc}\left(\frac{f_{l,n}^{(i)}}{F_0}\right). \tag{5.22}$$

According to (5.22), when $p = 0$ the equation (5.21) becomes:

$$\tilde{H}_{0,l,n}^{(i)} = \sqrt{\frac{P_{h,l}}{N_l}} S_{0,l,n}^{(i)-} \cos\left(\theta_{l,n}^{\prime(i)}\right) \exp\left[-j2\pi m_0 F_0 \tau_l\right]. \tag{5.23}$$

One can see that $\tilde{H}_{p,l,n}^{(i)}$ and $\tilde{H}_{p',l',n'}^{(i')}$ are independent variables if $(i,l,n) \neq (i',l',n')$. Moreover, as:

$$E\left[e^{\pm j\theta_{l,n}^{\prime(i)}}\right] = 0, \tag{5.24}$$

it comes:

$$E\left[\tilde{H}_p\right] = E\left[\tilde{H}_{p,l,n}^{(i)}\right] = 0, \tag{5.25}$$

$\forall (l,n) \in \Omega_{l,n}$, $\forall i \in \{1,2\}$ and $\forall p \in \Omega_p$.

Expression of $\tilde{E}_p^{(1)}$

The expression of $\tilde{E}_p^{(1)} = E\left[\tilde{H}_0^* \tilde{H}_p\right]$ is now deduced from (5.20), (5.21) and (5.23). Firstly, using (5.20) $\tilde{E}_p^{(1)}$ becomes:

$$\tilde{E}_p^{(1)} = \sum_{(l,n)\in\Omega_{l,n}} \sum_{(l',n')\in\Omega_{l,n}} E\left[\left(\tilde{H}_{0,l,n}^{(1)} + j\tilde{H}_{0,l,n}^{(2)}\right)^* \left(\tilde{H}_{p,l',n'}^{(1)} + j\tilde{H}_{p,l',n'}^{(2)}\right)\right]. \tag{5.26}$$

As $\tilde{H}_{p,l,n}^{(i)}$ and $\tilde{H}_{p',l',n'}^{(i')}$ are independent variables if $(i,l,n) \neq (i',l',n')$ and according to (5.25), the equation (5.26) becomes:

$$\tilde{E}_p^{(1)} = \sum_{(l,n)\in\Omega_{l,n}} \sum_{i\in\{1,2\}} E\left[\left(\tilde{H}_{0,l,n}^{(i)}\right)^* \tilde{H}_{p,l,n}^{(i)}\right]. \tag{5.27}$$

Then, using the development in Appendix B.3, the equation (5.27) becomes:

$$\tilde{E}_p^{(1)} = (-1)^p \sum_{(l,n)\in\Omega_{l,n}} \frac{P_{h,l}}{4N_l} \left(S_{0,l,n}^{(1)-}\left(S_{p,l,n}^{(1)-} + S_{p,l,n}^{(1)+}\right) + S_{0,l,n}^{(2)-}\left(S_{p,l,n}^{(2)-} + S_{p,l,n}^{(2)+}\right)\right) \exp\left[j2\pi p F_0 \tau_l\right]. \tag{5.28}$$

Finally, according to (5.22), when $p = 0$, $\tilde{E}_p^{(1)}$ becomes:

$$\tilde{E}_0^{(1)} = \sum_{(l,n)\in\Omega_{l,n}} \frac{P_{h,l}}{2N_l} \left(\left(S_{0,l,n}^{(1)-}\right)^2 + \left(S_{0,l,n}^{(2)-}\right)^2\right). \tag{5.29}$$

Expression of $\tilde{E}_p^{(2)}$

The expression of $\tilde{E}_p^{(2)} = E\left[\left|\tilde{H}_0^* \tilde{H}_p\right|^2\right]$ is deduced from (5.20), (5.21) and (5.23). Firstly, using (5.20), $\tilde{E}_p^{(2)}$ becomes:

$$\tilde{E}_p^{(2)} = \sum_{(l_1,n_1)\in\Omega_{l,n}} \sum_{(l_2,n_2)\in\Omega_{l,n}} \sum_{(l_3,n_3)\in\Omega_{l,n}} \sum_{(l_4,n_4)\in\Omega_{l,n}} E\left[\tilde{H}^*_{0,l_1,n_1} \tilde{H}_{p,l_2,n_2} \tilde{H}_{0,l_3,n_3} \tilde{H}^*_{p,l_4,n_4}\right]. \quad (5.30)$$

As $\tilde{H}_{p,l,n}$ and $\tilde{H}_{p',l',n'}$ are independent variables if $(l,n) \neq (l',n')$ and according to (5.25):

$$E\left[\tilde{H}^*_{0,l_1,n_1} \tilde{H}_{p,l_2,n_2} \tilde{H}_{0,l_3,n_3} \tilde{H}^*_{p,l_4,n_4}\right] = 0, \quad (5.31)$$

if one of the following cases is verified:

$$\begin{cases} (l_1,n_1) \notin \{(l_2,n_2),(l_3,n_3),(l_4,n_4)\}, \\ (l_2,n_2) \notin \{(l_1,n_1),(l_3,n_3),(l_4,n_4)\}, \\ (l_3,n_3) \notin \{(l_1,n_1),(l_2,n_2),(l_4,n_4)\}, \\ (l_4,n_4) \notin \{(l_1,n_1),(l_2,n_2),(l_3,n_3)\}. \end{cases} \quad (5.32)$$

Therefore, (5.30) can be simplified as follows:

$$\begin{aligned} \tilde{E}_p^{(2)} &= \textstyle\sum_{(l,n)\in\Omega_{l,n}} E\left[\left|\tilde{H}^*_{0,l,n} \tilde{H}_{p,l,n}\right|^2\right] \\ &+ \textstyle\sum_{(l,n)\in\Omega_{l,n}} \sum_{(l',n')\in\{\Omega_{l,n}\setminus(l,n)\}} E\left[\left|\tilde{H}_{0,l,n}\right|^2\right] E\left[\left|\tilde{H}_{p,l',n'}\right|^2\right] \\ &+ \textstyle\sum_{(l,n)\in\Omega_{l,n}} \sum_{(l',n')\in\{\Omega_{l,n}\setminus(l,n)\}} E\left[\tilde{H}^*_{0,l,n} \tilde{H}_{p,l,n}\right] E\left[\tilde{H}^*_{0,l',n'} \tilde{H}_{p,l',n'}\right]^* \\ &+ \textstyle\sum_{(l,n)\in\Omega_{l,n}} \sum_{(l',n')\in\{\Omega_{l,n}\setminus(l,n)\}} E\left[\tilde{H}_{0,l,n} \tilde{H}_{p,l,n}\right] E\left[\tilde{H}_{0,l',n'} \tilde{H}_{p,l',n'}\right]^*, \end{aligned} \quad (5.33)$$

or equivalently:

$$\begin{aligned} \tilde{E}_p^{(2)} &= \sum_{(l,n)\in\Omega_{l,n}} E\left[\left|\tilde{H}^*_{0,l,n} \tilde{H}_{p,l,n}\right|^2\right] - E\left[\left|\tilde{H}_{0,l,n}\right|^2\right] E\left[\left|\tilde{H}_{p,l,n}\right|^2\right] \\ &\qquad - \left|E\left[\tilde{H}^*_{0,l,n} \tilde{H}_{p,l,n}\right]\right|^2 - \left|E\left[\tilde{H}_{0,l,n} \tilde{H}_{p,l,n}\right]\right|^2 \\ &+ \left(\sum_{(l,n)\in\Omega_{l,n}} E\left[\left|\tilde{H}_{0,l,n}\right|^2\right]\right)\left(\sum_{(l,n)\in\Omega_{l,n}} E\left[\left|\tilde{H}_{p,l,n}\right|^2\right]\right) \\ &+ \left|\sum_{(l,n)\in\Omega_{l,n}} E\left[\tilde{H}^*_{0,l,n} \tilde{H}_{p,l,n}\right]\right|^2 + \left|\sum_{(l,n)\in\Omega_{l,n}} E\left[\tilde{H}_{0,l,n} \tilde{H}_{p,l,n}\right]\right|^2. \end{aligned} \quad (5.34)$$

$$
\begin{aligned}
\tilde{E}_p^{(2)} &= \left(\sum_{(l,n)\in\Omega_{l,n}} -\frac{P_{h,l}^2}{8N_l^2} \left(S_{0,l,n}^{(1)-}\right)^2 \left(\left(S_{p,l,n}^{(1)-}\right)^2 + \left(S_{p,l,n}^{(1)+}\right)^2 + S_{p,l,n}^{(1)-} S_{p,l,n}^{(1)+} \right) \right) \\
&+ \left(\sum_{(l,n)\in\Omega_{l,n}} -\frac{P_{h,l}^2}{8N_l^2} \left(S_{0,l,n}^{(2)-}\right)^2 \left(\left(S_{p,l,n}^{(2)-}\right)^2 + \left(S_{p,l,n}^{(2)+}\right)^2 + S_{p,l,n}^{(2)-} S_{p,l,n}^{(2)+} \right) \right) \\
&+ \left(\sum_{(l,n)\in\Omega_{l,n}} \frac{P_{h,l}^2}{8N_l^2} \left(\left(S_{0,l,n}^{(1)-}\right)^2 + \left(S_{0,l,n}^{(2)-}\right)^2 \right) \right) \\
&\qquad \times \left(\sum_{(l,n)\in\Omega_{l,n}} \frac{P_{h,l}}{4N_l} \left(\left(S_{p,l,n}^{(1)-}\right)^2 + \left(S_{p,l,n}^{(1)+}\right)^2 + \left(S_{p,l,n}^{(2)-}\right)^2 + \left(S_{p,l,n}^{(2)+}\right)^2 \right) \right) \\
&+ \left| \sum_{(l,n)\in\Omega_{l,n}} \frac{P_{h,l}}{4N_l} \left(S_{0,l,n}^{(1)-} \left(S_{p,l,n}^{(1)-} + S_{p,l,n}^{(1)+} \right) + S_{0,l,n}^{(2)-} \left(S_{p,l,n}^{(2)-} + S_{p,l,n}^{(2)+} \right) \right) e^{j2\pi p F_0 \tau_l} \right|^2 \\
&+ \left| \sum_{(l,n)\in\Omega_{l,n}} \frac{P_{h,l}}{4N_l} \left(S_{0,l,n}^{(1)-} \left(S_{p,l,n}^{(1)-} + S_{p,l,n}^{(1)+} \right) - S_{0,l,n}^{(2)-} \left(S_{p,l,n}^{(2)-} + S_{p,l,n}^{(2)+} \right) \right) e^{-j2\pi(2m_0-p) F_0 \tau_l} \right|^2
\end{aligned}
\tag{5.35}
$$

Therefore, the development in Appendix B.4 gives the equation (5.35). According to (5.22), when $p = 0$, $\tilde{E}_p^{(2)}$ becomes:

$$
\begin{aligned}
\tilde{E}_0^{(2)} &= \sum_{(l,n)\in\Omega_{l,n}} -\frac{3P_{h,l}^2}{8N_l^2} \left(\left(S_{0,l,n}^{(1)-}\right)^4 + \left(S_{0,l,n}^{(2)-}\right)^4 \right) \\
&+ 2 \left(\sum_{(l,n)\in\Omega_{l,n}} \frac{P_{h,l}}{2N_l} \left(\left(S_{0,l,n}^{(1)-}\right)^2 + \left(S_{0,l,n}^{(2)-}\right)^2 \right) \right)^2 \\
&+ \left| \sum_{(l,n)\in\Omega_{l,n}} \frac{P_{h,l}}{2N_l} \left(\left(S_{0,l,n}^{(1)-}\right)^2 - \left(S_{0,l,n}^{(2)-}\right)^2 \right) e^{-j4\pi m_0 F_0 \tau_l} \right|^2 .
\end{aligned}
\tag{5.36}
$$

In part 5.1.1, the asymptotic SIR γ_∞ is expressed with the equation (5.7). Moreover, Proposition 1 is given in order to verify the increase of the SIR with the increase of the number of receive antennas N_r. Both results rely on the statistical channel properties $\tilde{E}_p^{(1)}$ and $\tilde{E}_p^{(2)}$ defined respectively in (5.8) and (5.13). Then, the analytical results of part 5.1.2 allow computing the variables $\tilde{E}_p^{(1)}$ and $\tilde{E}_p^{(2)}$, knowing some basic channel parameters, with the equations (5.28) and (5.35) respectively. Combining these two analytical results, it is now possible to compute the asymptotic SIR γ_∞ and to verify the increase of the SIR with the increase of the number of receive antennas N_r (Proposition 1) knowing the following channel parameters:

- the average power of each multipath component: $P_{h,l}$,
- the normalized delay of each multipath component: $\tau_l.F_0$,
- the normalized maximum Doppler frequency: f_D^{max}/F_0,
- the sub-carrier index: m_0 (only for Proposition 1).

5.2 Numerical Results

In this part, numerical results are provided in order to verify the analytical results of part 5.1 and to visualize the impact of the Doppler effect as a function of the number of receive antennas. The set of useful sub-carriers considered here is $\Omega_p = [-300\ ,\ 300]$. Moreover, three channel models are investigated. The first one is a single-path propagation channel, meaning $L_h = 1$, $P_0 = 0$ dB and $\tau_0 = 0$ s. With such a propagation channel, the expressions of $\tilde{E}_p^{(1)}$ and $\tilde{E}_p^{(2)}$, respectively in (5.28) and (5.35), only rely on the normalized maximum Doppler frequency (f_D^{max}/F_0). Additionally, two multi-path channel models are also considered, namely the EVA and Extended Typical Urban (ETU) channel models defined in [92, 93]. Their delays τ_l and corresponding average powers P_l are given in Appendix A. For these channel models, the inter-carrier spacing is set to F_0= 15 KHz and the considered sub-carrier index is $m_0 = 512$. Finally, the FFT size of the OFDM modulation for the simulations is set to M= 1024, while the number of sinusoids is set to $N_l = 30$, $\forall l \in [0\ ,\ L_h - 1]$, as it is the maximum value considered in [29].

Computation of γ_∞ and Γ_{ref}:

In part 5.1, the asymptotic SIR γ_∞ is expressed with the equation (5.7). Moreover, Proposition 1 establishes that the SIR statistically grows with the increase of the number of receive antennas N_r if, and only if $\gamma_\infty > \Gamma_{ref}$. Therefore, In order to evaluate these analytical results, the values of γ_∞ and Γ_{ref} are numerically computed in this part with the three considered channel models. These values are drawn in Figures 5.1 as a function of the normalized maximum Doppler frequency (f_D^{max}/F_0).

Firstly, the values of γ_∞ are similar whatever the channel model (single-path, EVA or ETU). Therefore, the impact of the frequency selectivity of the channel on the value of γ_∞ seems to be negligible. This result is in line with that from [11], where the author stated that the effect of the frequency selectivity of the channel vanishes in the limit of an infinite number of antennas.

As expected, the asymptotic SIR γ_∞ defined in (5.7) decreases with the increase of the normalized maximum Doppler frequency. Indeed, the greater the normalized maximum Doppler frequency, the greater the impact of the Doppler effect. The asymptotic SIR is thus approximately equal to 43 dB when $f_D^{max}/F_0 = 10\%$ and decreases up to 30 dB when f_D^{max}/F_0 reaches 20% whatever the channel model.

As for γ_∞, the values of Γ_{ref} are similar whatever the channel model (single-path, EVA or ETU) and thus the impact of the frequency selectivity of the channel on these values seems to be negligible. Moreover, γ_∞ is always greater than Γ_{ref}. Therefore, according to Proposition 1, in theory the SIR should increase with the increase of the number of receive antennas N_r whatever the channel model. This result proves that a massive MIMO system with a large

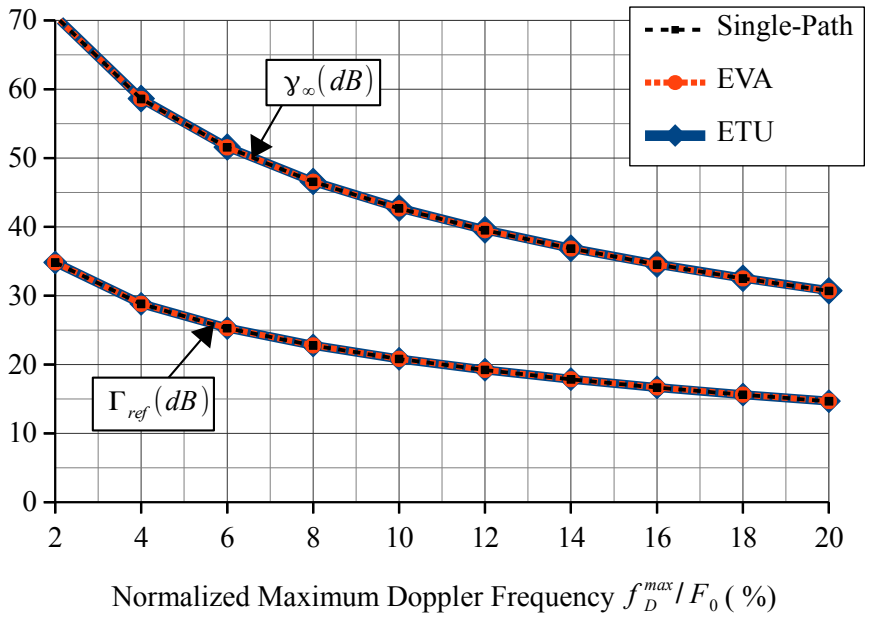

Figure 5.1: Values of γ_∞ and Γ_{ref} as a function of the normalized maximum Doppler frequency (f_D^{max}/F_0) for the single-path, the EVA and the ETU channel models.

number of antennas on the BS side can be used to reduce the impact of the Doppler effect.

Simulation Results:

In this part, the SIR of the considered massive MIMO uplink system is evaluated thanks to simulations for the three considered channel models and for 2, 8, 32 and 128 receive antennas. The results are given in Figures 5.2, 5.3 and 5.4 as a function of the normalized maximum Doppler frequency (f_D^{max}/F_0) respectively for the single-path, EVA and ETU channel models. In order to verify the equation (5.7), the values of γ_∞ for the three considered channel models are also given in these Figures.

As expected, in Figures 5.2, 5.3 and 5.4, the SIR always increases with the increase of N_r. Therefore, the increase of the SIR with the increase of the number of receive antennas N_r demonstrated previously is verified by the simulation results. This increase is significant. For the three channel models, there is a gain of approximately 5 dB between a system with $N_r = 8$ receive antennas and a system with $N_r = 32$ receive antennas.

As the number of receive antennas increases, the blue lines seem to tend to the black dotted lines. Therefore, the simulation results allow confirming the expression of the asymptotic SIR γ_∞ defined in (5.7).

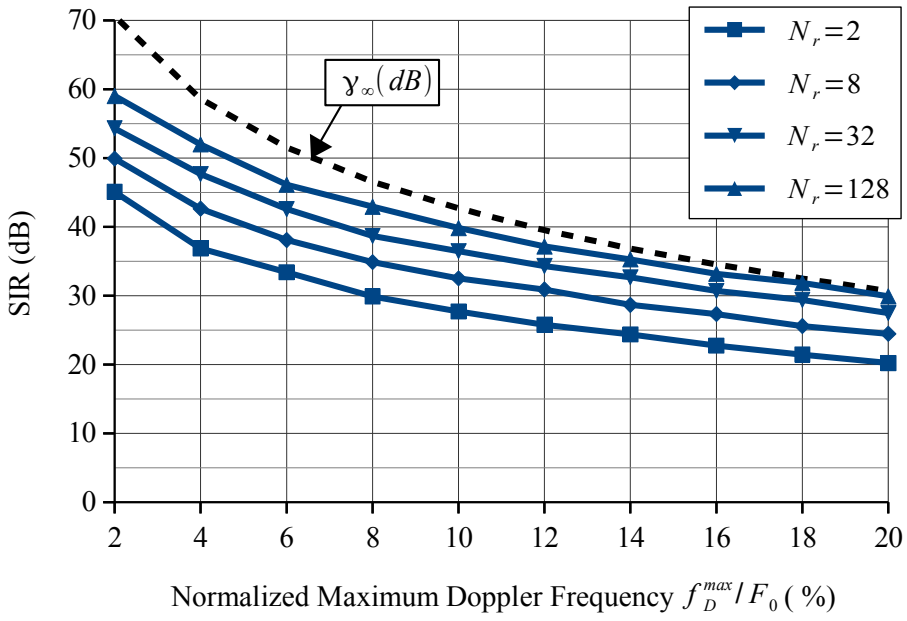

Figure 5.2: Asymptotic SIR γ_∞ and simulated SIR as a function of the normalized maximum Doppler frequency (f_D^{max}/F_0) for the single-path channel model.

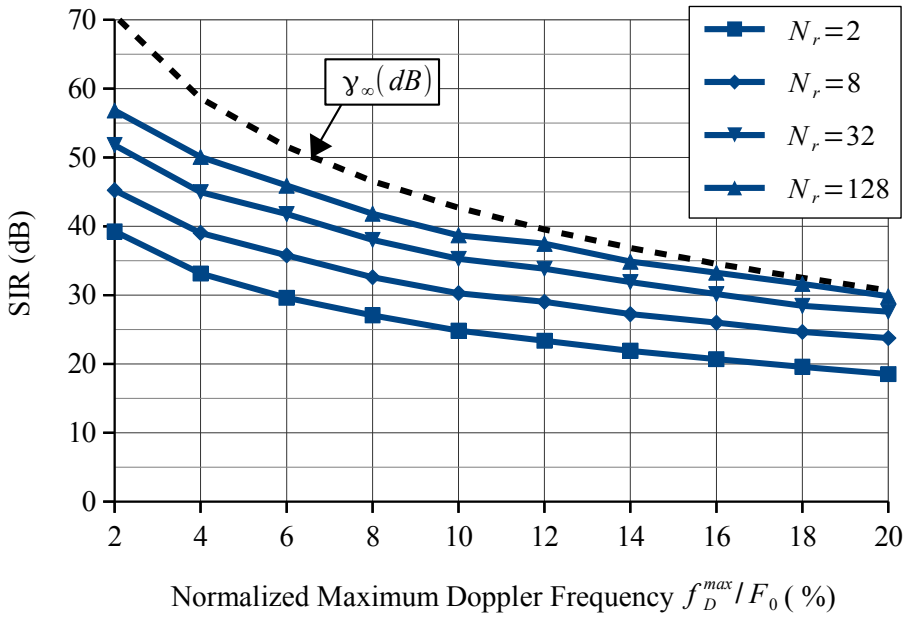

Figure 5.3: Asymptotic SIR γ_∞ and simulated SIR as a function of the normalized maximum Doppler frequency (f_D^{max}/F_0) for the EVA channel model.

5.3 Conclusion

In vehicular scenarios such as V2X, the speed of the users can be as high as 500 km/h. In this context, the interference due to the Doppler effect, highlighted in Chapter 4, might have

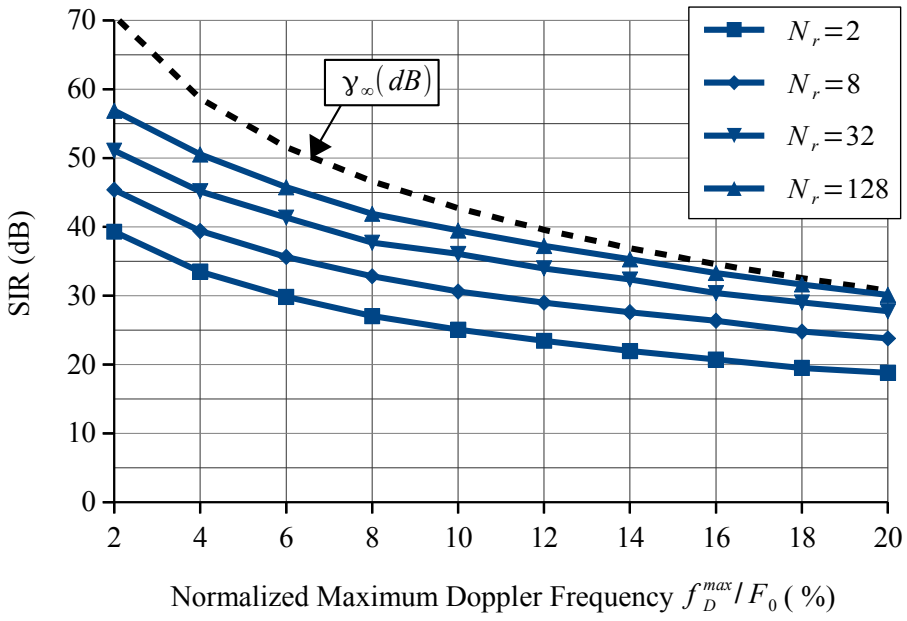

Figure 5.4: Asymptotic SIR γ_∞ and simulated SIR as a function of the normalized maximum Doppler frequency (f_D^{max}/F_0) for the ETU channel model.

a detrimental impact on the performance of the systems.

The effect of a very large number of uncorrelated receive antennas on the ICI due to the Doppler effect has been studied in this Chapter considering an OFDM NLOS communication with a simple MRC receiver. Relaying on analytical and numerical results, the contribution of this Chapter is twofold. Firstly, the asymptotic value of the SIR, when the number of receive antennas tends to infinity, has been analytically expressed. Secondly, it was proven that increasing the number of receive antennas allows for reducing the interference due to the Doppler effect.

This study helps to better evaluate the benefits of massive MIMO systems for 5G in the presence of mobility. From a more practical point of view, this Chapter highlights the ability to improve the performance of vehicular communications when using a massive MIMO system with a low-complexity MRC receiver.

As this study only considers NLOS propagation channels, it might be interesting to extend the considered scenario with propagation channels having a LOS component. Additionally, the study of the BER would help to evaluate the performance of the system. Moreover, compared to the OFDM modulation, the FBMC/OQAM modulation is known to offer a better robustness against the Doppler effect in a SISO system. Therefore, the comparison of the OFDM modulation and of the FBMC/OQAM modulation in a massive MIMO uplink system would be interesting. These aspects are investigated in the next Chapter.

Summary of this Chapter:

- This Chapter considers the **OFDM** modulation and studies **the effect of massive MIMO systems on the interference due to the Doppler effect in a NLOS environment**.
- An **analytical study** is carried out by **evaluating the value of the SIR** as a function of the number of receive antennas and by **expressing statistical channel properties** thanks to a **sum-of-sinusoid representation**.
- Relaying on the **analytical study**, **the asymptotic value of the SIR**, when the number of receive antennas tends to infinity, **is expressed**.
- **Numerical results** highlight that **the impact of the frequency selectivity of the channel on the value of the asymptotic SIR is negligible**.
- Relaying on the **analytical study** and on **numerical results**, **it is proven that increasing the number of receive antennas allows for reducing the interference due to the Doppler effect**.
- **Simulation results** allow **validating the analytical results**.

Related Publication:

- A. Bazin, B. Jahan and M. Hélard, "Doppler Effect Reduction in an OFDM System Thanks to Massive MIMO," in *IEEE Access*, vol. 6, pp. 38498-38511, 2018.

6

OFDM Versus FBMC/OQAM

In the previous Chapter, the impact of an increase of the number of receive antennas on a massive MIMO uplink system with mobility was studied considering an OFDM NLOS communication with a simple MRC receiver. In particular, it was shown that the impact of the Doppler spread created by the variations over time of the NLOS propagation channel is reduced when a large number of receive antennas is combined with a MRC receiver.

If a communication with a LOS component is considered, a Doppler shift adds to the Doppler spread as discussed in Chapter 1. Doppler shift compensation techniques have been widely studied in the literature and can improve the performance of the systems [94, 95]. In [94], a predictive algorithm allows compensating the Doppler shift with the aid of informations coming from sensors. In [95], the Doppler shift compensation technique is based on a matching pursuit algorithm. However, both solutions come at the price of an increased complexity. Considering a massive MIMO system, a simple MRC receiver may not be robust in the same manner to the Doppler shift and to the Doppler spread. Additionally, it is widely known that the FBMC/OQAM modulation described in part 2.2 presents a better robustness against the Doppler effect compared to the OFDM modulation in a SISO context [30–33]. However, one may wonder if the superiority of the FBMC/OQAM modulation is also valid in the considered massive MIMO context.

In this Chapter, the OFDM and the FBMC/OQAM modulations are compared in a massive MIMO uplink system with mobility. Unlike in Chapter 5, propagation channels with and without LOS components are considered in this Chapter. Based on the system model defined in Chapter 4, the asymptotic system capacity, when the number of receive antennas tends to infinity, is analytically evaluated in part 6.1 for the OFDM and the FBMC/OQAM modulations. Then, the choice of the prototype filter for the FBMC/OQAM modulation is discussed in part 6.2 by comparing the analytical asymptotic system capacity obtained with four different filters. In part 6.3, simulations are performed in order to evaluate the performance of the system in terms of system capacity. The objective is to verify the analytical results and to conclude on the impact of the Doppler shift and on the benefit of the FBMC/OQAM

modulation compared to the OFDM modulation in this context. The BER with and without channel coding is then computed in part 6.4 in order to evaluate the performance of these two modulations in practice.

6.1 Asymptotic Analytical Study

This part focuses on the asymptotic behavior, when the number or receive antennas N_r tends to infinity. In this context, the asymptotic system capacity is evaluated based on the system model defined in Chapter 4. This study considers a propagation channel with a LOS component and both the OFDM and the FBMC/OQAM modulations.

6.1.1 OFDM Modulation

The OFDM modulation is first considered. Owing to the law of large number, when $N_r \to +\infty$, the noise component vanishes according to [11] and the equation (4.26) becomes:

$$\hat{c}^{\infty} = c_0 + \sum_{p \in \Omega_p^*} \frac{N_r E\left[(H_0^{n_r})^* H_p^{n_r}\right]}{N_r E\left[|H_0^{n_r}|^2\right]} c_p = c_0 + \sum_{p \in \Omega_p^*} \frac{E\left[(H_0^{n_r})^* H_p^{n_r}\right]}{E\left[|H_0^{n_r}|^2\right]} c_p. \tag{6.1}$$

Moreover, as $\tilde{H}_p^{n_r}$ and $\check{H}_p^{n_r}$ are independent variables:

$$\begin{aligned} E\left[(H_0^{n_r})^* H_p^{n_r}\right] &= E\left[\left(\tilde{H}_0^{n_r} + \check{H}_0^{n_r}\right)^* \left(\tilde{H}_p^{n_r} + \check{H}_p^{n_r}\right)\right] \\ &= E\left[\left(\tilde{H}_0^{n_r}\right)^* \tilde{H}_p^{n_r}\right] + E\left[\left(\check{H}_0^{n_r}\right)^* \check{H}_p^{n_r}\right] \\ &\quad + E\left[\tilde{H}_0^{n_r}\right]^* E\left[\check{H}_p^{n_r}\right] + E\left[\check{H}_0^{n_r}\right]^* E\left[\tilde{H}_p^{n_r}\right]. \end{aligned} \tag{6.2}$$

Finally, according to (5.25), it comes:

$$E\left[(H_0^{n_r})^* H_p^{n_r}\right] = \tilde{E}_p^{(1)} + \check{E}_p^{(1)}, \tag{6.3}$$

with:

$$\begin{cases} \tilde{E}_p^{(1)} = E\left[\left(\tilde{H}_0^{n_r}\right)^* \tilde{H}_p^{n_r}\right] \;\Rightarrow\; \text{Doppler Spread}, \\ \check{E}_p^{(1)} = E\left[\left(\check{H}_0^{n_r}\right)^* \check{H}_p^{n_r}\right] \;\Rightarrow\; \text{Doppler Shift}. \end{cases} \tag{6.4}$$

In (6.4), $\tilde{E}_p^{(1)}$ is relative to the channel components due to the Doppler spread, while $\check{E}_p^{(1)}$ is relative to the channel components due to the Doppler shift. Their expressions are evaluated thereafter.

As in the previous Chapter, the component of the propagation channel due to the Doppler spread is now modeled by the sum-of-sinusoid method defined in [29] and described in part

1.3.1 with N_l the considered number of sinusoids for the l^{th} path and $f_{l,n}^{(i)}$ defined by:

$$f_{l,n}^{(i)} = f_D^{max} \cos\left(\frac{\pi}{2N_l}\left(n-\frac{1}{2}\right) + (-1)^{i-1}\frac{\pi}{4N_l}\frac{l}{L_h+2}\right), \tag{6.5}$$

f_D^{max} being the maximum Doppler frequency. The mathematical set of integer $\Omega_{l,n}$ is defined as follow:

$$\Omega_{l,n} = \left\{(l,n) \in \mathbb{N}^2 \mid 0 \leq l \leq (L_h-1) \text{ and } 1 \leq n \leq N_l\right\} \tag{6.6}$$

and the following variables are given:

$$\begin{cases} S_{p,l,n}^{(i)-} = \text{sinc}\left(p - \frac{f_{l,n}^{(i)}}{F_0}\right), \\ S_{p,l,n}^{(i)+} = \text{sinc}\left(p + \frac{f_{l,n}^{(i)}}{F_0}\right), \\ S_p^{shift} = \text{sinc}\left(p - \frac{f_D^{shift}}{F_0}\right). \end{cases} \tag{6.7}$$

The value of $\tilde{E}_p^{(1)}$ is already expressed in part 5.1.2 of the previous Chapter based on the sum-of-sinusoid representation. This study gives:

$$\tilde{E}_p^{(1)} = (-1)^p \sum_{(l,n)\in\Omega_{l,n}} \frac{P_{h,l}}{4N_l}\left(S_{0,l,n}^{(1)-}\left(S_{p,l,n}^{(1)-} + S_{p,l,n}^{(1)+}\right) + S_{0,l,n}^{(2)-}\left(S_{p,l,n}^{(2)-} + S_{p,l,n}^{(2)+}\right)\right)\exp\left[j2\pi p F_0 \tau_l\right], \tag{6.8}$$

and:

$$\tilde{E}_0^{(1)} = \sum_{(l,n)\in\Omega_{l,n}} \frac{P_{h,l}}{2N_l}\left(\left(S_{0,l,n}^{(1)-}\right)^2 + \left(S_{0,l,n}^{(2)-}\right)^2\right), \tag{6.9}$$

when $p = 0$. Additionally, for the components due to the Doppler shift, the development in appendix C.1 gives:

$$\check{E}_p^{(1)} = (-1)^p \; \check{P}_{h,0} \; S_0^{shift} \; S_p^{shift} \; e^{j2\pi p F_0 \tau_0}. \tag{6.10}$$

Therefore, when $p = 0$, it comes:

$$\check{E}_0^{(1)} = \check{P}_{h,0} \; \left(S_0^{shift}\right)^2. \tag{6.11}$$

According to (6.1) and (6.3), the asymptotic SIR when the number of receive antennas tends to infinity is:

$$\gamma_{OFDM}^{\infty} = \frac{\left(E\left[|H_0^{n_r}|^2\right]\right)^2}{\sum\limits_{p\in\Omega_p^*} \left|E\left[(H_0^{n_r})^* \, H_p^{n_r}\right]\right|^2} = \frac{\left(\tilde{E}_0^{(1)} + \check{E}_0^{(1)}\right)^2}{\sum\limits_{p\in\Omega_p^*} \left|\tilde{E}_p^{(1)} + \check{E}_p^{(1)}\right|^2}, \tag{6.12}$$

for the OFDM modulation. Based on the expression of γ_{OFDM}^{∞}, the asymptotic system

capacity can be computed as follows:

$$\begin{aligned} R_{OFDM}^{\infty} &= \frac{T_0}{T_0+T_{CP}}\log_2\left(1+\gamma_{OFDM}^{\infty}\right) \\ &= \frac{T_0}{T_0+T_{CP}}\log_2\left(1+\frac{\left(\tilde{E}_0^{(1)}+\check{E}_0^{(1)}\right)^2}{\sum\limits_{p\in\Omega_p^*}\left|\tilde{E}_p^{(1)}+\check{E}_p^{(1)}\right|^2}\right). \end{aligned} \tag{6.13}$$

One can note that, unlike the SIR, the expression of the asymptotic system capacity takes into account the loss of spectral efficiency induced by the addition of a CP. Using the expression of $\tilde{E}_p^{(1)}$ in (6.8) and $\check{E}_p^{(1)}$ in (6.10), the asymptotic system capacity for the OFDM modulation R_{OFDM}^{∞} can thus be analytically expressed according to (6.13).

6.1.2 FBMC/OQAM Modulation

The FBMC/OQAM modulation is now considered. Owing to the law of large number, when $N_r \to +\infty$, the noise component vanishes according to [11] and the equation (4.44) becomes:

$$\begin{aligned} \hat{a}^{\infty} &= a_{0,0} + \sum_{(p,q)\in\Omega_{p,q}^*} \Re\left[\frac{N_r E\left[\left(H_{0,0}^{n_r}\right)^* H_{p,q}^{n_r}\right]}{N_r E\left[\left|H_{0,0}^{n_r}\right|^2\right]}\right] a_{p,q} \\ &= a_{0,0} + \sum_{(p,q)\in\Omega_{p,q}^*} \Re\left[\frac{E\left[\left(H_{0,0}^{n_r}\right)^* H_{p,q}^{n_r}\right]}{E\left[\left|H_{0,0}^{n_r}\right|^2\right]}\right] a_{p,q}. \end{aligned} \tag{6.14}$$

Moreover, as $\tilde{H}_{p,q}^{n_r}$ and $\check{H}_{p,q}^{n_r}$ are independent variables, it comes:

$$\begin{aligned} E\left[\left(H_{0,0}^{n_r}\right)^* H_{p,q}^{n_r}\right] &= E\left[\left(\tilde{H}_{0,0}^{n_r}+\check{H}_{0,0}^{n_r}\right)^*\left(\tilde{H}_{p,q}^{n_r}+\check{H}_{p,q}^{n_r}\right)\right] \\ &= E\left[\left(\tilde{H}_{0,0}^{n_r}\right)^*\tilde{H}_{p,q}^{n_r}\right] + E\left[\left(\check{H}_{0,0}^{n_r}\right)^*\check{H}_{p,q}^{n_r}\right] \\ &\quad + E\left[\tilde{H}_{0,0}^{n_r}\right]^* E\left[\check{H}_{p,q}^{n_r}\right] + E\left[\check{H}_{0,0}^{n_r}\right]^* E\left[\tilde{H}_{p,q}^{n_r}\right] \\ &= \tilde{E}_{p,q}^{(1)} + \check{E}_{p,q}^{(1)} + E\left[\tilde{H}_{0,0}^{n_r}\right]^* E\left[\check{H}_{p,q}^{n_r}\right] + E\left[\check{H}_{0,0}^{n_r}\right]^* E\left[\tilde{H}_{p,q}^{n_r}\right], \end{aligned} \tag{6.15}$$

with:

$$\begin{cases} \tilde{E}_{p,q}^{(1)} = E\left[\left(\tilde{H}_{0,0}^{n_r}\right)^*\tilde{H}_{p,q}^{n_r}\right] \Rightarrow \text{Doppler Spread}, \\ \check{E}_{p,q}^{(1)} = E\left[\left(\check{H}_{0,0}^{n_r}\right)^*\check{H}_{p,q}^{n_r}\right] \Rightarrow \text{Doppler Shift}. \end{cases} \tag{6.16}$$

In (6.16), $\tilde{E}_{p,q}^{(1)}$ is relative to the channel components due to the Doppler spread, while $\check{E}_{p,q}^{(1)}$ is relative to the channel components due to the Doppler shift. Their expressions are evaluated thereafter.

The components due to the Doppler spread $\tilde{H}_{p,q}^{n_r}$ are modeled using the sum-of-sinusoid representation defined in [29] and described in part 1.3.1. Thereby:

$$\tilde{h}_l^{n_r}(t) = \sqrt{P_{h,l}} \times \frac{\tilde{h}_l^{n_r(1)}(t) + j\tilde{h}_l^{n_r(2)}(t)}{\sqrt{2}}, \tag{6.17}$$

with $P_{h,l}$ being the average power of the l^{th} path and $\tilde{h}_l^{n_r(i)}(t)$ defined by:

$$\tilde{h}_l^{n_r(i)}(t) = \sqrt{\frac{2}{N_l}} \sum_{n=1}^{N_l} \cos\left(2\pi f_{l,n}^{(i)} t + \theta_{l,n}^{n_r(i)}\right). \tag{6.18}$$

In (6.18), N_l is the considered number of sinusoids for the l^{th} path, $\theta_{l,n}^{n_r(i)}$ is a random variable having a uniform distribution over the interval $]0, 2\pi]$ and $f_{l,n}^{(i)}$ is defined as follows:

$$f_{l,n}^{(i)} = f_D^{max} \cos\left(\frac{\pi}{2N_l}\left(n - \frac{1}{2}\right) + (-1)^{i-1}\frac{\pi}{4N_l}\frac{l}{L_h + 2}\right), \tag{6.19}$$

f_D^{max} being the maximum Doppler frequency. Moreover, $\theta_{l,n}^{n_r(i)}$ and $\theta_{l',n'}^{n_r(i')}$ are two independent variables if $(i,l,n) \neq (i',l',n')$. Additionally, the ambiguity function of $g(t)$ is defined as follows:

$$A_g(\tau,\nu) = \int_{\mathbb{R}} g(t)g^*(t-\tau)e^{j2\pi\nu t}dt, \tag{6.20}$$

and the following notations are given:

$$\begin{cases} A_{p,q,l,n}^{(i)-} = A_g\left(\tau_l - q\frac{T_0}{2}, -F_0\left(p - \dfrac{f_{l,n}^{(i)}}{F_0}\right)\right), \\ A_{p,q,l,n}^{(i)+} = A_g\left(\tau_l - q\frac{T_0}{2}, -F_0\left(p + \dfrac{f_{l,n}^{(i)}}{F_0}\right)\right), \\ A_{p,q}^{shift} = A_g\left(\tau_0 - q\frac{T_0}{2}, -F_0\left(p - \dfrac{f_D^{shift}}{F_0}\right)\right). \end{cases} \tag{6.21}$$

Using the results of Appendix C.2, it comes:

$$E\left[\tilde{H}_{p,q}^{n_r}\right] = 0, \tag{6.22}$$

and thus:

$$E\left[\left(H_{0,0}^{n_r}\right)^H H_{p,q}^{n_r}\right] = \tilde{E}_{p,q}^{(1)} + \check{E}_{p,q}^{(1)}. \tag{6.23}$$

Moreover, Appendix C.2 shows that:

$$\tilde{E}_{p,q}^{(1)} = e^{j(\phi_{p,q}-\phi_{0,0})} \sum_{(l,n)\in\Omega_{l,n}} \frac{\tilde{P}_{h,l}}{4N_l} \left(\sum_{i\in\{1,2\}} \left(\left(A_{0,0,l,n}^{(i)-}\right)^* A_{p,q,l,n}^{(i)-} + \left(A_{0,0,l,n}^{(i)+}\right)^* A_{p,q,l,n}^{(i)+} \right) \right) e^{j2\pi p F_0 \tau_l}. \tag{6.24}$$

As $g(t)$ is real, it comes $A_g(\tau,-\nu) = A_g^*(\tau,\nu)$ and:

$$\tilde{E}_{0,0}^{(1)} = \sum_{(l,n)\in\Omega_{l,n}} \frac{\tilde{P}_{h,l}}{2N_l} \left(\left|A_{0,0,l,n}^{(1)-}\right|^2 + \left|A_{0,0,l,n}^{(2)-}\right|^2 \right), \tag{6.25}$$

when $(p,q) = (0,0)$. Additionally, the development in Appendix C.3 gives:

$$\check{E}_{p,q}^{(1)} = \check{P}_{h,0}\ e^{j(\phi_{p,q}-\phi_{0,0})}\ \left(A_{0,0}^{shift}\right)^*\ A_{p,q}^{shift}\ e^{j2\pi p F_0 \tau_0}, \tag{6.26}$$

and thus, when $(p,q) = (0,0)$, it comes:

$$\check{E}_{0,0}^{(1)} = \check{P}_{h,0}\ \left|A_{0,0}^{shift}\right|^2. \tag{6.27}$$

According to (6.14) and (6.23), the asymptotic SIR when the number of receive antennas tends to infinity is:

$$\begin{aligned} \gamma_{FBMC}^{\infty} &= \frac{E\left[\left|H_{0,0}^{n_r}\right|^2\right]^2}{\sum\limits_{(p,q)\in\Omega_{p,q}^*} \Re\left[E\left[\left(H_{0,0}^{n_r}\right)^* H_{p,q}^{n_r}\right]\right]^2} \\ &= \frac{\left(\tilde{E}_{0,0}^{(1)} + \check{E}_{0,0}^{(1)}\right)^2}{\sum\limits_{(p,q)\in\Omega_{p,q}^*} \Re\left[\tilde{E}_{p,q}^{(1)} + \check{E}_{p,q}^{(1)}\right]^2}, \end{aligned} \tag{6.28}$$

for the FBMC/OQAM modulation. The asymptotic system capacity is thus equal to:

$$\begin{aligned} R_{FBMC}^{\infty} &= \log_2\left(1+\gamma_{FBMC}^{\infty}\right) \\ &= \log_2\left(1 + \frac{\left(\tilde{E}_{0,0}^{(1)} + \check{E}_{0,0}^{(1)}\right)^2}{\sum\limits_{(p,q)\in\Omega_{p,q}^*} \Re\left[\tilde{E}_{p,q}^{(1)} + \check{E}_{p,q}^{(1)}\right]^2}\right). \end{aligned} \tag{6.29}$$

Therefore, the FBMC/OQAM modulation does not use a CP and thus avoids the loss of spectral efficiency associated. Moreover, the asymptotic system capacity for the FBMC/OQAM modulation can be analytically expressed thanks to the value of $\tilde{E}_{p,q}^{(1)}$ defined in (6.24) and $\check{E}_{p,q}^{(1)}$ defined in (6.26) and according to the equation (6.29).

6.2 Choice of the Filter for the FBMC/OQAM Modulation

In this part, the asymptotic system capacity with the FBMC/OQAM modulation R^{∞}_{FBMC} is computed as a function of the normalized maximum Doppler frequency f_D^{max}/F_0 for different prototype filters and according to the equation (6.29). The objective is to find the filter that leads to the best performance in terms of asymptotic system capacity. Four filters are studied, the Time Frequency Localization (K=1) (TFL1) filter of overlapping factor 1 defined in [96] and the Phydyas filters of overlapping factor 2, 3 and 4 defined in [97] and further named Phydyas2, Phydyas3 and Phydyas4 respectively. Moreover, the inter-carrier spacing is set to F_0= 15 kHz, the set of useful sub-carriers considered here is $\Omega_{p,q} = ([-300\ ,\ 300], [(-2K+1), 2K])$ and the number of sinusoids is set to $N_l = 30, \forall l \in [0\ ,\ L_h-1]$, as it is the maximum value considered in [29]. This study is performed on propagation channels with and without a LOS component.

6.2.1 NLOS Environment

The asymptotic system capacity R^{∞}_{FBMC} is first computed on two NLOS channel models, namely the EVA and ETU channel models defined in [92,93]. Their delays τ_l and corresponding average powers P_l are given in Appendix A. As there is no LOS component ($\check{P}_{h,0} = 0$) the Doppler effect is characterized by the Doppler spread and thus $\check{E}^{(1)}_{p,q} = 0$, $\forall (p,q) \in \Omega_{p,q}$. The results are given by Figure 6.1 (a) for the EVA channel model and by Figure 6.1 (b) for the ETU channel model.

Firstly, the focus is put on the asymptotic system capacity for low maximum Doppler frequency ($f_D^{max}/F_0 < 5\%$). In this context, the impact of the Doppler spread is low and the system is mostly affected by the intrinsic interference due to the frequency selectivity of the channel. This interference is actually higher for the ETU channel model as it presents a higher frequency selectivity than the EVA channel model. Indeed the root mean square delay spread is $\tau_{rms} = 357\ ns$ for the EVA channel model, while the root mean square delay spread is $\tau_{rms} = 991\ ns$ for the ETU channel model. Therefore, Figure 6.1 shows that for a given prototype filter the asymptotic system capacity R^{∞}_{FBMC} is lower with the ETU channel model than with EVA channel model. For example, with a normalized maximum Doppler frequency equal to 2% and a TFL1 prototype filter, there is a difference of 2 bit/sec/Hz between the asymptotic system capacity with the EVA channel model and the asymptotic system capacity with the ETU channel model.

Additionally, for low maximum Doppler frequency ($f_D^{max}/F_0 < 5\%$), the robustness against the intrinsic interference due to the frequency selectivity of the channel depends on the length of the prototype filter and thus on its overlapping factor K. Indeed, Figure 6.1 shows that the longer the prototype filter, the higher the asymptotic system capacity and thus the higher

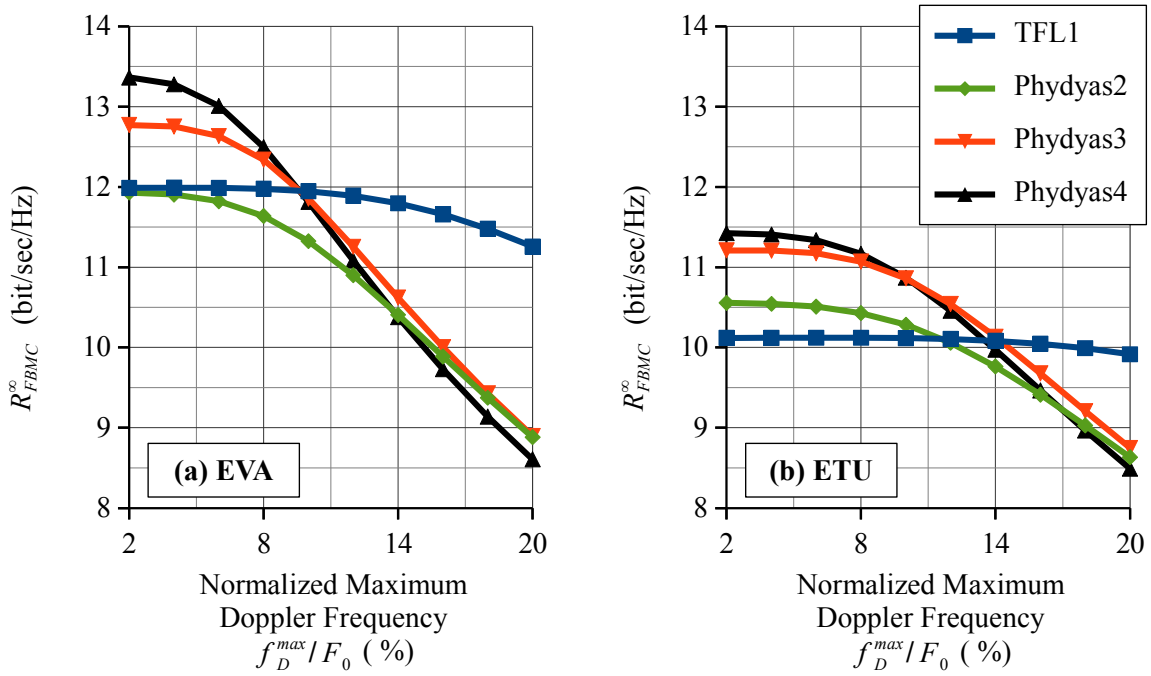

Figure 6.1: Asymptotic system capacity R^{∞}_{FBMC} with the FBMC/OQAM modulation as a function of the normalized maximum Doppler frequency f_D^{max}/F_0 and of the prototype filter for (a) the EVA channel model and (b) the ETU channel model.

the robustness against the intrinsic interference. For example, with a normalized maximum Doppler frequency equal to 2%, the Phydyas4 filter (K= 4) outperforms the TFL1 filter (K= 1) with a gain of approximately 1.4 bit/sec/Hz for both the EVA and ETU channel models. As a conclusion, for a NLOS propagation channel with low maximum Doppler frequency, a long prototype filter is preferable because of its better robustness against the intrinsic interference.

When the maximum Doppler frequency increases and reaches higher values (f_D^{max}/F_0> 15%), the system becomes mostly affected by the interference due to the time selectivity of the channel caused by the Doppler spread. Moreover, the robustness against the interference due to the Doppler spread also depends on the length of the prototype filter and thus on its overlapping factor K. Figure 6.1 shows that the shorter the filter, the higher the asymptotic system capacity and thus the higher the robustness against the Doppler spread. In particular, the TFL1 filter (K= 1) outperforms the Phydyas4 filter (K= 4) when the normalized maximum Doppler frequency is equal to 20%, with a gain of 2.8 bit/sec/Hz (respectively 1.4 bit/sec/Hz) on the EVA channel model (respectively ETU channel model). As a conclusion, for a NLOS propagation channel with high maximum Doppler frequency, a short prototype filter is preferable because of its better robustness against the interference due to the Doppler spread.

6.2.2 LOS Environment

The asymptotic system capacity R^{∞}_{FBMC} is now computed on a propagation channel with a LOS component, namely the Rural Area with 4 taps (RA4) channel model defined in [98]. Its delays τ_l and corresponding average powers P_l are given in Appendix A. As this channel model presents a LOS component, a Doppler shift adds to the Doppler spread. For the RA4 channel model, the value of the Doppler shift frequency f_D^{shift} is proportional to the value of the maximum Doppler frequency f_D^{max}: $f_D^{shift} = 0.7 \times f_D^{max}$ [98]. Therefore, the Doppler effect is only quantified by the value of f_D^{max}. Figure 6.2 gives the results for the LOS RA4 channel model.

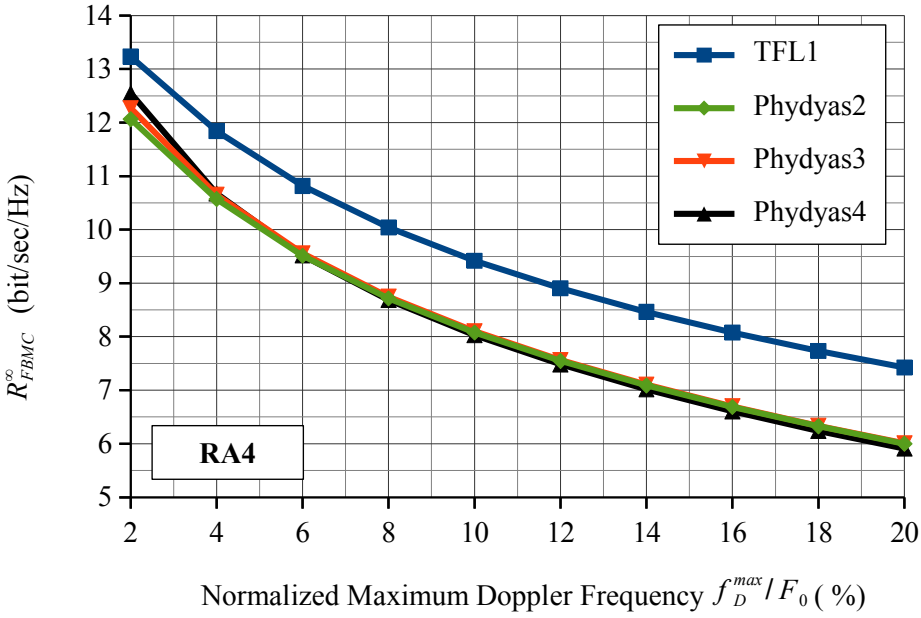

Figure 6.2: Asymptotic system capacity R^{∞}_{FBMC} with the FBMC/OQAM modulation as a function of the normalized maximum Doppler frequency f_D^{max}/F_0 and of the prototype filter for the RA4 channel model.

Unlike the EVA and ETU channel models, the RA4 channel model presents a very low frequency selectivity because of its strong LOS component ($\tau_{rms} = 126\ ns$). Therefore, the system is mostly affected by the interference to the time selectivity of the channel caused by the Doppler effect (Doppler shift and Doppler spread). Figure 6.2 shows that the asymptotic system capacity R^{∞}_{FBMC} rapidly decreases with the increase of the maximum Doppler frequency whatever the prototype filter. For example, with a Phydyas4 prototype filter, the asymptotic system capacity is of 12.5 bit/sec/Hz when the normalized maximum Doppler frequency is equal to 2% but is reduced to 5.8 bit/sec/Hz when the normalized maximum Doppler frequency is equal to 20%.

Figure 6.2 shows that the robustness against the interference due to the time selectivity of the channel caused by the Doppler effect depends on the length of the prototype filter and thus

on its overlapping factor K. In particular, the shorter the filter, the higher the asymptotic system capacity and thus the higher the robustness against the Doppler effect (Doppler shift and Doppler spread). Therefore, the TFL1 filter always outperforms the Phydyas filters in this context with a gain up to 1.5 bit/sec/Hz when the normalized maximum Doppler frequency is equal to 20%. As a conclusion, for a propagation channel with a LOS component, a short prototype filter is preferable whatever the value of the maximum Doppler frequency because of its better robustness against the interference due to the Doppler shift.

6.3 Simulations: Comparison in Terms of System Capacity

Simulations are now conducted in order to evaluate the performance of the systems in terms of system capacity. The first objective is to verify the analytical results of part 6.1, meaning the expressions of R^{∞}_{OFDM} in (6.13) and R^{∞}_{FBMC} in (6.29). The second objective is to evaluate the impact of the Doppler spread and Doppler shift in a massive MIMO uplink system for the OFDM modulation and the FBMC/OQAM modulation. These simulations are performed with the parameters given in table 6.1. These simulations are carried out on propagation

Table 6.1: Simulation parameters for the comparison in terms of system capacity.

FFT size: M	1024
Number of useful sub-carriers	600
Inter-carrier spacing: F_0	15 kHz
SNR	20 dB
Number of receive antennas: N_r	128
CP duration for the OFDM modulation: T_{CP}	4.7 μs

channels with and without a LOS component.

6.3.1 NLOS Environment

The simulations are first carried out on the EVA and the ETU NLOS channel models [92,93]. Their delays τ_l and corresponding average powers P_l are given in Appendix A. According to part 6.2, the Phydyas4 and the TFL1 filters are used for the FBMC/OQAM modulation as they give the best asymptotic system capacity respectively for low and high maximum Doppler frequency. Figures 6.3 and 6.4 give the results respectively for the EVA and the ETU channel models. Additionally, the theoretical asymptotic capacities R^{∞}_{OFDM} and R^{∞}_{FBMC} are also computed thanks to (6.13) and (6.29) and are added on these Figures in oder to verify their expressions.

Regarding the FBMC/OQAM modulation, the values of R^{∞}_{FBMC} given by the black plain lines for the Phydyas4 filter and by the red plain lines for the TFL1 filter in Figures 6.3

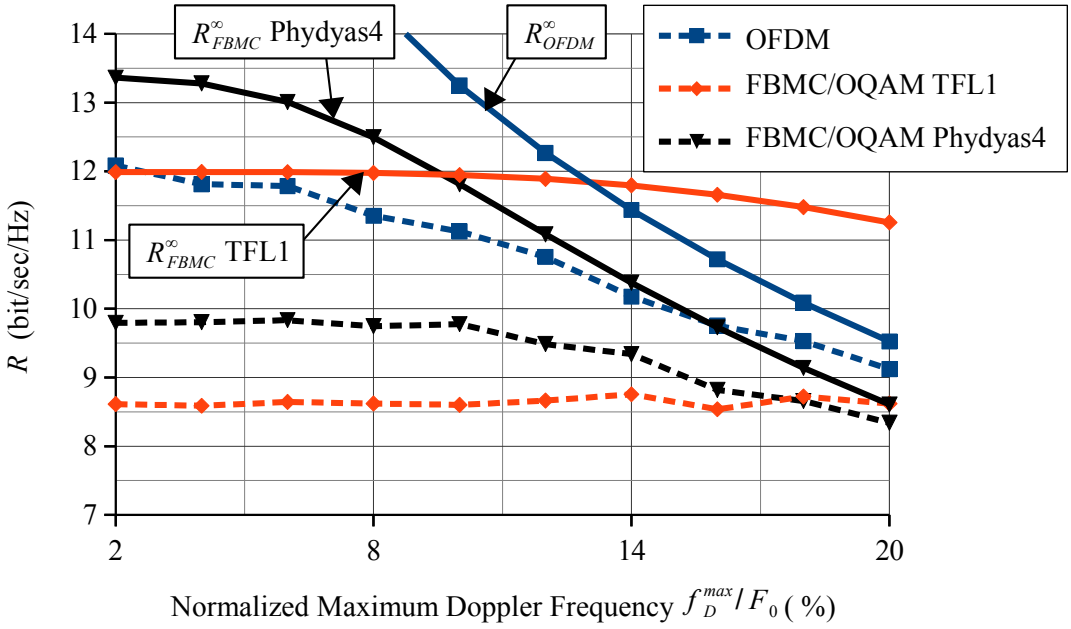

Figure 6.3: System capacity R as a function of the normalized maximum Doppler frequency f_D^{max}/F_0 with the EVA channel model.

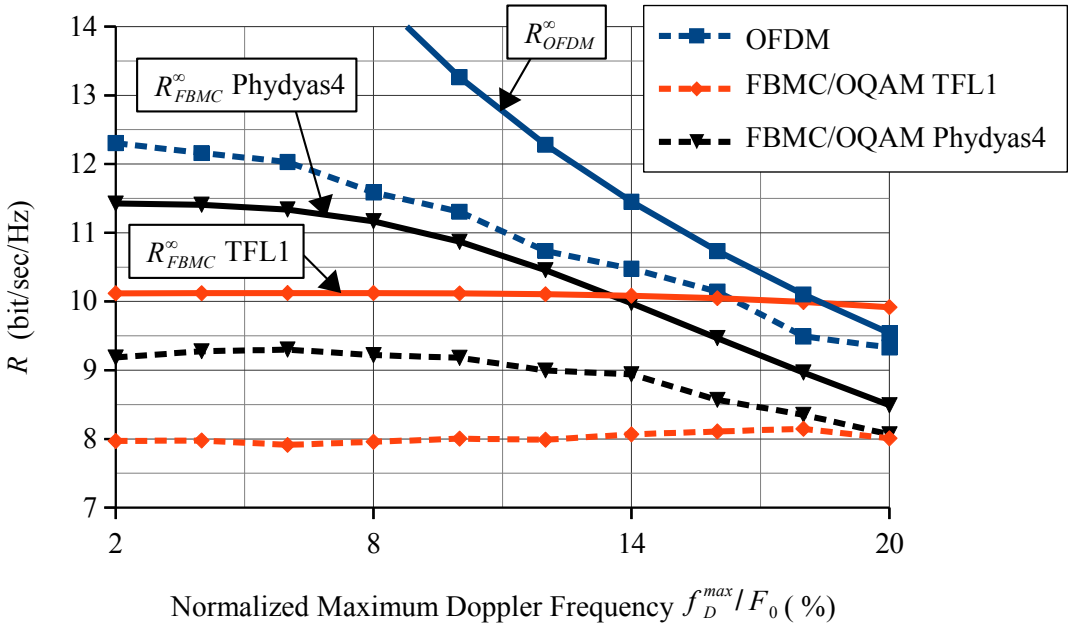

Figure 6.4: System capacity R as a function of the normalized maximum Doppler frequency f_D^{max}/F_0 with the ETU channel model.

and 6.4 are in concordance with the simulation results given by the black and red dotted curves respectively for the Phydyas4 filter and the TFL1 filter. Indeed, the values of R^{∞}_{FBMC} give the upper limit of the simulated capacities. On a NLOS channel model, the results of part 6.2.1 show that the asymptotic system capacity with the FBMC/OQAM modulation R^{∞}_{FBMC} is limited by the intrinsic interference for low maximum Doppler frequency and by

the Doppler spread for high maximum Doppler frequency. However, simulation results show that the increase of the maximum Doppler frequency has only a limited impact on the system capacity. With the TFL1 filter, the system capacity is approximately stable on both the EVA and the ETU channel models. With the Phydyas4 filter, between a normalized maximum Doppler frequency of 2% and of 20%, there is only a loss of 1.5 bit/sec/Hz on the EVA channel model and 1 bit/sec/Hz on the ETU channel model. Therefore, the Phydyas4 prototype filter outperforms the TFL1 prototype filter in this context. However, its long length induces an increased latency and thus the TFL1 prototype filter may still be considered.

Regarding the OFDM modulation, the asymptotic capacities R_{OFDM}^{∞} are given by the plain blue curves in Figures 6.3 and 6.4. These curves are in concordance with the simulated capacities given by the dotted blue curves in Figures 6.3 and 6.4. Unlike the FBMC/OQAM modulation, the OFDM does not suffer from intrinsic interference and thus, for low maximum Doppler frequency ($f_D^{max}/F_0 < 5\%$) the OFDM modulation outperforms the FBMC/OQAM modulation. For a normalized maximum Doppler frequency equal to 2%, the OFDM modulation offers a gain of 2.1 bit/sec/Hz on the EVA channel model and 3 bit/sec/Hz on the ETU channel model compared to the FBMC/OQAM modulation with a Phydyas4 filter. For high maximum Doppler frequency ($f_D^{max}/F_0 > 15\%$), the system capacity with an OFDM modulation is impacted by the Doppler spread as shown by the decrease of the asymptotic system capacity curves in Figures 6.3 and 6.4. However, thanks to the Doppler spread reduction proved in Chapter 5, the impact of the Doppler effect remains limited and the OFDM modulation always outperforms the FBMC/OQAM modulation. For a normalized maximum Doppler frequency equal to 20%, the OFDM modulation offers a gain of 0.5 bit/sec/Hz on the EVA channel model and 1.3 bit/sec/Hz on the ETU channel model compared to the FBMC/OQAM modulation with a TFL1 filter. To conclude, thanks to the reduction of the impact of the Doppler spread, the OFDM modulation leads to the best performance in terms of system capacity on a NLOS channel model.

6.3.2 LOS Environment

The simulations are now conducted on a propagation channel with a LOS component, the RA4 channel model [98]. Its delays τ_l and corresponding average powers P_l are given in Appendix A. For this channel model, the value of the Doppler shift frequency f_D^{shift} is proportional to the value of the maximum Doppler frequency f_D^{max}: $f_D^{shift} = 0.7 \times f_D^{max}$ [98]. Therefore, the Doppler effect is only quantified by the value of f_D^{max}. According to part 6.2, the TFL1 filter is used for the FBMC/OQAM modulation as it gives the best asymptotic system capacity on propagation channels with a LOS component. Figure 6.5 gives the results of these simulations. Additionally, the theoretical asymptotic capacities R_{OFDM}^{∞} and R_{FBMC}^{∞} are also computed thanks to (6.13) and (6.29) and are added on this Figure in oder to verify their expressions.

Firstly, the values of R_{OFDM}^{∞} and R_{FBMC}^{∞} given respectively by the blue and red plain curves are in concordance with the simulation results given by the blue and red dotted curves.

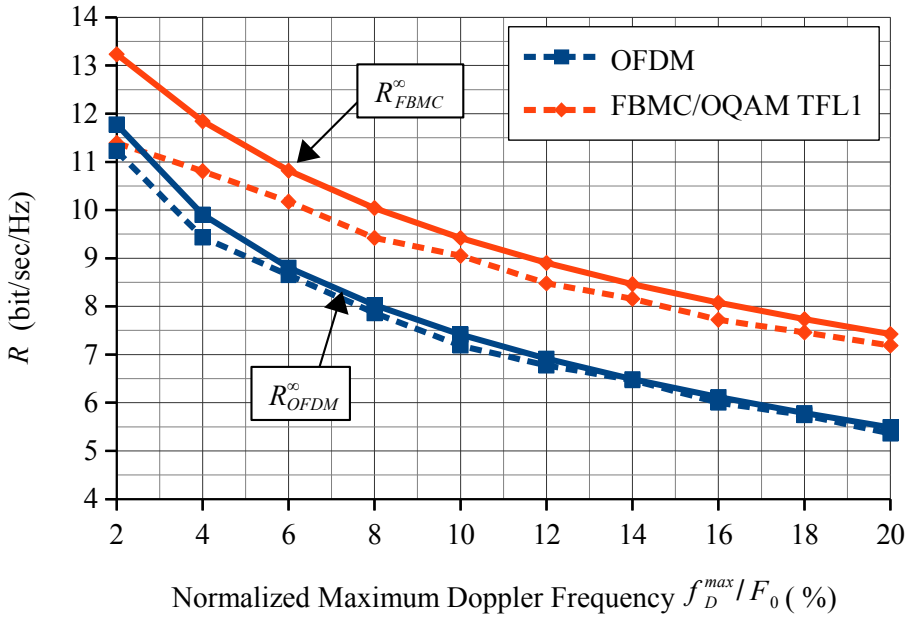

Figure 6.5: System capacity R as a function of the normalized maximum Doppler frequency f_D^{max}/F_0 with the RA4 channel model.

As the RA4 channel model presents a strong LOS component, the intrinsic interference due to the frequency selectivity of the channel is low ($\tau_{rms} = 126\ ns$) and the Doppler shift might impact the performance of the system. Therefore, Figure 6.5 shows that the FBMC/OQAM modulation offers a better robustness against the Doppler shift and always outperforms the OFDM modulation in this context even for low maximum Doppler frequency. In Figure 6.5, there is a gain of 2 bit/sec/Hz with the FBMC/OQAM modulation compared to the OFDM modulation when the normalized maximum Doppler frequency is equal to 20%. To conclude, thanks to its better robustness against the Doppler shift, the FBMC/OQAM modulation leads to the best performance in terms of system capacity on a channel model with a LOS component even for low maximum Doppler frequency.

6.4 Simulations: Comparison in Terms of BER

The simulation results in terms of system capacity presented previously are useful to validate the analytical results and to evaluate the impact of the Doppler effect for the OFDM and the FBMC/OQAM modulations. However, they do not give a precise idea about the performance of the systems in practice. Therefore, the BER is computed in this part with and without channel coding in order to visualize the performance of the studied massive MIMO system in practice. For these simulations, the parameters given by Table 6.2 are used. According to the previous results, the Phydyas4 prototype filter leads to the best performance in NLOS environments. However, its long length increases the complexity and induces a more important latency. Therefore, only the TFL1 prototype filter is considered in this part for the

Table 6.2: Simulation parameters for the comparison in terms of BER.

FFT size: M	1024
Number of useful sub-carriers	600
Inter-carrier spacing: F_0	15 kHz
CP duration for the OFDM modulation: T_{CP}	4.7 μs
Prototype filter for the FBMC/OQAM modulation	TFL1

FBMC/OQAM modulation.

6.4.1 NLOS Environment

The simulations are first carried out on the NLOS EVA and ETU channel models defined in [92, 93]. Their delays τ_l and corresponding average powers P_l are given in Appendix A.

BER Without Channel Coding

The BER is first computed without channel coding and with a 16QAM per sub-carrier modulation. The maximum Doppler frequency is arbitrary high in order to visualize the impact of the Doppler effect, meaning $f_D^{max} = 3000$ Hz. It corresponds to a normalized maximum Doppler frequency (f_D^{max}/F_0) equal to 20% and, according to (1.8), to a speed of $v = 540$ km/h with a central frequency of $F_c = 6$ GHz. Figures 6.6 and 6.7 give the results respectively for the EVA and ETU channel models. Additionally, the BER without channel coding of a SISO system on a Gaussian channel without mobility is also added on these Figures to serve as a baseline.

Firstly, by looking at Figures 6.6 and 6.7, one can see that the Doppler spread has a strong impact on the performance of the system when only one antenna is used on the receiver side (N_r= 1 antenna). Indeed, an error floor of approximately 7.10^{-2} (respectively 3.10^{-2}) appears for the OFDM modulation (respectively the FBMC/OQAM modulation). These results are in line with those of [30–33] as the FBMC/OQAM modulation leads to the best performance in a SISO system.

Then, as expected the increase of the number of receive antennas N_r induces a reduction of the impact of the Doppler spread (see Chapter 5) and thereby an improvement of the performance in terms of BER. Thus, when the number of antennas increases, the performance of the proposed system with mobility tends to the performance of a SISO system on a Gaussian channel without mobility. The impact of the Doppler spread is actually highly reduced even with a relatively low number of receive antennas. For example, when N_r= 16 antennas, there is no error floor neither for the OFDM modulation nor for the FBMC/OQAM modulation.

Finally, in a massive MIMO context with a very large number of receive antennas (for example N_r= 64 antennas), the two considered modulations lead to the same performance in terms of BER. Moreover, this performance is very close from the performance of a SISO

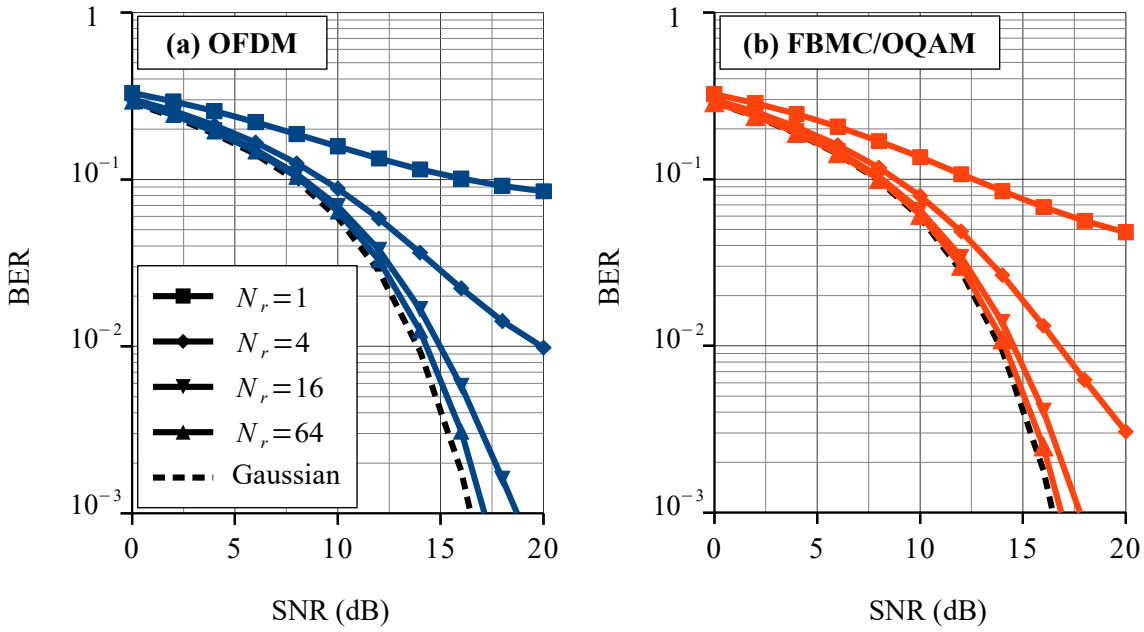

Figure 6.6: BER without channel coding as a function of the SNR with the EVA channel model. (a) The OFDM modulation is used. (b) The FBMC/OQAM modulation is used.

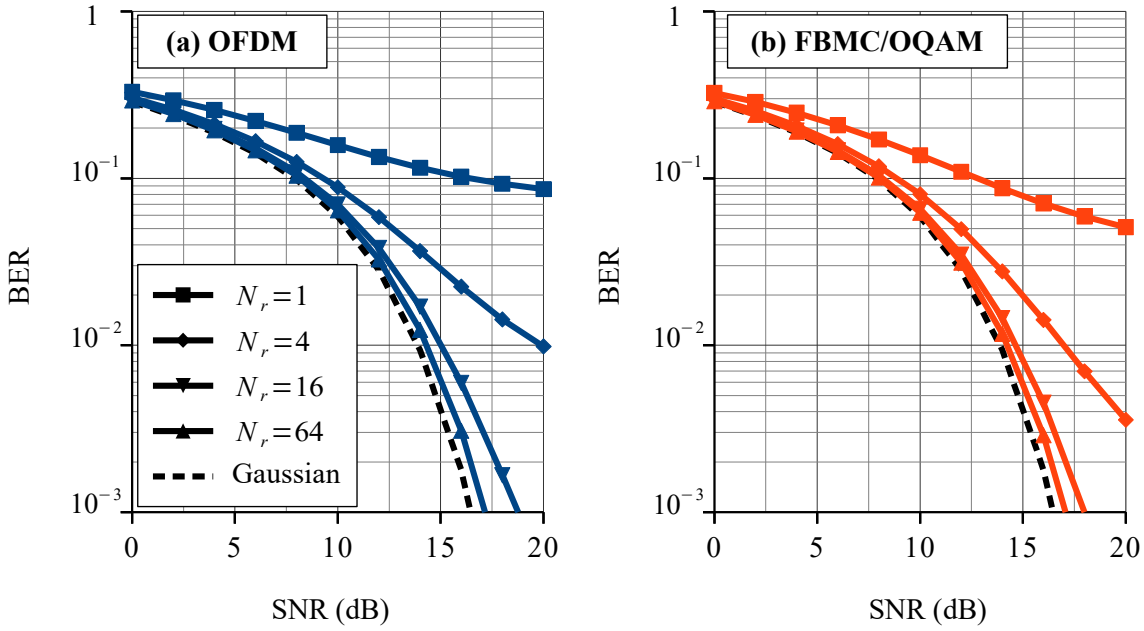

Figure 6.7: BER without channel coding as a function of the SNR with the ETU channel model. (a) The OFDM modulation is used. (b) The FBMC/OQAM modulation is used.

system on a Gaussian channel without mobility.

BER Error Floor

According to the previous results, the impact of the Doppler effect can be analyzed by knowing the value of the BER error floor. Therefore, this value is now computed as a function of the maximum Doppler frequency f_D^{max} for a 16QAM per sub-carrier modulation. Figures 6.8 and 6.9 give the results respectively for the EVA and ETU channel models.

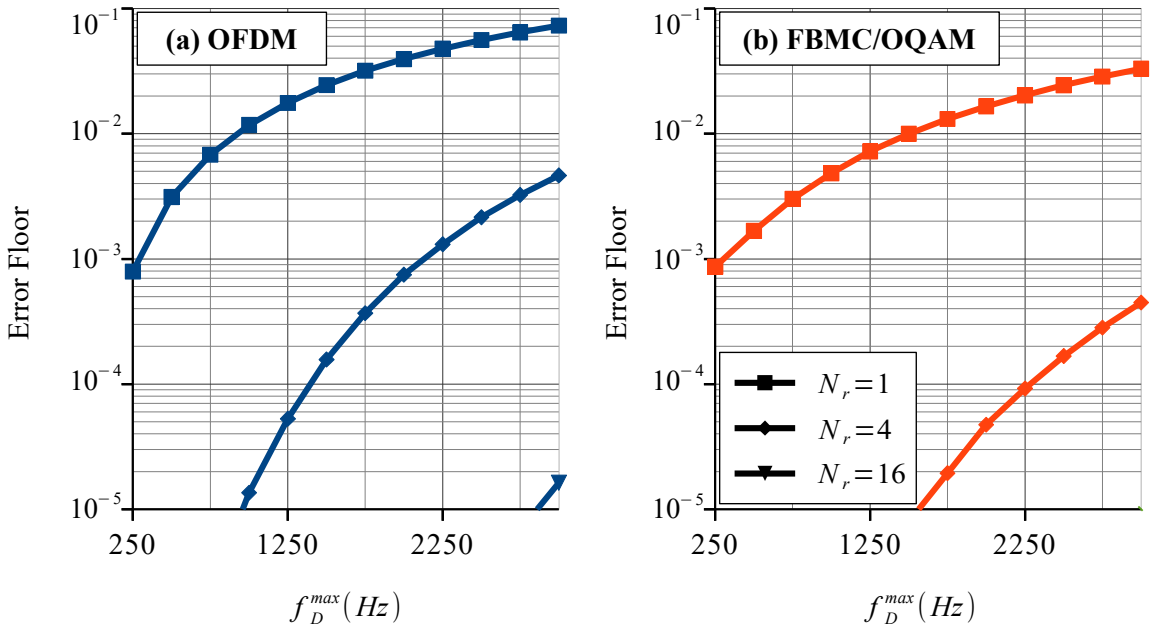

Figure 6.8: Error floor as a function of the maximum Doppler frequency f_D^{max} with the EVA channel model. (a) The OFDM modulation is used. (b) The FBMC/OQAM modulation is used.

On a SISO system (N_r= 1), the higher the maximum Doppler frequency f_D^{max}, the higher the impact of the Doppler effect and the higher the value of the error floor. For example, on the EVA channel model and with the OFDM modulation, the error floor of the system is multiply by 100 when the maximum Doppler frequency increases from 250 Hz to 3000 Hz. Therefore, when the speed of the user increases, the impact of the Doppler effect becomes rapidly important. In this context, the FBMC/OQAM modulation becomes interesting when the maximum Doppler frequency is high, as it leads to a lower error floor. These results are in line with these of [30–33].

As expected, increasing the number of receive antennas N_r induces a drastic reduction of the impact of the Doppler spread for the OFDM modulation and thus a drastic reduction of the value of the error floor. With N_r= 16 antennas and a maximum Doppler frequency of 3000 Hz, the error floor is of the order of 10^{-5} for the OFDM modulation on both the EVA and ETU channel models. This reduction is even more important with the FBMC/OQAM modulation. Indeed, with N_r= 16 antennas and a maximum Doppler frequency of 3000 Hz, the error floor is below 10^{-5} and does not appear on Figures 6.8 and 6.9. Therefore, using

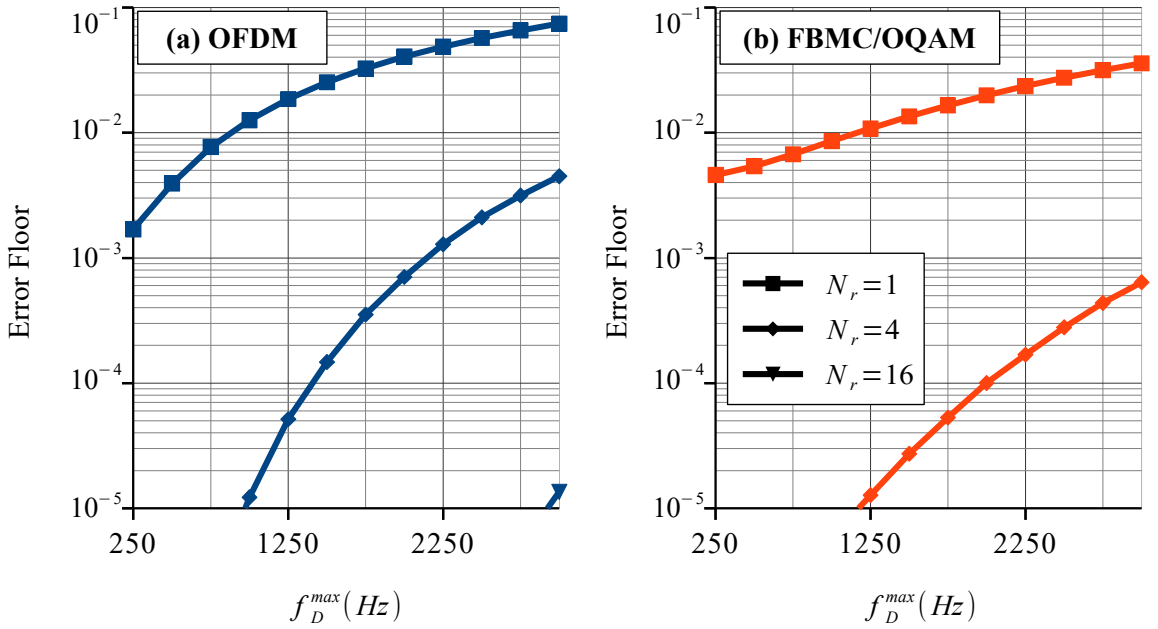

Figure 6.9: Error floor as a function of the maximum Doppler frequency f_D^{max} with the ETU channel model. (a) The OFDM modulation is used. (b) The FBMC/OQAM modulation is used.

a massive MIMO system with a simple MRC receiver allows for a drastic reduction of the impact of the Doppler spread even with a relatively low number of receive antennas. In this context, the performance of the OFDM modulation and the FBMC/OQAM modulation are comparable.

BER With Channel Coding

As a final contribution, the BER is now computed with channel coding in order to have a more precise idea about the performance of the systems in practice. This BER with channel coding is evaluated as a function of the SNR with a LTE turbo-code, a 64QAM per sub-carrier modulation and a coding rate of 0.75. Moreover, the maximum Doppler frequency is arbitrarily high and is set to 3000 Hz. Figures 6.10 and 6.11 give the results respectively for the EVA and ETU channel models. Additionally, the BER of a SISO system on a Gaussian channel without mobility is also added on these Figures to serve as a baseline.

The results are in line with the previous results and confirm the following points. The Doppler effect has a strong impact on the BER when a SISO system is considered. Indeed, one can see on Figures 6.10 and 6.11 that an error floor higher than 10^{-1} appears when only one antenna is considered, for both the OFDM and FBMC/OQAM modulations. Thanks to the reduction of the impact of the Doppler spread proved in Chapter 5, increasing the number of receive antennas N_r allows for a drastic improvement of the performance of the systems. Therefore, when N_r increases, the performance of the proposed system with mobility tends to the performance of a SISO system on a Gaussian channel without mobility. Moreover, it

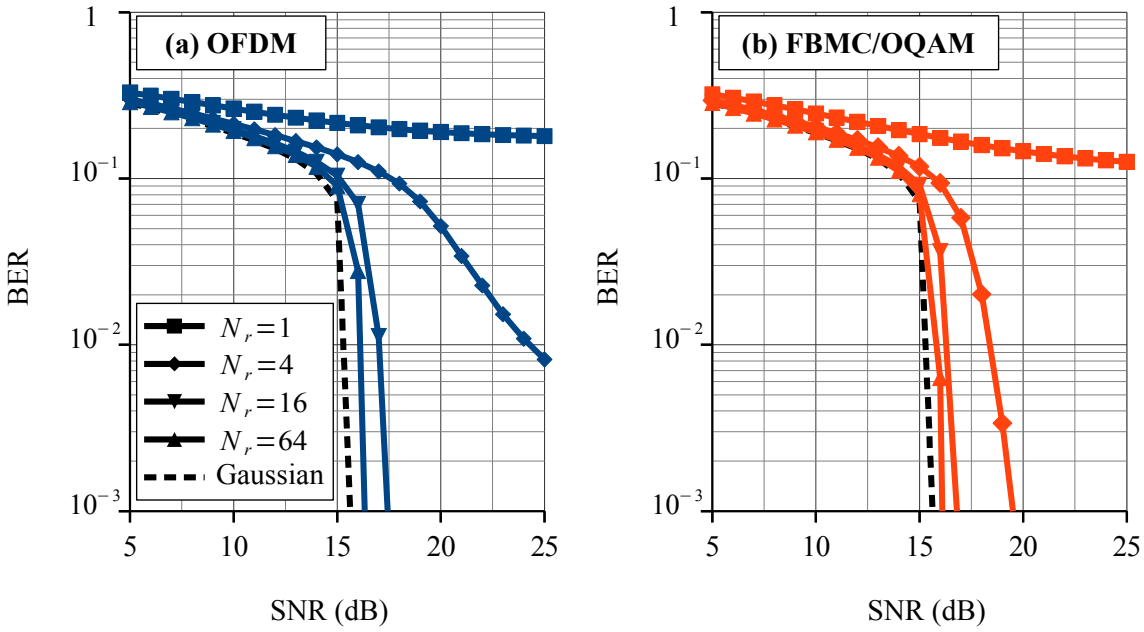

Figure 6.10: BER with channel coding as a function of the SNR with the EVA channel model. (a) The OFDM modulation is used. (b) The FBMC/OQAM modulation is used.

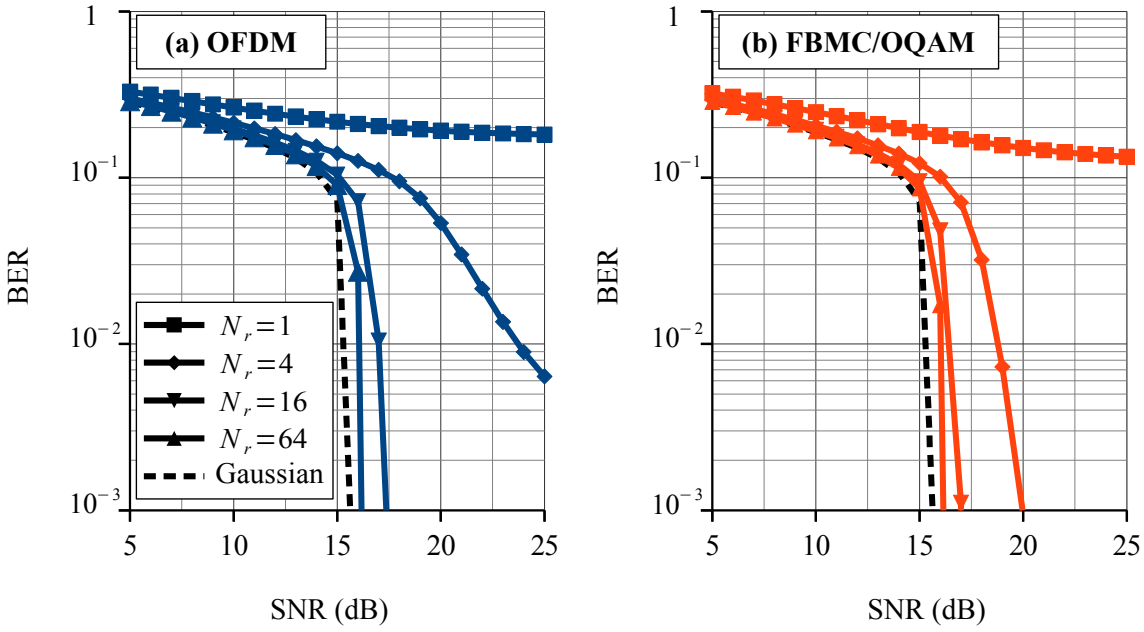

Figure 6.11: BER with channel coding as a function of the SNR with the ETU channel model. (a) The OFDM modulation is used. (b) The FBMC/OQAM modulation is used.

can be noticed that this reduction is actually greater with the FBMC/OQAM modulation when N_r increases. Finally, The impact of the Doppler spread is highly reduced even with a relatively low number of receive antennas and the results in Figures 6.10 and 6.11 show that the performance is very good with N_r= 16 receive antennas. In this context, the OFDM modulation and the FBMC/OQAM modulation lead to the same performance in terms of

BER with channel coding.

6.4.2 LOS Environment

The simulations are now conducted on a channel model with a LOS component, the RA4 channel model defined in [98]. Its delays τ_l and corresponding average powers P_l are given in Appendix A. Therefore, a Doppler shift quantified by the Doppler shift frequency f_D^{shift} adds to the Doppler spread in this context. For this channel model, the value of the Doppler shift frequency f_D^{shift} is proportional to the value of the maximum Doppler frequency f_D^{max}: $f_D^{shift} = 0.7 \times f_D^{max}$ [98]. Therefore, the Doppler effect can be quantified by the value of f_D^{max}.

BER Without Channel Coding

The BER is first computed without channel coding, with a 16QAM per sub-carrier modulation and with a maximum Doppler frequency f_D^{max} equal to 3000 Hz. Figure 6.12 gives the simulation results along with the BER of a SISO system on a Gaussian channel without mobility to serve as a baseline.

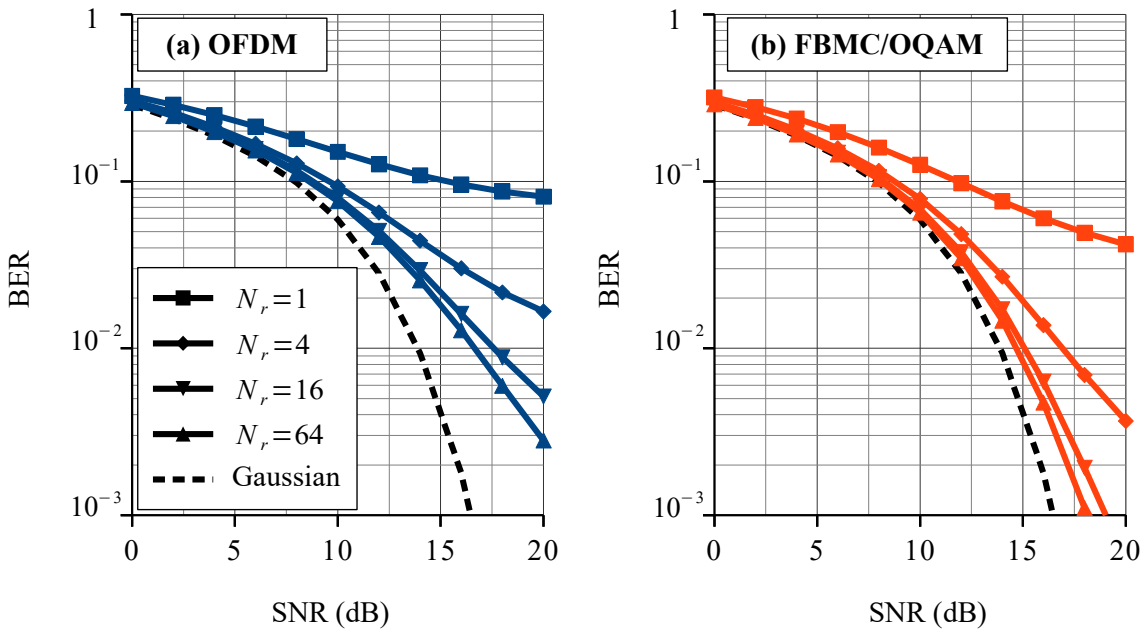

Figure 6.12: BER without channel coding as a function of the SNR with the RA4 channel model. (a) The OFDM modulation is used. (b) The FBMC/OQAM modulation is used.

In the presence of a LOS component, a Doppler shift adds to the Doppler spread. Figure 6.12 highlights the impact of a massive MIMO system on this Doppler shift component. As with the EVA and ETU channel models, the impact of the Doppler effect is important with $N_r = 1$ antenna and decreases with the increase of the number of receive antennas N_r. However, the Doppler shift still impacts the performance of the OFDM system even with a

very large number of receive antennas. Additionally, the FBMC/OQAM modulation offers a better robustness against the Doppler shift. Therefore, this modulation leads to a significant improvement of the BER compared to the OFDM modulation. Indeed, one can see on Figure 6.12 that a system combining the FBMC/OQAM modulation and N_r= 16 antennas outperforms a system combining the OFDM modulation and N_r= 64 antennas.

BER Error Floor

The BER error floor is now evaluated as a function of the maximum Doppler frequency f_D^{max} for a 16QAM per sub-carrier modulation. The results are given by Figure 6.13.

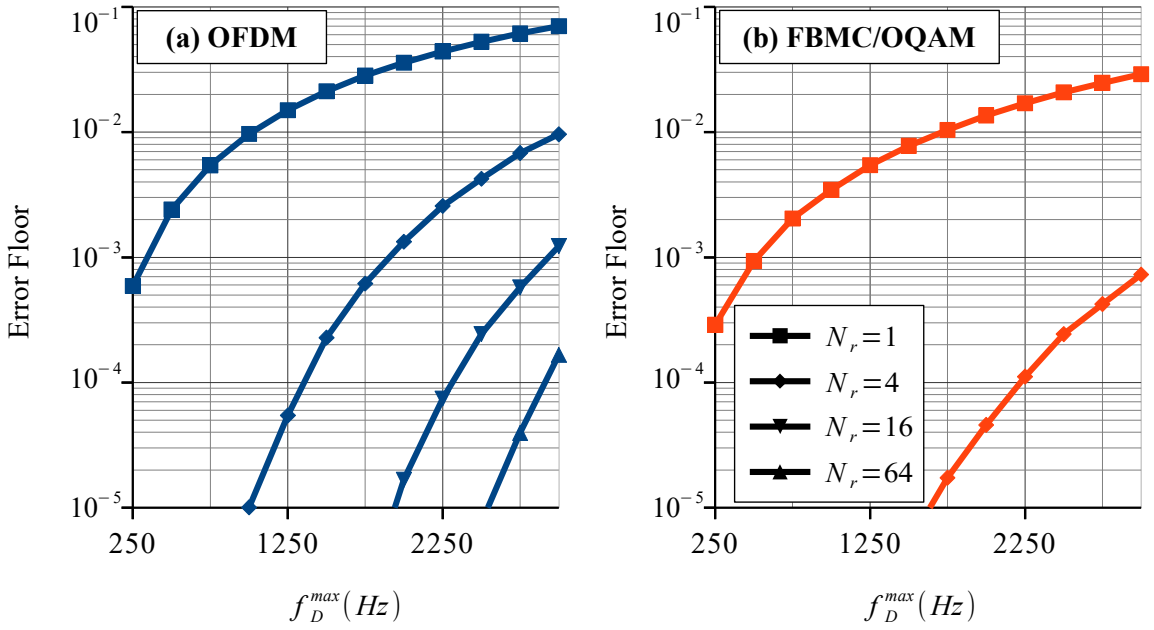

Figure 6.13: Error floor as a function of the maximum Doppler frequency f_D^{max} with the RA4 channel model. (a) The OFDM modulation is used. (b) The FBMC/OQAM modulation is used.

As on the NLOS channel models, the value of the error floor increases with the increase of the maximum Doppler frequency, but decreases with the increase of the number of receive antennas N_r. However, the Doppler shift induced by the LOS component of the RA4 propagation channel limits this reduction with the OFDM modulation. Indeed, with a maximum Doppler frequency of 3000 Hz and 64 receive antennas, the error floor is still above 10^{-4}. On the contrary, this Doppler shift does not seem to affect the FBMC/OQAM modulation and, with a maximum Doppler frequency of 3000 Hz and 16 receive antennas, the error floor is below 10^{-5} and does not appear in Figure 6.13. These results are in line with these of part 6.3.

BER With Channel Coding

Finally, the BER is computed with channel coding in order to have a more precise idea about the performance of the systems in practice. This BER with channel coding is evaluated as a function of the SNR with a LTE turbo-code, a 64QAM per sub-carrier modulation and a coding rate of 0.75. Moreover, the maximum Doppler frequency is set to 3000 Hz. Figures 6.14 gives the results along with the BER of a SISO system on a Gaussian channel without mobility to serve as a baseline.

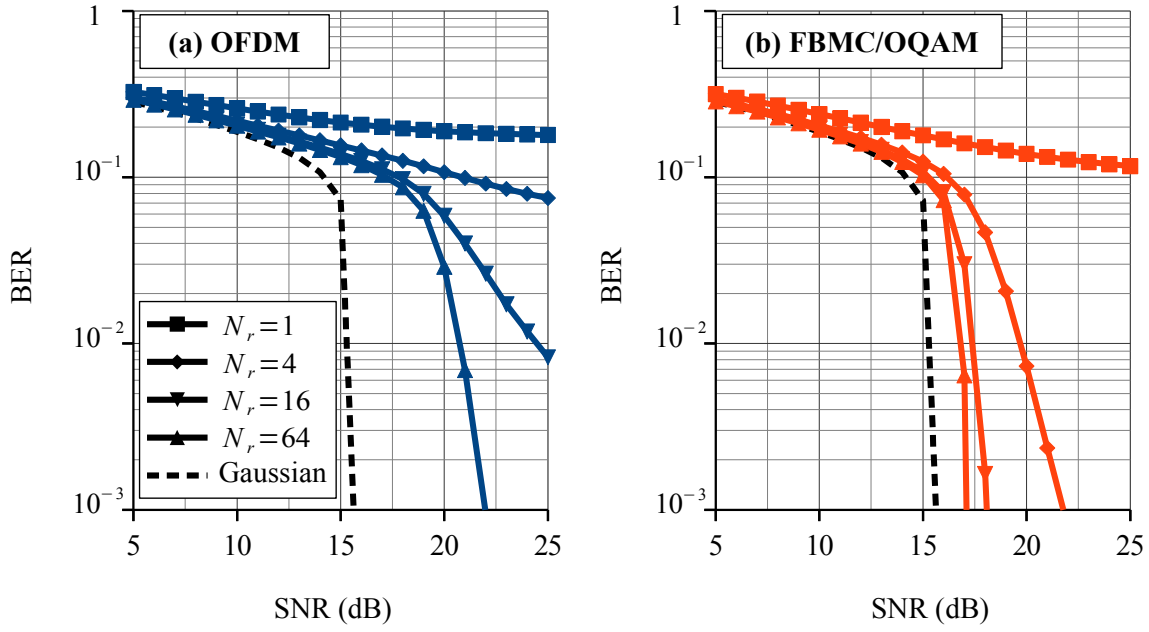

Figure 6.14: BER with channel coding as a function of the SNR with the RA4 channel model. (a) The OFDM modulation is used. (b) The FBMC/OQAM modulation is used.

The results are in line with the previous results and confirm the following points. The Doppler effect has a strong impact on the BER when a SISO system is considered. Indeed, one can see on Figure 6.14 that an error floor higher than 10^{-1} appears when only one antenna is considered, for both the OFDM and the FBMC/OQAM modulations. Moreover, this impact decreases with the increase of the number of receive antennas N_r as on NLOS propagation channels. However, the Doppler shift still impacts the performance of the OFDM system even with a very large number of receive antennas. Additionally, the FBMC/OQAM modulation offers a better robustness against the Doppler shift. Therefore, this modulation leads to a significant improvement of the BER compared to the OFDM modulation. Indeed, one can see on Figure 6.14 that a system combining the FBMC/OQAM modulation and N_r= 4 antennas outperforms a system combining the OFDM modulation and N_r= 64 antennas.

6.5 Conclusion

In Chapter 5, it is highlighted that the increase of the number of receive antennas in a massive MIMO uplink system with mobility allows for reducing the impact of the Doppler spread when an OFDM NLOS communication with a simple MRC receiver is considered. In this Chapter, both the OFDM modulation and the FBMC/OQAM modulation are considered with an eventual LOS component for the propagation channel.

Based on the system model defined in Chapter 4, the asymptotic value of the system capacity, when the number of receive antennas tends to infinity, has been analytically expressed for the OFDM modulation and for the FBMC/OQAM modulation. This study allows discussing the choice of the prototype filter for the FBMC/OQAM modulation and to conclude that a short prototype filter is preferable to counteract the impact of the Doppler effect. Moreover, simulation results are in line with the analytical expression of the asymptotic system capacity.

The simulations carried out in this Chapter aim at comparing the two considered modulations in terms of BER (with or without channel coding), in NLOS and LOS environments. In a NLOS environment, the impact of the Doppler effect is drastically reduced thanks to the reduction of the impact of the Doppler spread proved in Chapter 5. Therefore, the OFDM and the FBMC/OQAM modulations lead to similar performance in terms of BER. However, in a LOS environment, the Doppler shift highly impacts the performance of the OFDM modulation. Therefore, the FBMC/OQAM modulation leads to a significant improvement in terms of BER (with or without channel coding) compared to the OFDM modulation.

Summary of this Chapter:

- In a massive MIMO uplink system with mobility, **the asymptotic value of the system capacity, when the number of receive antennas tends to infinity, is analytically expressed** in this Chapter for the OFDM modulation and for the FBMC/OQAM modulation.
- **For the FBMC/OQAM modulation, the performance in terms of asymptotic system capacity depends on the length of the prototype filter**. On the one hand, **the shorter the prototype filter** the lower the interference due to the Doppler effect and thus, **the better the robustness against the time selectivity of the propagation channel**. On the other hand, **the longer the prototype filter**, the lower the intrinsic interference and thus, **the better the robustness against the frequency selectivity of the propagation channel**.
- In this Chapter, **simulations** are carried out in order to **compare the OFDM and the FBMC/OQAM modulations** in terms of **system capacity** and of **BER** (with or without channel coding), in **NLOS and LOS environments**.

- **In a NLOS environment**, the FBMC/OQAM modulation is always outperformed by the OFDM modulation in terms of system capacity because of its intrinsic interference. In terms of BER (with or without channel coding) the impact of the Doppler effect rapidly decreases thanks to the reduction of the impact of the Doppler spread proved in Chapter 5. Therefore, **the impact of the Doppler effect is negligible even with a relatively low number of receive antennas** (N_r= 16). Finally, **the performance of the two considered modulations are comparable** in terms of BER (with or without channel coding).

- **In a LOS environment**, the FBMC/OQAM modulation offers a better robustness against the Doppler shift and outperforms the OFDM modulation in terms of system capacity. In terms of BER (with or without channel coding), this **Doppler shift impacts the OFDM modulation even with a high number of receive antennas**. Therefore, **the FBMC/OQAM modulation leads to a significant improvement of the performance in terms of BER** (with or without channel coding) compared to the OFDM modulation.

Related Publications:

- A. Bazin, B. Jahan and M. Hélard, "Réduction de l'impact de l'effet Doppler dans un système OFDM grâce au « massive MIMO »," in *26th GRETSI Seminar*, September 2017.

- A. Bazin, B. Jahan and M. Hélard, "Impact of the Doppler effect on the capacity of massive MIMO uplink systems: OFDM versus FBMC/OQAM," in *24th International Conference on Telecommunications (ICT)*, May 2017.

Part III

Massive MIMO for Wireless BH

7 Context and System Model

7.1 Context of the Study

Mobile networks are constantly evolving and thus more and more people have access to the Internet. The development of 5G should boost this aspect. However, there are still inequalities regarding the ease of access to the Internet [99]. In low Average Revenue Per User (ARPU) areas, the deployment of the cellular network is by definition constrained by its cost, which slows down its development. In particular, the deployment of the links between the BSs and the core network, the BH links, is an expensive task when using a classical optical fiber communication [34]. Nevertheless, a wireless link between two BSs, the first one acting as a relay for the second one, avoids the use of an optical fiber between the core network and the second BS. Thereby, this wireless BH link can be an appropriate solution to reduce the cost in low ARPU networks [34]. In particular, it should be a long range link of several kilometers and it should provide a sufficient data rate in order to maintain a good quality of service. Moreover, an adaptive link is preferable in order to counteract the damage caused by weather conditions. For example, the wind can move the antennas and can deflect the BH beam [100].

Radio-relay technologies are classical solutions to provide long-range wireless links of typically tens of kilometers [101]. These technologies are well-known since the first radio relay link was built in 1934 [101]. However, this solution is not adaptive and is more likely impacted by weather conditions (rain, temperature, wind, etc.). Moreover, even if some radio-relay technologies can achieve a data rate above 1 Gbps, their usual capabilities in terms of data rate are rather limited. Finally, a radio relay link requires a dedicated frequency band subject to regulation, which induces additional costs. For these reasons, radio-relay technologies may not be the best solutions for wireless BH in low ARPU areas.

In order to cover several kilometers, the use of sub-6 GHz frequencies seems to be appropriate since they experience lower path loss than higher frequencies. However, under 6 GHz the frequency resources are very scarce and expensive, which eliminates the possibility

of using a dedicated frequency band for the BH. An interesting solution is therefore to use an in-band wireless BH, where the access links, between the BSs and the users, and the BH link use the same frequency band. The feasibility of such a solution was discussed in [102–107]. In these contributions, the authors multiplex the BH link and the access links in the time and frequency domains to avoid the spatial interference but at the price of a low spectral efficiency. They show that an in-band wireless BH is an interesting solution to improve the throughput of the cellular networks [102, 104–107] or to extend their coverage at a low cost [103].

Additionally, massive MIMO systems described in Chapter 3 are of particular interest. Indeed, combined with appropriate signal processing techniques, massive MIMO systems offer a substantial number of advantages. On the transmitter side, they are able to focus the energy in the space domain [19, 21], as shown in part 3.2. On the receiver side, they can increase the SINR [12, 15], as shown in part 3.1. More generally, massive MIMO systems are interesting solutions to provide SDMA and to improve the spectral and energy efficiency of the systems [13, 14]. For wireless BH, massive MIMO techniques are suitable as they are adaptive solutions able to counteract the damage caused by weather conditions. Moreover, by improving the SINR on the receiver side, they can provide high data rates. The feasibility and challenges of massive MIMO for wireless BH in 5G ultra dense networks was discussed in [108] in the context of millimeter waves communications. Additionally, in [108] the authors developed a new massive MIMO hybrid precoding/combining scheme to provide point-to-multipoint wireless BH links. However, a dedicated frequency band is used for the BH link in [108].

This Chapter considers an in-band wireless BH using a massive MIMO system in order to multiplex the BH link and the access links in the space domain. This solution allows an increase of the spectral efficiency compared to these attained in [102–107]. Such a system has been recently studied in [35–39] for small cells deployment in 5G networks. In these studies, the BH links are deployed to serve small cell BSs inside the coverage of a macro cell.

- In [35], the authors proposed a massive MIMO precoder on the BS side to provide an in-band wireless BH with the objective of maximizing the system throughput. Moreover, the massive MIMO precoder used on the BS side cancels the spatial interference on the small cell users.
- In [36], the massive MIMO precoder used on the BS side is designed to simultaneously handle the access links for macro cell users and the BH links for small cell BSs. In parallel, a reverse TDD scheme is used in order to avoid the spatial interference. It means that the uplink of the small cells happens during the downlink of the macro cell, and vice versa.
- In [37] and [38], the massive MIMO precoder on the BS side provides the BH links but does not control the potential spatial interference on the user side. Therefore, in order to improve the system capacity, they proposed a mix of in-band BH and out-of-band BH.

- In [39], the massive MIMO precoder on the BS side simultaneously handles the access links for macro cell users and the BH links for small cell BSs but is also designed to suppress the spatial interference for small cell users.

All these studies could be extended to the case of a long-range in-band wireless BH link, where the BH link serves a neighboring macro cell. However, they are subject to the following limitations.

- On the one hand, regarding the long distance between the two considered BSs in low ARPU networks, a very directive BH link is required and the use of highly directive antennas is preferable for this BH link. On the other hand, the access links need to cover the entire macro-cell and the antennas should not be too directive for these access links. Therefore, using the same massive MIMO antennas for the BH link and for the access links as in [36, 39] might not be adapted in the considered context.

- In general, the amount of data transmitted for the downlink is larger than the amount of data transmitted for the uplink. In a TDD scheme, it is thus preferable to have a longer time slot for the downlink than for the uplink. The reverse TDD scheme used in [36] imposes the same duration for the downlink and the uplink time slots. Therefore, the solution used in [36] is not suitable in the considered context and reduces the spectral efficiency of the system.

- Using the mix of in-band BH and out-of-band BH proposed in [37, 38] significantly reduces the spectral efficiency of the system as a dedicated frequency band is required for the out-of-band BH.

- The complete suppression of the interference on the user side as in [35, 39] induces a reduced received power on the receiving BS [19, 21]. This aspect is even more important regarding the long-range BH link studied in this Chapter.

Contribution of this Chapter:

In this Chapter, the system model defined in part 3.2 of Chapter 3 is modified in order to represent the particularities of the problem raised here. Unlike in [36, 39], the massive MIMO antenna arrays used in this Chapter are dedicated to the BH link and can be added on the top of the existing BSs. Thereby, these massive MIMO antenna arrays can use highly directive antennas, which is necessary in order to optimize the gain of the BH link. Moreover, the downlink of the BH link happens during the downlink of the access links. This solution is more adapted and more flexible than the reverse TDD scheme used in [36] as the time slot used for the downlink can be longer than the time slot used for the uplink. This Chapter is used as a basis for Chapters 8 and 9.

Contribution of Chapter 8:

In Chapter 8, a new massive MIMO precoding technique, called Regularized Zero Forcing with Controlled Interference (RZF-CI), is introduced to maximize the received power on the receiving BS, while limiting the interference power on the user side to a predetermined level. In order to evaluate the performance of the proposed RZF-CI precoder, an analytical comparison is carried out with the classical MRT precoder [64] described in part 3.2.2, which maximizes the received power but does not control the interference on the user side as in [37, 38], when the in-band BH is considered. Moreover the RZF-CI precoder is also analytically compared with the ZF precoder [73] described in part 3.2.2, which completely suppresses the interference on the user side as in [35, 39]. Finally, the performance of the proposed RZF-CI precoder is evaluated and compared to the MRT and the ZF precoders thanks to simulations for a realistic scenario using a GSCM.

Contribution of Chapter 9:

The results of Chapter 8 rely on the assumption of a strict time and frequency synchronization between the BH link and the access link. However, this assumption might not be feasible in a real system because of hardware limitations. Therefore, in Chapter 9, the impact of a time desynchronization between the access link and the BH link is studied. Additionally, the use of the FBMC/OQAM modulation for the BH link is also discussed in order to improve its spectral efficiency.

7.2 Scenario and System Model

The aim of this paper is to study the deployment of an in-band BH link between two neighboring macro cells. Part 7.2.1 provides details regarding the considered scenario. Then, the system model is defined in parts 7.2.2, 7.2.3 and 7.2.4 respectively for the propagation channel, the transmitters and the receivers.

7.2.1 Considered Scenario

As described by Figure 7.1, this Chapter considers two neighboring macro-cells, the cell 1 and the cell 2, which are respectively served by the BS 1 and the BS 2. In particular, the UEs of the cell 1 (respectively the cell 2) are served by the BS 1 (respectively the BS 2) via the access links. These access links are represented in Figure 7.1 by the solid green arrows and are provided by dedicated antennas on the BS 1 and on the BS 2, which are further called access antennas in this Chapter. For the BH links between the core network and the two BSs, two schemes can be considered. On the one hand, in the classical wired BH scheme

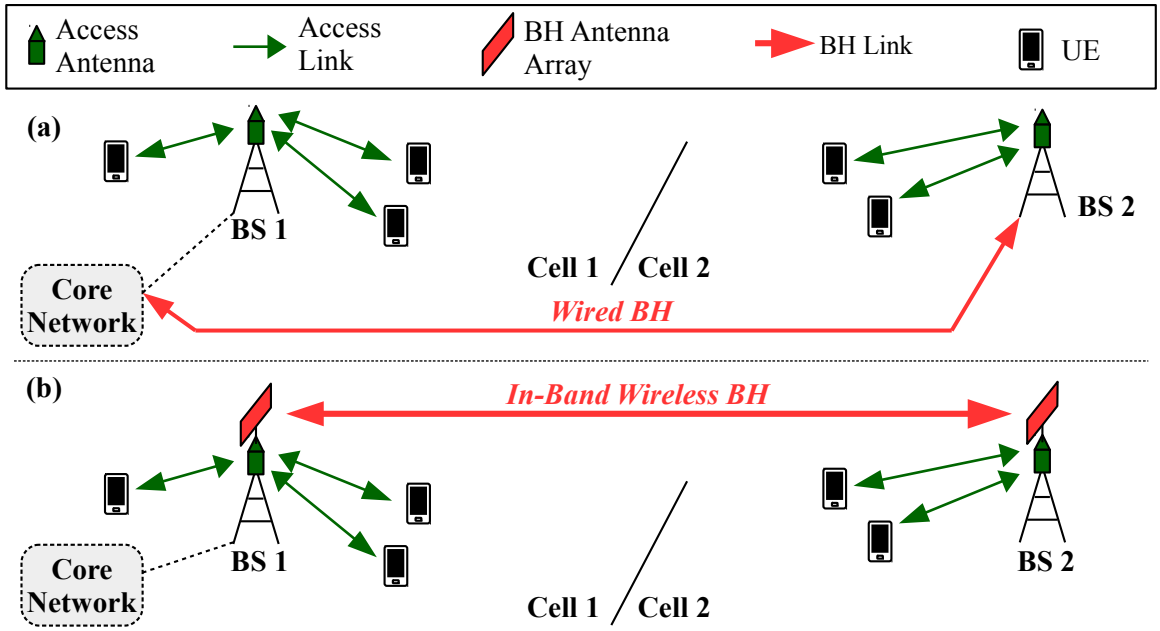

Figure 7.1: Scenario comparison between (a) a wired BH and (b) an in-band wireless BH.

illustrated in Figure 7.1 (a), both the BS 1 and the BS 2 are connected to the core network via wired BH links. On the other hand, in the in-band wireless BH scheme illustrated in Figure 7.1 (b), the BS 1 is connected to the core network via a wired BH link and acts as a relay for the BS 2 via a wireless BH link between the BS 1 and the BS 2. This wireless BH link is represented in Figure 7.1 (b) by the solid red arrow and is created thanks to massive MIMO antenna arrays added on the top of each BS, facing each other and further called BH antenna arrays. These massive MIMO antenna arrays are made of directive antennas and are thus adapted for the BH link as previously highlighted. In this Chapter, the second scheme illustrated by Figure 7.1 (b) is considered as a potential solution to reduce the cost of deployment.

It is a known fact that the channel estimation process in a massive MIMO system can be a complicated task when a FDD scheme is considered [13, 14, 23]. Therefore, a TDD system, which takes advantage of the channel reciprocity, is preferable for the considered scenario and is assumed in this Chapter. Moreover, the uplink and the downlink for the cell 1, for the cell 2 and for the BH are assumed to be synchronized as in [35–39]. As highlighted previously, the amount of data transmitted for the downlink is generally larger than the amount of data transmitted for the uplink. Therefore, unlike in [36], the same time slot is used for the downlink of the cell 1, the downlink of the cell 2 and the downlink of the BH, from the BS 1 to the BS 2. Similarly, the same time slot is used for the uplink of the cell 1, the uplink of the cell 2 and the uplink of the BH, from the BS 2 to the BS 1. This scheme is summarized by Figure 7.2, where the solid green arrows represent the access links and the solid red arrow represents the BH link.

The downlink of the considered TDD system is illustrated by Figure 7.2 (a). For the BH

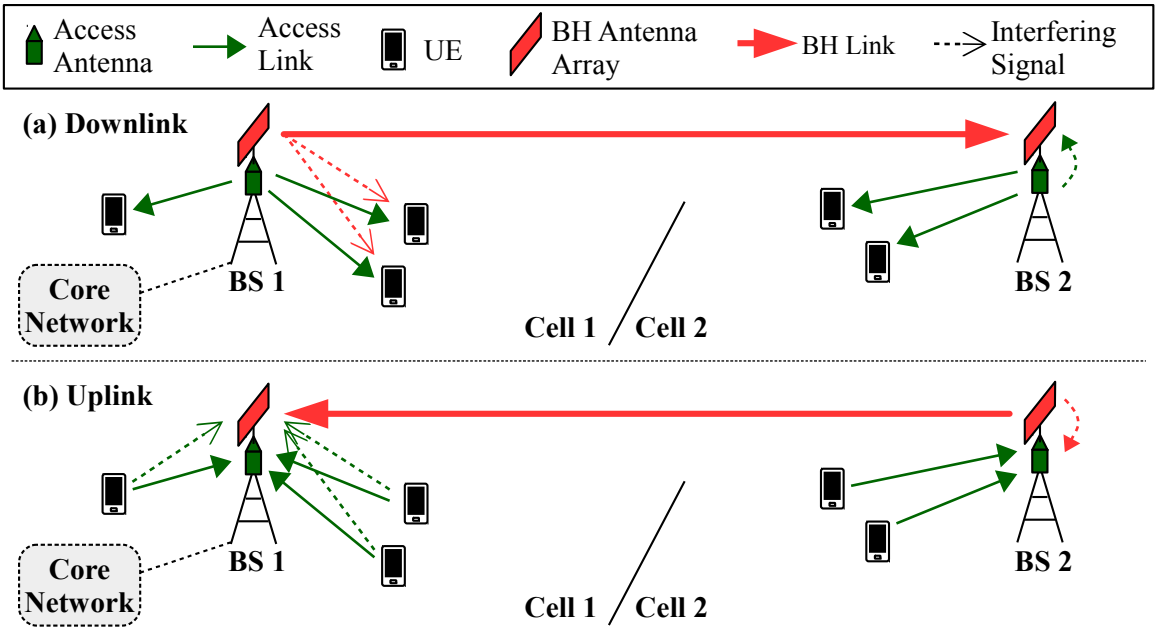

Figure 7.2: Description of (a) the downlink and (b) the uplink of the considered in-band wireless BH scenario.

link, a beam is created between the BH antenna array of the BS 1 and the BH antenna array of the BS 2 thanks to a massive MIMO precoding technique applied on the BH antenna array of the BS 1. However, this BH link uses the same frequency band as the access links and thus the secondary lobes of the created beam induce interfering signals between the BH antenna array of the BS 1 and part of the UEs. It is assumed in this Chapter that this interference is located near the BS 1 and thus only the UEs of the cell 1 are impacted. This assumption will be further verified through simulations in part 8.4 of the next Chapter. These interfering signals are represented by the dotted red arrows in Figure 7.2 (a). Additionally, the access antenna of the BS 2 sends data to the UEs of the cell 2, creating interfering signals on the BH antenna array of the BS 2. These interfering signals are represented by the dotted green arrow in Figure 7.2 (a).

The uplink of the considered scenario is illustrated by Figure 7.2 (b). For the BH link, a beam is created between the BH antenna array of the BS 2 and the BH antenna array of the BS 1 thanks to a massive MIMO precoding technique used on the BH antenna array of the BS 2. This transmission creates interfering signals on the access antenna of the BS 2. These interfering signals are represented by the dotted red arrow in Figure 7.2 (b). Additionally, the UEs of the cell 1 send data to the access antenna of the BS 1, creating interfering signals on the BH antenna array of the BS 1. These interfering signals are represented by the dotted green arrow in Figure 7.2 (b).

As in [37–39], this Chapter does not study the overall TDD system but focuses on the downlink of the considered scenario described by Figure 7.2 (a). In particular, the massive MIMO precoding technique used on the BH antenna array of the BS 1 is investigated. For

the rest of this Chapter, an OFDM modulation is used for the access and the BH links and the Frequency-Division Multiple-Access (FDMA) method is used to serve the UEs for the access links. Moreover, each sub-carrier is independently processed and the focus is put on a particular sub-carrier. Finally, single-antenna UEs are considered in this Chapter for the sake of simplicity.

7.2.2 Propagation Channel

The propagation channel for the considered scenario can be divided in three parts:

- the useful channel, between the two BH antenna arrays,
- the interference channel, between the BH antenna array of the BS 1 and the UEs of the cell 1,
- the access channel, between the access antenna of the BS 1 and the UEs of the cell 1.

They are defined more thoroughly thereafter.

Useful Channel

The propagation channel between the N_t antennas of the first BH antenna array and the N_r antennas of the second BH antenna array is further called the useful channel in this Chapter. It can be described by the $(N_r \times N_t)$ matrix $\sqrt{P'_U}\mathbf{H}'_U$, where P'_U is the path loss between the BH antenna array of the BS 1 and the BH antenna array of the BS 2. Unlike in Chapter 3, this path loss can be represented by a scalar instead of a matrix. Indeed, the distance between a given transmit antenna and a given receive antenna can be assumed as equal whatever the considered antennas and thus, the path loss does not depend on the considered antennas. Additionally, the matrix $\mathbf{H}'_U$ is defined by:

$$\mathbf{H}'_U = \left[\left(\mathbf{H}'^{0}_U\right)^T \quad \left(\mathbf{H}'^{1}_U\right)^T \quad \cdots \quad \left(\mathbf{H}'^{N_r-1}_U\right)^T \right]^T, \tag{7.1}$$

where $\mathbf{H}'^{n_r}_U$ is a $(1 \times N_t)$ vector, which defines the propagation channel between the N_t transmit antennas and the receive antenna of index n_r.

An important particularity of the useful propagation channel studied in this Chapter is that it is mainly characterized by a long distance and by a strong LOS component. Thanks to theoretical studies and measurement campaigns [109–111], it is a known fact that, with such a LOS propagation channel, the received signals on the BH antenna array of the BS 2 can be seen as plane waves and the channel matrix $\mathbf{H}'_U$ can be assumed to be of rank-1. These particularities lead to the following statements.

- While this massive MIMO system can improve the SNR thanks to its high number of antennas, with such a rank-1 channel matrix, no multiplexing gain can be expected.

- As the two BH antenna arrays are facing each other, the received plane waves are coplanar with the BH antenna array of the BS 2. Therefore, the propagation channel is considered to be the same whatever the receive antenna, meaning:

$$\mathbf{H}_U'^{n_r} = \mathbf{H}_U'^{n_r'} = \mathbf{H}_U \quad \forall (n_r, n_r') \in [0, N_r - 1]^2. \tag{7.2}$$

According to these statements, the definition of the useful channel can be simplified. In particular, the system model does not consider the full massive MIMO channel matrix $\mathbf{H}_U'$ but only the $(1 \times N_t)$ MISO channel vector $\mathbf{H}_U$:

$$\mathbf{H}_U = \begin{bmatrix} H_U^0 & H_U^1 & \cdots & H_U^{N_t-1} \end{bmatrix}, \tag{7.3}$$

with:

$$E\left[|H_U^{n_t}|^2\right] = 1, \tag{7.4}$$

as in (2.17).

Interference Channel

As the FDMA method is used for the access links, at most one UE is impacted by the BH link on the considered sub-carrier. Moreover, as the UEs are equipped with a single antenna, the propagation channel between the BH antenna array of the BS 1 and the impacted UE is defined by a vector of size $(1 \times N_t)$ and denoted by $\sqrt{P_I}.\mathbf{H}_I$. P_I is the path loss of this channel and $\mathbf{H}_I$ is defined by:

$$\mathbf{H}_I = \begin{bmatrix} H_I^0 & H_I^1 & \cdots & H_I^{N_t-1} \end{bmatrix}, \tag{7.5}$$

with:

$$E\left[|H_I^{n_t}|^2\right] = 1, \tag{7.6}$$

as in (2.17). This propagation channel is further called the interference channel in this Chapter.

Access Channel

The propagation channel between the access antenna of the BS 1 and the impacted UE is further called the access channel in this Chapter. It is denoted by the complex scalar $\sqrt{P_{Acc}}.H_{Acc}$ with P_{Acc} the path loss of this channel and with:

$$E\left[|H_{Acc}|^2\right] = 1, \tag{7.7}$$

as in (2.17).

7.2.3 Transmitters

For the proposed scenario, two transmitters are considered: the BH antenna array of the BS 1 and the access antenna of the BS 1.

BH Antenna Array of the BS 1

As the channel matrix $\mathbf{H}'_U$ is a rank-1 channel matrix, only one symbol per channel use is sent from the BS 1 to the BS 2. In particular, on the considered sub-carrier, the data c of variance σ_c^2 is sent towards the BH antenna array of the BS 2. This transmission is realized using the precoder described by the vector $\mathbf{W}_U$ of size $(N_t \times 1)$. Therefore, according to (3.17), the vector of precoded data is defined by:

$$\mathbf{x}_{BH} = \begin{bmatrix} x_{BH}^0 & x_{BH}^1 & \cdots & x_{BH}^{N_t-1} \end{bmatrix}^T = \frac{\mathbf{W}_U}{\sqrt{\xi_W}} c, \tag{7.8}$$

where:

$$\mathbf{W}_U = \begin{bmatrix} W_U^0 & W_U^1 & \cdots & W_U^{N_t-1} \end{bmatrix}^T, \tag{7.9}$$

and where $\xi_W = \|\mathbf{W}_U\|^2$ is the instantaneous power normalization factor, which is necessary to keep a total transmit power equal to σ_c^2.

Access Antenna of the BS 1

The access antenna of the BS 1 sends the data x_{Acc} dedicated to a UE of the cell 1. This transmission is assumed to be synchronous with the BH transmission.

7.2.4 Receivers

Two receivers are considered in the system: the BH antenna array of the BS 2 and the UE of the cell 1 served on the considered sub-carrier.

BH Antenna Array of the BS 2

On the BH antenna array of the BS 2, the received data on the antenna n_r coming from the BH antenna array of the BS 1 is, according to (7.2):

$$y_{BH}^{U,n_r} = \sqrt{P'_U} \mathbf{H}_U . \mathbf{x}_{BH}. \tag{7.10}$$

Therefore, it comes:

$$y_{BH}^{U,n_r} = y_{BH}^{U,n'_r} \ \ \forall (n_r, n'_r) \in [0, N_r - 1]^2, \tag{7.11}$$

and the received useful signal is approximately the same whatever the considered receive antenna.

Additionally, there is an interference component coming from the access antenna of the BS 2. On the antenna n_r, this interference component is denoted by y_{BH}^{I,n_r}. Finally, the noise component on the antenna n_r is denoted by $b_{BH}^{n_r}$.

In this Chapter, the MRC technique defined in part 3.1.2 is used on the BH antenna array of the BS 2 because of its low complexity, as explained thereafter. Indeed, it does not need to know the propagation channel between the access antenna of the BS 2 and the BH antenna array of the BS 2. Moreover, according to (7.11), the received useful signals on the BH antenna array of the BS 2 are similar whatever the considered antenna. Therefore, the received useful signals arrive consistently and the MRC combiner only consists in adding all the received signals in order to maximize the received useful power.

After adding all the received signals, the received data y_{BH} on the BH antenna array of the BS 2 is defined as follows:

$$y_{BH} = y_{BH}^{U} + y_{BH}^{I} + b_{BH}. \tag{7.12}$$

In (7.12), the noise component of variance $\sigma_{b,BH}^2$ is:

$$b_{BH} = \sum_{n_r=0}^{N_r-1} b_{BH}^{n_r}, \tag{7.13}$$

and the interference component coming from the access antenna of the BS 2 is:

$$y_{BH}^{I} = \sum_{n_r=0}^{N_r-1} y_{BH}^{I,n_r}. \tag{7.14}$$

Moreover, according to (7.10), the received useful signal coming from the BH antenna array of the BS 1 is:

$$y_{BH}^{U} = \sum_{n_r=0}^{N_r-1} y_{BH}^{U,n_r} = Nr.\sqrt{P'_U}.\mathbf{H}_U.\mathbf{x}_{BH} = \sqrt{P_U}.\mathbf{H}_U.\mathbf{x}_{BH}, \tag{7.15}$$

with:

$$P_U = N_r^2.P'_U. \tag{7.16}$$

Therefore, according to (7.8), it comes:

$$y_{BH}^{U} = \sqrt{P_U}\frac{\mathbf{H}_U\mathbf{W}_U}{\sqrt{\xi_W}}c. \tag{7.17}$$

In (7.15), the signals y_{BH}^{U,n_r} add up consistently, while the noise components $b_{BH}^{n_r}$ in (7.13) and the interference components y_{BH}^{I,n_r} in (7.14) add up in a non-consistent way. Thus, the MRC

technique used in this Chapter allows increasing the SINR on the BH antenna array of the BS 2 for a very low complexity.

UE of cell 1

On the UE side, the UE antenna receives the useful data from the access antenna y^U_{Acc} defined as follows:

$$y^U_{Acc} = \sqrt{P_{Acc}}.H_{Acc}.x_{Acc}. \tag{7.18}$$

However, it also receives the interfering data y^I_{Acc} coming from the BH antenna array of the BS 1 and defined by:

$$y^I_{Acc} = \sqrt{P_I}.\mathbf{H}_I.\mathbf{x}_{BH}, \tag{7.19}$$

and thus, according to (7.8):

$$y^I_{Acc} = \sqrt{P_I}\frac{\mathbf{H}_I\mathbf{W}_U}{\sqrt{\xi_W}}c. \tag{7.20}$$

The received signal y_{Acc} is thus defined as follows:

$$y_{Acc} = y^U_{Acc} + y^I_{Acc} + b_{Acc}, \tag{7.21}$$

where b_{Acc} is the noise component of variance $\sigma^2_{b,Acc} = \sigma^2_b$.

The system model for the considered scenario is illustrated by Figure 7.3.

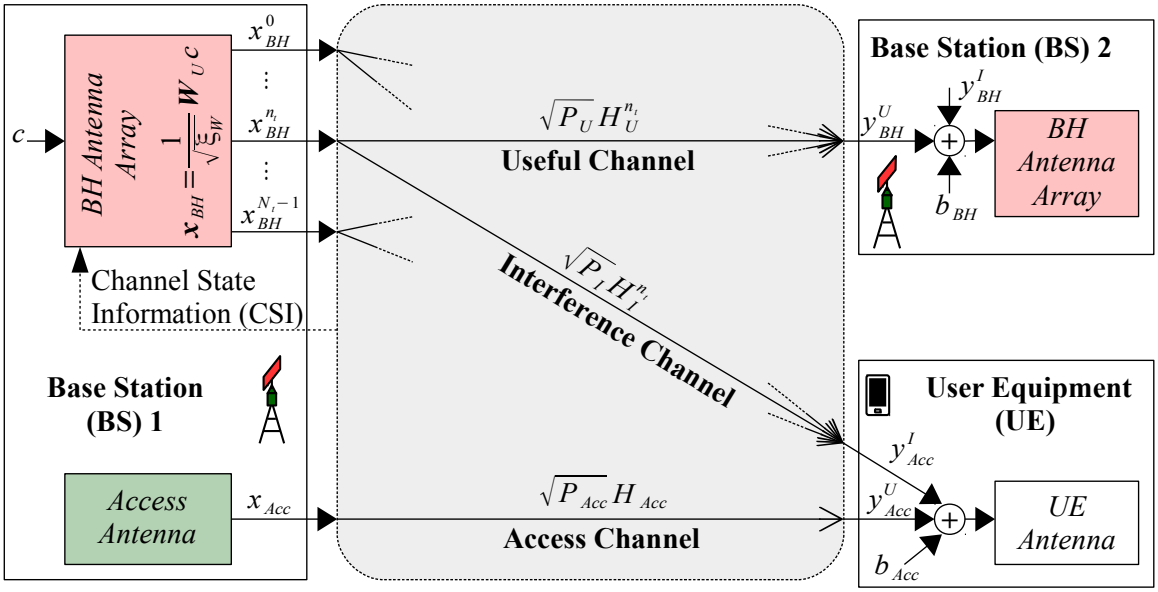

Figure 7.3: System model for an in-band wireless BH transmission.

Summary of this Chapter:

- The **context of the study** is described in this Chapter. An **in-band wireless BH**

is proposed in order to **enhance the coverage of the cellular networks at a low cost in low ARPU areas**. Moreover, a **massive MIMO system** is **dedicated to the BH link**. It allows **multiplexing the BH link and the access links in the space domain**.

- The **scenario** of the proposed system is described. In particular, the **downlink of a TDD scheme** is considered.
- The **system model** of the considered scenario is also described. It **takes into account the particularities of the propagation channel** between the two antenna arrays used for the BH link: a **long distance** and a **strong LOS component**.

8

New Precoder for Long Range In-Band Wireless Backhaul (BH)

In wide underserved areas or low ARPU areas, the deployment of the network is highly constrained in terms of cost. In the previous Chapter, massive MIMO systems were introduced as a potential solution to provide a long-range in-band wireless BH link and thus to extend the coverage in low ARPU networks at a low cost. Additionally, the downlink system model of Chapter 3 was modified in order to represent the particularities of the problem raised.

This Chapter focuses on the precoding techniques associated with the proposed massive MIMO system. In particular, based on the system model of Chapter 7 and on the problem statement of part 8.1, a new precoding technique, called RZF-CI, is presented in part 8.2 along with some state-of-the-art precoding techniques. The proposed RZF-CI precoder aims at controlling the interference on the user side unlike in [37, 38], when the in-band BH is considered. Moreover, it does not completely suppress the interference on the user side unlike in [35,39]. Thereby, the received power on the receiving BS might be increased. The proposed precoder is then evaluated thanks to an analytical study in part 8.3 and to simulations in part 8.4. Finally, a conclusion is drawn in the last part.

8.1 Problem Statement

According to (7.21), the SNR on the UE side is defined by:

$$\rho = \frac{\left|y^U_{Acc}\right|^2}{\sigma_b^2}, \tag{8.1}$$

while the SINR is defined as follows:

$$\gamma = \frac{\left|y^U_{Acc}\right|^2}{\left|y^I_{Acc}\right|^2 + \sigma_b^2}. \tag{8.2}$$

In order to evaluate the damage caused by the BH link on the UE side, the metric Δ is defined as follows:

$$\Delta \;=\; \frac{\rho}{\gamma} \;=\; \frac{\left|y^I_{Acc}\right|^2 + \sigma_b^2}{\sigma_b^2} \;=\; 1 + \frac{\left|y^I_{Acc}\right|^2}{\sigma_b^2}, \tag{8.3}$$

or equivalently, according to (7.20):

$$\Delta \;=\; 1 + \frac{\left|\mathbf{H}_I\mathbf{W}_U\right|^2}{\xi_W}\frac{P_I\sigma_c^2}{\sigma_b^2}. \tag{8.4}$$

Therefore, $\Delta \geq 1$ and the higher the value of Δ, the bigger the detrimental impact of the BH link on the UE side.

In order to limit the damage caused by the BH link, the value Δ must be under a given value Δ_{max}. The value of Δ_{max} is set on the BS 1 side. It can be either small enough to consider a negligible impact of the BH link or chosen depending on the quality of service required for the impacted UE. As the system capacity on the UE side is equal to:

$$R_{UE} = E\left[\log_2\left(1+\gamma\right)\right], \tag{8.5}$$

keeping Δ under Δ_{max} induces a guaranteed minimum system capacity R^{min}_{UE} given by:

$$R^{min}_{UE} = \log_2\left(1 + \frac{1}{\Delta_{max}}\rho\right). \tag{8.6}$$

On the BH antenna array of the BS 2, the system capacity of the BH link is equal to:

$$R_{BH} = E\left[\log_2\left(1 + \frac{\left|y^U_{BH}\right|^2}{\left|y^I_{BH}\right|^2 + \left|b_{BH}\right|^2}\right)\right]. \tag{8.7}$$

While the precoder design has no impact on the interference power $|y^I_{BH}|^2$ or the noise power $|b_{BH}|^2$, it can increase the system capacity of the BH link R_{BH} by increasing the useful power $|y^U_{BH}|^2$. According to (7.17), the received useful power on the BS 2 is defined by:

$$\left|y^U_{BH}\right|^2 = P_U\sigma_c^2\frac{\left|\mathbf{H}_U\mathbf{W}_U\right|^2}{\xi_W}. \tag{8.8}$$

Moreover:

$$\left|y^U_{BH}\right|^2 \leq \left|\|\mathbf{H}_U\|.\frac{\|\mathbf{W}_U\|}{\sqrt{\xi_W}}\right|^2 \times P_U\sigma_c^2, \tag{8.9}$$

and as $(\|\mathbf{W}_U\|^2/\xi_W) = 1$, it comes:

$$\left|y^U_{BH}\right|^2 \leq \left(P_U\|\mathbf{H}_U\|^2\right) \times \sigma_c^2. \tag{8.10}$$

The problem addressed in this Chapter can therefore be posed as follows:

$$\begin{array}{ll} \underset{\mathbf{W}_U \in \mathbb{C}^{N_t}}{\text{maximize}} & \left| y_{BH}^{U} \right|^2 \\ \text{subject to} & \Delta \leq \Delta_{max}. \end{array} \tag{8.11}$$

Equivalently, using (8.8), (8.4) and as $\xi_W = \|\mathbf{W}_U\|^2$, the problem (8.11) is equivalent to:

$$\begin{array}{ll} \underset{\mathbf{W}_U \in \mathbb{C}^{N_t}}{\text{maximize}} & \dfrac{|\mathbf{H}_U \mathbf{W}_U|^2}{\|\mathbf{W}_U\|^2} \\ \text{subject to} & \dfrac{|\mathbf{H}_I \mathbf{W}_U|^2}{\|\mathbf{W}_U\|^2} \leq \dfrac{\sigma_b^2}{P_I \sigma_c^2} \left(\Delta_{max} - 1 \right). \end{array} \tag{8.12}$$

By setting $\mathbf{W}'_U = \mathbf{W}_U / \|\mathbf{W}_U\|$, the problem (8.12) can be rewritten as follows:

$$\begin{array}{ll} \underset{\mathbf{W}'_U \in \mathbb{C}^{N_t}}{\text{minimize}} & -|\mathbf{H}_U \mathbf{W}'_U|^2 \\ \text{subject to} & |\mathbf{H}_I \mathbf{W}'_U|^2 \leq \dfrac{\sigma_b^2}{P_I \sigma_c^2} \left(\Delta_{max} - 1 \right) \\ \text{and} & \|\mathbf{W}'_U\|^2 = 1. \end{array} \tag{8.13}$$

In the problem (8.13), the objective function $-|\mathbf{H}_U \mathbf{W}'_U|^2$ is a concave function, the function $|\mathbf{H}_I \mathbf{W}'_U|^2$ in the inequality constraint is a convex function and the function $\|\mathbf{W}'_U\|^2$ in the equality constraint is a convex function. To the best of the authors' knowledge, the problem (8.13) does not describe a classical optimization problem and, in particular, is a non-convex optimization problem [112]. In this Chapter, we decide to simplify this problem. To this end, the use of a RZF precoding structure is proposed in the next part as in [73].

8.2 Studied Precoding Techniques

The presented precoding techniques are derived from the Multi-User Multiple-Input Multiple-Output (MU-MIMO) precoding matrices defined in [21, 73]. Indeed, our system can be seen as a MU-MIMO system with 2 users, where the data $c_{BH} = c$ is sent to the BH antenna array of the BS 2 and the data $c_{UE} = 0$ is sent to the UE. The ($N_t \times 2$) precoding matrix $\mathbf{W}$ is defined as follows:

$$\mathbf{W} = \begin{bmatrix} \mathbf{W}_U & \mathbf{W}_I \end{bmatrix}, \tag{8.14}$$

with $\mathbf{W}_I$ being the ($N_t \times 1$) precoding vector intended to send the data c_{UE}. Additionally, the ($2 \times N_t$) channel matrix $\mathbf{H}$ is described as follows:

$$\mathbf{H} = \begin{bmatrix} \mathbf{H}_U^T & \mathbf{H}_I^T \end{bmatrix}^T. \tag{8.15}$$

Finally, the correlation factor Γ_H is defined by:

$$\Gamma_H = \frac{\mathbf{H}_I}{\|\mathbf{H}_I\|}.\frac{\mathbf{H}_U^H}{\|\mathbf{H}_U\|}, \tag{8.16}$$

and thus $0 \leq |\Gamma_H| \leq 1$. This correlation factor reflects the correlation between the useful channel $\mathbf{H}_U$ and the interference channel $\mathbf{H}_I$ so that the higher the value of $|\Gamma_H|$, the higher the correlation between $\mathbf{H}_U$ and $\mathbf{H}_I$.

In this part, three precoding techniques are introduced: the MRT and ZF precoders as well as the proposed RZF-CI precoder.

8.2.1 Maximum Ratio Transmission (MRT)

The MRT precoder [64] is intended to maximize the received power without controlling the MUI, as in [37, 38]. It is defined as follows for MU-MIMO systems:

$$\mathbf{W} = \mathbf{H}^H. \tag{8.17}$$

As $\xi_W = \|\mathbf{W}_U\|^2$ and according to (8.14) and (8.15), the precoding vector for wireless BH can be written as follows:

$$\begin{cases} \mathbf{W}_U &= \dfrac{\mathbf{H}_U^H}{\|\mathbf{H}_U\|}, \\ \\ \xi_W &= 1. \end{cases} \tag{8.18}$$

8.2.2 Zero Forcing (ZF)

The ZF precoder is designed to suppress the MUI, as in [35,39], and is defined by the following matrix:

$$\mathbf{W} = \mathbf{H}^H \left(\mathbf{H}\mathbf{H}^H\right)^{-1}, \tag{8.19}$$

for MU-MIMO systems. The inversion of a (2×2) matrix $\mathbf{A}$ gives:

$$\mathbf{A}^{-1} = \frac{1}{det(\mathbf{A})} adj(\mathbf{A}), \tag{8.20}$$

where $det(\mathbf{A})$ is the determinant of $\mathbf{A}$ and $adj(\mathbf{A})$ is the adjugate matrix of $\mathbf{A}$. Therefore, according to (8.15) and (8.16), it simply comes:

$$\mathbf{H}\mathbf{H}^H = \begin{bmatrix} \|\mathbf{H}_U\|^2 & \left(\mathbf{H}_I\mathbf{H}_U^H\right)^* \\ \mathbf{H}_I\mathbf{H}_U^H & \|\mathbf{H}_I\|^2 \end{bmatrix} = \|\mathbf{H}_U\| \, \|\mathbf{H}_I\| \begin{bmatrix} \dfrac{\|\mathbf{H}_U\|}{\|\mathbf{H}_I\|} & \Gamma_H^* \\ \Gamma_H & \dfrac{\|\mathbf{H}_I\|}{\|\mathbf{H}_U\|} \end{bmatrix}, \tag{8.21}$$

and (8.20) gives:

$$\begin{aligned}\left(\mathbf{H}\mathbf{H}^H\right)^{-1} &= \frac{\|\mathbf{H}_U\|\,\|\mathbf{H}_I\|}{det\left(\mathbf{H}\mathbf{H}^H\right)}\begin{bmatrix}\frac{\|\mathbf{H}_I\|}{\|\mathbf{H}_U\|} & -\Gamma_H^* \\ -\Gamma_H & \frac{\|\mathbf{H}_U\|}{\|\mathbf{H}_I\|}\end{bmatrix} \\ &= \frac{\|\mathbf{H}_U\|\,\|\mathbf{H}_I\|^2}{det\left(\mathbf{H}\mathbf{H}^H\right)}\begin{bmatrix}\frac{1}{\|\mathbf{H}_U\|} & -\frac{\Gamma_H^*}{\|\mathbf{H}_I\|} \\ -\frac{\Gamma_H}{\|\mathbf{H}_I\|} & \frac{\|\mathbf{H}_U\|}{\|\mathbf{H}_I\|^2}\end{bmatrix}.\end{aligned} \tag{8.22}$$

Therefore, as $\xi_W = \|\mathbf{W}_U\|^2$ and according to (8.14) and (8.15), the precoding vector for wireless BH can be written as follows:

$$\begin{cases}\mathbf{W}_U &= \frac{\mathbf{H}_U^H}{\|\mathbf{H}_U\|} - \Gamma_H\frac{\mathbf{H}_I^H}{\|\mathbf{H}_I\|}, \\ \xi_W &= 1 - |\Gamma_H|^2.\end{cases} \tag{8.23}$$

One can see that the complexity is low for wireless BH transmissions as no matrix inversion is needed.

8.2.3 Regularized Zero Forcing with Controlled Interference (RZF-CI)

The proposed RZF-CI precoder is based on the RZF matrix structure, which is defined by:

$$\mathbf{W} = \mathbf{H}^H\left(\mathbf{H}\mathbf{H}^H + \alpha'\mathbf{I}_2\right)^{-1}, \tag{8.24}$$

with $\alpha' \in \mathbb{R}^+$, for MU-MIMO systems. On the one hand, when $\alpha' \to +\infty$ the RZF precoder is equivalent to a MRT precoder. On the other hand, when $\alpha' = 0$ the RZF precoder is equivalent to a ZF precoder. Therefore, the RZF precoder structure allows reaching a trade-off between the MRT precoder and the ZF precoder. According to (8.15) and (8.16), it comes:

$$\begin{aligned}\mathbf{H}\mathbf{H}^H + \alpha'\mathbf{I}_2 &= \begin{bmatrix}\|\mathbf{H}_U\|^2 + \alpha' & \left(\mathbf{H}_I\mathbf{H}_U^H\right)^* \\ \mathbf{H}_I\mathbf{H}_U^H & \|\mathbf{H}_I\|^2 + \alpha'\end{bmatrix} \\ &= \|\mathbf{H}_U\|\,\|\mathbf{H}_I\|\begin{bmatrix}\frac{\|\mathbf{H}_U\|^2 + \alpha'}{\|\mathbf{H}_U\|\,\|\mathbf{H}_I\|} & \Gamma_H^* \\ \Gamma_H & \frac{\|\mathbf{H}_I\|^2 + \alpha'}{\|\mathbf{H}_U\|\,\|\mathbf{H}_I\|}\end{bmatrix}.\end{aligned} \tag{8.25}$$

Therefore, (8.20) gives:

$$\left(\mathbf{H}\mathbf{H}^H + \alpha'\mathbf{I}_2\right)^{-1} = \frac{\|\mathbf{H}_U\|\,\|\mathbf{H}_I\|}{det\left(\mathbf{H}\mathbf{H}^H + \alpha'\mathbf{I}_2\right)} \begin{bmatrix} \dfrac{\|\mathbf{H}_I\|^2 + \alpha'}{\|\mathbf{H}_U\|\,\|\mathbf{H}_I\|} & -\Gamma_H^* \\ -\Gamma_H & \dfrac{\|\mathbf{H}_U\|^2 + \alpha'}{\|\mathbf{H}_U\|\,\|\mathbf{H}_I\|} \end{bmatrix}, \tag{8.26}$$

or equivalently:

$$\left(\mathbf{H}\mathbf{H}^H + \alpha'\mathbf{I}_2\right)^{-1} = \frac{\|\mathbf{H}_U\|\,\|\mathbf{H}_I\|^2}{det\left(\mathbf{H}\mathbf{H}^H + \alpha'\mathbf{I}_2\right)} \begin{bmatrix} \dfrac{1}{\|\mathbf{H}_U\|}\left(1 + \dfrac{\alpha'}{\|\mathbf{H}_I\|^2}\right) & -\dfrac{\Gamma_H^*}{\|\mathbf{H}_I\|} \\ -\dfrac{\Gamma_H}{\|\mathbf{H}_I\|} & \dfrac{\|\mathbf{H}_U\|}{\|\mathbf{H}_I\|^2}\left(1 + \dfrac{\alpha'}{\|\mathbf{H}_U\|^2}\right) \end{bmatrix}. \tag{8.27}$$

Therefore, as $\xi_W = \|\mathbf{W}_U\|^2$ and according to (8.14) and (8.15), the precoding vector for wireless BH can be written as follows:

$$\begin{cases} \mathbf{W}_U &= (1+\alpha)\dfrac{\mathbf{H}_U^H}{\|\mathbf{H}_U\|} - \Gamma_H \dfrac{\mathbf{H}_I^H}{\|\mathbf{H}_I\|}, \\ \xi_W &= (1+\alpha)^2 - 2(1+\alpha)|\Gamma_H|^2 + |\Gamma_H|^2, \end{cases} \tag{8.28}$$

with:

$$\alpha = \frac{\alpha'}{\|\mathbf{H}_I\|^2}, \tag{8.29}$$

$\alpha \in \mathbb{R}^+$. With this RZF structure, the received useful power on the second BH antenna array $|y_{BH}^U|^2$, defined in (8.8), and the metric Δ, defined in (8.4), are now function of the variable α. Therefore, $|y_{BH}^U|^2$ and Δ become $|y_{BH}^U(\alpha)|^2$ and $\Delta(\alpha)$.

The RZF structure provides a degree of freedom with the variable α. Based on the RZF structure described before, the proposed RZF-CI precoder exploits this degree of freedom. It uses the optimal value of α to maximize the received power on the receiving BS, while keeping the interference power on the UE side under a given power level. In particular, the value of α is chosen to solve the following problem:

$$\begin{array}{ll} \underset{\alpha\in\mathbb{R}^+}{\text{maximize}} & \left|y_{BH}^U(\alpha)\right|^2 \\ \text{subject to} & \Delta(\alpha) \leq \Delta_{max}. \end{array} \tag{8.30}$$

The variable Δ_∞ is defined as follows:

$$\Delta_\infty = \Delta(\alpha \to +\infty) = 1 + |\Gamma_H|^2 \left(P_I \|\mathbf{H}_I\|^2\right) \times \frac{\sigma_c^2}{\sigma_b^2}. \tag{8.31}$$

Δ_∞ corresponds to the value of Δ when the MRT precoder is used and it can be computed on the UE side during a preliminary step and sent to the BS 1 during the uplink. Additionally,

the variable α_0 is defined as follows:

$$\alpha_0 = \frac{(1-|\Gamma_H|^2) + \sqrt{(1-|\Gamma_H|^2)\left(\frac{\Delta_\infty - 1}{\Delta_{max}-1} - |\Gamma_H|^2\right)}}{\frac{\Delta_\infty - 1}{\Delta_{max}-1} - 1}. \tag{8.32}$$

This value can be computed by knowing the values of Δ_{max}, Δ_∞ and $|\Gamma_H|^2$.

Appendix D.1 shows that the problem (8.30) is easier to solve than the problem (8.11), as the variable to be optimized is the real positive scalar α instead of the complex vector $\mathbf{W}_U$. Moreover, Appendix D.1 also gives the optimal solution of the problem (8.30). In particular, it gives the following structure for the RZF-CI precoder if $\Delta_\infty \leq \Delta_{max}$:

$$\begin{cases} \mathbf{W}_U &= \dfrac{\mathbf{H}_U^H}{\|\mathbf{H}_U\|}, \\ \xi_W &= 1, \end{cases} \tag{8.33}$$

and, if $\Delta_\infty > \Delta_{max}$:

$$\begin{cases} \mathbf{W}_U &= (1+\alpha_0)\dfrac{\mathbf{H}_U^H}{\|\mathbf{H}_U\|} - \Gamma_H \dfrac{\mathbf{H}_I^H}{\|\mathbf{H}_I\|}, \\ \xi_W &= (1+\alpha_0)^2 - 2(1+\alpha_0)|\Gamma_H|^2 + |\Gamma_H|^2. \end{cases} \tag{8.34}$$

One can see that $\mathbf{W}_U$ is equivalent to a MRT precoder when $\Delta_{max} \geq \Delta_\infty$ and to a ZF precoder when Δ_{max} is set to its minimum value 1. Moreover, the complexity of the RZF-CI precoder is slightly increased compared to this of the ZF precoder defined in (8.23) but remains low as no matrix inversion is needed.

8.3 Theoretical Performance Analysis

The performance of the studied precoders, defined in the previous part, are now analytically compared in terms of received useful power on the BH antenna array of the BS 2 and of interference power on the UE side.

Proposition 2. *With the MRT precoder, the received useful power on the BH antenna array of the BS 2 is maximized and equal to:*

$$\left|y_{BH}^U\right|^2 = \left(P_U \|\mathbf{H}_U\|^2\right) \times \sigma_c^2. \tag{8.35}$$

However, the interference on the UE side is not controlled and thus this precoding technique might not fulfill the condition $\Delta \leq \Delta_{max}$.

Proof. Using (8.18) in (8.8) directly leads to (8.35). This is the maximum value for the

received power on the receiving BS according to (8.10). Moreover, using (8.18) in (8.4), it comes:

$$\Delta = \Delta_{\infty} = 1 + |\Gamma_H|^2 \left(P_I \|\mathbf{H}_I\|^2\right) \times \frac{\sigma_c^2}{\sigma_b^2}. \tag{8.36}$$

Therefore, the condition $\Delta \leq \Delta_{max}$ is fulfilled only if:

$$|\Gamma_H|^2 \leq (\Delta_{max} - 1) \frac{\sigma_b^2}{\left(P_I \|\mathbf{H}_I\|^2\right) \times \sigma_c^2}. \tag{8.37}$$

□

Proposition 3. *With the ZF precoder, the received useful power on the BH antenna array of the BS 2 is equal to:*

$$\left|y_{BH}^U\right|^2 = \left(P_U \|\mathbf{H}_U\|^2\right) \times \sigma_c^2 \times \left(1 - |\Gamma_H|^2\right), \tag{8.38}$$

and is maximized only if $|\Gamma_H| = 0$*. Additionally, the value of* Δ *is minimized and thus the condition* $\Delta \leq \Delta_{max}$ *is always fulfilled.*

Proof. using (8.23) and (8.16) in (8.8), the received useful power on the BH antenna array of the BS 2 is equal to:

$$\begin{aligned} \left|y_{BH}^U\right|^2 &= P_U \sigma_c^2 \frac{\left|\|\mathbf{H}_U\| - |\Gamma_H|^2 \|\mathbf{H}_U\|\right|^2}{1 - |\Gamma_H|^2} \\ &= \left(P_U \|\mathbf{H}_U\|^2\right) \times \sigma_c^2 \times \frac{\left|1 - |\Gamma_H|^2\right|^2}{1 - |\Gamma_H|^2} \\ &= \left(P_U \|\mathbf{H}_U\|^2\right) \times \sigma_c^2 \times \left(1 - |\Gamma_H|^2\right). \end{aligned} \tag{8.39}$$

According to (8.10), the received useful power on the BS 2 is maximized only if $|\Gamma_H| = 0$. Moreover, using (8.23) in (8.4), it comes:

$$\Delta = 1 + \frac{\left|\mathbf{H}_I \left(\mathbf{H}_U^H / \|\mathbf{H}_U\| - \Gamma_H \mathbf{H}_I^H / \|\mathbf{H}_I\|\right)\right|^2}{1 - |\Gamma_H|^2} \frac{P_I \sigma_c^2}{\sigma_b^2}. \tag{8.40}$$

According to (8.16), it comes:

$$\Delta = 1 + \frac{\left|(\|\mathbf{H}_I\|\Gamma_H - \|\mathbf{H}_I\|\Gamma_H)\right|^2}{1 - |\Gamma_H|^2} \frac{P_I \sigma_c^2}{\sigma_b^2} = 1. \tag{8.41}$$

Therefore, Δ is equal to its minimum value. □

Proposition 4. *With the RZF-CI precoder, the received useful power on the BH antenna*

array of the BS 2 is equal to:

$$\left|y_{BH}^{U}\right|^2 = \begin{cases} \left(P_U \left\|\mathbf{H}_U\right\|^2\right) \times \sigma_c^2 & \text{if} \quad \Delta_\infty \leq \Delta_{max}, \\ \left(P_U \left\|\mathbf{H}_U\right\|^2\right) \times \sigma_c^2 \times \left(1 - \varepsilon.|\Gamma_H|^2\right) & \text{if} \quad \Delta_\infty > \Delta_{max}, \end{cases} \tag{8.42}$$

with:

$$\varepsilon = \left(1 + 2\alpha_0 + \frac{\alpha_0^2}{1 - |\Gamma_H|^2}\right)^{-1}, \tag{8.43}$$

and with:

$$0 \geq \varepsilon \geq 1. \tag{8.44}$$

Therefore, the received power with the RZF-CI precoder is always higher or equal to the received useful power with the ZF precoder. Additionally, the condition $\Delta \leq \Delta_{max}$ is always fulfilled.

Proof. Appendix D.2 provides the detailed theoretical derivation of the expression of the received useful power with the RZF-CI precoder. Moreover, The RZF-CI precoder is designed to fulfill the condition $\Delta \leq \Delta_{max}$ as explained in part 8.2.3. □

Based on these theoretical results, Figure 8.1 gives the theoretical received power on the BS 2 with the MRT, the ZF and the proposed RZF-CI precoders as a function of the correlation factor Γ_H and of the ratio $(\Delta_\infty - 1)/(\Delta_{max} - 1)$ for the RZF-CI precoder. This

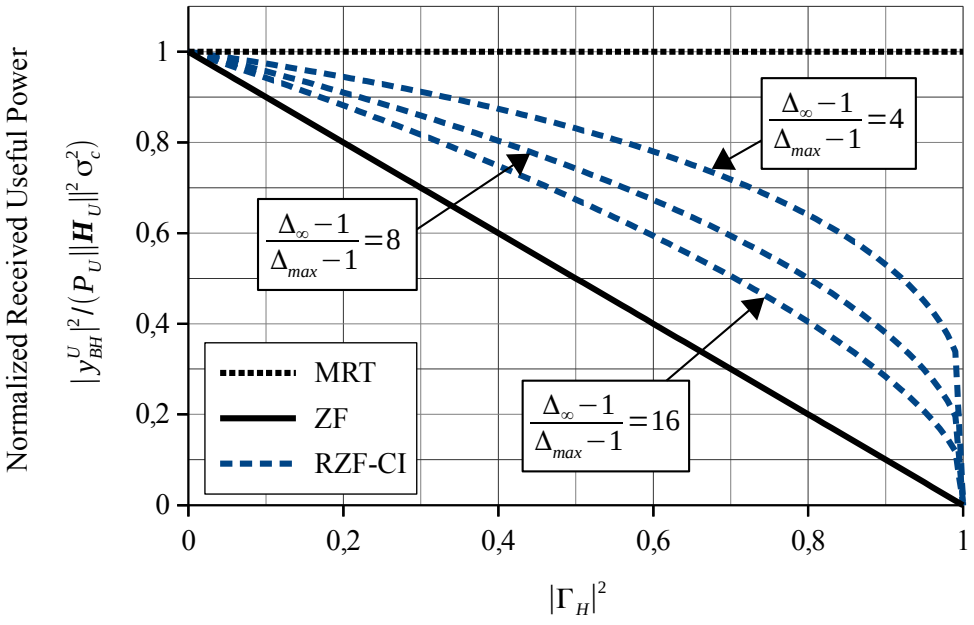

Figure 8.1: Theoretical normalized received useful power on the BH antenna array of the BS 2 as a function of the correlation factor Γ_H, for the three considered precoding techniques.

ratio can be seen as the amount of interference to suppress as it increases when the impact of the BH link on the UE side increases, meaning when Δ_∞ increases and decreases when

the limit Δ_{max} increases. As expected, the RZF-CI precoder is a trade-off between the MRT precoder, comparable to those used in [37,38], and the ZF precoder, similar to the precoders used in [35,39]. Moreover, the received power with the RZF-CI precoder increases when the ratio $(\Delta_\infty - 1)/(\Delta_{max} - 1)$ decreases, meaning when the amount of interference to suppress decreases.

8.4 Simulations

In order to numerically evaluate the performance of the RZF-CI precoder, the QuaDRiGa 3D channel simulator [40, 54] is used in this part to simulate GSCM. The simulations thus take into account the geometry of the propagation environment and the correlation between the antennas, which is important as the correlation factor Γ_H depends on these aspects and has a significant impact on the performance of the system as shown in the previous part. The BH antenna arrays are identical uniform rectangular arrays facing each other and the channel model used between these two antenna arrays is the 3GPP 38.901 Rural Macro-cell (RMa) LOS spatial channel model [52]. Moreover, the considered UE is equipped with an omni-directional antenna, is located on the straight line joining the BS 1 and the BS 2 and the 3GPP 38.901 RMa LOS spatial channel model is also used between the BS 1 and this UE. This configuration corresponds to the worst case for the UE, which might be highly impacted by the BH link. For the sake of simplicity, a perfect channel estimation is assumed. The simulation parameters are given by Table 8.1.

Table 8.1: Simulation parameters.

FFT size	1024
Inter-carrier spacing	15 kHz
CP length	4.7 μs
Center frequency	4 GHz
BH antenna arrays: number of antennas per column	16
BH antenna arrays: number of antennas per line	4
BH antenna arrays: inter-antenna spacing	10 cm
BH antenna arrays: half-power beamwidth	30°
BH antenna arrays: height	35 m
Distance between the BS 1 and the BS 2	10 km
UE: height	1.5 m

The normalized interference power on the UE side is first drawn in Figure 8.2 as a function of the distance d_{BS-UE} between the BS 1 and the UE when the MRT precoder is used. This Figure shows that the secondary lobes of the created beam induce interference peaks with a significant power when the distance between the BS 1 and the UE is below 1 km. After 1 km, the path loss induces a reduction of the interference power, which constantly decreases and loses more than 20 dB at a distance of 5 km. Therefore, and in accordance with preliminary assumptions described in Chapter 7, the interference on the UE side is predominant for UEs

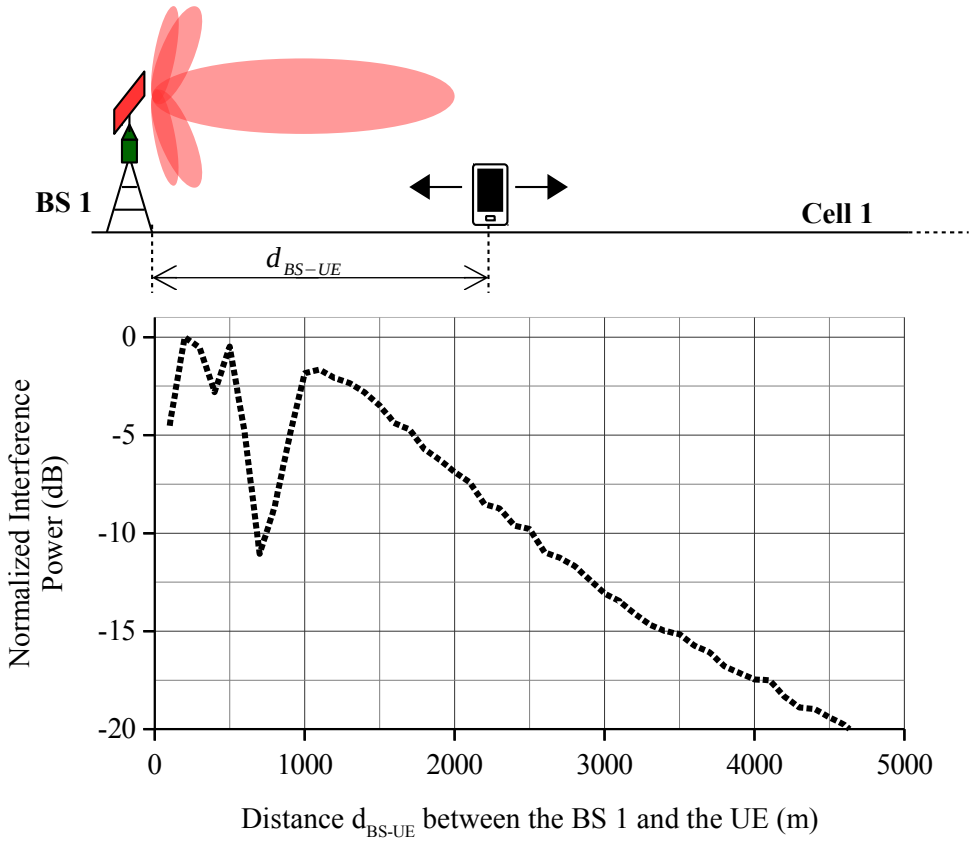

Figure 8.2: Normalized interference power on the UE side as a function of the distance d_{BS-UE} between the BS 1 and the UE when the MRT precoder is used.

located near the BS 1.

The BER on the UE side is then computed as a function of the SNR when the MRT, the ZF and the RZF-CI precoders (with $\Delta_{max} = 0.5\ dB$ and $\Delta_{max} = 1\ dB$) are used. The distance d_{BS-UE} between the BS 1 and the UE is set to 2 km. The results are given by Figure 8.3. The interference on the UE side is canceled using the ZF precoder, which experiences the best results in terms of BER on the UE side. Conversely, the interference on the UE side highly impacts the BER when the MRT precoder is used as it does not control this interference. Therefore, to reach a BER of 10^{-2} when the MRT precoder is used, the UE needs a SNR greater than 20 dB while only 14.5 dB is necessary when the ZF precoder is used. As the interference level is high for a UE at this position, the value of Δ_∞ is greater than Δ_{max}. Therefore, in Figure 8.3 the curves for the proposed RZF-CI precoder are shifted versions of the ZF curve with a shift equal to the value of Δ_{max}. As expected, the performance of the RZF-CI precoder is thus slightly worse than this of the ZF precoder but remains under control.

The normalized received useful power on the BS 2 $|y_{BH}^U|^2 \ / \ (P_U \|\mathbf{H}_U\|^2 \sigma_c^2)$ is now computed as a function of the distance d_{BS-UE} between the BS 1 and the UE when the MRT, the ZF and the RZF-CI precoders (with $\Delta_{max} = 0.5\ dB$ and $\Delta_{max} = 1\ dB$) are used. The results are

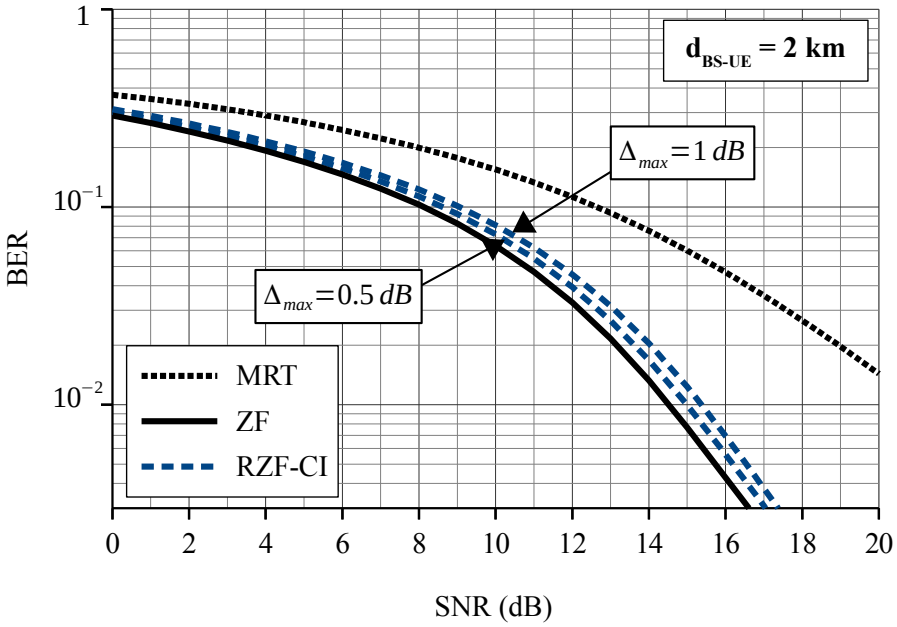

Figure 8.3: BER on the UE side as a function of the SNR with a distance d_{BS-UE} of 2 km between the UE and the BS 1, for the three considered precoding techniques.

given by Figure 8.4. On the one hand, while the MRT precoder offers poor performance in

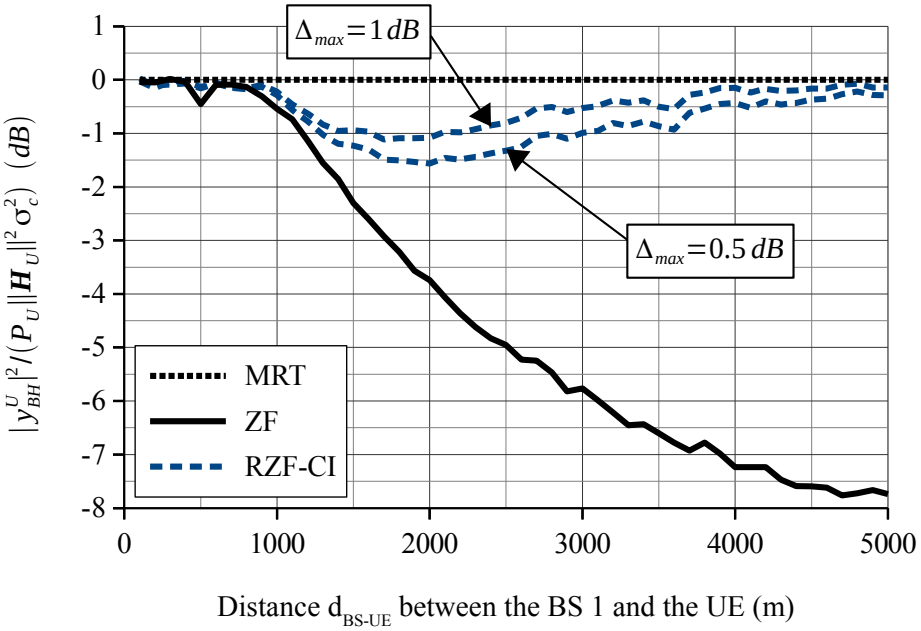

Figure 8.4: Normalized received useful power on the BH antenna array of the BS 2 as a function of the distance d_{BS-UE} between the BS 1 and the UE for the three considered precoding techniques.

terms of BER on the UE side, it always maximizes the received useful power on the BS 2. On the other hand, the good performance of the ZF precoder in terms of BER on the UE side is balanced by the high loss in terms of received useful power on the BS 2. Therefore, a loss of

almost 8 dB can occur, compared to the received useful power reached by the MRT precoder, when the UE is at the cell-edge. As expected, the RZF-CI precoding technique outperforms the ZF precoding technique in terms of received useful power on the BS 2. Moreover, this result is consistent with the theoretical results as the higher the value of Δ_{max}, the higher the received useful power on the BS 2. Finally, the loss of received useful power is very limited compared to the received useful power reached by the MRT precoder. The RZF-CI precoder looses at most 1.5 dB when $\Delta_{max} = 0.5\ dB$ and 1 dB when $\Delta_{max} = 1\ dB$.

To conclude, the proposed RZF-CI precoding technique appears to be a good trade-off between the MRT and the ZF precoding techniques used in the literature [35, 37–39]. By choosing the value of Δ_{max}, the performance in terms of BER on the UE side is controlled and the loss of received useful power on the BS 2 remains limited. Therefore, the simulations highlight the superiority of the proposed solution compared to the MRT and ZF precoders without leading to an excessive complexity.

8.5 Conclusion

In Chapter 7, the use of a massive MIMO system was proposed in order to provide a long-range in-and wireless BH link and thereby to reduce the cost of deployment of the network in wide underserved areas.

A new massive MIMO precoder called RZF-CI is proposed in this Chapter. This precoder is intended to provide a long-range in-band wireless BH link between two BSs. The particularity of the RZF-CI precoder is its ability to control the interference on the UE side, unlike the classical MRT precoder so that a minimum capacity is guaranteed for each UE. Moreover, in this Chapter, an analytical study proved that the proposed solution always outperforms the ZF precoder used in the literature in terms of received power on the receiving BS and thus allows a higher system capacity for the BH link.

The simulations conducted in this Chapter highlight the benefits of this novel precoding technique. In terms of BER on the UE side, the degradation is controlled with the proposed RZF-CI precoder, while the performance with the MRT precoder is highly impacted by the in-band communication. In terms of received useful power on the receiving BS, the RZF-CI precoder allows an important gain compared with the ZF precoder (up to 8 dB), while the loss of power is rather limited compared with the MRT precoder (up to 1.5 dB).

By combining the flexibility and the low complexity of the new RZF-CI precoder with the advantages of having an in-band wireless BH link, the proposed solution is a cheap and effective way to extend the coverage of the cellular networks and to improve the quality of service in low ARPU networks.

Summary of this Chapter:

- A **new massive MIMO precoder called Regularized Zero Forcing with Controlled Interference (RZF-CI)** is proposed in this Chapter. The particularity of the RZF-CI precoder is its ability to **control the interference on the UE side, unlike the classical MRT precoder**. Moreover, the proposed solution **does not completely suppress the interference on the UE side, unlike the ZF precoder**.
- The analytical study proved that **the proposed RZF-CI precoder always outperforms the ZF precoder used in the literature in terms of received useful power on the receiving BS**.
- **The simulations conducted in this Chapter highlight the benefits of this novel precoding technique**. **In terms of BER on the UE side, the degradation is controlled** with the proposed RZF-CI precoder, while the performance with the MRT precoder is highly impacted by the in-band communication. **In terms of received useful power on the receiving BS, the RZF-CI precoder allows an important gain compared with the ZF precoder**, while the loss of power is rather limited compared with the MRT precoder.

Related Publication:

- A. Bazin and B. Jahan, "Système de télécommunication avec système d'antennes massive-MIMO pour un lien backhaul sans fil et procédé correspondant", french patent under submission.

9

Asynchronous Wireless Backhaul (BH)

In the previous Chapter, a new massive MIMO precoder (RZF-CI) was proposed in order to provide a long-range in-band wireless BH link and to reduce the cost of deployment of the network in wide underserved areas. Additionally, simulation results showed that the proposed RZF-CI precoder allows controlling the interference on the UE side unlike the MRT precoder and improving the received useful power on the receiving BS compared to the ZF precoder.

In the previous Chapter, both the access link fed by the access antenna of the BS 1 and the BH link sent by the BH antenna array of the BS 1 used an OFDM modulation, with the same parameters (CP length, FFT size, etc.). Moreover, a perfect time and frequency synchronization between the BH link and the access link was considered, meaning that the BH signal and the access signal are sent exactly at the same time. However, such a synchronization is not feasible in a real system because of hardware limitations. Additionally, a complete asynchronous wireless BH would add a degree of freedom and thereby would reduce the complexity of the overall system. Thanks to this degree of freedom, the asynchronous BH link could use different parameters than those used by the access link, such as a different CP length. Moreover, one can envisioned the use of an alternative multi-carrier modulation for the BH link in order to improve the spectral efficiency for example. In this Chapter, the impact of a time desynchronization between the access link and the BH link is evaluated thanks to an analytical study and to simulations. Furthermore, the use of the FBMC/OQAM modulation for the BH link is discussed and its performance is evaluated.

Firstly, in part 9.1 the system model defined in Chapter 7 is modified in order to take into account a time desynchronization between the BH link and the access link. Then, part 9.2 aims at analytically studying the impact of such a time desynchronization in terms of interference power on the UE side. In part 9.3, simulations are carried out in order to evaluate the impact of a time desynchronization and to investigate the use of the FBMC/OQAM modulation for the BH link. Finally, a conclusion is drawn in the last part.

9.1 System Model

In this Chapter, a time desynchronization between the BH link and the access link is considered. In particular, while the access signal $s_{Acc}(t)$ is sent at a given time t_0, all the BH signals $s_{BH}^{n_t}(t)$, $\forall n_t \in [0, N_t - 1]$, are sent at the time $t_0 + \Delta t$, where Δt is the value of the time desynchronization offset. In order to study the impact of such a desynchronization on the UE side, the impact of Δt on the interference power coming from the BH antenna array of the BS 1 is studied. Figure 9.1 describes this study with a time domain system model.

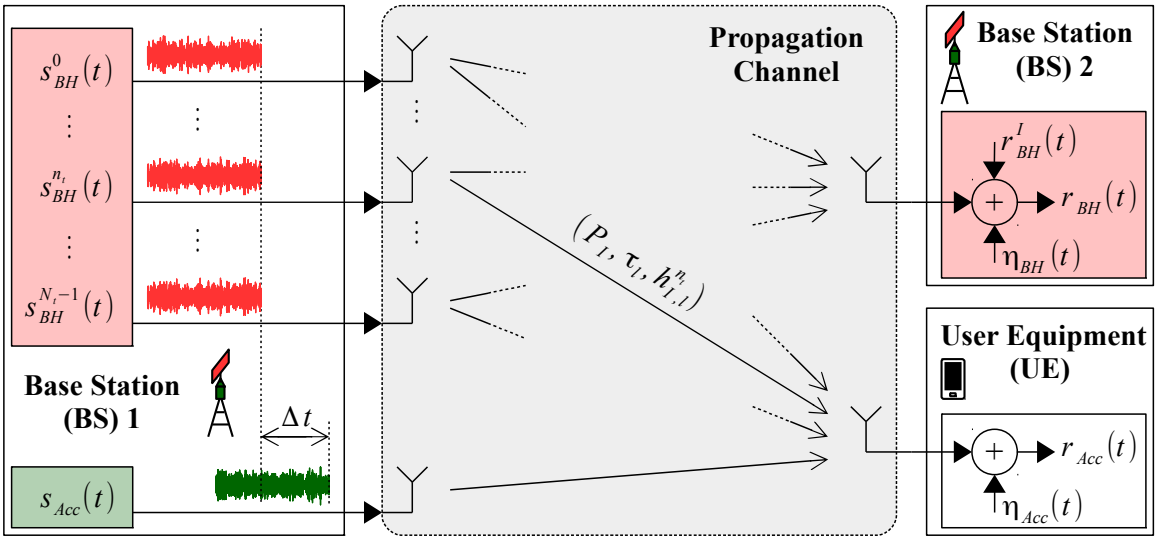

Figure 9.1: Time domain system model for an in-band wireless BH transmission with a time desynchronization Δt between the BH link and the access link.

On the BH antenna array of the BS 1, the transmitted signal from the antenna n_t can be described as follows according to (7.8):

$$s_{BH}^{n_t}(t) = \sum_{n\in\mathbb{Z}} \sum_{m=0}^{M-1} \underbrace{\left(\frac{1}{\sqrt{\xi_W[m]}} W_U^{n_t}[m] c[m,n] \right)}_{x_{BH}^{n_t}[m,n]} \Pi_{m,n}(t - \Delta t), \tag{9.1}$$

with $c[m,n]$ the complex data carried by the sub-carrier m for the time index n, $W_U^{n_t}[m]$ the precoding factor on the sub-carrier m and on the antenna n_t, $\xi_W[m]$ the power normalization factor on the sub-carrier m and $\Pi_{m,n}(t)$ defined by (2.2). The data $c[m,n]$ has a mean value equal to 0 and a variance equal to σ_c^2. Moreover, a significant time desynchronization and thus a large value of Δt is considered. In particular, $T_{CP} < \Delta t < T_0$, with T_{CP} being the CP duration and $T_0 = 1/F_0$ being the symbol duration, and $\Delta t \gg \tau_l \ \forall l \in [0, L_h - 1]$, with τ_l being the delay of the l^{th} multipath component.

On the UE side, the received signal $r_{Acc}(t)$ can be described as follows:

$$r_{Acc}(t) = r^{U}_{Acc}(t) + r^{I}_{Acc}(t) + \eta_{Acc}(t), \tag{9.2}$$

where $r^{U}_{Acc}(t)$ is the received useful signal coming from the access antenna of the BS 1, $r^{I}_{Acc}(t)$ is the received interference signal coming from the BH antenna array of the BS 1 and $\eta_{Acc}(t)$ is the time domain noise component. In particular, the received interference signal can be described as follows:

$$r^{I}_{Acc}(t) = \sum_{n_t=0}^{N_t-1} \sqrt{P_I} \left(\sum_{l=0}^{L_h-1} h^{n_t}_{I,l} s^{n_t}_{BH}(t-\tau_l) \right), \tag{9.3}$$

with P_I being the path loss, $h^{n_t}_{I,l}$ being the amplitude of the l^{th} multipath component of the interference channel between the antenna n_t of the BH antenna array of the BS 1 and the UE antenna, τ_l being its delay with $\tau_l < T_{CP}\ \forall l \in [0, L_h - 1]$ and L_h being the number of multipath components. Therefore, using (9.1) in (9.3), it comes:

$$r^{I}_{Acc}(t) = \sum_{n_t=0}^{N_t-1} \sqrt{P_I} \sum_{n\in\mathbb{Z}} \sum_{m=0}^{M-1} \frac{W^{n_t}_{U}[m]}{\sqrt{\xi_W[m]}} c[m,n] \left(\sum_{l=0}^{L_h-1} h^{n_t}_{I,l} \Pi_{m,n}(t - \Delta t - \tau_l) \right). \tag{9.4}$$

The demodulation process is carried out on the UE side according to the useful signal coming from the access antenna of the BS 1: $r^{U}_{Acc}(t)$. Therefore, according to (2.9), for the frequency and time indexes (m_0, n_0), the received data after the demodulation is:

$$\begin{aligned} y_{Acc}[m_0,n_0] &= \int_{\mathbb{R}} r_{Acc}(t) \left(\Pi^{0}_{m_0,n_0}(t) \right)^{*} dt \\ &= y^{U}_{Acc}[m_0,n_0] + y^{I}_{Acc}[m_0,n_0] + b_{Acc}[m_0,n_0], \end{aligned} \tag{9.5}$$

with:

$$y^{U}_{Acc}[m_0,n_0] = \int_{\mathbb{R}} r^{U}_{Acc}(t) \left(\Pi^{0}_{m_0,n_0}(t) \right)^{*} dt, \tag{9.6}$$

being the received useful data,

$$y^{I}_{Acc}[m_0,n_0] = \int_{\mathbb{R}} r^{I}_{Acc}(t) \left(\Pi^{0}_{m_0,n_0}(t) \right)^{*} dt, \tag{9.7}$$

being the received interference data and:

$$b_{Acc}[m_0,n_0] = \int_{\mathbb{R}} \eta_{Acc}(t) \left(\Pi^{0}_{m_0,n_0}(t) \right)^{*} dt, \tag{9.8}$$

being the frequency domain noise component.

The focus is put on the received interference data: $y^{I}_{Acc}[m_0, n_0]$. For the sake of simplicity, the time index n_0 used for the rest of this part is $n_0 = 0$. Moreover, the notations $m =$

$(m_0 - p)$, $n = (n_0 - q)$ and $y^I_{Acc} = y^I_{Acc}[m_0, n_0]$ are given and the mathematical set of useful sub-carriers Ω_p is defined as follows:

$$\Omega_p = \{p \in \mathbb{Z} \mid c[m_0 - p, 0] \neq 0\}\,. \tag{9.9}$$

The development in Appendix E shows that y^I_{Acc} can be rewritten as follows:

$$y^I_{Acc} = y^I_{Acc,0} + y^I_{Acc,1}, \tag{9.10}$$

with:

$$\begin{aligned} y^I_{Acc,0} \;&\approx\; \sqrt{P_I} \sum_{p\in\Omega_p} \frac{\sum_{n_t=0}^{N_t-1} W_U^{n_t}[m_0 - p] H^{n_t}_{I,p}}{\sqrt{\xi_W[m_0 - p]}} c[m_0 - p, 0] \exp\left[-j2\pi(m_0 - p)F_0\Delta t\right] \\ &\times\; \left(1 - \frac{\Delta t - T_{CP}}{T_0}\right) \mathrm{sinc}\left(p\left(1 - \frac{\Delta t - T_{CP}}{T_0}\right)\right) \exp\left[-j\pi p\left(1 + \frac{\Delta t - T_{CP}}{T_0}\right)\right], \end{aligned} \tag{9.11}$$

and:

$$\begin{aligned} y^I_{Acc,1} \;&\approx\; \sqrt{P_I} \sum_{p\in\Omega_p} \frac{\sum_{n_t=0}^{N_t-1} W_U^{n_t}[m_0 - p] H^{n_t}_{I,p}}{\sqrt{\xi_W[m_0 - p]}} c[m_0 - p, -1] \\ &\times\; \exp\left[j2\pi(m_0 - p)F_0\left(T_0 + T_{CP} - \Delta t\right)\right] \\ &\times\; \frac{\Delta t - T_{CP}}{T_0} \mathrm{sinc}\left(p\frac{\Delta t - T_{CP}}{T_0}\right) \exp\left[-j\pi p\frac{\Delta t - T_{CP}}{T_0}\right], \end{aligned} \tag{9.12}$$

and:

$$H^{n_t}_{I,p} = \sum_{l=0}^{L_h-1} h^{n_t}_{I,l} \exp\left[-j2\pi(m_0 - p)F_0\tau_l\right]. \tag{9.13}$$

In (9.10), $y^I_{Acc,0}$ is the interference data of the time index $n_0 = 0$, while $y^I_{Acc,1}$ is the interference data of the time index $(n_0 - 1) = -1$. Moreover, $H^{n_t}_{I,p}$ represents the frequency domain propagation channel on the frequency index $(m_0 - p)$ between the BH antenna n_t and the UE antenna.

9.2 Analytical Study

The impact of a time desynchronization is analytically evaluated in this part. To this end, the interference coming from the BH antenna array of the BS 1 is expressed with a perfect time synchronization ($\Delta t = 0$) and with a large time desynchronization ($\Delta t \gg 0$). Then, it is shown how the desynchronization creates a spreading of the interference in the frequency domain. These preliminary results allow concluding on the impact of a time desynchronization in the last part.

9.2.1 Interference Power

The interference power coming from the BH antenna array of the BS 1 is expressed here with a perfect time synchronization ($\Delta t = 0$) and with a large time desynchronization ($\Delta t \gg 0$).

Interference Power with a Perfect Time Synchronization

According to (7.20), when the BH link and the access link are synchronized, the received interference signal coming from the BH antenna array of the BS 1 is:

$$y^I_{Acc,Sync} = \sqrt{P_I} \sum_{n_t=0}^{N_t-1} H^{n_t}_{I,0} \underbrace{\frac{1}{\sqrt{\xi_W[m_0]}} W^{n_t}_U[m_0] c[m_0, 0]}_{x^{n_t}_{BH}[m_0,0]}, \tag{9.14}$$

and the received interference power is thus:

$$\left| y^I_{Acc,Sync} \right|^2 = P_I \frac{\left| \sum_{n_t=0}^{N_t-1} W^{n_t}_U[m_0] H^{n_t}_{I,0} \right|^2}{\xi_W[m_0]} \sigma_c^2. \tag{9.15}$$

Therefore, with a perfect time synchronization, the interference is only due to the data sent on the sub-carrier m_0.

Interference Power with a Time Desynchronization

With desynchronized signals, according to (9.10), (9.11) and (9.12), as $c[m, n]$ and $c[m', n']$ are two independent variables if $(m, n) \neq (m', n')$ and as the mean value of $c[m, n]$ is equal to 0, the received interference power is:

$$\left| y^I_{Acc} \right|^2 = \left| y^I_{Acc,0} \right|^2 + \left| y^I_{Acc,1} \right|^2, \tag{9.16}$$

with:

$$\begin{aligned} \left| y^I_{Acc,0} \right|^2 &\approx \sum_{p \in \Omega_p} \left(1 - \frac{\Delta t - T_{CP}}{T_0} \right)^2 \mathrm{sinc}^2 \left(p \left(1 - \frac{\Delta t - T_{CP}}{T_0} \right) \right) \\ &\times P_I \frac{\left| \sum_{n_t=0}^{N_t-1} W^{n_t}_U[m_0 - p] H^{n_t}_{I,p} \right|^2}{\xi_W[m_0 - p]} \sigma_c^2, \end{aligned} \tag{9.17}$$

and:

$$\left| y^I_{Acc,1} \right|^2 \approx \sum_{p \in \Omega_p} \left(\frac{\Delta t - T_{CP}}{T_0} \right)^2 \mathrm{sinc}^2 \left(p \frac{\Delta t - T_{CP}}{T_0} \right) \times P_I \frac{\left| \sum_{n_t=0}^{N_t-1} W^{n_t}_U[m_0 - p] H^{n_t}_{I,p} \right|^2}{\xi_W[m_0 - p]} \sigma_c^2. \tag{9.18}$$

Therefore, it comes:

$$\left|y_{Acc}^{I}\right|^2 \approx \sum_{p\in\Omega_p} \alpha_p \times P_I \frac{\left|\sum_{n_t=0}^{N_t-1} W_U^{n_t}[m_0-p]H_{I,p}^{n_t}\right|^2}{\xi_W[m_0-p]}\sigma_c^2, \tag{9.19}$$

with:

$$\alpha_p = \left(\frac{\Delta t - T_{CP}}{T_0}\right)^2 \mathrm{sinc}^2\left(p\frac{\Delta t - T_{CP}}{T_0}\right) + \left(1-\frac{\Delta t - T_{CP}}{T_0}\right)^2 \mathrm{sinc}^2\left(p\left(1-\frac{\Delta t - T_{CP}}{T_0}\right)\right). \tag{9.20}$$

In (9.19), one can see that the interference power coming from the BH antenna array of the BS 1 ($|y_{Acc}^{I}|^2$) is not only due to the data sent on the sub-carrier m_0, but also to the neighboring data sent on the sub-carriers (m_0-p), $|p|>0$. Therefore, the time desynchronization induces a spreading of the interference in the frequency domain, which is evaluated thereafter.

9.2.2 Spreading of the Interference in the Frequency Domain

This part focuses on the values of α_p, which are the only values in (9.19) that depend on Δt. Therefore, they can represent the spreading of the interference in the frequency domain due to the time desynchronization.

According to (9.20), it can be noticed that:

$$\alpha_{-p} = \alpha_p. \tag{9.21}$$

While the delay spread of a multipath propagation channel can be quantified by its root mean square delay τ_{rms}, the spreading of the interference in the frequency domain can be evaluated in a similar way with the following metric:

$$p_{rms} = \sqrt{\frac{\sum_{p\geq 0}(p-\bar{p})^2\alpha_p}{\sum_{p\geq 0}\alpha_p}}, \tag{9.22}$$

with:

$$\bar{p} = \frac{\sum_{p\geq 0} p.\alpha_p}{\sum_{p\geq 0}\alpha_p}. \tag{9.23}$$

Therefore, the higher the value of p_{rms}, the larger the spreading of the interference in the frequency domain.

In Figure 9.2 the value of p_{rms} is shown as a function of $(\Delta t - T_{CP})/T_0$ for $T_{CP} \leq \Delta t \leq (T_0 - T_{CP})$. In particular, the value of p_{rms} is maximum when $(\Delta t - T_{CP})/T_0 = 0.5$ and thus the spreading is maximized when $\Delta t = T_0/2 + T_{CP}$. Therefore, for the rest of this Chapter, the value of Δt is set to:

$$\Delta t = \frac{T_0}{2} + T_{CP}, \tag{9.24}$$

as it corresponds to the worst case in terms of spreading.

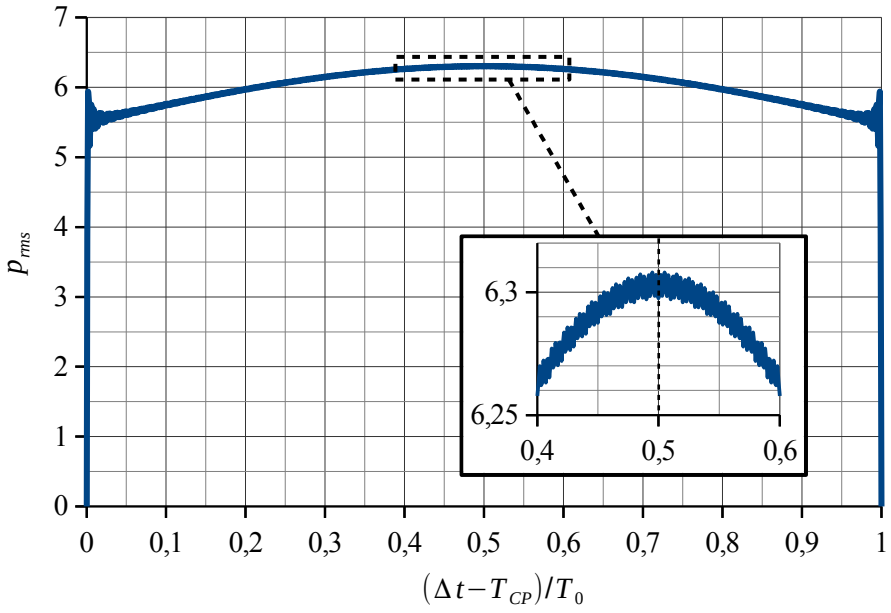

Figure 9.2: Value of p_{rms} as a function of $(\Delta t - T_{CP})/T_0$.

Additionally, with such a value of Δt, the spreading remains contained as:

$$\frac{\sum_{p=-p_{max}}^{p_{max}} \alpha_p}{\sum_{p\in\mathbb{Z}} \alpha_p} > 95\%, \quad with\ p_{max} = 3. \tag{9.25}$$

Therefore, most of the interference power comes from the frequency band $[m_0 - p_{max}, m_0 + p_{max}]$, with $p_{max} = 3$.

Finally, on the frequency band $[m_0 - p_{max}, m_0 + p_{max}]$, $p_{max} = 3$, the propagation channel between the BH antenna n_t and the UE antenna can be considered as constant and thus:

$$H_{I,p}^{n_t} \approx H_{I,0}^{n_t}. \tag{9.26}$$

9.2.3 Impact of the Time Desynchronization

In order to evaluate the impact of a time desynchronization between the BH link and the access link, a comparison is carried out between the received interference power on the UE side with a perfect time synchronization and the received interference power on the UE side with a large time desynchronization. According to (9.19), this impact relies on the precoding factors applied on the considered sub-carrier: $W_U^{n_t}[m_0]$, but also on the precoding factors applied on its neighboring sub-carrier: $W_U^{n_t}[m_0 - p]$, $|p| > 0$. Therefore, the impact of a time desynchronization is not the same depending on the considered sub-carrier m_0. That is why this work is divided in two cases. Firstly, a sub-carrier in the middle of the UE band is considered, where the precoding factors $W_U^{n_t}[m_0 - p]$ with $-p_{max} \leq p \leq p_{max}$ are all defined for the considered UE. Secondly, a sub-carrier at the edge of the UE band is considered,

where some precoding factors $W_U^{n_t}[m_0 - p]$ with $-p_{max} \leq p \leq p_{max}$ are defined for another UE.

Case 1: A Sub-Carrier in the Middle of the UE Band

In this part, we consider the interference spreading for a sub-carrier of index m_0 placed in the middle of the frequency band dedicated to the considered UE, as illustrated in Figure 9.3. The RZF-CI precoder is build according to the useful channel, denoted by $H_U^{n_t}[m]$ for

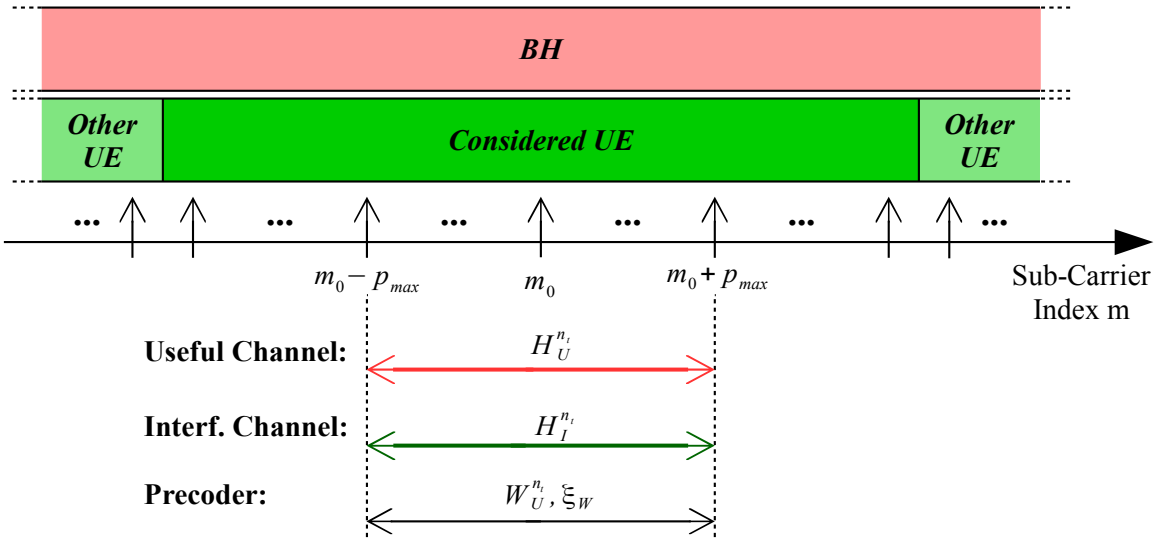

Figure 9.3: Illustration of case 1: a sub-carrier in the middle of the UE band.

the BH antenna n_t of the BS 1 and for the sub-carrier m, and according to the interference channel, denoted by $H_I^{n_t}[m]$ for the BH antenna n_t of the BS 1 and for the sub-carrier m. On the frequency band $[m_0 - p_{max}, m_0 + p_{max}]$ ($p_{max} = 3$), the following assumptions can be made regarding the useful channel and the interference channel.

- The useful channel between the BH antenna array of the BS 1 and the BH antenna array of the BS 2, can be assumed constant in the frequency domain. Therefore, it comes $H_U^{n_t}[m] \approx H_U^{n_t}[m_0] = H_U^{n_t}$, $\forall (m_0 - p_{max}) \leq m \leq (m_0 + p_{max})$.
- Only the considered UE is served on the frequency band $[m_0 - p_{max}, m_0 + p_{max}]$ ($p_{max} = 3$). Therefore, the interference channel used to build the precoder is the propagation channel between the BH antenna array of the BS 1 and the considered UE and thus $H_I^{n_t}[m_0 - p]$ is equal to $H_{I,p}^{n_t}$. Moreover, according to (9.26), it comes $H_I^{n_t}[m] = H_{I,p}^{n_t} \approx H_{I,0}^{n_t} = H_I^{n_t}$, $\forall (m_0 - p_{max}) \leq m \leq (m_0 + p_{max})$.

On the frequency band $[m_0 - p_{max}, m_0 + p_{max}]$ ($p_{max} = 3$), the RZF-CI precoder is thus build according to the useful channel $H_U^{n_t}$ and to the interference channel $H_I^{n_t}$. Therefore, the precoding vector and the normalization factor are nearly constant on the considered frequency

band, meaning $W_U^{n_t}[m] \approx W_U^{n_t}[m_0] = W_U^{n_t}$ and $\xi_W[m] \approx \xi_W[m_0] = \xi_W$, $\forall(m_0 - p_{max}) \leq m \leq (m_0 + p_{max})$.

Using the previous approximations and notations and according to (9.26), the equation (9.19) becomes:

$$\left|y_{Acc}^I\right|^2 \approx \left(\sum_{p=-p_{max}}^{p_{max}} \alpha_p\right) \times \left(P_I \frac{\left|\sum_{n_t=0}^{N_t-1} W_U^{n_t} H_{I,0}^{n_t}\right|^2}{\xi_W} \sigma_c^2\right) + \varepsilon_{|y_{Acc}^I|^2}, \tag{9.27}$$

where $\varepsilon_{|y_{Acc}^I|^2}$ denotes the interference power coming from the sub-carriers $m \notin [m_0 - p_{max}, m_0 + p_{max}]$. According to (9.25), the value of $\varepsilon_{|y_{Acc}^I|^2}$ is small compared to the rest of the interference power. Moreover, as:

$$\sum_{p=-p_{max}}^{p_{max}} \alpha_p = 0.95, \tag{9.28}$$

the following approximation can be made:

$$\left|y_{Acc}^I\right|^2 \approx P_I \frac{\left|\sum_{n_t=0}^{N_t-1} W_U^{n_t} H_{I,0}^{n_t}\right|^2}{\xi_W} \sigma_c^2. \tag{9.29}$$

Additionally, when a perfect time synchronization is considered, the equation (9.15) becomes:

$$\left|y_{Acc,Sync}^I\right|^2 = P_I \frac{\left|\sum_{n_t=0}^{N_t-1} W_U^{n_t} H_{I,0}^{n_t}\right|^2}{\xi_W} \sigma_c^2. \tag{9.30}$$

Therefore, it comes:

$$\left|y_{Acc}^I\right|^2 \approx \left|y_{Acc,Sync}^I\right|^2, \tag{9.31}$$

and the time desynchronization has no detrimental impact on the interference power when the considered sub-carrier is in the middle of the UE band.

Case 2: A Sub-Carrier at the Edge of the UE Band

The considered sub-carrier of index m_0 is now at the edge of the frequency band dedicated to the considered UE, as illustrated in Figure 9.4. As in the previous case, the RZF-CI precoder is build according to the useful channel, denoted by $H_U^{n_t}[m]$ for the BH antenna n_t and the sub-carrier m, and according to the interference channel, denoted by $H_I^{n_t}[m]$ for the BH antenna n_t and the sub-carrier m. On the frequency band $[m_0 - p_{max}, m_0 + p_{max}]$ ($p_{max} = 3$), the following assumptions can be made regarding the useful channel and the interference channel.

- The useful channel between the BH antenna array of the BS 1 and the BH antenna array of the BS 2, can be considered constant on the frequency band $[m_0 - p_{max}, m_0 + p_{max}]$

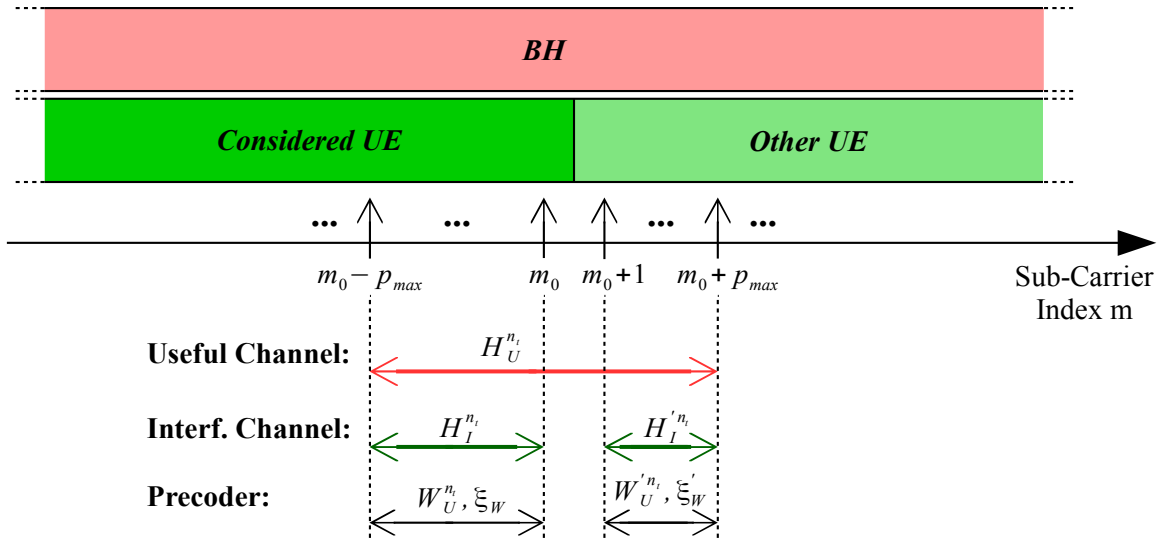

Figure 9.4: Illustration of case 2: a sub-carrier at the edge of the UE band.

($p_{max} = 3$). Therefore, it comes $H_U^{n_t}[m] \approx H_U^{n_t}$, $\forall (m_0 - p_{max}) \leq m \leq (m_0 + p_{max})$.

- The considered UE is served on the frequency band $[m_0 - p_{max}, m_0]$, while another UE is served on the frequency band $[m_0 + 1, m_0 + p_{max}]$. Therefore, on the frequency band $[m_0 - p_{max}, m_0]$, the interference channel used to build the precoder is the propagation channel between the BH antenna array of the BS 1 and the considered UE, while, on the frequency band $[m_0 + 1, m_0 + p_{max}]$, the interference channel used to build the precoder is the propagation channel between the BH antenna array of the BS 1 and the other UE. In other words, $H_I^{n_t}[m_0 - p] = H_{I,p}^{n_t}$ for $0 \geq p \geq p_{max}$ but $H_I^{n_t}[m_0 - p] \neq H_{I,p}^{n_t}$ for $-p_{max} \geq p \geq -1$. Moreover, the interference channel can be considered as constant on the frequency band $[m_0 - p_{max}, m_0]$, respectively $[m_0 + 1, m_0 + p_{max}]$, and it comes $H_I^{n_t}[m] = H_{I,p}^{n_t} \approx H_{I,0}^{n_t} = H_I^{n_t}$, $\forall (m_0 - p_{max}) \leq m \leq m_0$, respectively $H_I^{n_t}[m] \approx H_I^{\prime n_t}$, $\forall (m_0 + 1) \leq m \leq (m_0 + p_{max})$.

On the one hand, on the frequency band $[m_0 - p_{max}, m_0]$, the RZF-CI precoder is build according to the useful channel $H_U^{n_t}$ and to the interference channel $H_I^{n_t}$. On the other hand, on the frequency band $[m_0 + 1, m_0 + p_{max}]$, the RZF-CI precoder is build according to the useful channel $H_U^{n_t}$ and to the interference channel $H_I^{\prime n_t}$. Therefore, the precoding vector and the normalization factor are equal to $W_U^{n_t}$ and ξ_W respectively for $(m_0 - p_{max}) \leq m \leq m_0$ and equal to $W_U^{\prime n_t}$ and ξ_W' respectively for $(m_0 + 1) \leq m \leq (m_0 + p_{max})$.

Using the previous approximations and notations and according to (9.15) and (9.26), it

comes:

$$\frac{\left|y^I_{Acc}\right|^2}{\left|y^I_{Acc,Sync}\right|^2} \approx \left(\sum_{p=0}^{p_{max}} \alpha_p\right) + \left(\sum_{p=-p_{max}}^{-1} \alpha_p\right) \times \frac{\xi_W \left|\sum_{n_t=0}^{N_t-1} W_U'^{,n_t} H_{I,0}^{n_t}\right|^2}{\xi'_W \left|\sum_{n_t=0}^{N_t-1} W_U^{n_t} H_{I,0}^{n_t}\right|^2} + \varepsilon_{|y^I_{Acc}|^2}$$

$$\approx 0.725 + 0.225 \times \frac{\xi_W \left|\sum_{n_t=0}^{N_t-1} W_U'^{,n_t} H_{I,0}^{n_t}\right|^2}{\xi'_W \left|\sum_{n_t=0}^{N_t-1} W_U^{n_t} H_{I,0}^{n_t}\right|^2} + \varepsilon_{|y^I_{Acc}|^2}, \tag{9.32}$$

where $\varepsilon_{|y^I_{Acc}|^2}$ denotes the interference power coming from the sub-carriers $m \notin [m_0 - p_{max}, m_0 + p_{max}]$. According to (9.25), the value of $\varepsilon_{|y^I_{Acc}|^2}$ is small compared to the rest of the interference power. Thus, it comes:

$$\left|y^I_{Acc}\right|^2 > \left|y^I_{Acc,Sync}\right|^2, \tag{9.33}$$

if:

$$\frac{\xi_W \left|\sum_{n_t=0}^{N_t-1} W_U'^{,n_t} H_{I,0}^{n_t}\right|^2}{\xi'_W \left|\sum_{n_t=0}^{N_t-1} W_U^{n_t} H_{I,0}^{n_t}\right|^2} > \frac{0.275 - \varepsilon_{|y^I_{Acc}|^2}}{0.225}. \tag{9.34}$$

A time desynchronization of the signals can thus increase the interference power on the UE side when the considered sub-carrier is at the edge of the considered UE band.

Taking into account all the sub-carriers used for the considered UE, the potential increase of the interference power only comes from the edge sub-carriers. Therefore, one can expect to have a relatively contained impact of the time desynchronization. In the next part, simulation results allow confirming this expectation and evaluating the impact of the time desynchronization.

9.3 Simulations

In order to numerically evaluate the impact of a time desynchronization between the BH link and the access link, simulations are conducted in this part using the QuaDRiGa 3D channel simulator [40, 54]. The simulation parameters are similar to those of Chapter 8. The BH antenna arrays are identical uniform rectangular arrays facing each other and the channel model used between these two antenna arrays is the 3GPP 38.901 RMa LOS spatial channel model [52]. Moreover, the UE is equipped with an omni-directional antenna, is located on the straight line joining the BS 1 and the BS 2 and the 3GPP 38.901 RMa LOS spatial channel model is also used between the BS 1 and the considered UE. For the sake of simplicity, a perfect channel estimation is assumed. In a first part, the OFDM modulation is used for the BH link. Unlike in Chapter 8, a time desynchronization is added between the BH link and the access link. The simulation parameters are given by Table 9.1.

Table 9.1: Simulation parameters.

FFT size	1024
Number of sub-carriers for the BH link	600
Number of sub-carriers for the considered UE	120
Inter-carrier spacing	15 kHz
CP length for the OFDM modulation	4.7 μs
Desynchronization between the BH link and the access link	$\Delta t = T_0/2 + T_{CP} = 38\mu s$
Center frequency	4 GHz
BH antenna arrays: number of antennas per column	16
BH antenna arrays: number of antennas per line	4
BH antenna arrays: inter-antenna spacing	10 cm
BH antenna arrays: half-power beamwidth	30°
BH antenna arrays: height	35 m
Distance between the BS 1 and the BS 2	10 km
UE: height	1.5 m

9.3.1 BER with a Time Desynchronization

The impact of a time desynchronization is evaluated by comparing the BER on the UE side with the RZF-CI precoder, considering a perfect time synchronization ($\Delta t = 0\mu s$) and considering a large time desynchronization ($\Delta t = T_0/2 + T_{CP} = 38\mu s$). The OFDM modulation is used for both the BH link and the access link with similar parameters. The results are given by Figure 9.5 for a distance of (a) $d_{BS-UE} = 500m$ and (b) $d_{BS-UE} = 1000m$ between the BS 1 and the considered UE. Additionally, Figure 9.6 gives the results for a distance of (a) $d_{BS-UE} = 1500m$ and (b) $d_{BS-UE} = 2000m$ between the BS 1 and the considered UE.

Figures 9.5 and 9.6 allow visualizing the impact of a time desynchronization between the BH link and the access link in terms of BER on the UE side. In particular, the BER curve with a large desynchronization is slightly shifted compared with the BER curve with a perfect synchronization. This shift reaches its maximum value when the distance between the BS 1 and the UE is of 500 m and decreases when the distance d_{BS-UE} increases. Indeed, the interference power decreases with the increase of d_{BS-UE} as shown by Figure 8.2 in Chapter 8. However, this impact remains largely contained (below 1 dB) and can be considered as negligible whatever the value of d_{BS-UE}. The conclusion of these results is that the BH link and the access link can be completely desynchronized while maintaining the same performance.

9.3.2 Extention with the FBMC/OQAM Modulation

According to the previous results, the BH link and the access link can be completely asynchronous with a negligible impact on the BER on the UE side. From this assessment, one can envisioned to use different simulation parameters for the access link and for the BH link, such as a different CP length. Additionally, an alternative multi-carrier modulation can be

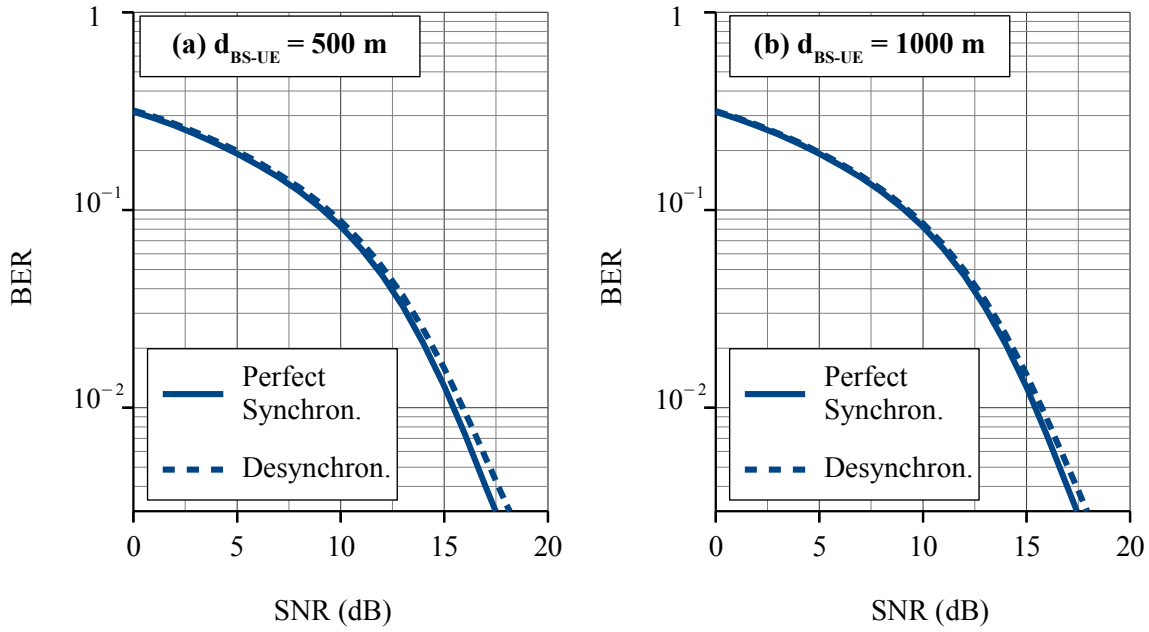

Figure 9.5: BER on the UE side with the RZF-CI precoder as a function of the SNR (dB), considering a perfect time synchronization ($\Delta t = 0\mu s$) and considering a large time desynchronization ($\Delta t = T_0/2 + T_{CP} = 38\mu s$). The OFDM modulation is used for both the BH link and the access link and the distance between the BS 1 and the considered UE is (a) $d_{BS-UE} = 500m$ and (b) $d_{BS-UE} = 1000m$.

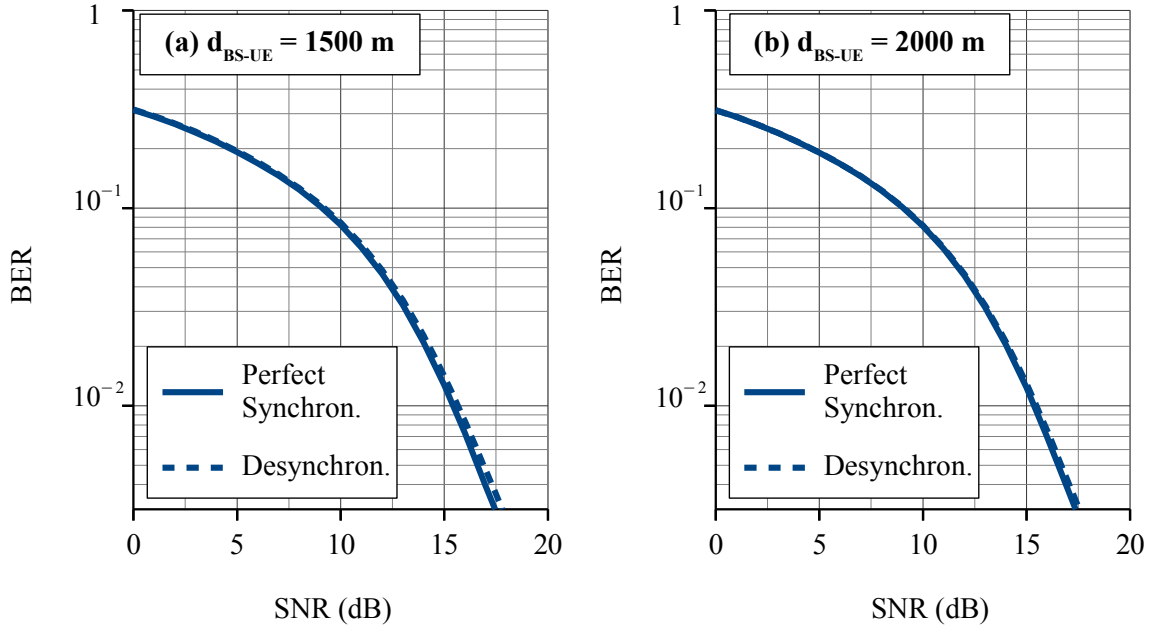

Figure 9.6: BER on the UE side with the RZF-CI precoder as a function of the SNR (dB), considering a perfect time synchronization ($\Delta t = 0\mu s$) and considering a large time desynchronization ($\Delta t = T_0/2 + T_{CP} = 38\mu s$). The OFDM modulation is used for both the BH link and the access link and the distance between the BS 1 and the considered UE is (a) $d_{BS-UE} = 1500m$ and (b) $d_{BS-UE} = 2000m$.

used for the BH link. In this part, the use of the FBMC/OQAM modulation for the BH link is proposed in order to improve the spectral efficiency. Indeed, as stated in part 2.2, this modulation does not use any CP and, as it presents a better frequency localization than the OFDM modulation, the number of guard band sub-carriers can be reduced.

Therefore, the BER on the UE side is now evaluated with the RZF-CI precoder, considering the FBMC/OQAM modulation for the BH link. The TFL1 prototype filter is used because of its small length ($K = 1$), which leads to a lower complexity compared to longer prototype filters. Moreover, a large time desynchronization ($\Delta t = 38\mu s$) is considered between the BH link and the access link. The performance in this context are compared with the performance of a system using the OFDM modulation for the BH link and the access link and with a perfect time synchronization. The results are given by Figure 9.7 for a distance of (a) $d_{BS-UE} = 500m$ and (b) $d_{BS-UE} = 1000m$ between the BS 1 and the considered UE. Additionally, Figure 9.8 gives the results for a distance of (a) $d_{BS-UE} = 1500m$ and (b) $d_{BS-UE} = 2000m$ between the BS 1 and the considered UE.

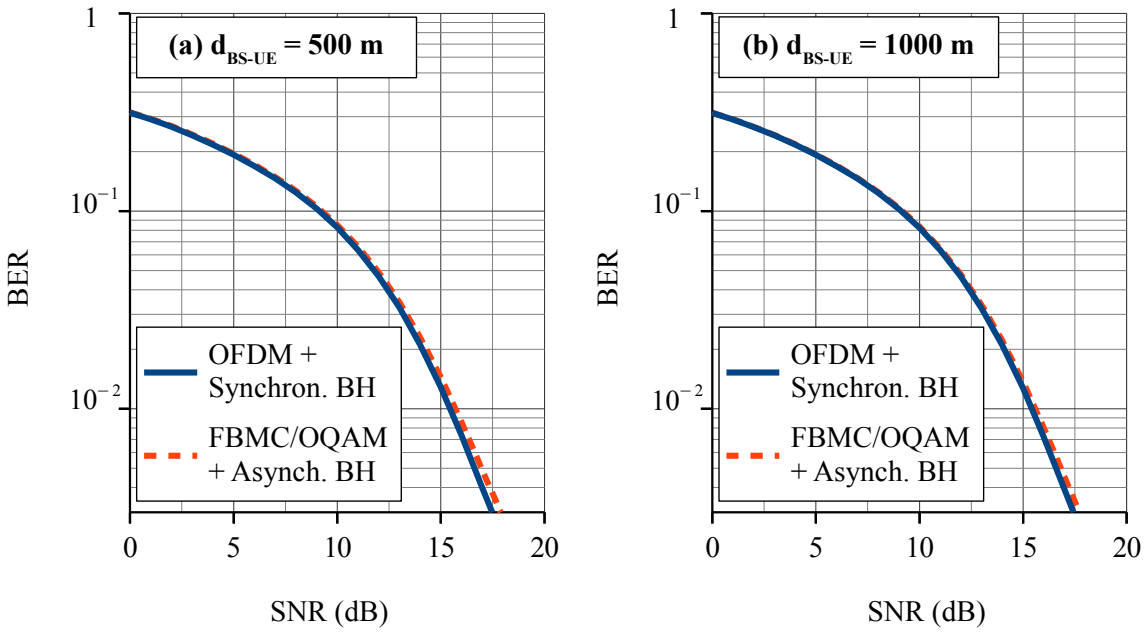

Figure 9.7: BER on the UE side with the RZF-CI precoder as a function of the SNR (dB). A BH link with the OFDM modulation and a perfect time synchronization as well as a BH link with the FBMC/OQAM modulation and a large time desynchronization ($\Delta t = 38\mu s$) are considered. The distance between the BS 1 and the considered UE is (a) $d_{BS-UE} = 500m$ and (b) $d_{BS-UE} = 1000m$.

In Figures 9.7 and 9.8, one can see that the results are similar whatever the value of d_{BS-UE}. Indeed, the use of an asynchronous wireless BH link with the FBMC/OQAM modulation does not affect significantly the BER on the UE side. To conclude, the FBMC/OQAM modulation can be used for the BH link in an asynchronous manner in order to increase the spectral efficiency. Indeed, the FBMC/OQAM modulation does not use any CP and, as it

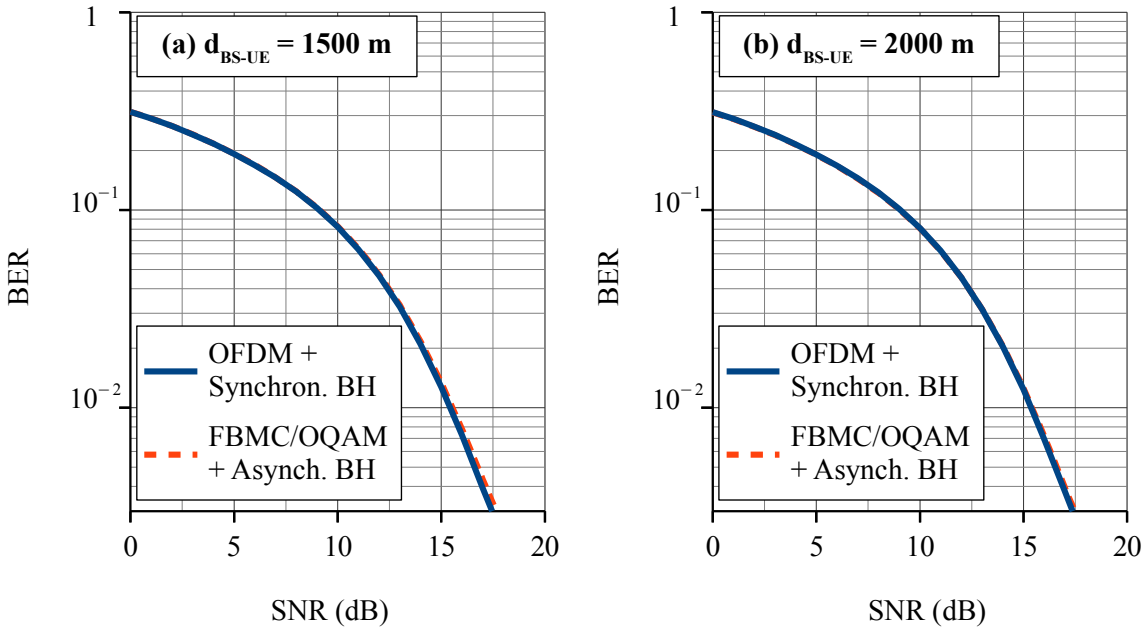

Figure 9.8: BER on the UE side with the RZF-CI precoder as a function of the SNR (dB). A BH link with the OFDM modulation and a perfect time synchronization as well as a BH link with the FBMC/OQAM modulation and a large time desynchronization ($\Delta t = 38\mu s$) are considered. The distance between the BS 1 and the considered UE is (a) $d_{BS-UE} = 1500m$ and (b) $d_{BS-UE} = 2000m$.

presents a better frequency localization than the OFDM modulation, the number of guard band sub-carriers can be reduced.

9.4 Conclusion

In the previous Chapter, a new massive MIMO precoder, the RZF-CI precoder, was proposed in order to provide a long-range in-band wireless BH link. The results rely on the assumption of a perfect time synchronization between the BH link and the access link. In this Chapter, the impact of a time desynchronization between the BH link and the access link is evaluated. Additionally, the use of the FBMC/OQAM modulation for the BH link is also envisioned in order to improve the spectral efficiency.

The analytical study shows that a time desynchronization between the BH link and the access link induces a spreading in the frequency domain of the interference on the UE side, coming from the BH link. However, when the BH link and the access link are asynchronous, only the edge sub-carriers of the considered UE induce additional interference power from the BH link. Simulation results show that the impact of a time desynchronization between the BH link and the access link on the BER is negligible and thus an asynchronous BH link can be considered. Using this degree of freedom, the FBMC/OQAM modulation can be used for the BH link without adding additional interference in order to improve the spectral efficiency

of the BH link.

Summary of this Chapter:

- The **impact of a time desynchronization** between the BH link and the access link is evaluated.
- **A time desynchronization between the BH link and the access link induces a spreading in the frequency domain of the interference** on the UE side, coming from the BH link.
- When **the BH link and the access link are asynchronous**, **only the edge sub-carriers of the considered UE induce additional interference power** from the BH link.
- Simulation results show that **the impact of a time desynchronization between the BH link and the access link on the BER is negligible and thus an asynchronous BH link can be considered**.
- **The FBMC/OQAM modulation can be used for the BH link without adding additional interference**. This leads to **a better spectral efficiency for the BH link** compared to the OFDM modulation because the FBMC/OQAM modulation does not need any CP and because the number of guard band sub-carriers can be reduced in this context.

General Conclusion and Prospects

With the increase of the global data traffic, the multiplication of the connected devices and the diversification of the communication types, a new generation of cellular networks will be needed in the coming years. That is why 5G is currently under development with very challenging requirements. This thesis took place in the context of the development of this new generation of cellular networks. In particular, the very promising massive MIMO systems, which uses a large number of antennas, have been studied along with an alternative multi-carrier modulation, the FBMC/OQAM modulation. This thesis focused on two use cases, V2X communications where the speed of the users can reach 500 km/h and communications in wide underserved areas where a wireless Backhaul (BH) link can reduce the cost of deployment of the cellular networks.

Massive MIMO for Vehicular Applications

With the development of connected cars and the deployment of high speed railways, the vehicular communications or V2X communications have gained a growing interest. That is why 5G should be able to connect users with a speed up to 500 km/h. This high speed raises a number of issues and, in particular, the Doppler effect creates interference which have a detrimental impact on the performance of the systems. In this thesis, the use of a massive MIMO system with a low complexity MRC receiver was proposed in order to counteract this effect. Moreover, the use of the FBMC/OQAM modulation instead of the OFDM modulation was discussed.

The work conducted on this topic leads to the following contributions.

- In a NLOS environment, the Doppler effect is limited to the Doppler spread. With the OFDM modulation, the SIR in a massive MIMO system combined with a simple MRC receiver has been analytically studied. Thereby, **it has been proven that increasing the number of receive antennas in this context allows reducing**

the interference induced by this Doppler spread.

- Simulation results have shown that **the reduction of the impact of the Doppler spread induced by the increase of the number of receive antennas is significant**. **In a NLOS environment**, the impact of the Doppler spread in terms of BER becomes negligible even with a relatively low number of receive antennas (N_r= 16). In this context, **the OFDM modulation and the FBMC/OQAM modulation lead to similar performance in terms of BER**.

- **In the presence of a LOS component**, a Doppler shift adds to the Doppler spread. An analytical study of the asymptotic system capacity, when the number of receive antennas tends to infinity, allowed evaluating the impact of this Doppler shift in a massive MIMO system combined with a simple MRC receiver. Therefore, unlike the Doppler spread, **the Doppler shift impacts the performance of the OFDM system** even with a high number of receive antennas. In this context, **the FBMC/OQAM modulation** offers a better robustness against the Doppler shift and simulation results highlighted that this modulation **significantly outperforms the OFDM modulation in terms of BER**.

This work paves the way for further studies. In particular, investigating the following aspects would be interesting.

- A perfect channel estimation is assumed in this work for the sake of simplicity. However, it is clear that the time selectivity of the propagation channel impacts the channel estimation process. Therefore, a study of the **channel estimation techniques in high mobility environment** would be of particular interest to complete this work.

- A single-antenna user is considered in this study. A potential approach for future studies would be to extend this work with **multi-user communications and multi-antenna users**. In this context, combining techniques such as ZF or MMSE could be used as an alternative to MRC.

- The antennas were considered as uncorrelated in this work. However, taking into account **the correlation between the antennas** on the BS side would lead to more suitable results in practice. A GSCM can be used to this end.

Massive MIMO for Wireless Backhaul (BH)

In wide underserved areas, or low ARPU areas, the deployment of the cellular networks is highly constrained in terms of cost. In particular, the deployment of the BH links, between the core network and the BSs, is an expensive task especially when an optical fiber is used. In this thesis, a massive MIMO system was proposed in order to provide a long-range wireless BH link between two BSs, the first one acting as a relay for the second one. Thereby, no

wired connection is needed to link the second BS to the core network. Moreover, an in-band communication was proposed for this link, meaning that the same frequency band is used for the BH link and the access link.

The contributions of this thesis regarding this topic are the following.

- When using an **in-band** communication for the BH link, **interference appears on the UE side** and significantly impacts its performance if they are not controlled. **A new massive MIMO precoder called RZF-CI was defined in order to control this interference, unlike the classical MRT precoder**, so that a minimum system capacity is guaranteed for each UE. Moreover, analytical and simulation results have shown that **the proposed RZF-CI precoder significantly outperforms the ZF precoder in terms of received power on the receiving BS**.
- **The impact of a time desynchronization between the BH link and the access link** was then studied. On the UE side, it has been shown that **such a desynchronization spreads the interference due to the in-band communication in the frequency domain**. However, **only the edge sub-carriers of the considered UE suffer from this spreading**. In this context, simulation results have shown that **the BH link can be completely desynchronized while maintaining the same performance**.
- **The use of the FBMC/OQAM modulation for the BH link** has been proposed in order to **improve the spectral efficiency** and thereby **increase the BH data rate**. Simulation results confirmed the interest of such a solution as **it does not induce additional interference**.

Further studies could complete this topic. Indeed, the following aspect could be investigated.

- This study focused on the downlink of a TDD system. Therefore, **the uplink** of the proposed system can be investigated. Moreover, one could also study the case of a **FDD system**.
- FDMA is considered in this study to separate the UEs. It would be interesting to extend the study with **MU-MIMO systems**, where multiple UEs share the same frequency-time resources.
- **Hybrid beamforming** systems could be considered in order to reduce the complexity of the proposed solution. Thus, the integration of the RZF-CI precoding technique in a hybrid beamforming system can be studied.

Publications

Peer Reviewed International Journal Paper

- A. Bazin, B. Jahan and M. Hélard, "Doppler Effect Reduction in an OFDM System Thanks to Massive MIMO," in *IEEE Access*, vol. 6, pp. 38498-38511, 2018.

Peer Reviewed National Conference

- A. Bazin, B. Jahan and M. Hélard, "Réduction de l'impact de l'effet Doppler dans un système OFDM grâce au « massive MIMO »," in *26th GRETSI Seminar*, September 2017.

Peer Reviewed International Conference

- A. Bazin, B. Jahan and M. Hélard, "Impact of the Doppler effect on the capacity of massive MIMO uplink systems: OFDM versus FBMC/OQAM," in *24th International Conference on Telecommunications (ICT)*, May 2017.

Patent

- A. Bazin and B. Jahan, "Système de télécommunication avec système d'antennes massive-MIMO pour un lien backhaul sans fil et procédé correspondant", french patent under submission.

Part IV

Appendices

A

Description of the Channel Models

Extended Vehicular A (EVA)

The EVA channel model is a NLOS channel model defined for vehicular LTE communications in [92, 93]. Its tap delays and corresponding average power are given in Table A.1.

Table A.1: Tap delays and corresponding average power of the EVA channel model.

Tap Delay (ns)	0	30	150	310	370	710	1090	1730	2510
Average Power (dB)	0.0	-1.5	-1.4	-3.6	-0.6	-9.1	-7.0	-12.0	-16.9

Extended Typical Urban (ETU)

The ETU channel model is a NLOS channel model defined for urban LTE communications in [92, 93]. Its tap delays and corresponding average power are given in Table A.2.

Table A.2: Tap delays and corresponding average power of the ETU channel model.

Tap Delay (ns)	0	50	120	200	230	500	1600	2300	5000
Average Power (dB)	-1.0	-1.0	-1.0	0.0	0.0	0.0	-3.0	-5.0	-7.0

Rural Area with 4 taps (RA4)

The RA4 channel model is a channel model with a LOS component having a Rician K-factor of 6.7. It is defined in [98] and its tap delays and corresponding average power are given in Table A.3.

Table A.3: Tap delays and corresponding average power of the RA4 channel model.

Tap Delay (ns)	0	200	400	600
Average Power (dB)	0.0	-2.0	-10.0	-20.0

Concerning Chapter 5

B.1 Proof of Proposition 1

With non-correlated antennas, it can be seen that:

$$\begin{aligned} E\left[\left|\left(\tilde{\mathbf{H}}_0^{(N_r)}\right)^H \tilde{\mathbf{H}}_p^{(N_r)}\right|^2\right] &= E\left[\left|\sum_{n_r=0}^{N_r-1}\left(\tilde{H}_0^{n_r}\right)^* \tilde{H}_p^{n_r}\right|^2\right] \\ &= N_r E\left[\left|\left(\tilde{H}_0^{n_r}\right)^* \tilde{H}_p^{n_r}\right|^2\right] + N_r(N_r-1)\left|E\left[\left(\tilde{H}_0^{n_r}\right)^* \tilde{H}_p^{n_r}\right]\right|^2 \\ &= N_r\tilde{E}_p^{(2)} + N_r(N_r-1)\left|\tilde{E}_p^{(1)}\right|^2. \end{aligned} \tag{B.1}$$

Then, the special case where $p = 0$ gives:

$$E\left[\left\|\tilde{\mathbf{H}}_0^{(N_r)}\right\|^4\right] = N_r\tilde{E}_0^{(2)} + N_r(N_r-1)\left|\tilde{E}_0^{(1)}\right|^2. \tag{B.2}$$

With $(N_r{+}1)$ receive antennas, the equation (B.1) becomes:

$$E\left[\left|\left(\tilde{\mathbf{H}}_0^{(N_r+1)}\right)^H \tilde{\mathbf{H}}_p^{(N_r+1)}\right|^2\right] = (N_r+1)\tilde{E}_p^{(2)} + (N_r+1)N_r\left|\tilde{E}_p^{(1)}\right|^2, \tag{B.3}$$

and when $p = 0$:

$$E\left[\left\|\tilde{\mathbf{H}}_0^{(N_r+1)}\right\|^4\right] = (N_r+1)\tilde{E}_0^{(2)} + (N_r+1)N_r\left|\tilde{E}_0^{(1)}\right|^2. \tag{B.4}$$

Using (B.1), (B.2), (B.3) and (B.4), the inequation (5.10) becomes:

$$\begin{aligned}\left((N_r+1)\tilde{E}_0^{(2)}+(N_r+1)N_r\left|\tilde{E}_0^{(1)}\right|^2\right)\times\sum_{p\in\Omega_p^*}\left(N_r\tilde{E}_p^{(2)}+N_r(N_r-1)\left|\tilde{E}_p^{(1)}\right|^2\right)\\ >\left(N_r\tilde{E}_0^{(2)}+N_r(N_r-1)\left|\tilde{E}_0^{(1)}\right|^2\right)\times\sum_{p\in\Omega_p^*}\left((N_r+1)\tilde{E}_p^{(2)}+(N_r+1)N_r\left|\tilde{E}_p^{(1)}\right|^2\right).\end{aligned} \tag{B.5}$$

Divided by $N_r(N_r+1)$, the inequation (B.5) becomes:

$$\begin{aligned}\left(\tilde{E}_0^{(2)}+N_r\left|\tilde{E}_0^{(1)}\right|^2\right)\times\sum_{p\in\Omega_p^*}\left(\tilde{E}_p^{(2)}+(N_r-1)\left|\tilde{E}_p^{(1)}\right|^2\right)\\ >\left(\tilde{E}_0^{(2)}+(N_r-1)\left|\tilde{E}_0^{(1)}\right|^2\right)\times\sum_{p\in\Omega_p^*}\left(\tilde{E}_p^{(2)}+N_r\left|\tilde{E}_p^{(1)}\right|^2\right).\end{aligned} \tag{B.6}$$

Then, subtracting

$$\left(\tilde{E}_0^{(2)}+N_r\left|\tilde{E}_0^{(1)}\right|^2\right)\times\sum_{p\in\Omega_p^*}\left(\tilde{E}_p^{(2)}+N_r\left|\tilde{E}_p^{(1)}\right|^2\right)$$

on both sides of (B.6), it comes:

$$\left(\tilde{E}_0^{(2)}+N_r\left|\tilde{E}_0^{(1)}\right|^2\right)\times\sum_{p\in\Omega_p^*}\left(-\left|\tilde{E}_p^{(1)}\right|^2\right)>\left(-\left|\tilde{E}_0^{(1)}\right|^2\right)\times\sum_{p\in\Omega_p^*}\left(\tilde{E}_p^{(2)}+N_r\left|\tilde{E}_p^{(1)}\right|^2\right). \tag{B.7}$$

Finally, adding $N_r\left|\tilde{E}_0^{(1)}\right|^2\left(\sum_{p\in\Omega_p^*}\left|\tilde{E}_p^{(1)}\right|^2\right)$, (B.7) becomes:

$$\tilde{E}_0^{(2)}\left(\sum_{p\in\Omega_p^*}-\left|\tilde{E}_p^{(1)}\right|^2\right)>\left(-\left|\tilde{E}_0^{(1)}\right|^2\right)\left(\sum_{p\in\Omega_p^*}\tilde{E}_p^{(2)}\right), \tag{B.8}$$

which is equivalent to:

$$\frac{\left|\tilde{E}_0^{(1)}\right|^2}{\sum_{p\in\Omega_p^*}\left|\tilde{E}_p^{(1)}\right|^2}>\frac{\tilde{E}_0^{(2)}}{\sum_{p\in\Omega_p^*}\tilde{E}_p^{(2)}}. \tag{B.9}$$

B.2 Development of $\tilde{\mathbf{H}}_\mathbf{p}$

Using (5.14) and (5.15) in (4.15) the components $\tilde{H}_p$ can be described as follows:

$$\tilde{H}_p=\sum_{(l,n)\in\Omega_{l,n}}\tilde{H}_{p,l,n}^{(1)}+j\tilde{H}_{p,l,n}^{(2)}, \tag{B.10}$$

with:

$$\tilde{H}_{p,l,n}^{(i)}=\sqrt{\frac{P_{h,l}}{N_l}}\frac{1}{T_0}\left(\int_0^{T_0}\cos\left(2\pi f_{l,n}^{(i)}t+\theta_{l,n}^{(i)}\right)e^{-j2\pi pF_0t}dt\right)\exp\left[-j2\pi(m_0-p)F_0\tau_l\right]. \tag{B.11}$$

Using the Fourier transform, the equation (B.11) becomes:

$$\tilde{H}_{p,l,n}^{(i)} = \sqrt{\frac{P_{h,l}}{N_l}}\frac{1}{T_0} \times \mathcal{F}_{f=pF_0}\left[\cos\left(2\pi f_{l,n}^{(i)}t + \theta_{l,n}^{(i)}\right).\Pi_{T_0}\left(t-\frac{T_0}{2}\right)\right] \times \exp\left[-j2\pi(m_0-p)F_0\tau_l\right], \tag{B.12}$$

with $\Pi_T(t)$ defined by (2.4). As:

$$\begin{aligned}
\mathcal{F}\left[\cos\left(2\pi f_{l,n}^{(i)}t + \theta_{l,n}^{(i)}\right)\right] &= \mathcal{F}\left[\cos\left(2\pi f_{l,n}^{(i)}\left(t + \frac{\theta_{l,n}^{(i)}}{2\pi f_{l,n}^{(i)}}\right)\right)\right], \\
&= \frac{1}{2}\left(\delta\left(f - f_{l,n}^{(i)}\right) + \delta\left(f + f_{l,n}^{(i)}\right)\right)\exp\left[j2\pi f\frac{\theta_{l,n}^{(i)}}{2\pi f_{l,n}^{(i)}}\right], \\
&= \frac{1}{2}\left(e^{j\theta_{l,n}^{(i)}}\delta\left(f - f_{l,n}^{(i)}\right) + e^{-j\theta_{l,n}^{(i)}}\delta\left(f + f_{l,n}^{(i)}\right)\right),
\end{aligned} \tag{B.13}$$

and as:

$$\mathcal{F}\left[\Pi_{T_0}\left(t-\frac{T_0}{2}\right)\right] = T_0\,\mathrm{sinc}\left(T_0 f\right)\exp\left[-j2\pi f\frac{T_0}{2}\right], \tag{B.14}$$

it comes:

$$\mathcal{F}\left[\cos\left(2\pi f_{l,n}^{(i)}t + \theta_{l,n}^{(i)}\right).\Pi_{T_0}\left(t-\frac{T_0}{2}\right)\right] = \mathcal{F}\left[\cos\left(2\pi f_{l,n}^{(i)}t + \theta_{l,n}^{(i)}\right)\right] * \mathcal{F}\left[\Pi_{T_0}\left(t-\frac{T_0}{2}\right)\right] \tag{B.15}$$

and thus:

$$\begin{aligned}
&\mathcal{F}_{f=pF_0}\left[\cos\left(2\pi f_{l,n}^{(i)}t + \theta_{l,n}^{(i)}\right).\Pi_{T_0}\left(t-\tfrac{T_0}{2}\right)\right] \\
&\quad= \int_{\mathbb{R}}\frac{1}{2}\left(e^{j\theta_{l,n}^{(i)}}\delta\left(f - f_{l,n}^{(i)}\right) + e^{-j\theta_{l,n}^{(i)}}\delta\left(f + f_{l,n}^{(i)}\right)\right) \\
&\qquad\qquad \times T_0\,\mathrm{sinc}\left(T_0\left(pF_0 - f\right)\right)\exp\left[-j2\pi\left(pF_0 - f\right)\tfrac{T_0}{2}\right]df, \\
&\quad= \frac{T_0}{2}e^{-j\pi p}\mathrm{sinc}\left(p - \frac{f_{l,n}^{(i)}}{F_0}\right)\exp\left[j\left(\pi\tfrac{f_{l,n}^{(i)}}{F_0} + \theta_{l,n}^{(i)}\right)\right] \\
&\qquad\qquad + \frac{T_0}{2}e^{-j\pi p}\mathrm{sinc}\left(p + \frac{f_{l,n}^{(i)}}{F_0}\right)\exp\left[-j\left(\pi\tfrac{f_{l,n}^{(i)}}{F_0} + \theta_{l,n}^{(i)}\right)\right].
\end{aligned} \tag{B.16}$$

Therefore the equation (B.12) becomes:

$$\begin{aligned}
\tilde{H}_{p,l,n}^{(i)} &= \sqrt{\frac{P_{h,l}}{4N_l}}(-1)^p\mathrm{sinc}\left(p - \frac{f_{l,n}^{(i)}}{F_0}\right)\exp\left[j\left(\pi\tfrac{f_{l,n}^{(i)}}{F_0} + \theta_{l,n}^{(i)}\right)\right]\exp\left[-j2\pi(m_0-p)F_0\tau_l\right] \\
&+ \sqrt{\frac{P_{h,l}}{4N_l}}(-1)^p\mathrm{sinc}\left(p + \frac{f_{l,n}^{(i)}}{F_0}\right)\exp\left[-j\left(\pi\tfrac{f_{l,n}^{(i)}}{F_0} + \theta_{l,n}^{(i)}\right)\right]\exp\left[-j2\pi(m_0-p)F_0\tau_l\right].
\end{aligned} \tag{B.17}$$

Finally, using the notations in (5.18) and (5.19), the equation (B.17) can be rewritten as follows:

$$\tilde{H}_{p,l,n}^{(i)} = \sqrt{\frac{P_{h,l}}{4N_l}}(-1)^p \left(S_{p,l,n}^{(i)-} e^{j\theta_{l,n}'^{(i)}} + S_{p,l,n}^{(i)+} e^{-j\theta_{l,n}'^{(i)}} \right) \exp\left[-j2\pi(m_0 - p)F_0\tau_l\right]. \tag{B.18}$$

B.3 Development of $\tilde{\mathbf{E}}_{\mathbf{p}}^{(\mathbf{1})}$

Using (5.21) and (5.23), the expression of $(\tilde{H}_{0,l,n}^{(i)})^* \tilde{H}_{p,l,n}^{(i)}$ is:

$$(\tilde{H}_{0,l,n}^{(i)})^* \tilde{H}_{p,l,n}^{(i)} = \frac{P_{h,l}}{2N_l}(-1)^p S_{0,l,n}^{(i)-} \cos\left(\theta_{l,n}'^{(i)}\right) \left(S_{p,l,n}^{(i)-} e^{j\theta_{l,n}'^{(i)}} + S_{p,l,n}^{(i)+} e^{-j\theta_{l,n}'^{(i)}} \right) \exp\left[j2\pi p F_0 \tau_l\right]. \tag{B.19}$$

Knowing that $\theta_{l,n}'^{(i)}$ is a random variable having a uniform distribution over the interval $]0, 2\pi]$, it comes:

$$E\left[\cos\left(\theta_{l,n}'^{(i)}\right) e^{\pm j\theta_{l,n}'^{(i)}}\right] = E\left[\frac{1}{2}\left(e^{j\theta_{l,n}'^{(i)}} + e^{-j\theta_{l,n}'^{(i)}}\right) e^{\pm j\theta_{l,n}'^{(i)}}\right] = \frac{1}{2}. \tag{B.20}$$

Therefore, the expression of $E[(\tilde{H}_{0,l,n}^{(i)})^* \tilde{H}_{p,l,n}^{(i)}]$ is:

$$E\left[\left(\tilde{H}_{0,l,n}^{(i)}\right)^* \tilde{H}_{p,l,n}^{(i)}\right] = \frac{P_{h,l}}{4N_l}(-1)^p S_{0,l,n}^{(i)-} \left(S_{p,l,n}^{(i)-} + S_{p,l,n}^{(i)+} \right) \exp\left[j2\pi p F_0 \tau_l\right]. \tag{B.21}$$

Finally, using (B.21) in (5.27), it comes:

$$\tilde{E}_p^{(1)} = (-1)^p \sum_{(l,n)\in\Omega_{l,n}} \frac{P_{h,l}}{4N_l} \left(S_{0,l,n}^{(1)-} \left(S_{p,l,n}^{(1)-} + S_{p,l,n}^{(1)+} \right) + S_{0,l,n}^{(2)-} \left(S_{p,l,n}^{(2)-} + S_{p,l,n}^{(2)+} \right) \right) \exp\left[j2\pi p F_0 \tau_l\right]. \tag{B.22}$$

B.4 Development of $\tilde{\mathbf{E}}_{\mathbf{p}}^{(\mathbf{2})}$

In order to develop $\tilde{E}_p^{(2)}$, the expressions of $E[|\tilde{H}_{p,l,n}|^2]$, $E[\tilde{H}_{0,l,n}\tilde{H}_{p,l,n}]$ and $E[|\tilde{H}_{0,l,n}^*\tilde{H}_{p,l,n}|^2]$ are first given thereafter.

Expression of $\mathbf{E}[|\tilde{\mathbf{H}}_{\mathbf{p,l,n}}|^{\mathbf{2}}]$

Using (5.20), the expression of $|\tilde{H}_{p,l,n}|^2$ is:

$$\left|\tilde{H}_{p,l,n}\right|^2 = \left(\tilde{H}_{p,l,n}^{(1)} + j\tilde{H}_{p,l,n}^{(2)}\right)^* \left(\tilde{H}_{p,l,n}^{(1)} + j\tilde{H}_{p,l,n}^{(2)}\right). \tag{B.23}$$

Therefore, as $\tilde{H}_{p,l,n}^{(1)}$ and $\tilde{H}_{p,l,n}^{(2)}$ are two independent variables and according to (5.25), it comes:

$$E\left[\left|\tilde{H}_{p,l,n}\right|^2\right] = E\left[\left|\tilde{H}_{p,l,n}^{(1)}\right|^2\right] + E\left[\left|\tilde{H}_{p,l,n}^{(2)}\right|^2\right]. \tag{B.24}$$

Using (5.21), it comes:

$$\begin{aligned}\left|\tilde{H}_{p,l,n}^{(i)}\right|^2 &= \frac{P_{h,l}}{4N_l}\left|S_{p,l,n}^{(i)-}e^{j\theta_{l,n}^{\prime(i)}} + S_{p,l,n}^{(i)+}e^{-j\theta_{l,n}^{\prime(i)}}\right|^2, \\ &= \frac{P_{h,l}}{4N_l}\left(\left(S_{p,l,n}^{(i)-}\right)^2 + \left(S_{p,l,n}^{(i)+}\right)^2 + S_{p,l,n}^{(i)-}S_{p,l,n}^{(i)+}\left(e^{j2\theta_{l,n}^{\prime(i)}} + e^{-j2\theta_{l,n}^{\prime(i)}}\right)\right).\end{aligned} \tag{B.25}$$

Therefore, as $\theta_{l,n}^{\prime(i)}$ is a random variable having a uniform distribution over the interval $]0, 2\pi]$, it comes:

$$E\left[\left|\tilde{H}_{p,l,n}^{(i)}\right|^2\right] = \frac{P_{h,l}}{4N_l}\left(\left(S_{p,l,n}^{(i)-}\right)^2 + \left(S_{p,l,n}^{(i)+}\right)^2\right), \tag{B.26}$$

and thus, according to (B.24):

$$E\left[\left|\tilde{H}_{p,l,n}\right|^2\right] = \frac{P_{h,l}}{4N_l}\left(\left(S_{p,l,n}^{(1)-}\right)^2 + \left(S_{p,l,n}^{(1)+}\right)^2 + \left(S_{p,l,n}^{(2)-}\right)^2 + \left(S_{p,l,n}^{(2)+}\right)^2\right). \tag{B.27}$$

Finally, according to (5.22), when $p = 0$, the expression of $E[|\tilde{H}_{p,l,n}|^2]$ becomes:

$$E\left[\left|\tilde{H}_{0,l,n}\right|^2\right] = \frac{P_{h,l}}{2N_l}\left(\left(S_{0,l,n}^{(1)-}\right)^2 + \left(S_{0,l,n}^{(2)-}\right)^2\right). \tag{B.28}$$

Expression of $\mathbf{E[\tilde{H}_{0,l,n}\tilde{H}_{p,l,n}]}$

Using (5.20), the expression of $\tilde{H}_{0,l,n}\tilde{H}_{p,l,n}$ is:

$$\tilde{H}_{0,l,n}\tilde{H}_{p,l,n} = \left(\tilde{H}_{0,l,n}^{(1)} + j\tilde{H}_{0,l,n}^{(2)}\right)\left(\tilde{H}_{p,l,n}^{(1)} + j\tilde{H}_{p,l,n}^{(2)}\right). \tag{B.29}$$

Therefore, as $\tilde{H}_{p,l,n}^{(1)}$ and $\tilde{H}_{p,l,n}^{(2)}$ are two independent variables and according to (5.25), it comes:

$$E\left[\tilde{H}_{0,l,n}\tilde{H}_{p,l,n}\right] = E\left[\tilde{H}_{0,l,n}^{(1)}\tilde{H}_{p,l,n}^{(1)}\right] - E\left[\tilde{H}_{0,l,n}^{(2)}\tilde{H}_{p,l,n}^{(2)}\right]. \tag{B.30}$$

Using (5.21), it comes:

$$\tilde{H}_{0,l,n}^{(i)}\tilde{H}_{p,l,n}^{(i)} = \frac{P_{h,l}}{2N_l}(-1)^p S_{0,l,n}^{(i)-}\cos\left(\theta_{l,n}^{\prime(i)}\right)\left(S_{p,l,n}^{(i)-}e^{j\theta_{l,n}^{\prime(i)}} + S_{p,l,n}^{(i)+}e^{-j\theta_{l,n}^{\prime(i)}}\right)e^{-j2\pi(2m_0-p)F_0\tau_l}. \tag{B.31}$$

Therefore, as $\theta_{l,n}^{\prime(i)}$ is a random variable having a uniform distribution over the interval $]0, 2\pi]$, it comes:

$$E\left[\cos\left(\theta_{l,n}^{\prime(i)}\right)e^{\pm j\theta_{l,n}^{\prime(i)}}\right] = E\left[\frac{1}{2}\left(e^{j\theta_{l,n}^{\prime(i)}} + e^{-j\theta_{l,n}^{\prime(i)}}\right)e^{\pm j\theta_{l,n}^{\prime(i)}}\right] = \frac{1}{2}, \tag{B.32}$$

and thus:

$$E\left[\tilde{H}^{(i)}_{0,l,n}\tilde{H}^{(i)}_{p,l,n}\right] = \frac{P_{h,l}}{4N_l}(-1)^p S^{(i)-}_{0,l,n}\left(S^{(i)-}_{p,l,n} + S^{(i)+}_{p,l,n}\right)e^{-j2\pi(2m_0-p)F_0\tau_l}. \tag{B.33}$$

Finally, according to (B.30), the expression of $E[\tilde{H}_{0,l,n}\tilde{H}_{p,l,n}]$ is:

$$\begin{aligned} &E\left[\tilde{H}_{0,l,n}\tilde{H}_{p,l,n}\right] \\ &\quad = \frac{P_{h,l}}{4N_l}(-1)^p\left(S^{(1)-}_{0,l,n}\left(S^{(1)-}_{p,l,n} + S^{(1)+}_{p,l,n}\right) - S^{(2)-}_{0,l,n}\left(S^{(2)-}_{p,l,n} + S^{(2)+}_{p,l,n}\right)\right)e^{-j2\pi(2m_0-p)F_0\tau_l}. \end{aligned} \tag{B.34}$$

Expression of $\mathbf{E}[|\tilde{\mathbf{H}}^*_{\mathbf{0,l,n}}\tilde{\mathbf{H}}_{\mathbf{p,l,n}}|^{\mathbf{2}}]$

Using (5.23), the expression of $|\tilde{H}^{(i)}_{0,l,n}|^2$ is:

$$\left|\tilde{H}^{(i)}_{0,l,n}\right|^2 = \frac{P_{h,l}}{N_l}\left(S^{(i)-}_{0,l,n}\right)^2\cos^2\left(\theta'^{(i)}_{l,n}\right), \tag{B.35}$$

which is a real value. Moreover, using the equations (5.20) and (B.35), the expression of $|\tilde{H}^*_{0,l,n}\tilde{H}_{p,l,n}|^2$ is:

$$\begin{aligned} \left|\tilde{H}^*_{0,l,n}\tilde{H}_{p,l,n}\right|^2 &= \left|\tilde{H}_{0,l,n}\right|^2\left|\tilde{H}_{p,l,n}\right|^2, \\ &= \left(\left|\tilde{H}^{(1)}_{0,l,n}\right|^2 + \left|\tilde{H}^{(2)}_{0,l,n}\right|^2\right)\left(\tilde{H}^{(1)}_{p,l,n} + j\tilde{H}^{(2)}_{p,l,n}\right)^*\left(\tilde{H}^{(1)}_{p,l,n} + j\tilde{H}^{(2)}_{p,l,n}\right), \\ &= \left(\left|\tilde{H}^{(1)}_{0,l,n}\right|^2 + \left|\tilde{H}^{(2)}_{0,l,n}\right|^2\right) \\ &\qquad \times\left(\left|\tilde{H}^{(1)}_{p,l,n}\right|^2 + j\left(\tilde{H}^{(1)}_{p,l,n}\right)^*\tilde{H}^{(2)}_{p,l,n} - j\left(\tilde{H}^{(2)}_{p,l,n}\right)^*\tilde{H}^{(1)}_{p,l,n} + \left|\tilde{H}^{(2)}_{p,l,n}\right|^2\right). \end{aligned} \tag{B.36}$$

Therefore, as $\tilde{H}^{(1)}_{p,l,n}$ and $\tilde{H}^{(2)}_{p,l,n}$ are two independent variables and according to (5.25), it comes:

$$\begin{aligned} E\left[\left|\tilde{H}^*_{0,l,n}\tilde{H}_{p,l,n}\right|^2\right] &= E\left[\left|\tilde{H}^{(1)}_{0,l,n}\right|^2\left|\tilde{H}^{(1)}_{p,l,n}\right|^2\right] + E\left[\left|\tilde{H}^{(2)}_{0,l,n}\right|^2\left|\tilde{H}^{(2)}_{p,l,n}\right|^2\right] \\ &+ E\left[\left|\tilde{H}^{(1)}_{0,l,n}\right|^2\right]E\left[\left|\tilde{H}^{(2)}_{p,l,n}\right|^2\right] + E\left[\left|\tilde{H}^{(2)}_{0,l,n}\right|^2\right]E\left[\left|\tilde{H}^{(1)}_{p,l,n}\right|^2\right]. \end{aligned} \tag{B.37}$$

Using (B.25) and (B.35), it comes:

$$\begin{aligned} E\left[\left|\tilde{H}^{(i)}_{0,l,n}\right|^2\left|\tilde{H}^{(i)}_{p,l,n}\right|^2\right] &= \frac{P^2_{h,l}}{4N^2_l}\left(S^{(i)-}_{0,l,n}\right)^2\left(\left(S^{(i)-}_{p,l,n}\right)^2 + \left(S^{(i)+}_{p,l,n}\right)^2\right)E\left[\cos^2\left(\theta'^{(i)}_{l,n}\right)\right] \\ &+ \frac{P^2_{h,l}}{4N^2_l}\left(S^{(i)-}_{0,l,n}\right)^2 S^{(i)-}_{p,l,n}S^{(i)+}_{p,l,n}E\left[\cos^2\left(\theta'^{(i)}_{l,n}\right)\left(e^{j2\theta'^{(i)}_{l,n}} + e^{-j2\theta'^{(i)}_{l,n}}\right)\right]. \end{aligned} \tag{B.38}$$

Moreover, as $\theta'^{(i)}_{l,n}$ is a random variable having a uniform distribution over the interval $]0, 2\pi]$,

it comes:

$$E\left[\cos^2\left(\theta_{l,n}^{\prime(i)}\right)\right] = \frac{1}{2}, \tag{B.39}$$

and:

$$E\left[\cos^2\left(\theta_{l,n}^{\prime(i)}\right) e^{\pm j2\theta_{l,n}^{\prime(i)}}\right] = E\left[\frac{1}{4}\left(e^{j2\theta_{l,n}^{\prime(i)}} + e^{-j2\theta_{l,n}^{\prime(i)}} + 2\right) e^{\pm j2\theta_{l,n}^{\prime(i)}}\right] = \frac{1}{4}. \tag{B.40}$$

Therefore, the expression of $E[|\tilde{H}_{0,l,n}^{(i)}|^2|\tilde{H}_{p,l,n}^{(i)}|^2]$ is:

$$E\left[\left|\tilde{H}_{0,l,n}^{(i)}\right|^2\left|\tilde{H}_{p,l,n}^{(i)}\right|^2\right] = \frac{P_{h,l}^2}{8N_l^2}\left(S_{0,l,n}^{(i)-}\right)^2\left(\left(S_{p,l,n}^{(i)-}\right)^2 + \left(S_{p,l,n}^{(i)+}\right)^2 + S_{p,l,n}^{(i)-}S_{p,l,n}^{(i)+}\right). \tag{B.41}$$

Finally, using (B.41) and (B.26) in (B.37), it comes:

$$\begin{aligned} E\left[\left|\tilde{H}_{0,l,n}^{*}\tilde{H}_{p,l,n}\right|^2\right] &= \frac{P_{h,l}^2}{8N_l^2}\left(S_{0,l,n}^{(1)-}\right)^2\left(\left(S_{p,l,n}^{(1)-}\right)^2 + \left(S_{p,l,n}^{(1)+}\right)^2 + S_{p,l,n}^{(1)-}S_{p,l,n}^{(1)+}\right) \\ &+ \frac{P_{h,l}^2}{8N_l^2}\left(S_{0,l,n}^{(2)-}\right)^2\left(\left(S_{p,l,n}^{(2)-}\right)^2 + \left(S_{p,l,n}^{(2)+}\right)^2 + S_{p,l,n}^{(2)-}S_{p,l,n}^{(2)+}\right) \\ &+ \frac{P_{h,l}^2}{8N_l^2}\left(S_{0,l,n}^{(1)-}\right)^2\left(\left(S_{p,l,n}^{(2)-}\right)^2 + \left(S_{p,l,n}^{(2)+}\right)^2\right) \\ &+ \frac{P_{h,l}^2}{8N_l^2}\left(S_{0,l,n}^{(2)-}\right)^2\left(\left(S_{p,l,n}^{(1)-}\right)^2 + \left(S_{p,l,n}^{(1)+}\right)^2\right), \end{aligned} \tag{B.42}$$

and thus:

$$\begin{aligned} E\left[\left|\tilde{H}_{0,l,n}^{*}\tilde{H}_{p,l,n}\right|^2\right] &= \frac{P_{h,l}^2}{8N_l^2}\left(\left(S_{0,l,n}^{(1)-}\right)^2 + \left(S_{0,l,n}^{(2)-}\right)^2\right)\left(\left(S_{p,l,n}^{(1)-}\right)^2 + \left(S_{p,l,n}^{(1)+}\right)^2 + \left(S_{p,l,n}^{(2)-}\right)^2 + \left(S_{p,l,n}^{(2)+}\right)^2\right) \\ &+ \frac{P_{h,l}^2}{8N_l^2}\left(\left(S_{0,l,n}^{(1)-}\right)^2 S_{p,l,n}^{(1)-}S_{p,l,n}^{(1)+} + \left(S_{0,l,n}^{(2)-}\right)^2 S_{p,l,n}^{(2)-}S_{p,l,n}^{(2)+}\right). \end{aligned} \tag{B.43}$$

Expression of $\tilde{\mathbf{E}}_{\mathbf{p}}^{(\mathbf{2})}$

Using the expressions of $E[|\tilde{H}_{0,l,n}|^2]$ in (B.28) and $E[|\tilde{H}_{p,l,n}|^2]$ in (B.27), the expression of $E[|\tilde{H}_{0,l,n}|^2]E[|\tilde{H}_{p,l,n}|^2]$ can be deduced:

$$\begin{aligned} &E\left[\left|\tilde{H}_{0,l,n}\right|^2\right]E\left[\left|\tilde{H}_{p,l,n}\right|^2\right] \\ &\quad = \frac{P_{h,l}^2}{8N_l^2}\left(\left(S_{0,l,n}^{(1)-}\right)^2 + \left(S_{0,l,n}^{(2)-}\right)^2\right)\left(\left(S_{p,l,n}^{(1)-}\right)^2 + \left(S_{p,l,n}^{(1)+}\right)^2 + \left(S_{p,l,n}^{(2)-}\right)^2 + \left(S_{p,l,n}^{(2)+}\right)^2\right). \end{aligned} \tag{B.44}$$

Moreover, as $\tilde{H}_{p,l,n}^{(i)}$ and $\tilde{H}_{p',l',n'}^{(i')}$ are independent variables if $(i,l,n) \neq (i',l',n')$ and according to (5.25), it comes:

$$\left|E\left[\tilde{H}_{0,l,n}^{*}\tilde{H}_{p,l,n}\right]\right|^2 = \left|E\left[\left(\tilde{H}_{0,l,n}^{(1)}\right)^{*}\tilde{H}_{p,l,n}^{(1)}\right] + E\left[\left(\tilde{H}_{0,l,n}^{(2)}\right)^{*}\tilde{H}_{p,l,n}^{(2)}\right]\right|^2, \tag{B.45}$$

and thus, using the expression of $E[(\tilde{H}^{(i)}_{0,l,n})^* \tilde{H}^{(i)}_{p,l,n}]$ in (B.21), the expression of $|E[\tilde{H}^*_{0,l,n}\tilde{H}_{p,l,n}]|^2$ can be deduced:

$$\left|E\left[\tilde{H}^*_{0,l,n}\tilde{H}_{p,l,n}\right]\right|^2 = \frac{P^2_{h,l}}{16N_l^2}\left(S^{(1)-}_{0,l,n}\left(S^{(1)-}_{p,l,n}+S^{(1)+}_{p,l,n}\right)+S^{(2)-}_{0,l,n}\left(S^{(2)-}_{p,l,n}+S^{(2)+}_{p,l,n}\right)\right)^2. \quad \text{(B.46)}$$

Then, the expression of $E[\tilde{H}_{0,l,n}\tilde{H}_{p,l,n}]$ in equation (B.34) gives the following expression for $|E\left[\tilde{H}_{0,l,n}\tilde{H}_{p,l,n}\right]|^2$:

$$\left|E\left[\tilde{H}_{0,l,n}\tilde{H}_{p,l,n}\right]\right|^2 = \frac{P^2_{h,l}}{16N_l^2}\left(S^{(1)-}_{0,l,n}\left(S^{(1)-}_{p,l,n}+S^{(1)+}_{p,l,n}\right)-S^{(2)-}_{0,l,n}\left(S^{(2)-}_{p,l,n}+S^{(2)+}_{p,l,n}\right)\right)^2. \quad \text{(B.47)}$$

Therefore, using the equations (B.43), (B.44), (B.46) and (B.47), it comes:

$$\begin{aligned}
&E\left[\left|\tilde{H}^*_{0,l,n}\tilde{H}_{p,l,n}\right|^2\right] - E\left[\left|\tilde{H}_{0,l,n}\right|^2\right]E\left[\left|\tilde{H}_{p,l,n}\right|^2\right] - \left|E\left[\tilde{H}^*_{0,l,n}\tilde{H}_{p,l,n}\right]\right|^2 - \left|E\left[\tilde{H}_{0,l,n}\tilde{H}_{p,l,n}\right]\right|^2 \\
&\quad = \frac{P^2_{h,l}}{8N_l^2}\left(\left(S^{(1)-}_{0,l,n}\right)^2 S^{(1)-}_{p,l,n}S^{(1)+}_{p,l,n} + \left(S^{(2)-}_{0,l,n}\right)^2 S^{(2)-}_{p,l,n}S^{(2)+}_{p,l,n}\right) \\
&\qquad - \frac{P^2_{h,l}}{8N_l^2}\left(\left(S^{(1)-}_{0,l,n}\right)^2\left(S^{(1)-}_{p,l,n}+S^{(1)+}_{p,l,n}\right)^2 + \left(S^{(2)-}_{0,l,n}\right)^2\left(S^{(2)-}_{p,l,n}+S^{(2)+}_{p,l,n}\right)^2\right).
\end{aligned} \quad \text{(B.48)}$$

Finally, using (B.48), (B.27), (B.28), (B.21) and (B.34), the equation (5.34) becomes the equation (5.35).

C

Concerning Chapter 6

C.1 Development of $\check{\mathbf{E}}_{\mathbf{p}}^{(\mathbf{1})}$ for the OFDM Modulation

Using (4.3) in (4.16), it comes:

$$\check{H}_p^{n_r} = \frac{1}{T_0}\left(\int_0^{T_0} \sqrt{\check{P}_{h,0}} e^{j\theta^{n_r}} e^{-j2\pi\left(pF_0 - f_D^{shift}\right)t} dt\right) \exp\left[-j2\pi(m_0-p)F_0\tau_0\right]. \tag{C.1}$$

Using the Fourier transform, the previous equation becomes:

$$\check{H}_p^{n_r} = \frac{1}{T_0}\sqrt{\check{P}_{h,0}}\, e^{j\theta^{n_r}} \times \mathcal{F}_{f=(pF_0 - f_D^{shift})}\left[\Pi_{T_0}\left(t-\frac{T_0}{2}\right)\right] \times \exp\left[-j2\pi(m_0-p)F_0\tau_0\right], \tag{C.2}$$

with $\Pi_T(t)$ defined by (2.4). As:

$$\mathcal{F}\left[\Pi_{T_0}\left(t-\frac{T_0}{2}\right)\right] = T_0\,\mathrm{sinc}\left(T_0 f\right)\exp\left[-j2\pi f\frac{T_0}{2}\right], \tag{C.3}$$

it comes:

$$\check{H}_p^{n_r} = \sqrt{\check{P}_{h,0}}\, e^{j\theta^{n_r}}\; S_p^{shift}\; e^{-j\pi\left(p-\frac{f_D^{shift}}{F_0}\right)}\; \exp\left[-j2\pi(m_0-p)F_0\tau_0\right], \tag{C.4}$$

using the notations in (6.7). Finally, as $\exp(-j\pi p) = (-1)^p$, it comes:

$$\check{E}_p^{(1)} = \left(\check{H}_0^{n_r}\right)^* \check{H}_p^{n_r} = (-1)^p\; \check{P}_{h,0}\; S_0^{shift}\; S_p^{shift}\; \exp\left[j2\pi pF_0\tau_0\right]. \tag{C.5}$$

C.2 Development of $\tilde{\mathbf{E}}_{\mathbf{p,q}}^{(\mathbf{1})}$ for the FBMC/OQAM Modulation

Using (6.17) and (6.18) in (4.35) the components $\tilde{H}_{p,q}^{n_r}$ can be described as follows:

$$\tilde{H}_{p,q}^{n_r} = \sum_{(l,n)\in\Omega_{l,n}} \tilde{H}_{p,q,l,n}^{n_r(1)} + j\tilde{H}_{p,q,l,n}^{n_r(2)}, \tag{C.6}$$

with:

$$\begin{aligned}\tilde{H}_{p,q,l,n}^{n_r(i)} &= e^{j(\phi_{p,q}-\phi_{0,0})}\sqrt{\frac{\tilde{P}_{h,l}}{N_l}}\left(\int_{\mathbb{R}} \cos\left(2\pi f_{l,n}^{(i)}t + \theta_{l,n}^{n_r(i)}\right) g\left(t\right) g\left(t-\tau_l+q\tfrac{T_0}{2}\right) e^{-j2\pi pF_0 t}dt\right)\\ &\times \exp\left[-j2\pi(m_0-p)F_0\tau_l\right].\end{aligned} \tag{C.7}$$

Using the Fourier transform, it comes:

$$\begin{aligned}\tilde{H}_{p,q,l,n}^{n_r(i)} &= e^{j(\phi_{p,q}-\phi_{0,0})}\sqrt{\frac{\tilde{P}_{h,l}}{N_l}} \times \mathcal{F}_{f=pF_0}\left[\cos\left(2\pi f_{l,n}^{(i)}t + \theta_{l,n}^{n_r(i)}\right).g\left(t\right) g\left(t-\tau_l+q\tfrac{T_0}{2}\right)\right]\\ &\times \exp\left[-j2\pi(m_0-p)F_0\tau_l\right].\end{aligned} \tag{C.8}$$

On the one hand:

$$\begin{aligned}\mathcal{F}\left[\cos\left(2\pi f_{l,n}^{(i)}t + \theta_{l,n}^{n_r(i)}\right)\right] &= \mathcal{F}\left[\cos\left(2\pi f_{l,n}^{(i)}\left(t+\frac{\theta_{l,n}^{n_r(i)}}{2\pi f_{l,n}^{(i)}}\right)\right)\right]\\ &= \frac{1}{2}\left(\delta\left(f-f_{l,n}^{(i)}\right)+\delta\left(f+f_{l,n}^{(i)}\right)\right)\exp\left[j2\pi f\frac{\theta_{l,n}^{n_r(i)}}{2\pi f_{l,n}^{(i)}}\right]\\ &= \frac{1}{2}\left(e^{j\theta_{l,n}^{n_r(i)}}\delta\left(f-f_{l,n}^{(i)}\right)+e^{-j\theta_{l,n}^{n_r(i)}}\delta\left(f+f_{l,n}^{(i)}\right)\right).\end{aligned} \tag{C.9}$$

On the other hand, as $g(t)$ is a real function and using (6.20):

$$\begin{aligned}\mathcal{F}\left[g\left(t\right) g\left(t-\tau_l+\tfrac{q}{2F_0}\right)\right] &= \int_{\mathbb{R}} g\left(t\right) g^*\left(t-\left(\tau_l-q\tfrac{T_0}{2}\right)\right) e^{j2\pi(-f)t}dt,\\ &= A_g\left(\tau_l-q\tfrac{T_0}{2},-f\right).\end{aligned} \tag{C.10}$$

Therefore:

$$\begin{aligned}&\mathcal{F}\left[\cos\left(2\pi f_{l,n}^{(i)}t + \theta_{l,n}^{n_r(i)}\right).g\left(t\right) g\left(t-\tau_l+q\tfrac{T_0}{2}\right)\right]\\ &\qquad = \mathcal{F}\left[\cos\left(2\pi f_{l,n}^{(i)}t + \theta_{l,n}^{n_r(i)}\right)\right] * \mathcal{F}\left[g\left(t\right) g\left(t-\tau_l+q\tfrac{T_0}{2}\right)\right],\end{aligned} \tag{C.11}$$

and:

$$\begin{aligned}\tilde{H}^{n_r(i)}_{p,q,l,n} &= e^{j(\phi_{p,q}-\phi_{0,0})}\sqrt{\frac{\tilde{P}_{h,l}}{N_l}} \\ &\times \left(\int_{\mathbb{R}} \frac{1}{2}\left(e^{j\theta^{n_r(i)}_{l,n}}\delta\left(f-f^{(i)}_{l,n}\right)+e^{-j\theta^{n_r(i)}_{l,n}}\delta\left(f+f^{(i)}_{l,n}\right)\right)A_g\left(\tau_l-q\tfrac{T_0}{2},f-pF0\right)df\right) \\ &\times \exp\left[-j2\pi(m_0-p)F_0\tau_l\right].\end{aligned} \tag{C.12}$$

Finally, using (6.21):

$$\tilde{H}^{n_r(i)}_{p,q,l,n} = \sqrt{\frac{\tilde{P}_{h,l}}{4N_l}}e^{j(\phi_{p,q}-\phi_{0,0})}\left(A^{(i)-}_{p,q,l,n}e^{j\theta^{n_r(i)}_{l,n}}+A^{(i)+}_{p,q,l,n}e^{-j\theta^{n_r(i)}_{l,n}}\right)\exp\left[-j2\pi(m_0-p)F_0\tau_l\right]. \tag{C.13}$$

Knowing that $\theta^{n_r(1)}_{l,n}$ and $\theta^{n_r(2)}_{l,n}$ are two independent random variables having a uniform distribution over the interval $]0,2\pi]$, it comes:

$$E\left[\tilde{H}^{n_r(i)}_{p,q,l,n}\right]=0, \tag{C.14}$$

and thus:

$$E\left[\tilde{H}^{n_r}_{p,q}\right]=0. \tag{C.15}$$

One can see that $\tilde{H}^{n_r(i)}_{p,q,l,n}$ and $\tilde{H}^{n_r(i')}_{p',q',l',n'}$ are independent variables if $(i,l,n)\neq(i',l',n')$. Therefore, it comes:

$$\tilde{E}^{(1)}_{p,q} = \sum_{(l,n)\in\Omega_{l,n}}\sum_{i\in\{1,2\}} E\left[\left(\tilde{H}^{n_r(i)}_{0,0,l,n}\right)^*\tilde{H}^{n_r(i)}_{p,q,l,n}\right]. \tag{C.16}$$

According to (C.13) the expression of $(\tilde{H}^{n_r(i)}_{0,0,l,n})^*\tilde{H}^{n_r(i)}_{p,q,l,n}$ is:

$$\begin{aligned}\left(\tilde{H}^{n_r(i)}_{0,0,l,n}\right)^*\tilde{H}^{n_r(i)}_{p,q,l,n} &= \frac{\tilde{P}_{h,l}}{4N_l}e^{j(\phi_{p,q}-\phi_{0,0})}\left(\left(A^{(i)-}_{0,0,l,n}\right)^*e^{-j\theta^{n_r(i)}_{l,n}}+\left(A^{(i)+}_{0,0,l,n}\right)^*e^{j\theta^{n_r(i)}_{l,n}}\right) \\ &\times \left(A^{(i)-}_{p,q,l,n}e^{j\theta^{n_r(i)}_{l,n}}+A^{(i)+}_{p,q,l,n}e^{-j\theta^{n_r(i)}_{l,n}}\right)\exp\left[j2\pi pF_0\tau_l\right].\end{aligned} \tag{C.17}$$

Therefore, knowing that $\theta^{n_r(1)}_{l,n}$ and $\theta^{n_r(2)}_{l,n}$ are two independent random variables having a uniform distribution over the interval $]0,2\pi]$, it comes:

$$E\left[\left(\tilde{H}^{n_r(i)}_{0,0,l,n}\right)^*\tilde{H}^{n_r(i)}_{p,q,l,n}\right] = e^{j(\phi_{p,q}-\phi_{0,0})}\frac{\tilde{P}_{h,l}}{4N_l}\left(\left(A^{(i)-}_{0,0,l,n}\right)^*A^{(i)-}_{p,q,l,n}+\left(A^{(i)+}_{0,0,l,n}\right)^*A^{(i)+}_{p,q,l,n}\right)e^{j2\pi pF_0\tau_l}, \tag{C.18}$$

and:

$$\tilde{E}^{(1)}_{p,q} = e^{j(\phi_{p,q}-\phi_{0,0})}\sum_{(l,n)\in\Omega_{l,n}}\frac{\tilde{P}_{h,l}}{4N_l}\left(\sum_{i\in\{1,2\}}\left(\left(A^{(i)-}_{0,0,l,n}\right)^*A^{(i)-}_{p,q,l,n}+\left(A^{(i)+}_{0,0,l,n}\right)^*A^{(i)+}_{p,q,l,n}\right)\right)e^{j2\pi pF_0\tau_l}. \tag{C.19}$$

C.3 Development of $\check{\mathbf{E}}^{(\mathbf{1})}_{\mathbf{p,q}}$ for the FBMC/OQAM Modulation

Using (4.3) in (4.36), it comes:

$$\check{H}^{n_r}_{p,q} = \sqrt{\check{P}_{h,0}} e^{j\theta^{n_r}} e^{j(\phi_{p,q}-\phi_{0,0})} \left(\int_{\mathbb{R}} g\left(t\right) g\left(t - \tau_0 + q\frac{T_0}{2}\right) e^{-j2\pi\left(pF_0 - f_D^{shift}\right)t} dt \right) e^{-j2\pi(m_0-p)F_0\tau_0}. \tag{C.20}$$

Using (6.20), the previous equation becomes:

$$\check{H}^{n_r}_{p,q} = \sqrt{\check{P}_{h,0}} e^{j\theta^{n_r}} e^{j(\phi_{p,q}-\phi_{0,0})} A_g\left(\tau_0 - q\frac{T_0}{2}, -F_0\left(p - \frac{f_D^{shift}}{F_0}\right)\right) e^{-j2\pi(m_0-p)F_0\tau_0}, \tag{C.21}$$

and the notations in (6.21) give:

$$\check{H}^{n_r}_{p,q} = \sqrt{\check{P}_{h,0}}\; e^{j\theta^{n_r}}\; e^{j(\phi_{p,q}-\phi_{0,0})}\; A^{shift}_{p,q}\; e^{-j2\pi(m_0-p)F_0\tau_0}. \tag{C.22}$$

Finally, it comes:

$$\check{E}^{(1)}_{p,q} = \left(\check{H}^{n_r}_{0,0}\right)^* \check{H}^{n_r}_{p,q} = \check{P}_{h,0}\; e^{j(\phi_{p,q}-\phi_{0,0})}\; \left(A^{shift}_{0,0}\right)^* A^{shift}_{p,q}\; e^{j2\pi pF_0\tau_0}. \tag{C.23}$$

D

Concerning Chapter 8

D.1 Solution of the Problem (8.30)

Using (8.28) in (8.8), it comes:

$$\begin{aligned}
\left|y_{BH}^{U}(\alpha)\right|^2 &= P_U\sigma_c^2\frac{\left|(1+\alpha)\left\|\mathbf{H}_U\right\| - |\Gamma_H|^2\left\|\mathbf{H}_U\right\|\right|^2}{(1+\alpha)^2 - 2(1+\alpha)|\Gamma_H|^2 + |\Gamma_H|^2} \\
&= \left(P_U\left\|\mathbf{H}_U\right\|^2\right)\times\sigma_c^2\times\frac{\left((1+\alpha)-|\Gamma_H|^2\right)^2}{\left((1+\alpha)-|\Gamma_H|^2\right)^2 + |\Gamma_H|^2 - |\Gamma_H|^4} \qquad \text{(D.1)} \\
&= \left(P_U\left\|\mathbf{H}_U\right\|^2\right)\times\sigma_c^2\times\left(1-\frac{|\Gamma_H|^2\left(1-|\Gamma_H|^2\right)}{\left(1+\alpha-|\Gamma_H|^2\right)^2 + |\Gamma_H|^2\left(1-|\Gamma_H|^2\right)}\right).
\end{aligned}$$

Therefore, as $0 \leq |\Gamma_H|^2 \leq 1$, the value of $\left|y_{BH}^{U}(\alpha)\right|^2$ increases with the increase of α and is thus an increasing function.

Additionally, using (8.28) in (8.4), it comes:

$$\begin{aligned}
\Delta(\alpha) &= 1+\frac{P_I\sigma_c^2}{\sigma_b^2}\frac{\left|(1+\alpha)\Gamma_H\left\|\mathbf{H}_I\right\| - \Gamma_H\left\|\mathbf{H}_I\right\|\right|^2}{(1+\alpha)^2 - 2(1+\alpha)|\Gamma_H|^2 + |\Gamma_H|^2} \\
&= 1+\left(P_I\left\|\mathbf{H}_I\right\|^2\right)\times\frac{\sigma_c^2}{\sigma_b^2}\times\frac{\alpha^2|\Gamma_H|^2}{\alpha^2 + 2(1-|\Gamma_H|^2)\alpha + (1-|\Gamma_H|^2)} \qquad \text{(D.2)} \\
&= 1+\left(P_I\left\|\mathbf{H}_I\right\|^2\right)\times\frac{\sigma_c^2}{\sigma_b^2}\times\frac{|\Gamma_H|^2}{1+2(1-|\Gamma_H|^2)\frac{1}{\alpha}+(1-|\Gamma_H|^2)\frac{1}{\alpha^2}}.
\end{aligned}$$

As $0 \leq |\Gamma_H|^2 \leq 1$, the value of $\Delta(\alpha)$ also increases with the increase of α and is thus an increasing function.

Let us define the variable Δ_∞ as follows:

$$\Delta_\infty = \Delta(\alpha \to +\infty) = 1 + |\Gamma_H|^2 \left(P_I \left\|\mathbf{H}_I\right\|^2\right) \times \frac{\sigma_c^2}{\sigma_b^2}. \tag{D.3}$$

If $\Delta_\infty \leq \Delta_{max}$, the value of $\left|y_{BH}^U(\alpha)\right|^2$ is not limited by the value of $\Delta(\alpha)$ and can reach its maximum value when $\alpha \to +\infty$. If $\Delta_\infty > \Delta_{max}$, the value of $\left|y_{BH}^U(\alpha)\right|^2$ is limited by the value of $\Delta(\alpha)$. As both $\left|y_{BH}^U(\alpha)\right|^2$ and $\Delta(\alpha)$ are increasing functions, the problem (8.30) is solved in this context when $\Delta(\alpha) = \Delta_{max}$. Therefore, the optimal value for α is:

$$\alpha = \begin{cases} +\infty & \text{if} \quad \Delta_\infty \leq \Delta_{max}, \\ \alpha_0 & \text{if} \quad \Delta_\infty > \Delta_{max}, \end{cases} \tag{D.4}$$

α_0 being the positive solution of the equation $\Delta(\alpha) = \Delta_{max}$. This equality is equivalent to:

$$\Delta(\alpha) - 1 = \Delta_{max} - 1, \tag{D.5}$$

or, using (D.3) in (D.2):

$$\frac{\alpha^2}{\alpha^2 + 2(1 - |\Gamma_H|^2)\alpha + (1 - |\Gamma_H|^2)} = \frac{\Delta_{max} - 1}{\Delta_\infty - 1}. \tag{D.6}$$

The equation (D.6) is equivalent to the following second order equation:

$$\left(1 - \frac{\Delta_\infty - 1}{\Delta_{max} - 1}\right) \alpha^2 + 2(1 - |\Gamma_H|^2)\alpha + (1 - |\Gamma_H|^2) = 0, \tag{D.7}$$

which has a unique positive solution when $\Delta_\infty > \Delta_{max}$:

$$\alpha_0 = \frac{(1 - |\Gamma_H|^2) + \sqrt{(1 - |\Gamma_H|^2)\left(\frac{\Delta_\infty - 1}{\Delta_{max} - 1} - |\Gamma_H|^2\right)}}{\frac{\Delta_\infty - 1}{\Delta_{max} - 1} - 1}. \tag{D.8}$$

D.2 Received Power with the RZF-CI Precoder

If $\Delta_\infty \leq \Delta_{max}$, then:

$$\mathbf{W}_U = \frac{\mathbf{H}_U^H}{\left\|\mathbf{H}_U\right\|}, \tag{D.9}$$

and using (8.8), it comes:

$$\left|y_{BH}^U\right|^2 = \left(P_U \left\|\mathbf{H}_U\right\|^2\right) \times \sigma_c^2. \tag{D.10}$$

If $\Delta_\infty > \Delta_{max}$, using (8.34) in (8.8), the received power on the BS 2 is equal to:

$$\begin{aligned}
\left|y_{BH}^{U}\right|^2 &= P_U\sigma_c^2 \frac{\left|(1+\alpha_0)\left\|\mathbf{H}_U\right\| - |\Gamma_H|^2 \left\|\mathbf{H}_U\right\|\right|^2}{(1+\alpha_0)^2 - 2(1+\alpha_0)|\Gamma_H|^2 + |\Gamma_H|^2} \\
&= \left(P_U \left\|\mathbf{H}_U\right\|^2\right) \times \sigma_c^2 \times \frac{\left((1+\alpha_0) - |\Gamma_H|^2\right)^2}{\left((1+\alpha_0) - |\Gamma_H|^2\right)^2 + |\Gamma_H|^2 - |\Gamma_H|^4} \qquad \text{(D.11)} \\
&= \left(P_U \left\|\mathbf{H}_U\right\|^2\right) \times \sigma_c^2 \times \left(1 - \frac{|\Gamma_H|^2\left(1-|\Gamma_H|^2\right)}{\left(1+\alpha_0-|\Gamma_H|^2\right)^2 + |\Gamma_H|^2\left(1-|\Gamma_H|^2\right)}\right).
\end{aligned}$$

Finally, the received power on the BS 2 is equal to:

$$\left|y_{BH}^{U}\right|^2 = \left(P_U \left\|\mathbf{H}_U\right\|^2\right) \times \sigma_c^2 \times \left(1 - \varepsilon.|\Gamma_H|^2\right), \qquad \text{(D.12)}$$

with:

$$\begin{aligned}
\varepsilon &= \left(\frac{\left(1+\alpha_0-|\Gamma_H|^2\right)^2}{1-|\Gamma_H|^2} + |\Gamma_H|^2\right)^{-1}, \\
&= \left((1-|\Gamma_H|^2) + 2\alpha_0 + \tfrac{\alpha_0^2}{1-|\Gamma_H|^2} + |\Gamma_H|^2\right)^{-1}, \qquad \text{(D.13)} \\
&= \left(1 + 2\alpha_0 + \frac{\alpha_0^2}{1-|\Gamma_H|^2}\right)^{-1}.
\end{aligned}$$

As $\alpha_0 \geq 0$ and $|\Gamma_H|^2 \leq 1$, it comes $0 \leq \varepsilon \leq 1$.

E

Concerning Chapter 9

Development of $\mathbf{y^I_{Acc}}$

As $T_{CP} < \Delta t < T_0$, using (9.4) in (9.7), it comes:

$$\begin{aligned} y^I_{Acc} &= \sum_{n_t=0}^{N_t-1} \sqrt{P_I} \sum_{q\in\{0,1\}} \sum_{p\in\Omega_p} \frac{W_U^{n_t}[m_0-p]}{\sqrt{\xi_W[m_0-p]}} c[m_0-p,-q] \\ &\times \sum_{l=0}^{L_h-1} h_{I,l}^{n_t} \int_{\mathbb{R}} \Pi_{mo-p,-q}(t-\Delta t-\tau_l) \left(\Pi^0_{m_0,0}(t)\right)^* dt, \end{aligned} \tag{E.1}$$

and thus:

$$y^I_{Acc} = y^I_{Acc,0} + y^I_{Acc,1}, \tag{E.2}$$

with:

$$\begin{aligned} y^I_{Acc,0} &= \sum_{n_t=0}^{N_t-1} \sqrt{P_I} \sum_{p\in\Omega_p} \frac{W_U^{n_t}[m_0-p]}{\sqrt{\xi_W[m_0-p]}} c[m_0-p,0] \\ &\times \sum_{l=0}^{L_h-1} h_{I,l}^{n_t} \int_{\mathbb{R}} \Pi_{mo-p,0}(t-\Delta t-\tau_l) \left(\Pi^0_{m_0,0}(t)\right)^* dt, \end{aligned} \tag{E.3}$$

and:

$$\begin{aligned} y^I_{Acc,1} &= \sum_{n_t=0}^{N_t-1} \sqrt{P_I} \sum_{p\in\Omega_p} \frac{W_U^{n_t}[m_0-p]}{\sqrt{\xi_W[m_0-p]}} c[m_0-p,-1] \\ &\times \sum_{l=0}^{L_h-1} h_{I,l}^{n_t} \int_{\mathbb{R}} \Pi_{mo-p,-1}(t-\Delta t-\tau_l) \left(\Pi^0_{m_0,0}(t)\right)^* dt. \end{aligned} \tag{E.4}$$

According to (2.2) and (2.3), it comes:

$$\begin{aligned} y^I_{Acc,0} &= \sum_{n_t=0}^{N_t-1} \sqrt{P_I} \sum_{p\in\Omega_p} \frac{W_U^{n_t}[m_0-p]}{\sqrt{\xi_W[m_0-p]}} c[m_0-p,0] \\ &\times \sum_{l=0}^{L_h-1} h_l^{n_t} \exp\left[j2\pi(m_0-p)F_0\left(-\Delta t-\tau_l\right)\right] \\ &\times \frac{1}{T_0}\left(\int_{\mathbb{R}} \Pi_{(T_0+T_{CP})}\left(t-\tfrac{T_0-T_{CP}}{2}-\Delta t-\tau_l\right)\Pi_{T_0}\left(t-\tfrac{T_0}{2}\right)e^{-j2\pi pF_0 t}dt\right), \end{aligned} \tag{E.5}$$

and:

$$\begin{aligned} y^I_{Acc,1} &= \sum_{n_t=0}^{N_t-1} \sqrt{P_I} \sum_{p\in\Omega_p} \frac{W_U^{n_t}[m_0-p]}{\sqrt{\xi_W[m_0-p]}} c[m_0-p,-1] \\ &\times \sum_{l=0}^{L_h-1} h_{I,l}^{n_t} \exp\left[j2\pi(m_0-p)F_0\left(T_0+T_{CP}-\Delta t-\tau_l\right)\right] \\ &\times \frac{1}{T_0}\left(\int_{\mathbb{R}} \Pi_{(T_0+T_{CP})}\left(t+\tfrac{T_0+3T_{CP}}{2}-\Delta t-\tau_l\right)\Pi_{T_0}\left(t-\tfrac{T_0}{2}\right)e^{-j2\pi pF_0 t}dt\right). \end{aligned} \tag{E.6}$$

Additionally, as $\Delta t \gg \tau_l$:

$$\begin{aligned} &\frac{1}{T_0}\left(\int_{\mathbb{R}} \Pi_{(T_0+T_{CP})}\left(t-\tfrac{T_0-T_{CP}}{2}-\Delta t-\tau_l\right)\Pi_{T_0}\left(t-\tfrac{T_0}{2}\right)e^{-j2\pi pF_0 t}dt\right) \\ &\quad= \frac{1}{T_0}\mathcal{F}_{f=\frac{p}{T_0}}\left[\Pi_{(T_0+T_{CP}-\Delta t-\tau_l)}\left(t-\tfrac{T_0+\Delta t+\tau_l-T_{CP}}{2}\right)\right], \\ &\quad= \frac{T_0+T_{CP}-\Delta t-\tau_l}{T_0}\mathrm{sinc}\left(p\tfrac{T_0+T_{CP}-\Delta t-\tau_l}{T_0}\right)\exp\left[-j\pi p\tfrac{T_0+\Delta t+\tau_l-T_{CP}}{T_0}\right], \\ &\quad\approx \left(1-\frac{\Delta t-T_{CP}}{T_0}\right)\mathrm{sinc}\left(p\left(1-\frac{\Delta t-T_{CP}}{T_0}\right)\right)\exp\left[-j\pi p\left(1+\tfrac{\Delta t-T_{CP}}{T_0}\right)\right], \end{aligned} \tag{E.7}$$

and:

$$\begin{aligned} &\frac{1}{T_0}\left(\int_{\mathbb{R}} \Pi_{(T_0+T_{CP})}\left(t+\tfrac{T_0+3T_{CP}}{2}-\Delta t-\tau_l\right)\Pi_{T_0}\left(t-\tfrac{T_0}{2}\right)e^{-j2\pi pF_0 t}dt\right) \\ &\quad= \frac{1}{T_0}\mathcal{F}_{f=\frac{p}{T_0}}\left[\Pi_{(\Delta t+\tau_l-T_{CP})}\left(t-\tfrac{\Delta t+\tau_l-T_{CP}}{2}\right)\right], \\ &\quad= \frac{\Delta t+\tau_l-T_{CP}}{T_0}\mathrm{sinc}\left(p\tfrac{\Delta t+\tau_l-T_{CP}}{T_0}\right)\exp\left[-j\pi p\tfrac{\Delta t+\tau_l-T_{CP}}{T_0}\right], \\ &\quad\approx \frac{\Delta t-T_{CP}}{T_0}\mathrm{sinc}\left(p\frac{\Delta t-T_{CP}}{T_0}\right)\exp\left[-j\pi p\frac{\Delta t-T_{CP}}{T_0}\right]. \end{aligned} \tag{E.8}$$

Therefore, it comes:

$$\begin{aligned} y^I_{Acc,0} &\approx \sqrt{P_I} \sum_{p\in\Omega_p} \frac{\sum_{n_t=0}^{N_t-1} W_U^{n_t}[m_0-p]H_{I,p}^{n_t}}{\sqrt{\xi_W[m_0-p]}} c[m_0-p,0]\exp\left[-j2\pi(m_0-p)F_0\Delta t\right] \\ &\times \left(1-\frac{\Delta t-T_{CP}}{T_0}\right)\mathrm{sinc}\left(p\left(1-\frac{\Delta t-T_{CP}}{T_0}\right)\right)\exp\left[-j\pi p\left(1+\frac{\Delta t-T_{CP}}{T_0}\right)\right], \end{aligned} \tag{E.9}$$

and:

$$\begin{aligned} y^I_{Acc,1} &\approx \sqrt{P_I} \sum_{p\in\Omega_p} \frac{\sum_{n_t=0}^{N_t-1} W_U^{n_t}[m_0-p]H_{I,p}^{n_t}}{\sqrt{\xi_W[m_0-p]}} c[m_0-p,-1] \\ &\times \exp\left[j2\pi(m_0-p)F_0\left(T_0+T_{CP}-\Delta t\right)\right] \\ &\times \frac{\Delta t-T_{CP}}{T_0}\mathrm{sinc}\left(p\frac{\Delta t-T_{CP}}{T_0}\right)\exp\left[-j\pi p\frac{\Delta t-T_{CP}}{T_0}\right], \end{aligned} \tag{E.10}$$

with:

$$H_{I,p}^{n_t} = \sum_{l=0}^{L_h-1} h_{I,l}^{n_t}\exp\left[-j2\pi(m_0-p)F_0\tau_l\right]. \tag{E.11}$$

Bibliography

[1] "IMT Vision – Framework and overall objectives of the future development of IMT for 2020 and beyond," Tech. Rep. M.2083-0, ITU-R, Sept. 2015.

[2] A. Osseiran, F. Boccardi, V. Braun, K. Kusume, P. Marsch, M. Maternia, O. Queseth, M. Schellmann, H. Schotten, H. Taoka, H. Tullberg, M. A. Uusitalo, B. Timus, and M. Fallgren, "Scenarios for 5g mobile and wireless communications: the vision of the METIS project," *IEEE Communications Magazine*, vol. 52, pp. 26–35, May 2014.

[3] F. Schaich, B. Sayrac, M. Schubert, H. Lin, K. Pedersen, M. Shaat, G. Wunder, and A. Georgakopoulos, "FANTASTIC 5g: 5g - PPP Project on 5g Air Interface Below 6 GHz," tech. rep.

[4] J. G. Andrews, S. Buzzi, W. Choi, S. V. Hanly, A. Lozano, A. C. K. Soong, and J. C. Zhang, "What Will 5g Be?," *IEEE Journal on Selected Areas in Communications*, vol. 32, pp. 1065–1082, June 2014.

[5] D. Tse and P. Viswanath, *Fundamentals of Wireless Communication*. Cambridge: Cambridge University Press, May 2005.

[6] J. Proakis and M. Salehi, *Digital Communications, 5th Edition*. Boston, Mass.: McGraw-Hill Education, 5th edition ed., Nov. 2007.

[7] A. Peled and A. Ruiz, "Frequency domain data transmission using reduced computational complexity algorithms," in *Acoustics, Speech, and Signal Processing, IEEE International Conference on ICASSP '80.*, vol. 5, pp. 964–967, Apr. 1980.

[8] H. S. Stone, "R66-50 An Algorithm for the Machine Calculation of Complex Fourier Series," *IEEE Transactions on Electronic Computers*, vol. EC-15, pp. 680–681, Aug. 1966.

[9] P. Siohan, C. Siclet, and N. Lacaille, "Analysis and design of OFDM/OQAM systems based on filterbank theory," *IEEE Transactions on Signal Processing*, vol. 50, pp. 1170–1183, May 2002.

[10] T. Marzetta, "How Much Training is Required for Multiuser Mimo?," in *Fortieth Asilomar Conference on Signals, Systems and Computers, 2006. ACSSC '06*, pp. 359–363, Oct. 2006.

[11] T. Marzetta, "Noncooperative Cellular Wireless with Unlimited Numbers of Base Station Antennas," *IEEE Transactions on Wireless Communications*, vol. 9, pp. 3590–3600, Nov. 2010.

[12] H. Q. Ngo, E. Larsson, and T. Marzettat, "Uplink power efficiency of multiuser MIMO with very large antenna arrays," in *2011 49th Annual Allerton Conference on Communication, Control, and Computing (Allerton)*, pp. 1272–1279, Sept. 2011.

[13] F. Rusek, D. Persson, B. K. Lau, E. Larsson, T. Marzetta, O. Edfors, and F. Tufvesson, "Scaling Up MIMO: Opportunities and Challenges with Very Large Arrays," *IEEE Signal Processing Magazine*, vol. 30, pp. 40–60, Jan. 2013.

[14] J. Hoydis, S. ten Brink, and M. Debbah, "Massive MIMO in the UL/DL of Cellular Networks: How Many Antennas Do We Need?," *IEEE Journal on Selected Areas in Communications*, vol. 31, pp. 160–171, Feb. 2013.

[15] H. Q. Ngo, E. Larsson, and T. Marzetta, "Energy and Spectral Efficiency of Very Large Multiuser MIMO Systems," *IEEE Transactions on Communications*, vol. 61, pp. 1436–1449, Apr. 2013.

[16] J. Hoydis, K. Hosseini, S. T. Brink, and M. Debbah, "Making smart use of excess antennas: Massive MIMO, small cells, and TDD," *Bell Labs Technical Journal*, vol. 18, pp. 5–21, Sept. 2013.

[17] E. Björnson, J. Hoydis, M. Kountouris, and M. Debbah, "Massive MIMO Systems With Non-Ideal Hardware: Energy Efficiency, Estimation, and Capacity Limits," *IEEE Transactions on Information Theory*, vol. 60, pp. 7112–7139, Nov. 2014.

[18] U. Gustavsson, C. Sanchéz-Perez, T. Eriksson, F. Athley, G. Durisi, P. Landin, K. Hausmair, C. Fager, and L. Svensson, "On the impact of hardware impairments on massive MIMO," in *2014 IEEE Globecom Workshops (GC Wkshps)*, pp. 294–300, Dec. 2014.

[19] E. Björnson, M. Bengtsson, and B. Ottersten, "Optimal Multiuser Transmit Beamforming: A Difficult Problem with a Simple Solution Structure," *IEEE Signal Processing Magazine*, vol. 31, pp. 142–148, July 2014.

[20] E. Björnson, L. Sanguinetti, J. Hoydis, and M. Debbah, "Designing multi-user MIMO for energy efficiency: When is massive MIMO the answer?," in *2014 IEEE Wireless Communications and Networking Conference (WCNC)*, pp. 242–247, Apr. 2014.

[21] S. E. El-Khamy, K. H. Moussa, and A. A. El-Sherif, "C5. Performance analysis of massive MIMO multiuser transmit beamforming techniques over generalized spatial channel model," in *Radio Science Conference (NRSC), 2015 32nd National*, pp. 139–146, Mar. 2015.

[22] X. Gao, O. Edfors, F. Rusek, and F. Tufvesson, "Massive MIMO Performance Evaluation Based on Measured Propagation Data," *IEEE Transactions on Wireless Communications*, vol. 14, pp. 3899–3911, July 2015.

[23] E. Larsson, O. Edfors, F. Tufvesson, and T. Marzetta, "Massive MIMO for next generation wireless systems," *IEEE Communications Magazine*, vol. 52, pp. 186–195, Feb. 2014.

[24] J. Wu and P. Fan, "A Survey on High Mobility Wireless Communications: Challenges, Opportunities and Solutions," *IEEE Access*, vol. 4, pp. 450–476, 2016.

[25] Y. Hu, H. Li, Z. Chang, and Z. Han, "Scheduling Strategy for Multimedia Heterogeneous High-Speed Train Networks," *IEEE Transactions on Vehicular Technology*, vol. 66, pp. 3265–3279, Apr. 2017.

[26] L. Tian, J. Li, Y. Huang, J. Shi, and J. Zhou, "Seamless Dual-Link Handover Scheme in Broadband Wireless Communication Systems for High-Speed Rail," *IEEE Journal on Selected Areas in Communications*, vol. 30, pp. 708–718, May 2012.

[27] O. B. Karimi, J. Liu, and C. Wang, "Seamless Wireless Connectivity for Multimedia Services in High Speed Trains," *IEEE Journal on Selected Areas in Communications*, vol. 30, pp. 729–739, May 2012.

[28] J. Li and M. Kavehrad, "Effects of time selective multipath fading on OFDM systems for broadband mobile applications," *IEEE Communications Letters*, vol. 3, pp. 332–334, Dec. 1999.

[29] M. Patzold, C. X. Wang, and B. O. Hogstad, "Two new sum-of-sinusoids-based methods for the efficient generation of multiple uncorrelated rayleigh fading waveforms," *IEEE Transactions on Wireless Communications*, vol. 8, pp. 3122–3131, June 2009.

[30] B. L. Floch, M. Alard, and C. Berrou, "Coded orthogonal frequency division multiplex [TV broadcasting]," *Proceedings of the IEEE*, vol. 83, pp. 982–996, June 1995.

[31] R. Haas and J.-C. Belfiore, "A Time-Frequency Well-localized Pulse for Multiple Carrier Transmission," *Wireless Personal Communications*, vol. 5, pp. 1–18, July 1997.

[32] T. Strohmer and S. Beaver, "Optimal OFDM design for time-frequency dispersive channels," *IEEE Transactions on Communications*, vol. 51, pp. 1111–1122, July 2003.

[33] B. Farhang-Boroujeny, "OFDM Versus Filter Bank Multicarrier," *IEEE Signal Processing Magazine*, vol. 28, pp. 92–112, May 2011.

[34] T. Naveh, "Mobile Backhaul: Fiber vs. Microwaves. Case Study Analyzing Various Backhaul Technology Strategies," white Paper, Oct. 2009.

[35] B. Li, D. Zhu, and P. Liang, "Small Cell In-Band Wireless Backhaul in Massive MIMO Systems: A Cooperation of Next-Generation Techniques," *IEEE Transactions on Wireless Communications*, vol. 14, pp. 7057–7069, Dec. 2015.

[36] L. Sanguinetti, A. L. Moustakas, and M. Debbah, "Interference Management in 5g Reverse TDD HetNets With Wireless Backhaul: A Large System Analysis," *IEEE Journal on Selected Areas in Communications*, vol. 33, pp. 1187–1200, June 2015.

[37] H. Tabassum, A. H. Sakr, and E. Hossain, "Massive MIMO-Enabled Wireless Backhauls for Full-Duplex Small Cells," in *2015 IEEE Global Communications Conference (GLOBECOM)*, pp. 1–6, Dec. 2015.

[38] H. Tabassum, A. H. Sakr, and E. Hossain, "Analysis of Massive MIMO-Enabled Downlink Wireless Backhauling for Full-Duplex Small Cells," *IEEE Transactions on Communications*, vol. 64, pp. 2354–2369, June 2016.

[39] T. K. Vu, M. Bennis, S. Samarakoon, M. Debbah, and M. Latva-aho, "Joint In-Band Backhauling and Interference Mitigation in 5g Heterogeneous Networks," in *European Wireless 2016; 22th European Wireless Conference*, pp. 1–6, May 2016.

[40] S. Jaeckel, L. Raschkowski, K. Börner, L. Thiele, F. Burkhardt, and E. Eberlein, "QuaDRiGa - Quasi Deterministic Radio Channel Generator, User Manual and Documentation," Tech. Rep. v1.4.8-571, Fraunhofer Heinrich Hertz Institute, 2016.

[41] M. G. Bellanger, "Specification and design of a prototype filter for filter bank based multicarrier transmission," in *2001 IEEE International Conference on Acoustics, Speech, and Signal Processing, 2001. Proceedings. (ICASSP '01)*, vol. 4, pp. 2417–2420 vol.4, 2001.

[42] Cisco, "Cisco Visual Networking Index: Global Mobile Data Traffic Forecast Update, 2015-2020," tech. rep., Feb. 2016.

[43] G. P. Fettweis, "The Tactile Internet: Applications and Challenges," *IEEE Vehicular Technology Magazine*, vol. 9, pp. 64–70, Mar. 2014.

[44] Y. C. Chow, J. P. McGeehan, and A. R. Nix, "A simplified error bound analysis for M-DPSK in fading channels with diversity reception," in *1994 IEEE GLOBECOM. Communications: Communications Theory Mini-Conference Record,*, pp. 13–18, Nov. 1994.

[45] H. Fu and P. Y. Kam, "Effect of Doppler shift on performance of binary DPSK over fast Rician fading channels with diversity reception," in *2008 International Symposium on Information Theory and Its Applications*, pp. 1–6, Dec. 2008.

[46] P. Almers, E. Bonek, A. Burr, N. Czink, M. Debbah, V. Degli-Esposti, H. Hofstetter, P. Kyösti, D. Laurenson, G. Matz, A. F. Molisch, C. Oestges, and H. Özcelik, "Survey of Channel and Radio Propagation Models for Wireless MIMO Systems," *EURASIP Journal on Wireless Communications and Networking*, vol. 2007, p. 019070, Dec. 2007.

[47] "Spatial Channel Model for Multiple-Input Multiple Output Simulations," Tech. Rep. TR 25.996, 3GPP.

[48] "Final Report on Link Level and System Level Channel Models," Tech. Rep. D5.4, v.1.4, WINNER I, 2005.

[49] "WINNER II Channel Models," Tech. Rep. D1.1.2, v.1.2, WINNER II, 2008.

[50] "WINNER+ Final Channel Models," Tech. Rep. D5.3, v.1.0, WINNER+, 2010.

[51] "METIS Channel Models," Tech. Rep. D1.4, v.3, METIS, 2015.

[52] "Study on channel model for frequencies from 0.5 to 100 GHz," Tech. Rep. TR 38.901, 3GPP.

[53] "Study on 3d channel model for LTE," Tech. Rep. TR 36.873, 3GPP.

[54] S. Jaeckel, L. Raschkowski, K. Börner, and L. Thiele, "QuaDRiGa: A 3-D Multi-Cell Channel Model With Time Evolution for Enabling Virtual Field Trials," *IEEE Transactions on Antennas and Propagation*, vol. 62, pp. 3242–3256, June 2014.

[55] R. Chang, "High-speed multichannel data transmission with bandlimited orthogonal signals," *Bell System Technical Journal*, vol. 45, pp. 1775–1796, 1966.

[56] S. Weinstein and P. Ebert, "Data Transmission by Frequency-Division Multiplexing Using the Discrete Fourier Transform," *IEEE Transactions on Communication Technology*, vol. 19, pp. 628–634, Oct. 1971.

[57] B. Saltzberg, "Performance of an Efficient Parallel Data Transmission System," *IEEE Transactions on Communication Technology*, vol. 15, pp. 805–811, Dec. 1967.

[58] H. S. Malvar, "Lapped transforms for efficient transform/subband coding," *IEEE Transactions on Acoustics, Speech, and Signal Processing*, vol. 38, pp. 969–978, June 1990.

[59] E. Björnson, M. Kountouris, and M. Debbah, "Massive MIMO and small cells: Improving energy efficiency by optimal soft-cell coordination," in *ICT 2013*, pp. 1–5, May 2013.

[60] S. Verdú, *Multiuser detection*. Cambridge: Cambridge Univ. Press, reprinted ed., 2005. OCLC: 255583622.

[61] M. Costa, "Writing on dirty paper," *IEEE Transactions on Information Theory*, vol. 29, pp. 439–441, May 1983.

[62] W. Yu and J. M. Cioffi, "Trellis precoding for the broadcast channel," in *IEEE Global Telecommunications Conference, 2001. GLOBECOM '01*, vol. 2, pp. 1344–1348 vol.2, 2001.

[63] R. Zamir, S. Shamai, and U. Erez, "Nested linear/lattice codes for structured multiterminal binning," *IEEE Transactions on Information Theory*, vol. 48, pp. 1250–1276, June 2002.

[64] T. K. Y. Lo, "Maximum ratio transmission," *IEEE Transactions on Communications*, vol. 47, pp. 1458–1461, Oct. 1999.

[65] M. Fink, "Time reversal of ultrasonic fields. I. Basic principles," *IEEE Transactions on Ultrasonics, Ferroelectrics, and Frequency Control*, vol. 39, pp. 555–566, Sept. 1992.

[66] A. Khaleghi, G. E. Zein, and I. H. Naqvi, "Demonstration of Time-Reversal in Indoor Ultra-Wideband Communication: Time Domain Measurement," in *2007 4th International Symposium on Wireless Communication Systems*, pp. 465–468, Oct. 2007.

[67] D.-T. P. Huy, *Time reversal for mobile networks.* phdthesis, INSA de Rennes, Dec. 2015.

[68] T. Dubois, M. Hélard, M. Crussière, and C. Germond, "Performance of time reversal precoding technique for MISO-OFDM systems," *EURASIP Journal on Wireless Communications and Networking*, vol. 2013, no. 1, p. 260, 2013.

[69] S. K. Mohammed and E. G. Larsson, "Single-User Beamforming in Large-Scale MISO Systems with Per-Antenna Constant-Envelope Constraints: The Doughnut Channel," *IEEE Transactions on Wireless Communications*, vol. 11, pp. 3992–4005, Nov. 2012.

[70] S. K. Mohammed and E. G. Larsson, "Per-Antenna Constant Envelope Precoding for Large Multi-User MIMO Systems," *IEEE Transactions on Communications*, vol. 61, pp. 1059–1071, Mar. 2013.

[71] D. J. Love and R. W. Heath, "Equal gain transmission in multiple-input multiple-output wireless systems," *IEEE Transactions on Communications*, vol. 51, pp. 1102–1110, July 2003.

[72] H. Fu, M. Crussière, and M. Hélard, "BER Analysis for Equal Gain Transmission in Downlink Multiuser MIMO Systems," *IEEE Wireless Communications Letters*, vol. 4, pp. 533–536, Oct. 2015.

[73] C. B. Peel, B. M. Hochwald, and A. L. Swindlehurst, "A vector-perturbation technique for near-capacity multiantenna multiuser communication-part I: channel inversion and

regularization," *IEEE Transactions on Communications*, vol. 53, pp. 195–202, Jan. 2005.

[74] X. Cai and G. B. Giannakis, "Bounding performance and suppressing intercarrier interference in wireless mobile OFDM," *IEEE Transactions on Communications*, vol. 51, pp. 2047–2056, Dec. 2003.

[75] S. Chen, G. Dai, and W. Rao, "ICI mitigation and diversity gain for OFDM systems in time-varying multipath fading channels," *European Transactions on Telecommunications*, vol. 22, pp. 61–67, Mar. 2011.

[76] S. J. Nawaz, N. M. Khan, M. N. Patwary, and M. Moniri, "Effect of Directional Antenna on the Doppler Spectrum in 3-D Mobile Radio Propagation Environment," *IEEE Transactions on Vehicular Technology*, vol. 60, pp. 2895–2903, Sept. 2011.

[77] C. Ziółkowski and J. M. Kelner, "Antenna pattern in three-dimensional modelling of the arrival angle in simulation studies of wireless channels," *Antennas Propagation IET Microwaves*, vol. 11, no. 6, pp. 898–906, 2017.

[78] O. Norklit and R. G. Vaughan, "Angular partitioning to yield equal Doppler contributions," *IEEE Transactions on Vehicular Technology*, vol. 48, pp. 1437–1442, Sept. 1999.

[79] D. Chizhik, "Slowing the time-fluctuating MIMO channel by beam forming," *IEEE Transactions on Wireless Communications*, vol. 3, pp. 1554–1565, Sept. 2004.

[80] I. Shubhi and H. Murata, "Dynamic Precoder for Massive MIMO in the Presence of Large Doppler Spread," in *2017 IEEE 85th Vehicular Technology Conference (VTC Spring)*, pp. 1–5, June 2017.

[81] S. Serbetli and S. Baggen, "Doppler Compensation by Using Dual Antenna for Mobile OFDM Systems," in *VTC Spring 2008 - IEEE Vehicular Technology Conference*, pp. 1499–1503, May 2008.

[82] S. Serbetli, "Doppler compensation for mobile OFDM systems with multiple receive antennas," in *2012 19th IEEE Symposium on Communications and Vehicular Technology in the Benelux (SCVT)*, pp. 1–6, Nov. 2012.

[83] K. Gopala and D. Slock, "MIMO OFDM capacity maximizing beamforming for large Doppler scenarios," in *2016 IEEE 17th International Workshop on Signal Processing Advances in Wireless Communications (SPAWC)*, pp. 1–6, July 2016.

[84] K. Gopala and D. Slock, "High Doppler MIMO OFDM capacity maximizing spatial transceivers exploiting excess cyclic prefix," in *2016 International Symposium on Wireless Communication Systems (ISWCS)*, pp. 491–496, Sept. 2016.

[85] P. Banelli, S. Buzzi, G. Colavolpe, A. Modenini, F. Rusek, and A. Ugolini, "Modulation Formats and Waveforms for 5g Networks: Who Will Be the Heir of OFDM?: An overview of alternative modulation schemes for improved spectral efficiency," *IEEE Signal Processing Magazine*, vol. 31, pp. 80–93, Nov. 2014.

[86] B. Hirosaki, "An Orthogonally Multiplexed QAM System Using the Discrete Fourier Transform," *IEEE Transactions on Communications*, vol. 29, pp. 982–989, July 1981.

[87] A. Farhang, N. Marchetti, L. Doyle, and B. Farhang-Boroujeny, "Filter Bank Multicarrier for Massive MIMO," in *Vehicular Technology Conference (VTC Fall), 2014 IEEE 80th*, pp. 1–7, Sept. 2014.

[88] A. Aminjavaheri, A. Farhang, N. Marchetti, L. Doyle, and B. Farhang-Boroujeny, "Frequency spreading equalization in multicarrier massive MIMO," in *2015 IEEE International Conference on Communication Workshop (ICCW)*, pp. 1292–1297, June 2015.

[89] R. H. Clarke, "A statistical theory of mobile-radio reception," *The Bell System Technical Journal*, vol. 47, pp. 957–1000, July 1968.

[90] W. C. Jakes, ed., *Microwave mobile communications*. An IEEE Press classic reissue, New York, NY: IEEE Press [u.a.], nachdr. ed., 1995. OCLC: 249569885.

[91] The MathWorks, inc., *Communication System Toolbox (TM) User's Guide*. Natick, Massachusetts: The MathWorks, inc., 2016.

[92] "User Equipment (UE) Radio Transmission and Reception.," Tech. Rep. TS 36.101, 3GPP.

[93] "Base Station (BS) Radio Transmission and Reception.," Tech. Rep. TS 36.104, 3GPP.

[94] R. Alieiev, T. Hehn, A. Kwoczek, and T. Kürner, "Sensor-based communication prediction for dynamic Doppler-shift compensation," in *2017 15th International Conference on ITS Telecommunications (ITST)*, pp. 1–7, May 2017.

[95] K. Chelli and T. Herfet, "Doppler shift compensation in Vehicular Communication Systems," in *2016 2nd IEEE International Conference on Computer and Communications (ICCC)*, pp. 2188–2192, Oct. 2016.

[96] D. Pinchon and P. Siohan, "Derivation of analytical expressions for flexible PR low complexity FBMC systems," in *Signal Processing Conference (EUSIPCO), 2013 Proceedings of the 21st European*, pp. 1–5, Sept. 2013.

[97] M. Bellanger, "Physical layer for future broadband radio systems," in *2010 IEEE Radio and Wireless Symposium (RWS)*, pp. 436–439, Jan. 2010.

[98] "Digital land mobile radio communications," Tech. Rep. COST 207, COST, 1989.

[99] "ICT Facts and Figures 2017," tech. rep., International Telecommunication Union (ITU).

[100] S. Hur, T. Kim, D. J. Love, J. V. Krogmeier, T. A. Thomas, and A. Ghosh, "Millimeter Wave Beamforming for Wireless Backhaul and Access in Small Cell Networks," *IEEE Transactions on Communications*, vol. 61, pp. 4391–4403, Oct. 2013.

[101] A. A. Huurdeman, *Radio-relay systems*. The Artech House telecommunications library, Boston: Artech House, 1995. OCLC: 832307035.

[102] K. Balachandran, J. Kang, K. Karakayali, and J. Singh, "Capacity Benefits of Relays with In-Band Backhauling in Cellular Networks," in *2008 IEEE International Conference on Communications*, pp. 3736–3742, May 2008.

[103] S. Chia, M. Gasparroni, and P. Brick, "The next challenge for cellular networks: backhaul," *IEEE Microwave Magazine*, vol. 10, pp. 54–66, Aug. 2009.

[104] R. Taori and A. Sridharan, "Point-to-multipoint in-band mmwave backhaul for 5g networks," *IEEE Communications Magazine*, vol. 53, pp. 195–201, Jan. 2015.

[105] J. Góra and S. Redana, "Resource management issues for multi-carrier relay-enhanced systems," *EURASIP Journal on Wireless Communications and Networking*, vol. 2012, p. 124, Mar. 2012.

[106] T. M. de Moraes, M. D. Nisar, A. A. Gonzalez, and E. Seidel, "Resource allocation in relay enhanced LTE-Advanced networks," *EURASIP Journal on Wireless Communications and Networking*, vol. 2012, p. 364, Dec. 2012.

[107] S. Lagen, A. Agustin, and J. Vidal, "Network-MIMO for downlink in-band relay transmissions," *EURASIP Journal on Wireless Communications and Networking*, vol. 2013, p. 13, Jan. 2013.

[108] Z. Gao, L. Dai, D. Mi, Z. Wang, M. A. Imran, and M. Z. Shakir, "MmWave massive-MIMO-based wireless backhaul for the 5g ultra-dense network," *IEEE Wireless Communications*, vol. 22, pp. 13–21, Oct. 2015.

[109] K. Yu, M. Bengtsson, B. Ottersten, and M. Beach, "Narrowband MIMO Channel Modeling for LOS Indoor Scenarios," in *DIVA*, 2002.

[110] L. Cottatellucci, M. Debbah, and R. R. Muller, "On the capacity of MIMO rice channels," *42nd Annual Allerton Conference on Communication, Control and Computing*, 2004.

[111] K. Sakaguchi, H.-Y.-E. CHUA, and K. Araki, "MIMO channel capacity in an indoor Line-Of-Sight (LOS) environment," *IEICE Transactions on Communications*, vol. E88B, July 2005.

[112] S. Boyd and L. Vandenberghe, *Convex Optimization*. Cambridge: Cambridge University Press, 2004.

INSA de RENNES
Service des Formations

AVIS DU JURY SUR LA REPRODUCTION DE LA THESE SOUTENUE

Titre de la thèse:
Massive MIMO pour des scénarios 5G avec formes d'ondes OFDM et FBMC/OQAM

Nom Prénom de l'auteur : BAZIN ALEXIS

Membres du jury :
- Monsieur DEBBAH Mérouane
- Madame HELARD Maryline
- Monsieur ROVIRAS Daniel
- Monsieur ABDEL NOUR Charbel
- Monsieur SIMON Eric
- Monsieur JAHAN Bruno

Président du jury : ROVIRAS Daniel

Date de la soutenance : 24 Septembre 2018

Reproduction de la these soutenue

☒ Thèse pouvant être reproduite en l'état
☐ Thèse pouvant être reproduite après corrections suggérées

Fait à Rennes, le 24 Septembre 2018

Signature du président de jury

Le Directeur,

M'hamed DRISSI

Titre : Massive MIMO pour des Scénarios 5G avec Formes d'Ondes OFDM et FBMC/OQAM

Mots clés : Massive MIMO, 5G, OFDM, FBMC/OQAM

Résumé : Avec l'augmentation du trafic de données, la multiplication des objets connectés et la diversification des types de communication, la cinquième génération de réseaux cellulaires (5G) doit relever un grand nombre de défis. Dans ce contexte, les systèmes « massive MIMO » présentent de nombreux avantages en utilisant un grand nombre d'antennes combiné à des techniques de traitement de signal adaptées. De plus, l'utilisation de la modulation FBMC/OQAM au lieu de la modulation OFDM pourrait améliorer la performance des systèmes dans certaines situations.
En premier lieu, cette thèse se centre sur des scénarios véhiculaires. En particulier, les systèmes « massive MIMO » sont proposés dans le but de combattre les interférences dues à l'effet Doppler pour la voie montante. Nous montrons ainsi de manière analytique que l'augmentation du nombre d'antennes implique une réduction drastique de l'impact de l'effet Doppler. De plus, les performances des modulations OFDM et FBMC/OQAM sont comparées dans ce contexte pour des environnements « Non-Line-Of-Sight » (NLOS) et « Line-Of-Sight » (LOS).
Le second scénario étudié dans cette thèse considère les communications dans des zones mal desservies. Dans ce contexte, les systèmes « massive MIMO » permettent de créer un lien sans-fil longue-portée de type « backhaul » entre deux stations de base. Ainsi, le coût de déploiement des réseaux cellulaires est réduit. Dans cette thèse, un nouveau précodeur « massive MIMO » est proposé dans le but d'utiliser la même bande de fréquence pour les liens accès et « backhaul ». De plus, l'impact d'une désynchronisation entre les liens d'accès et le lien « backhaul » est étudié et l'utilisation de la modulation FBMC/OQAM pour le lien « backhaul » est examinée.

Title : Massive MIMO for 5G Scenarios with OFDM and FBMC/OQAM Waveforms

Keywords : Massive MIMO, 5G, OFDM, FBMC/OQAM

Abstract : With the increase of the global data traffic, the multiplication of connected devices and the diversification of the communication types, the fifth generation of cellular networks (5G) has to overcome a series of challenges. In this context, massive MIMO systems hold a wide range of benefits by using a large number of antennas combined with appropriate signal processing techniques. Additionally, the use of the FBMC/OQAM modulation instead of the classical OFDM modulation may enhance the performance of the systems in certain situations.
Firstly, this thesis focuses on vehicular scenarios. In particular, massive MIMO systems are proposed to overcome the interference due to the Doppler effect for the uplink. We thus analytically highlight that increasing the number of receive antennas induces a drastic reduction of the impact of the Doppler effect. Moreover, the performance of the OFDM and the FBMC/OQAM modulations are compared in this context for Non-Line-Of-Sight (NLOS) and Line-Of-Sight (LOS) environments.
The second scenario investigated in this thesis considers communications in wide underserved areas. In this context, massive MIMO systems allow to create a long-range wireless backhaul link between two base stations. Thereby, the cost of deployment of the cellular networks is reduced. In this thesis, a new massive MIMO precoding technique is proposed in order to use the same frequency band for the backhaul link and the access links. Moreover, the impact of a desynchronization between the backhaul link and the access links is studied and the use of the FBMC/OQAM modulation for the backhaul link is discussed.